Cranfield University

Ioannis Goulos

Simulation Framework Development for the Multidisciplinary Optimisation of Rotorcraft

SCHOOL OF ENGINEERING

PhD Thesis

Cranfield University
School of Engineering
PhD Thesis

2012

Ioannis Goulos

Simulation Framework Development for the Multidisciplinary Optimisation of Rotorcraft

Supervisor: Dr. V. Pachidis

This thesis is submitted in partial fulfillment of the requirements for the degree of Doctor of Philosophy

Acknowledgements

First of all, I would like to express my gratitude to my academic supervisor, Dr. V. Pachidis, for his continuous guidance and support throughout the entire period of my research activities at Cranfield. I also wish to extend my thanks and gratitude to Professor P. Pilidis from the department of Power & Propulsion, for providing me with the opportunity to pursue a PhD degree at Cranfield University. Thanks are also due to Dr. Vishal Sethi for his insightful advice and continuing support throughout the years of my studies.

I am forever indebted to my parents for all their love, understanding and encouragement towards overcoming boundaries in pursue of self-development. The magnitude of their contribution to the current status of my life has been truly immeasurable and I will forever be grateful.

I would also like to mention my gratitude and admiration towards my mentor, Professor Anestis Kalfas from the Department of Mechanical Engineering of the Aristotle University in Greece, for introducing me into the wonderful world of research as well as for being a role model for me during the last seven years of my life.

Last but not least, I would like to thank all of my colleagues and friends at Cranfield, for all the beautiful moments we shared throughout the three-year period of my studies. In particular, I want to express my gratitude to my friends Panos, Perikils and Pavlos for all the breaks we had in each other's offices, sharing our mutual excitement for our work, while attempting to temporarily rest our minds before digging in deep once again.

Abstract

The effective and efficient evaluation of conceptual product designs prior to manufacturing of prototypes, is of utmost importance for any industrial activity. The rotorcraft industry is no different. Accurate, thorough and cost-effective evaluation of conceptual rotorcraft designs requires an equivalently rigorous and simultaneously affordable methodology covering all aspects relative. The associated issues to be tackled are indeed multi-dimensional and include trim performance, rotor blade structural loads prediction, engine performance, mission analysis and associated environmental impact.

The aforementioned topics are now raising even more interest as rotorcraft traffic is expected to grow sharply within the next 20 years. Current rotorcraft operations imply the consumption of the equivalent of 400,000 tons of aviation fuel per year, only with regards to the European region. Maintaining current rotorcraft technologies is expected to lead to a quadruplicating of this figure. This is a direct result of the expected traffic augmentation. In recognition of this trend, a wide range of research & development activities is currently being undertaken at national and European levels. The objective is to effectively return within 20 years to the present global level of environmental impact, while sustaining the expected growth of rotorcraft services.

The objective set above is indeed an ambitious one. Due to the rather short time-scales involved, its realization requires for focus to be placed predominantly on the design of operational procedures. It is however realized that, in order to manage the environmental impact of civil rotorcraft aviation within larger time-scales, options concerning the design of conceptual configurations as well as incorporated operational procedures, need to be explored.

Two fundamental requirements are therefore identified and addressed within this work. The 1^{st} lies with regards to a generic methodology capable of designing optimum operational procedures in terms of fuel burn, gaseous emissions and ground noise impact. The 2^{nd} can be designated as a design assessment approach, capable of estimating the overall fuel consumption with regards to any designated operation. The employed method has to be capable of being utilized within the task of design while simultaneously maintaining a

reasonable computational overhead so as to be applicable in the context of multidisciplinary optimization.

This work elaborates on the development and application of an integrated approach, targeting the comprehensive assessment of combined helicopter–engine designs, within complete, three-dimensional operations. A series of individual modeling methods has been developed, each applicable to a different aspect of helicopter flight dynamics and performance. These comprise rotor blade modal analysis, aeroelasticity, flight dynamics trim solution, engine performance and three-dimensional flight path definition. The individual mathematical models are elaborately integrated within a numerical procedure solving for the total mission fuel consumption. Extensive validation with existing experimental and numerical data has been waged during each step of the development process.

The aspect of multidisciplinary design of optimum rotorcraft operations in terms of fuel burn and environmental impact is also tackled within the context of this work. An existing integrated tool capable of estimating the performance and emitted noise of any defined rotorcraft configuration within any designated mission has been incorporated. A comprehensive and cost-effective optimization strategy has been structured. The methodology has been applied to two generic – baseline missions representative of current rotorcraft operations. Missions optimally designed in a multidisciplinary manner for fuel burn, gaseous emissions and ground noise impact have been obtained.

The contribution to knowledge arising from the successful completion of this work, broadly comprises the development of methodologies applicable to the following aspects of civil rotorcraft aviation: (i) Comprehensive analysis of the overall flight dynamics and performance of any designated helicopter–engine integrated system, within realistically defined three-dimensional missions; (ii) Multidisciplinary design of optimum rotorcraft operations in terms of fuel consumption, gaseous and ground noise impact; Further to the above, contribution has been made through the analytical development of modeling approaches with application to: (i) Rotor blade modal analysis; (ii) Treatment of rotor blade flexibility; (iii) Rotor–fuselage aerodynamic interaction. The developed analytical methods have been utilized within this work to facilitate the achievement of the set objectives. The potential to comprehensively evaluate integrated helicopter–engine systems within complete three-dimensional operations, based on the solution of the aeroelastic behavior of the main rotor is demonstrated. The ability to design optimum operations in a multidisciplinary fashion using only a single design criterion has been exhibited.

Contents

List of Tables

List of Figures

Nomenclature

Roman Symbols

$\tilde{()}_{/A_i}$	Vector relative to the origin of the rotating reference frame of the i^{th} blade A_i
$\tilde{e}_x^{A_i},\ \tilde{e}_y^{A_i},\ \tilde{e}_z^{A_i}$	Rotating blade reference frame $A_i,\ i = 1, ...N_b$ unit vectors
$\tilde{e}_x^b,\ \tilde{e}_y^b,\ \tilde{e}_z^b$	Local blade element coordinate system unit vectors
$\tilde{e}_x^{hw},\ \tilde{e}_y^{hw},\ \tilde{e}_z^{hw}$	Hub-wind axes reference frame unit vectors
$\tilde{e}_x,\ \tilde{e}_y,\ \tilde{e}_z$	Global non-rotating O reference frame unit vectors
$\{\bar{q}^{flap/lag}\}_i$	i^{th} eigenvector of Lagrange's equation coefficient matrix $[A^{flap/lag}_{Lagrange}]$
$[A^{flap/lag}_{Lagrange}]$	Lagrange's equation coefficient matrix
$[A_{Bernoulli}]$	Bernoulli–Euler matrix of equation coefficients
$[A_i]$	Global O to rotating reference frame A_i transformation matrix, $i = 1, ...N_b$
$[G]^{flap/lag}$	Overall effective stiffness inter-modal coupling matrix
$[HW]$	Hub-wind axes system HW to global non-rotating reference frame O transformation matrix
$[M]^{flap/lag}$	Inertial inter-modal coupling matrix
$[T_i^b]$	Global non-rotating reference frame O to local blade element coordinate system b transformation matrix, $= [\lambda][\theta][\beta][\zeta][A_i]$
$\bar{u},\ \bar{v},\ \bar{w}$	Normalized fuselage induced velocity perturbations relative to the main rotor tip path plane
Δt	Employed time-step during the time marching procedure – Chapter 4, *sec*

Δt	Static time-step for mission analysis – Chapters 6, 7, *sec*
$\Delta W^{flap/lag}$	Virtual work done by the centrifugal force, *Joules*
$\tilde{\dot{u}}_o$	Translational acceleration vector of the global non-rotating O frame, $= [\dot{u}_o\ \dot{v}_o\ \dot{w}_o]^T$
$\tilde{f}^b_{aero}$, $\tilde{m}^b_{aero}$	Blade element aerodynamic force and moment per unit length vectors
$\tilde{F}^O_i(t)$, $\tilde{T}^O_i(t)$	Force and moment vectors of the i^{th} blade, $i = 1, ...N_b$
$\tilde{F}^O_{rotor}(t)$, $\tilde{F}^{hw}_{rotor}(t)$	Total force vector exerted by the main rotor on the aircraft fuselage, N
$\tilde{n}$	Unit vector perpendicular to dS of S_b, positive towards the direction of the potential jump
$\tilde{r}^{A_i}_{p/A_i}$	Position vector of beam element $p(r,t)$ relative to the origin of A_i
$\tilde{r}^{b,offset}_p$	Airfoil center gravity offset vector from the blade elastic axis
$\tilde{r}^O_{p/O}$	Position vector of beam element $p(r,t)$ relative to the origin of O
$\tilde{r}_{A_i/O}$	Position vector of the origin of A_i
$\tilde{T}^O_{i,offset}(t)$	Moment vector of the i^{th} blade due to root/hinge offset, $i = 1, ...N_b$
$\tilde{T}^O_{i,root}(t)$	Moment vector of the i^{th} blade due to root/hinge spring stiffness, $i = 1, ...N_b$
$\tilde{T}^O_{rotor}(t)$, $\tilde{T}^{hw}_{rotor}(t)$	Total moment vector exerted by the main rotor on the aircraft fuselage, Nm
$\tilde{u}^{A_i}_{p/A_i}$, $\tilde{a}^{A_i}_{p/A_i}$	Linear velocity and acceleration vectors of beam element $p(r,t)$ relative to the origin of A_i
$\tilde{u}^O_p$, $\tilde{u}^b_p$, $\tilde{a}^O_p$, $\tilde{a}^b_p$	Absolute linear velocity and acceleration vectors of beam element $p(r,t)$
$\tilde{u}_o$	Translational velocity vector of the global non-rotating O frame, $= [u_o\ v_o\ w_o]^T$
$\tilde{u}_{A_i/O}$, $\tilde{a}_{A_i/O}$	Absolute linear velocity and acceleration vectors of the origin of A_i

$\tilde{v}$	Induced velocity perturbation vector $= [u\ v\ w]^T$
$\tilde{V}_\infty$	Free-stream velocity vector, $= [U_\infty\ V_\infty\ W_\infty]^T$
$\{X_{Bernoulli}\}$	Bernoulli–Euler vector of integration constants, $= [A\ B\ C\ D]^T$
a	Rotor shaft angle relative to the free-stream flow – Chapter 4, deg
$A(r)$	Blade cross-sectional area, m^2
A, B, C, D	Bernoulli–Euler mode shape equation integration constants
a_f	Fuselage incidence, deg
A_i	Rotating reference frame of the i^{th} blade index, $i = 1, ...N_b$
a_s	Rotor shaft incidence – Chapter 5, deg
B_j	Influence coefficient of the j^{th} source panel element on the evaluation point with coordinates $(x,\ y,\ z)$
$C_{norm,i}$	Normalization constant for the i^{th} assumed modal function
$d\tilde{f}_p^O$, $d\tilde{m}_p^O$	Beam element total differential force and moment loads vectors
dF_x, dF_y, dF_z	Centrifugal force components acting on a beam element of differential mass dm on the X, Y and Z axes respectively, N
dm	Beam element differential mass, $= \rho A(r)dr$, kg
dt	Dynamic time-step – Chapter 7, sec
E	Material Young's modulus, Pa
e	Blade root/hinge offset distance from the center of rotation as a fraction of rotor blade radius
$f_{i,j}^{flap/lag}$	Hub-spring inter-modal coupling coefficient between the i^{th} and j^{th} assumed modes
$G_{i,j}^{flap/lag}$	Overall effective stiffness inter-modal coupling coefficient between the i^{th} and j^{th} assumed modes
$I^{flap/lag}(r)$	Blade cross-sectional area moment of inertia, m^4
$I_{i,j}^{flap/lag}$	Effective centrifugal stiffening inter-modal coupling coefficient between the i^{th} and j^{th} assumed modes

$K^{flap/lag}$	Blade hinge spring stiffness, Nm/rad
$k_{i,j}^{flap/lag}$	Elastic inter-modal coupling coefficient between the i^{th} and j^{th} assumed modes
l	Bernoulli–Euler beam length, $= R(1-e)$, m
$m_{i,j}^{flap/lag}$	Inertial inter-modal coupling coefficient between the i^{th} and j^{th} assumed modes
N	Number of assumed mode shapes
N_b	Number of blades
N_p	Number of quadrilateral panel elements
O	Global non-rotating reference frame index
P	Per rotor revolution
$p(r,t)$	Beam element of mass $dm = \rho A(r)dr$, located at beam radius r at time t
$P(x,y,z)$	Evaluation point with Cartesian coordinates (x,y,z)
P_{rotor}	Main rotor power required, kW
$Q_i^{flap/lag}$	Generalized centrifugal force corresponding to the i^{th} coordinate
$q_i^{flap/lag}(t)$	Time-dependent generalized coordinate of the i^{th} mode shape
R	Rotor blade radius, m
r	Geometric distance of source panel from evaluation point $P(x,y,z)$ – Chapter 5
r	Local beam element radius – Chapters 3, 4, m
s	Random search direction
S_b	Three-dimensional body surface
t	Time, sec
$T^{flap/lag}$	Kinetic energy of the rotor blade, $Joules$
$U^{flap/lag}$	Strain energy of the rotor blade, $Joules$

$u^{flap/lag}(r,t)$	Beam element X – axis displacement, m
V	Free-stream velocity, m/sec
V_{flight}	Helicopter flight speed, m/sec
$w^{flap/lag}(r,t)$	Blade flap/lag transverse displacement, m
x	Effective modal ordinate, $= r - eR$, m
$X_i^{flap/lag}(r)$	Shape for the i^{th} mode of motion, m

Greek Symbols

$[\lambda]$, $[\theta]$, $[\beta]$, $[\zeta]$	Local sweep, pitch, flap and lag angle rotation matrices
$[\Theta_0]$, $[\Psi_i]$	Rotor blade collective pitch and azimuth angle rotation matrices
$[B_{pre}]$, $[Z_{pre}]$	Rotor blade pre-cone and pre-sweep rotation matrices
$\bar{\mu}$	Advance ratio – Chapter 5, $\dfrac{V_{flight}}{\Omega R}$
β	Bernoulli–Euler beam modal frequency parameter, $= \sqrt[4]{\dfrac{\rho A}{EI}\omega^2}$
$\beta(r,t)$	Local beam element equivalent flap angle, $= \arcsin \dfrac{w^{flap}(r,t)}{r - eR}$, rad
β_0, β_{1c}, β_{1s}	Main rotor trim constant and 1^{st} harmonic flapping angles, deg
χ	Design variable
δ	Step length
λ	Number of designs
$\lambda(r)$	Local beam element sweep angle, rad
μ	Advance ratio – Chapters 4, 6, $= \dfrac{V}{\Omega R}$
μ	Doublet strength per unit area – Chapter 5
μ	Number of parent designs – Chapter 7
Ω	Main rotor nominal rotorspeed, rad/sec
ω	Bernoulli–Euler beam modal frequency – Chapter 3, rad/sec

$\omega_i^{flap/lag}$	Natural vibration frequency of the i^{th} mode of motion
$\phi_i^{flap/lag}(r)$	Assumed deformation function of the i^{th} mode shape, m
Φ_∞	Free-stream velocity potential, $= U_\infty x + V_\infty y + W_\infty z$
Φ_i	Induced velocity potential
Φ_{total}	Total velocity potential, $= \Phi_\infty + \Phi_i$
$\Phi_{total}^{int.}$	Total internal potential, enclosed by S_b
$\psi_i(t)$	Azimuth angle of the i^{th} blade root/hinge at time t, $i = 1, ...N_b$, rad
ρ	Material density, kg/m^3
σ	Source strength per unit area – Chapter 5
Θ, Φ, Ψ	Fuselage pitch, roll and yaw attitude angles, deg
θ_0, β_{pre}, ζ_{pre}	Rotor blade collective pitch, pre-cone and pre-sweep angles, rad
θ_0, θ_{1c}, θ_{1s}	Collective, longitudinal cyclic and lateral cyclic pitch angles, rad
$\theta_c(eR, t)$	Cyclic pitch angle at the rotor hub, positive for nose-up rotation, rad
$\theta_{tw}(r)$	Beam element pre-twist angle, positive for nose-up twist, rad
$\tilde{\dot{\omega}}_o$	Angular acceleration vector of the global non-rotating O frame, $= [\dot{p}_o\ \dot{q}_o\ \dot{r}_o]^T$
$\tilde{\omega}_{p/A_i}^{A_i}$, $\tilde{\dot{\omega}}_{p/A_i}^{A_i}$	Angular velocity and acceleration vectors of beam element $p(r, t)$ relative to the origin of A_i
$\tilde{\omega}_o$	Angular velocity vector of the global non-rotating O frame, $= [p_o\ q_o\ r_o]^T$
$\tilde{\omega}_{A_i/O}$, $\tilde{\dot{\omega}}_{A_i/O}$	Absolute angular velocity and acceleration vectors of the origin of A_i
ε	Lagrangian frequency parameter relative error
$\zeta(r, t)$	Local beam element equivalent lag angle, $= \arcsin \dfrac{w^{lag}(r, t)}{r - eR}$, rad

$\{\Phi^{flap/lag}(r)\}$	Assumed mode shape vector, $= [\phi_j^{flap/lag}(r),\ \ j = 1, ...N]^T$

Superscripts

$\dot{()}$, $\ddot{()}$	First and second derivatives with respect to time t
$\tilde{()}^{A_i}$	Vector expressed in the rotating reference frame of the i^{th} blade A_i
$\tilde{()}^{b}$	Vector expressed in the local blade element coordinate system b
$\tilde{()}^{hw}$	Vector expressed in the hub-wind axes reference system HW
$\tilde{()}^{O}$	Vector expressed in the global non-rotating reference frame O
$()'$	Derivative with respect to beam radius r or modal ordinate x
$()^{flap}$	Referring to the blade flap degree of freedom
$()^{k}$	generation index
$()^{lag}$	Referring to the blade lag degree of freedom

Subscripts

$\tilde{()}_{/O}$	Vector relative to the origin of the global non-rotating reference frame O
$\tilde{()}_{A_i/}$	Vector referring to the origin of the rotating reference frame of the i^{th} blade A_i
$\tilde{()}_{p/}$	Vector referring to beam element point $p(r, t)$
$()_{body}$	Referring to the region enclosed by the body surface S_b
$()_{i,j}$	Mode number indices – Chapter 3
$()_i$	Blade number index – Chapter 4
$()_i$	step direction – Chapter 7
$()_j$	Panel index – Chapter 5
$()_{midspan}$	Value corresponding to the blade's midspan position
$()_m$	member index

$()_p$	parent index
$()_{req}$	Value required
$()_{rsm}$	Value obtained from response surface model
$()_{sim}$	Value obtained from simulation

Abbreviations

ACARE	Advisory Council for Aeronautics Research in Europe
AGL	Above Ground Level
ATC	Air Traffic Control
ATS	Air Traffic System
AUM	All Up Mass, kg
CFD	Computational Fluid Dynamics
CO	Carbon Monoxide
CO_2	Carbon Dioxide
DOE	Design of Experiment
EHOC	European Helicopter Operators' Committee
EI	Emission Index
EPNL	Effective Perceived Noise Level
FAR	Combustor Fuel to Air Ratio
FEA	Finite Element Analysis
GA	Genetic Algorithm
GRC	Green RotorCraft
HPC	High Pressure Compressor
ICAO	International Civil Aviation Organization
IGE	In Ground Effect

ISA	International Standard Atmosphere
ITD	Integrated Technology Demonstrator
LHD	Latin Hypercube Design
LPC	Low Pressure Compressor
MTE	Mission Task Element
NBIM	Normal Boundary Intersection Method
NLPQL	Non-Linear Programming by Quadratic Lagrangian
OAG	Oil & Gas
ODEs	Ordinary Differential Equations
OEW	Operational Empty Weight, kg
OGE	Out of Ground Effect
OPR	Overall Pressure Ratio
OW	Operational Weight, kg
RMS	Root Mean Square
ROBIN	ROtor Body INteraction fuselage geometry
RSM	Response Surface Model
SAE	Self-Adaptive Evolution
SAR	Search & Rescue
SFC	Specific Fuel Consumption, kg/J
SOT	Stator Outlet Temperature, K
SQP	Sequential Quadratic Programming
TE	Technology Evaluator
WGS 84	World geodetic system dated in 1984

Chapter 1

Introduction

1.1 General Context

Flight dynamics simulation along with powerplant performance, mission analysis and design optimisation have always been important topics for the helicopter industry. These topics are now raising even more interest, as aspects related to fuel economy, chemical emissions and noise, gradually gain more importance in environmental and social impact assessments. Developments in technology within the 20^{th} and the 21^{st} century, mainly with respect to industrial as well as civil transport activities, have essentially led to a continuous worldwide rise in energy demand. Fossil fuel bound energy has been the dominant source explored and utilized for the satisfaction of this gradually increasing requirement. The progressively increasing rates of energy consumption, have inevitably resulted in the potential depletion of fossil fuels, as well as in the associated environmental impact due to the chemical emissions produced in the process (Ref. [1]).

The deployment of helicopters has been, until the present day, focusing mainly on activities such as civil transport, fire suppression, emergency medical evacuation, search & rescue, oil & gas and law enforcement. The aforementioned activities correspond to approximately 1,500,000 flight hours annually, only with respect to the European airspace. This figure may seem insignificant when compared to the equivalent of 10,000,000 flight hours per year, as regards the European commercial airlines (Ref. [2]).

It is noted however that, a sharp growth in rotorcraft operations is expected in the forth-coming future. This is a direct outcome of, among others, the European community's citizens' demands for a safer and more secure society. Considering solely the case of emergency medical services, the number of operations is expected to drastically increase due to recent developments in advanced treatment techniques along with the specialization of hospitals. Additionally, rotorcraft traffic related to passenger transport/air taxi requirements, that up to now has only been marginal, is also expected to grow rapidly

within the 2015–2020 period (Ref. [2]).

The aforementioned rotorcraft activities correspond to an annual consumption of the equivalent of roughly 400,000 tons of fuel, solely for the European region (Ref. [3]). The anticipated growth of rotorcraft services however, is expected to essentially quadruplicate this figure, should rotorcraft technology levels remain unchanged. In acknowledgement of this indication, a wide range of research & development activities is currently being carried out at national and European levels. The objective is to investigate potential paths leading to the realization of an effective return to the present global level of environmental impact within a time-frame of 20 years, while simultaneously catering for the expected rotorcraft traffic augmentation (Ref. [2]).

The Advisory Council for Aeronautics Research in Europe (ACARE), in an attempt to manage the environmental impact of civil aviation, has set a number of goals which are to be achieved by 2020. These goals include, among others, 50% reduction in CO_2 emissions through drastic reduction of overall fuel consumption. According to Clarke (Ref. [4]), if reductions in the environmental impact of aircraft operations are to be realized, then either (a) the number of operations must be reduced, (b) the type of aircraft must be changed, or (c) the aircraft operational rules and procedures must be changed.

As regards the helicopter industry, option (a) is not a viable path due to the aforementioned expected growth in rotorcraft traffic. Considering option (b), Brooker (Ref. [5]) points out that the timescales involved between the conception of an innovative aircraft design and the achievement of airworthiness certification can range from 20 to 50 years time (Ref. [5]). Thus, given the currently available time-frame, option (b) is not considered an effective response to the ACARE targets. It is therefore realized that, in terms of addressing the 2020 ACARE goals, emphasis needs to be placed towards the design and implementation of operational procedures leading to minimum required fuel consumption and associated environmental impact.

It is noted however that, although the investigation of conceptual designs may not effectively lead to the realization of the relatively short-termed ACARE goals, it still is a viable path towards a longer term solution. Therefore, in order to effectively control the long-term environmental impact of civil rotorcraft aviation while simultaneously catering for the expected traffic growth, options concerning both conceptual design configurations as well as incorporated operational procedures need to be thoroughly explored.

A large collaborative project focusing on the development and integration of innovative aircraft/rotorcraft design technologies as well as incorporated operational procedures, is the European Clean Sky JTI (Joint Technology Initiative) (Ref. [6]). Several industrial partners as well as research establishments are currently participating within Clean Sky, in an effort to develop and demonstrate technologies capable of addressing the aforementioned issues related to the environmental impact of civil aviation. Hence, a significant step is made towards achieving the environmental goals set by the ACARE as well as

catering for an effective longer-term approach with respect to addressing the aspects of fuel economy, produced chemical emissions and ground noise impact.

Investigation of conceptual helicopter designs and identification of more energy-efficient operational procedures, both require a respective comprehensive performance assessment approach. The methodology specifications may differ, since they are essentially targeting very different, but rather interrelated topics. It is understood however that, both tasks have a common denominator of being able to effectively address the issue of fuel economy within a designated operation. Therefore both methodologies need to be capable of providing accurate estimates of the required operational resources, in terms of mission time and fuel consumption, for any designated rotorcraft design within any specified type of operation.

As regards the context of multidisciplinary rotorcraft design, both comprehensiveness as well as computational efficiency are deemed as prerequisites with respect to the employed modeling approach. Key design variables, which might affect the overall performance of a helicopter–engine system within a designated type of operation, have to be readily identifiable by the deployed formulation. An advanced level of simulation fidelity is therefore required, so that the behavior of the associated performance trade-off between designs optimised in a multidisciplinary manner, is accurately captured. The associated computational overhead has to be maintained within an acceptable threshold, so that the employed approach is applicable within an iterative optimisation process. It is therefore realized that, an efficient compromise between modeling fidelity and computational efficiency has to be sought for.

1.2 Scope of Work

Padfield (Ref. [7]) has provided a three-level hierarchy of helicopter simulation models as a means of gauging the progress of attained simulation fidelity (Ref. [8]). Within level 1 modeling, a disc-like representation of the main rotor is incorporated along with linear blade aerodynamics. The wake-induced velocity at the rotor is essentially expressed as a superposition of finite flow states within a 1^{st} order dynamic inflow formulation. A level 2 approach may employ individual-blade representation coupled with a more refined induced flow model. At level 3, the complete aeroelastic behavior of the main rotor is catered for. This necessitates the deployment of a detailed structural representation of the elastic blades (modal or finite element approach), coupled with unsteady, nonlinear blade element aerodynamics and three-dimensional rotor wake induced flow modeling (free or prescribed) (Ref. [7]).

Level 1–2 models are mainly deployed for the analysis of parametric trends as regards flying qualities and flight performance well within the limits of the operational envelope. Level 3 models are predominantly utilized for rotor design, unsteady rotor loads prediction

and vibration analysis up to the limits defined by the safe flight envelope (Ref. [7]). It is thus understood that, investigation of environmentally–friendly operational procedures within a well-defined operational envelope, can be catered for with the incorporation of a level 1–2 modeling approach. It is also emphasized however that, a multidisciplinary rotor design process essentially requires to approximate the features of level 3 modeling fidelity, in order to identify the effects of key design parameters on the overall helicopter performance and unsteady rotor blade structural loads during flight.

It is noted that, state of the art models being currently employed for mission performance simulation (Refs. [2], [3]) belong to the 1^{st} level of Padfield's hierarchical paradigm. The implementation of higher order modeling capability in helicopter mission analysis applications, has until presently been hindered by the prohibitively large computational overhead associated with higher levels of modeling fidelity. Another reason for this lies within the fact that, the individuality of a complete rotorcraft operation has not until now been considered as a factor in the design process when it comes to fuel economy. Instead, the design process has been mostly focusing within designated sets of operating conditions, rather than catering for complete and realistic three-dimensional operations.

With respect to addressing arguments (b) and (c) raised by Clarke (Ref. [4]) and brought up in the "General Context" section of this chapter, while simultaneously accounting for the anticipated rotorcraft traffic growth, two fundamental requirements are identified:

- Generic methodology applicable to existing helicopter configurations, capable of designing optimum operational procedures in terms of fuel burn, chemical emissions and ground noise impact.

- Rotorcraft design assessment approach capable of estimating the overall fuel consumption with regards to a designated operation. The employed method has to approximate the 3^{rd} level of Padfield's hierarchical paradigm while simultaneously maintaining a reasonable computational overhead so as to be deployable in the context of multidisciplinary design.

An effort has been made within the scope of work presented in this Thesis to address both aspects identified above. It is noted however that, significant weight has been placed with regards to the latter approach, due to the fact that it essentially constitutes part of a longer-term solution towards addressing the environmental impact of civil aviation.

1.3 Objectives

Within the broader sense of the term, the "objectives" determined and addressed within the context of this work, essentially constitute an integrated response to the fundamen-

tal requirements outlined in section "Scope of Work" of this chapter. The undertaken objectives can therefore be categorized in a generalized aspect as stated below:

- Development and application of a generic, computationally-efficient methodology, capable of optimising civil helicopter operations in a multidisciplinary manner, with respect to total mission fuel consumption and associated environmental impact. The approach needs to be able to cater for the inherent individuality of a complete helicopter operation and as such, it needs to be adaptable to the operational environment dictated by the mission specifications.

- Analytical and computational development of an integrated approach, capable of assessing the overall performance of integrated helicopter–engine systems belonging to the single main/tail rotor class, approximating the 3^{rd} level of Padfield's hierarchy of simulation models. The method has to be able to provide reasonably accurate estimates of various parameters related to rotorcraft flight dynamics, unsteady rotor blade structural loads and engine performance within three-dimensional missions. The associated computational overhead needs to remain within an acceptable level, so that the developed approach can be deployed in a multidisciplinary design process.

It is noted that the single main/tail rotor helicopter class has been selected due to the fact that, the majority of rotorcraft deployed within the context of civil aviation follow the specific configuration.

In order to effectively cater for the 2^{nd} of the rather broadly defined objectives outlined above, a series of more specific goals related to the development of specialized analytical methods has been determined. Each of the developed analytical procedures has to comply with the fidelity specifications dictated by level 3 requirements, while simultaneously maintaining a relatively low computational overhead so as to be deployable in a mission analysis context. The individual goals comprise the development of analytical methodologies applicable to the aspects outlined below:

1. *Development of an analytical procedure applicable to the rapid estimation of natural vibration characteristics of helicopter rotor blades*

2. *Development of a mathematical approach for the treatment of rotor blade flexibility in helicopter aeroelasticity applications*

3. *Implementation of a computationally inexpensive methodology to account for in-flight aerodynamic rotor–fuselage interaction*

4. *Comprehensive assessment of combined helicopter–engine designs within three-dimensional operations*

The 4^{th} of the specialized goals specified above, can essentially be regarded as an effective integration and application of the products obtained from the successful completion of goals 1, 2 and 3.

1.4 Thesis Structure

Due to the diversity of the various modeling aspects tackled within the context of this work (described in section "Thesis Objectives" of this chapter), it has been deemed appropriate to treat each modeling area as a standalone entity. Each chapter essentially describes the development and implementation of a specific analytical procedure and is therefore accompanied with the corresponding literature, methodology, results & discussion and conclusions. Extensive validation with existing experimental, numerical or analytical data has been carried out where appropriate, in an effort to assess the predictive qualities of the corresponding methods.

It is emphasized that, there is a scalar hierarchy involved in the development of the individual modeling methods. This hierarchy is explicit in the sense that, each numerical approach is implicitly coupled with all mathematical models developed in the preceding chapters. Thus, the overall–integrated framework essentially initiates from a standalone fundamental baseline, and is gradually built up with the development and implementation of further analytical methods. The end result can effectively be regarded as an integrated approach towards addressing the broadly defined objectives in section "Thesis Objectives" of this chapter.

The 1^{st} chapter essentially constitutes an introduction to the content of work dealt within this Thesis. An overview of the underlying context is presented along with the scope of the developed methodology. The objectives of the undertaken project are discussed in detail along with the Thesis structure. Finally, the contribution to knowledge resulting from the successful completion of the undertaken project is outlined.

Chapter 2 offers a broad description of the methodology followed within each chapter. A general overview of the work presented in this Thesis is provided, while emphasis is placed on the most important aspects and outcomes of this work.

Chapters 3 describes the development of an analytical approach targeting the estimation of natural vibration characteristics of helicopter rotor blades. Chapter 4 subsequently elaborates on the treatment of rotor blade flexibility for helicopter aeroelasticity applications. The approach described within chapter 3 is implicitly coupled with a rotor wake and a blade element aerodynamics formulation in order to facilitate the development of a complete aeroelastic rotor model. The integration of the overall aeroelastic rotor model within an overall helicopter flight mechanics methodology is described. Chapter 5 subsequently focuses on the development of a mathematical approach, targeting the estimation of in-flight rotor–fuselage aerodynamic interaction effects on helicopter trim as well as on

unsteady structural loads.

The developed mathematical methods reported in chapters 3–5 of this Thesis, are subsequently coupled with an in-house engine performance simulation tool within chapter 6 through the development of an elaborate numerical approach for helicopter mission analysis. Thus, an integrated methodology is formulated targeting the comprehensive simulation of flight dynamics and engine performance within complete, three-dimensional helicopter missions. Chapter 7 subsequently, utilizes an existing level 1 simulation approach (Ref. [2]), in order to formulate an integrated framework for the optimisation of modern rotorcraft operations with respect to mission fuel consumption and associated environmental impact.

Chapter 8 recapitulates the most important conclusions of this work and identifies the fulfillment of the Thesis objectives. Various research aspects that have not been tackled within the work presented in this Thesis are also addressed. New areas of research with respect to both potential improvements as well as application of the developed approach are proposed.

Appendix A describes the analytical derivation of closed form expression applicable to the modal analysis of rotor blades with three different types of hub-support. Appendix B elaborates further on the analytical approach developed within chapter 3. Appendix C contains a list of references with regards to publications produced through the context of this work.

Substantial effort has been made towards assigning a unique identifier with respect to a designated physical quantity throughout the volume of work presented in this Thesis. It is noted however that, there is a limited number of annotative symbols which essentially correspond to different quantities depending on the chapter within which they appear. Thus, with respect to duplicate symbols, annotative expressions have been included in the "Nomenclature" section of this Thesis, identifying the chapter number for which the symbol is used with the corresponding definition.

1.5 Contribution

The main contribution arising from the successful completion of the undertaken project, is the computational development of an integrated simulation framework, capable of analyzing the overall performance of any designated helicopter–engine system, within complete and realistically defined three-dimensional operations. Simulations are performed, throughout the entire mission phase, within a fidelity level required for the purposes of preliminary design. This framework has been named "*HECTOR*" (HEliCopter Omnidisciplinary Research) after the homonymous Trojan prince who found his tragic demise in the hands of the ancient Greek Achilles. *HECTOR* is a standalone platform developed in FORTRAN 90/95, comprising approximately 50,000 lines of code. *HECTOR* has been

used to produce all numerical results presented in chapters 3–6, unless stated otherwise.

Furthermore, clear contribution has been made towards the European Clean Sky (Ref. [6]) throughout the three-year period of the undertaken project. The author has had an active role within the Technology Evaluator (TE) part of Clean Sky, as regards rotorcraft performance modeling activities being carried out in close collaboration with the Green Rotorcraft Integrated Technology Demonstrator (GRC–ITD). Specifically, contribution has been made with respect to the development, beta-testing and debugging of the integrated simulation framework "*Phoenix*" (Platform Hosting Operational & Environmental Investigations for Rotorcraft). *Phoenix* comprises a rotorcraft flight mechanics code, an engine performance simulation tool and a noise propagation analysis model. It is therefore capable of estimating the resources required, produced chemical emissions and associated ground noise impact with regards to any designated helicopter mission. *Phoenix* is currently being used within Clean Sky for the evaluation of various rotorcraft technologies at mission, operational as well as Air Traffic System (ATS) levels. Further information on *Phoenix* is provided in chapter 7 of this Thesis.

With respect to addressing the 1^{st} of major objectives outlined in section "Objectives" of this chapter, a second simulation framework has been developed based on *Phoenix*, capable of performing multi-disciplinary optimisation of complete rotorcraft operations in terms of fuel consumption as well as overall environmental impact. The specific piece of work has been conducted under the large umbrella of the European Clean Sky, and the developed framework has been made available for the investigation of optimal operational procedures for rotorcraft within the specific European project. The developed simulation framework has been used to produce all numerical results presented within the 7^{th} chapter of this thesis.

Further to the computational development of the simulation frameworks elaborated above, individual contribution has been made towards the various rotorcraft-related research subjects dealt within the respective chapters of this Thesis. These essentially comprise:

- Analytical development of a computationally efficient numerical approach for the rapid estimation of natural vibration characteristics of helicopter rotor blades.
- Analytical development of a generic methodology targeting the treatment of rotor blade flexibility in helicopter aeroelasticity applications.
- Investigation of in-flight fuselage aerodynamic interference effects on various helicopter trim parameters and unsteady blade structural loads.
- Development of an integrated methodology for the comprehensive assessment of combined helicopter–engine designs, within three-dimensional operations.

- Development and application of a generic, cost-efficient methodology, capable of optimising modern helicopter operations in a multidisciplinary manner, with respect to total mission fuel consumption and associated environmental impact.

It is noted that, all of the developed analytical methods outlined above, have been extensively validated with existing experimental or numerical data. The validation process has been presented within each of the corresponding chapters of this Thesis.

Chapter 2

Methodology Overview

2.1 General Outline

This chapter provides a general overview of the methodology developed for the purpose of addressing the project objectives outlined in section "Objectives" of chapter 1. The corresponding numerical methods elaborated within each of the following chapters are briefly discussed along with the most important conclusions derived from their individual application.

It is once again noted that, each of chapters 3–6 describes the development of a specific analytical approach, applicable to the simulation of helicopter flight dynamics, aeroelasticity, engine performance and mission analysis. The overall outcome can essentially be regarded as an integrated framework, applicable to the simulation of complete rotorcraft missions at the level of fidelity required for design purposes, whilst simultaneously allowing for an acceptable computational overhead.

Chapter 7 subsequently describes the application of an existing level 1 simulation approach, in order to explore the multidisciplinary design of operational procedures optimised in terms of mission fuel economy and associated environmental impact.

2.2 Developed Approach

The overall developed numerical approach initiates within chapter 3 with the formulation of a fundamental baseline targeting the rapid estimation of natural vibration characteristics of helicopter rotor blades. The proposed method is based on the application of Lagrange's equation of motion for the kinematics of flapwise and lagwise blade bending. Modal properties obtained from the deployment of Bernoulli–Euler beam theory for a uniform non-rotating continuous structure, are utilized as assumed deformation functions in order to approximate the time variations of strain and kinetic energy for each degree

of freedom. Integral expressions are derived describing the generalized centrifugal force acting on the blade in terms of normal coordinates for flap and lag transverse displacement. Closed form expressions are offered for the simulation of hingeless, freely-hinged and spring-hinged articulated rotor blades. The numerical performance of the developed approach is thoroughly assessed and the method is compared with the corresponding analytical/exact theories.

Results are presented in terms of predicted flap and lag natural frequencies as well as mode shapes for two separate small-scale rotor models. Comparisons with experimental measurements as well as nonlinear finite element analysis have been carried out. The proposed approach is shown to exhibit very good numerical behavior with definitive convergence characteristics for all modes presented. The comparisons suggest very good, in some cases excellent, accuracy levels especially considering the method's simplicity, cost-effectiveness and ease of implementation.

Chapter 4 describes the numerical development of a methodology applicable to the simulation of rotor blade flexibility in helicopter aeroelasticity applications. The treatment of three-dimensional elastic blade kinematics in the time domain is thoroughly discussed. A stable, 2^{nd} order accurate numerical differentiation scheme, previously used in the context of time-accurate free-wake analysis (Ref. [9]), is deployed for the estimation of the motion derivatives. Integral expressions are provided describing the unsteady rotor loads in the hub-wind axes system (Ref. [7]). The proposed method is coupled with a finite-state induced flow model (Ref. [10]) and an unsteady blade element aerodynamics model (Ref. [11]). The modal characteristics obtained from the Lagrangian method developed in chapter 3 are implicitly utilized, thus formulating a comprehensive aeroelastic rotor model suitable for helicopter flight dynamics. The integrated approach is subsequently deployed in order to investigate the trim parameters and the time-dependent structural loads of a full-scale, pre-coned hingeless rotor.

Extensive comparisons of predicted flapwise and chordwise blade bending moments with experimental data from wind tunnel and flight tests (Ref. [12]) are presented. Good structural loads predictive qualities are exhibited for a wide range of advance ratios. It is shown that, flapwise bending moment at the blade mid-span comprises predominantly harmonic content associated with the 2^{nd} and 3^{rd} elastic flap modes, while chordwise moment is mainly influenced by the 1^{st} corresponding mode shape.

The 5^{th} chapter describes the development of a computationally efficient approach, applicable to the simulation of steady-state fuselage aerodynamic interference effects on the helicopter main rotor during flight. A three-dimensional, potential flow source–panel method is developed and implemented. The scheme is deployed in order to predict the induced velocity perturbations arising from the existence of a generic helicopter fuselage in a free-stream. Results are presented in terms of three-dimensional induced velocity perturbations on the main rotor tip-path plane for a generic, scaled-down isolated fuse-

lage model. Good agreement is shown between flow-field predictions and experimental measurements conducted at the NASA Langley subsonic wind tunnel (Ref. [13]). The potential flow method is subsequently coupled with the aeroelastic rotor model developed and validated in chapters 3–4.

Extensive comparisons with flight test data (Ref. [12]) are carried out regarding predictions of trim parameters and unsteady rotor blade bending moments for the MBB Bo 105 helicopter over a wide range of advance ratios. Simulations suggest that, the longitudinal cyclic pitch angle (θ_{1c}) is the only trim parameter influenced significantly by the steady-state aerodynamic interference effects. The corresponding difference can be of the order of 75% relative to the case where fuselage induced flow is neglected.

The 6^{th} chapter discusses an integrated approach, targeting the comprehensive assessment of combined helicopter–engine designs within three-dimensional operations. The overall methodology comprises the mathematical models developed within chapters 3–5, elaborately integrated within a numerical procedure solving for the total fuel consumption of a designated mission. Thus, a complete simulation framework is formulated capable of performing helicopter mission analysis at the level of fidelity required for design purposes. The overall simulation framework is applied to the performance analysis of the Aérospatiale SA 330 helicopter within two generic, twin-engine medium helicopter missions. An extensive comparison with flight test data on main rotor trim controls, power requirements and unsteady blade structural loads is presented.

It is shown that, for the typical range of operating conditions encountered by modern twin-engine medium civil helicopters, the effect of operational altitude on fuel consumption is predominantly influenced by the corresponding effects induced on the engine rather than on airframe–rotor performance. The potential to comprehensively evaluate integrated helicopter–engine systems within three-dimensional operations, based on the solution of the aeroelastic behavior of the main rotor is demonstrated.

The work presented in chapter 7 focuses on the development and application of a generic methodology targeting the design of optimum rotorcraft operations in terms of fuel burn, gaseous emissions and ground noise impact. The development of *Phoenix* (Ref. [2]) is described. As elaborated within chapter 1, *Phoenix* is capable of estimating the performance and emitted noise of any defined rotorcraft configuration within any designated mission. A comprehensive and cost-effective optimisation strategy has been structured. The developed approach has been based on the initial design space exploration using a Latin-Hypercube Design Of Experiment (LHD–DOE) approach, followed by the numerical formulation of Response Surface Models (RSMs). The RSMs are subsequently utilized within a hybrid multidisciplinary optimisation approach, for the derivation of optimum operations in terms fuel consumption and associated environmental impact. The developed methodology has been applied to two generic – baseline missions representative of current twin-engine light civil rotorcraft operations. Optimally designed missions for

fuel burn, gaseous emissions and ground noise impact have been obtained. A comparative evaluation has been waged between the acquired optimum designs. The respective trade-off arising from the incorporation of flight paths optimised for different objectives is quantified. Pareto front derived models for fuel burn and emitted noise are structured for each mission. The Pareto models are subsequently deployed for the design of operations optimised in a multidisciplinary manner.

The results have shown that, the proposed methodology is promising with regards to achieving simultaneous reduction in fuel burn, gaseous emissions and ground noise impact for any defined mission. The obtainable reductions are found to be dependent on the type of operation. It has been demonstrated that, the selection of optimum flight conditions within a designated mission phase cannot be properly addressed without catering for the individuality of the complete operation. Finally, the potential to design operations optimised in a multidisciplinary fashion using only a single design criterion is demonstrated.

Closed form expressions are provided within Appendix A for the derivation of assumed modal functions for hingeless, freely-hinged and spring-hinged articulated rotor blades. Appendix B presents proof of orthogonality with respect to the acquired modes using the Lagrangian formulation presented in the 3^{rd} chapter of this Thesis.

Chapter 3

Rapid Estimation of Helicopter Rotor Blade Vibration Characteristics

3.1 Introduction – Literature

The main rotor of a helicopter is undoubtedly a mechanically complex structure. Part of the reason for its mechanical complexity arises due to its function as a propulsive and a control device simultaneously. Its constant operation within a highly unsteady aerodynamic environment in forward flight, essentially results in also highly unsteady exerted hub loads. Obtaining time-accurate estimates of the rotor imposed forces and moments on the aircraft fuselage is essential for flight dynamics simulation, especially regarding applications which include higher frequency rotor dynamics. This prerequisite has been brought to the helicopter community's attention, partially due to its necessity for the design of reliable hingeless and bearingless rotor control systems.

In an effort to address the aforementioned requirement, the departure from the typical disc-like treatment of the main rotor and the adaptation of methodologies involving individual blade treatment was necessary. This essentially acted as an enabler in terms of including more sophisticated rotor inflow and blade aerodynamics models. Some of the earliest individual–blade mathematical formulations would treat each blade as a rigid body. Hub springs and effective hinge offsets were assumed in order to simulate the actual hub stiffness of hingeless blades.

Several studies are reported in the literature where flexible blade models have been used in order to study the effects of blade elasticity on the dynamics of various helicopter rotors. Lewis (Ref. [14]) used a multi-body dynamics formulation in order to investigate the aforementioned effects on the dynamics of the UH-60 articulated rotor. The effects of

blade flexibility were found to be quite small in hover and increase slightly with increasing speed. Sturisky (Ref. [15]) reports, that for the AH-64 articulated rotor, inclusion of higher order inflow dynamics along with flexible blade modeling, may indeed improve the prediction accuracy of the rotor's off-axis response to pilot control inputs. Turnour *et al.* (Ref. [16]) deployed the elastic rotor model described in Ref. [17] coupled with the fuselage equations of the "UM-Genhel" flight dynamics model (Ref. [18]) and a finite-state induced flow model (Ref [10]). They concluded that, for the particular rotor configuration, including flexible blade modeling along with higher order inflow dynamics does not improve the prediction accuracy of the off-axis rotor response to pilot control inputs.

The elastic blade formulations deployed in the references above are based either on Finite Element Analysis (FEA) or on multi-body dynamics. Hence, they require detailed knowledge of the geometry and overall structural properties of the rotor blade and its support. They are also accompanied by a relatively large computational overhead which may be prohibitive with regards to the application for which they are designated for. It is therefore realized that a cost-effective methodology of sufficient fidelity, comprehensiveness, generality and ease of implementation is required, for the inclusion of rotor blade flexibility in flight dynamics applications. The formulation has to enable existing, as well as future potential flight simulation codes, to account for blade elasticity in a computationally inexpensive manner without resorting to cost-inducing finite element analysis or a multi-body dynamics approach.

This chapter describes a comprehensive methodology targeting the rapid estimation of natural vibration characteristics of helicopter rotor blades for flap and lag bending motion. The presented method makes use of the Lagrangian equation of motion for a rotating, continuous system of nonuniform mass and stiffness properties. Any set of boundary conditions corresponding to the hub support of a helicopter rotor blade is applicable. The proposed structural formulation is applied for an articulated and a hingeless small-scale experimental rotor model. It is shown that the current method exhibits very good numerical behavior with definite convergence characteristics for every mode of flap/lag bending motion. Comparisons are waged with experimental measurements as well as finite element analysis results. Very good agreement (excellent in some cases) is observed between the predictions and the experimental/FEA results with respect to the natural frequencies of both small-scale rotor configurations. Good agreement is also observed regarding the predicted mode shapes, with the exception of the first flap mode of the hingeless small-scale rotor at very high-speed rotating conditions.

3.1.1 Natural frequencies and mode shapes of rotor blades

The effort to determine the dynamic behavior of rotating blades started quite early in the literature. Houbolt & Brooks (Ref. [19]) derived the coupled differential equations of

motion for combined flapwise/chordwise bending and torsion for twisted nonuniform rotor blades. Their derivation was based on the principles of classical engineering beam theory. Nonlinear terms of secondary nature such as shear deformation and rotary inertia were omitted. Linear coupling terms mainly associated with the blade's centripetal acceleration due to the hinge's pre-cone angle and steady state blade flapping under external lift loads were included. Exact solutions for continuous systems that are governed by the Houbolt & Brooks equations do not yet exist. However, several analyses can be found in the literature where approximate solutions have been acquired for the coupled equations given in (Ref. [19]) or for some of their uncoupled sub-cases.

Murthy (Ref. [20]) deployed the Transmission Matrix (TM) method (Ref. [21]) in an effort to acquire approximate solutions to a series of sub-cases of the Houbolt & Brooks equations for twisted nonuniform rotating blades. The TM method requires that the differential equations of motion are reduced to a set of Ordinary Differential Equations (ODEs) of the first order by appropriate selection of a state vector. Murthy (Ref. [20]) noted that the state vector can be selected in several ways but it is preferable for it to consist of physical quantities such as deflections, slopes, moments and shears. Following the derivation of the transmission matrix of the defined ODEs, the frequency determinants and the modal functions were obtained for a given set of boundary conditions. The cases of combined flapwise bending–chordwise bending–torsion, flapwise bending–chordwise bending and flapwise bending–torsion were studied. Murthy concluded that the TM method yielded highly accurate results with regards to the specific application. He recommended its deployment for the investigation of the elastic–inertial coupling effects between the blade's degrees of freedom on the aeroelastic stability characteristics of helicopter rotors.

Hunter (Ref. [22]) applied the Integrating Matrix (IM) method in order to determine the natural vibration characteristics of a twisted, rotating propeller blade with nonuniform, asymmetrical cross section and cantilever boundary conditions. The integrating matrix can be regarded as a tensor operator of numerical integration which is applicable to any function expressed in terms of discrete values at equal increments of the independent variable. It was derived by essentially expressing an integral as a polynomial in the form of Newton's forward-difference interpolation formula. After expressing the differential equations of motion in matrix form, the constants of integration were evaluated based on the applied boundary conditions. The matrix differential equation was subsequently integrated repeatedly using the integrating matrix as an operator. This process resulted in the formulation of the classical eigenvalue problem. Hunter compared the IM method's predictions of natural vibration frequencies with experimental data as well as with known exact solutions. He concluded that the IM method yields very accurate results.

Surace *et al.* (Ref. [23]) applied an integral approach using structural influence (Green) functions in order to estimate the coupled motion modal characteristics of rotating,

nonuniform, pre-twisted blades. They utilized a system of appropriate Green functions for a cantilever beam in order to acquire approximate solutions to the Houbolt & Brooks equations. Weighting matrices were used for integration and differentiation similarly to the approach followed in Ref. [22]. As a result of its numerical formulation, the specific method requires a defined set of Green functions for any imposed set of boundary conditions that the analyst may wish to specify. Although Green functions are readily available for a cantilever beam, they may need to be re-derived for an articulated rotor with hub and lead-lag springs in order to comply with the corresponding boundary conditions. Thus the methodology presented in Ref. [23] is not readily applicable–implementable for the analysis of freely–hinged and spring–hinged articulated rotor blades.

3.1.2 Minimum potential energy methods

The methodologies described in the references above have tackled the problem of rotor blade flexibility by evaluating numerically the fundamental differential equations of motion for a nonuniform, pre-twisted rotating beam. Further to the references above, a series of analyses can be found in the literature where the sub-cases of the uncoupled problem have been addressed through the deployment of approximate energy methods such as Lagrange's and Rayleigh's methods as well as the classical and modified Rayleigh–Ritz procedures. These methodologies are based on the principle of minimum potential energy and the deployment of a finite series of assumed displacement functions–deformation modes in order to estimate the system's kinetic and strain energies as functions of time. Their detailed descriptions as well as derivations can be found in Refs. [24–26].

Wilde *et al.* (Ref. [27]) described a comprehensive methodology for the estimation of flapwise vibration frequencies and mode shapes of a helicopter rotor blade. They tried to acquire a numerical solution for the flapwise bending differential equation of motion which included the aerodynamic damping terms based on the assumption of linear aerodynamics. Their methodology consisted of a combination of Rayleigh's principle of variation and Fourier series expansion techniques. The solution method included the assumption of a pre-supposed, periodic aerodynamic loading which was expanded in a Fourier series about the blade azimuthal coordinate. The acquired series expression was subsequently included in the corresponding differential equation of motion. Thus, the specific methodology is not applicable for a complete aeroelasticity analysis where coupling with more refined aerodynamic response and rotor inflow theories may be required for time-domain analysis.

Fasana *et al.* (Ref. [28]) deployed the Rayleigh–Ritz method in order to investigate the vibration characteristics of sandwich beams with a constrained viscoelastic layer. Their analysis included the use of simple polynomial expressions as assumed deformation functions. A total of 20 polynomial functions were used in the analysis. It was reported that no sensible variation was detected in the acquired results when the number of polynomials

was increased up to a total of 80 functions. Predicted natural frequencies corresponding up to the fourth bending mode for a cantilever beam were presented. Results were compared with those from other various numerical schemes that can be found in the literature. Good agreement was observed regarding the lowest mode natural frequencies. There was however a noticeable deviation in the predicted higher mode frequencies among all compared techniques. Fasana *et al.* concluded that the Rayleigh–Ritz procedure was in concurrence with the rest of the compared schemes regarding the particular application.

It is understood from the above that, the accuracy of such methods has been limited so far to the realms of approximation and only for the lowest modes–frequencies. This is due to the fact that, their success is highly dependent on the selection of assumed displacement functions in terms of both quantity and quality. A relatively larger number of functions is required so that the system is allowed to deform within most of its potential displacement modes. Selecting a small number of assumed functions may essentially lead to artificially imposed stiffness in the system, which may result in acquired frequencies higher than normal. This is a well known deficiency of Rayleigh's method (Ref. [26]) which is based only on the first assumed mode of deformation.

The assumed displacement functions need to comply with 3 fundamental requirements in order to be used within the context of minimum potential energy analysis. These can be listed as follows: 1) They need to satisfy the structure's boundary conditions, 2) They must be linearly independent–orthogonal with one another, 3) They have to be as close as possible to the actual deformation modes (Ref. [26]). It is also desirable, but not a prerequisite, that the first and second spatial derivatives of the assumed functions are provided as analytical expressions. This is due to the fact that, numerical differentiation errors could hinder the accuracy of the overall procedure. This is especially important when exceptionally large terms need to be well conditioned within the deployed polynomial.

The first and second bending modes may be relatively easy to approximate using standard polynomial expressions that can be found in the literature (Refs. [29,30]). However, when it comes to refined modeling which may require the inclusion of higher order assumed functions, the deviation between such polynomial expressions and the actual modes of deformation becomes quite large. Hence, the use of the aforementioned polynomial expressions is rendered progressively invalid as the energy method is further refined and higher order assumed functions need to be included in the analysis.

This chapter describes a minimum potential energy method capable of rapidly estimating the natural frequencies and mode shapes of rotating helicopter blades for flapwise and lagwise bending. Lagrange's equation of motion is utilized for a continuous system of nonuniform mass and stiffness distribution. The aforementioned weakness of energy methods is alleviated with the employment of modal characteristics obtained from Bernoulli–Euler beam theory as assumed deformation functions, instead of standard polynomial expressions. The structure's boundary conditions are implicitly catered for in the

Lagrangian formulation through their application directly within Bernoulli–Euler beam theory. The cases of hingeless, freely-hinged and spring-hinged articulated rotor blades are treated in detail and closed form expressions are offered that can be readily implemented as assumed deformation functions. Integral expressions describing the generalized centrifugal force exerted on the blade are derived and employed within Lagrange's equation of motion. The classical eigenvalue problem for a nonuniform, rotating structure with any set of imposed boundary conditions can thus be formulated and solved with customary matrix techniques. The solution results in the structure's natural frequencies and mode shapes. The flap and lag degrees of freedom are treated separately and thus neither elastic, nor inertial coupling is taken into account during the formation of the Lagrangian eigenproblem.

It is thus understood that, the described method can act as a baseline for the transition from classical rigid blade based modeling to a complete framework for rotor aeroelasticity analysis without the need of a computationally expensive finite element simulation or a multi-body dynamics formulation.

3.2 Methodology

3.2.1 Assumed deformation functions derivation

As previously mentioned, in order to utilize the Lagrangian equation of motion, a finite series of assumed deformation functions is required. These can be obtained by treating the rotor blade as a solid beam and deploying the classical Bernoulli–Euler beam theory. Due to the potential existence of an actual root/hinge offset from the center of rotation, it is deemed appropriate to define an effective modal ordinate as the spatial independent variable based on the local beam radius $r \in (eR, R)$, where e is the hinge offset as a ratio of rotor blade radius R. The effective modal ordinate is defined as $x = r - eR,\ x \in (0, l)$, where $l = R(1 - e)$ is the actual beam length. This transformation is used in order to ensure correct application of boundary conditions. The governing equation for the time-dependent transverse displacement $w(x, t)$ of a non-rotating beam with variable bending stiffness $EI(x)$ and mass per unit length $\rho A(x)$, subjected to a vertical time varying distributed load per unit length $P(x, t)$ is a fourth order Partial Differential Equation (PDE):

$$\frac{\partial^2}{\partial x^2}(EI(x)\frac{\partial^2 w(x,t)}{\partial x^2}) + \rho A(x)\frac{\partial^2 w(x,t)}{\partial t^2} = P(x,t) \tag{3.1}$$

where t is time in seconds.

At this point, constant values of $\rho A(x)$ and $EI(x)$ along x are assumed. Representative values at the beam mid-span position are selected which give: $\rho A_{midspan} = \rho A(l/2)$ and $EI_{midspan} = EI(l/2)$. In order to obtain the natural frequencies and the respective mode

shapes of the idealized system, the eigenproblem has to be formulated. This is achieved with the application of free vibration conditions by setting $P(x,t) = 0$ in Eq. (3.1) which becomes:

$$EI_{midspan}\frac{\partial^4 w(x,t)}{\partial x^4} + \rho A_{midspan}\frac{\partial^2 w(x,t)}{\partial t^2} = 0 \tag{3.2}$$

Assuming that Eq. (3.2) is separable in terms of space x and time t, the transverse displacement $w(x,t)$ can be re-written:

$$w(x,t) = \Phi(x) \cdot Q(t) \tag{3.3}$$

where $\Phi(x)$ is the assumed spatial mode shape and $Q(t)$ is a time-dependent generalized coordinate. The mode shapes can be acquired from the solution of the spatial part of Eq. (3.2) which gives:

$$\frac{\partial^4 \Phi(x)}{\partial x^4} - \beta^4 \Phi(x) = 0 \tag{3.4}$$

where β is the Bernoulli–Euler frequency parameter defined as:

$$\beta^4 = \frac{\rho A_{midspan}}{EI_{midspan}}\omega^2 \tag{3.5}$$

with ω being the natural frequency of vibration of the idealized Bernoulli–Euler beam.

Equation 3.4 has a known solution of the form:

$$\Phi(x) = A\sin\beta x + B\cos\beta x + C\sinh\beta x + D\cosh\beta x \tag{3.6}$$

Equation 3.6 provides the Bernoulli–Euler beam mode shape for a given frequency parameter β. The parameters A, B, C and D are constants of integration that are determined through application of the appropriate boundary conditions. Those are essentially defined by the rotor blade's hub support. Applying the corresponding boundary conditions at the blade hub ($x = 0$) and tip ($x = l$) modal ordinates, results in the formation of a linear system of equations:

$$[A_{Bernoulli}]\{x_{Bernoulli}\} = \{0\} \tag{3.7}$$

where $\{x_{Bernoulli}\} = [A\ B\ C\ D]^T$ and $[A_{Bernoulli}]$ is a matrix containing coefficients that depend on the frequency parameter β and the total beam length l. The $\{x_{Bernoulli}\}$ vector is essentially the eigenvector of the $[A_{Bernoulli}]$ matrix. For the case of a spring-hinged articulated rotor blade, certain coefficients of $[A_{Bernoulli}]$ depend on the hub spring stiffness (K^{flap} or K^{lag} depending on the degree of freedom under investigation) and the beam's bending stiffness $EI_{midspan}$. For the cases of a hingeless and a freely-hinged articulated rotor blade, two of the integration constants vanish due to the boundary conditions (B & D for the freely-hinged case and C & D for the hingeless case) and Eq. (3.7) becomes a 2×2 equation. For the spring-hinged articulated blade case, all of the integration constants are retained and a 4×4 matrix equation is formed.

In order for Eq. (3.7) to have a non-trivial solution, the determinant of the $[A_{Bernoulli}]$ must be equal to zero which gives:

$$\det A_{Bernoulli} = 0 \tag{3.8}$$

Solution of Eq. (3.8) will provide the required values of the frequency parameter β for the calculation of the Bernoulli–Euler mode shapes from Eq. (3.6). Due to the nature of the $[A_{Bernoulli}]$ matrix coefficients, Eq. (3.8) is a transcendental equation with infinite solutions that can only be solved numerically for the first N mode shapes that the user wishes to include in the Lagrangian analysis. Subsequent use of Eq. (3.7) leads to the designation of the ratios of the integration constants contained in $\{x_{Bernoulli}\}$. Application of a normalization condition, results in the final mode shape for a given frequency parameter β. The normalization condition used within the context of this work, can be expressed as:

$$\int_0^l \rho A_{midspan} \Phi^2(x)\, \mathrm{d}x = 1 \tag{3.9}$$

Appendix A presents the application of the corresponding boundary conditions for hingeless, freely-hinged and spring-hinged articulated rotor blades in detail. Readily deployable analytical expressions are offered for the derivation of the desired mode shapes for the three blade configurations mentioned above. The analytical form of the acquired mode shapes allows for their spatial derivatives to be also analytically acquired.

The aforementioned process is applied for the N first mode shapes with respect to both flapwise and lagwise blade motion. The acquired modes are subsequently transferred from the effective modal ordinate domain x, to the beam element local radius domain r and are expressed as $\phi_i^{flap}(r)$, $\phi_i^{lag}(r)$, $i = 1, ...N$. Thus, the N first deformation modes for both flap and lag degrees of freedom of an idealized, non-rotating structure with constant bending stiffness and mass per unit length distribution along the beam radius, are obtained. The acquired functions are orthogonal with one another, they comply with the structure's boundary conditions, they are relatively good approximations to the actual mode shapes of the nonuniform–rotating structure (Ref. [25]) and their derivatives with respect to r are readily available in analytical form. Hence, they are deemed excellent candidates for use as assumed deformations functions in Lagrange's equation of motion.

3.2.2 Lagrangian formulation for rotor blade flap/lag dynamics

Having derived a finite series of well-conditioned assumed deformation functions, the Lagrangian problem can be formulated. This process requires that the strain and kinetic energy of the system as well as the virtual work done by the external forces, are expressed as functions of generalized coordinates. The rotor blade is now treated as a continuous system of variable bending stiffness and mass per unit length distribution along the blade

radius. Neither elastic, nor inertial coupling between flap/lag blade motion is accounted for during the formulation described in this chapter and thus the two degrees of freedom are approached separately. Instead of the local modal ordinate x, the local beam radius r is used as the independent variable.

Lagrange's equation of motion (Ref. [26]) for a system whose space configuration can be expressed by a finite series of time-dependent generalized coordinates $q_i(t),\ i = 1, ...N$ dictates that:

$$\frac{d}{dt}(\frac{\partial T}{\partial \dot{q}_i}) - \frac{\partial T}{\partial q_i} + \frac{\partial U}{\partial q_i} = Q_i, \qquad i = 1, ...N \tag{3.10}$$

where T and U are the kinetic and strain energy of the system in that order and Q_i is the generalized external force corresponding to the i^{th} coordinate. Expressing the time-dependent transverse displacement for flap and lag bending motion in terms of the finite series of assumed deformation functions obtained from Bernoulli–Euler beam theory gives:

$$w^{flap}(r,t) = \sum_{i=1}^{N} \phi_i^{flap}(r) q_i^{flap}(t) \tag{3.11a}$$

$$w^{lag}(r,t) = \sum_{i=1}^{N} \phi_i^{lag}(r) q_i^{lag}(t) \tag{3.11b}$$

where $q_i^{flap}(t)$ and $q_i^{lag}(t)$ are generalized coordinates expressing the contribution of the assumed modes on the blade's transverse displacement for flap and lag motion respectively. Assumption of small beam element displacements in terms of $w^{flap}(r,t)$ and $w^{lag}(r,t)$ allows us to set $\dfrac{\partial T}{\partial q_i} \approx 0$ in Eq. (3.10) which becomes:

$$\frac{d}{dt}(\frac{\partial T}{\partial \dot{q}_i}) + \frac{\partial U}{\partial q_i} = Q_i, \qquad i = 1, ...N \tag{3.12}$$

The next step is to express the blade's strain and kinetic energy as functions of the defined generalized coordinates. For the formulation presented in this chapter, the assumed kinetic energy includes only terms associated with the first derivative of the transverse displacement. This is due to the fact that, any inertial terms related to the blade's rotation are treated as external forces. The virtual work done on the blade due to them is therefore calculated independently. The blade's strain and kinetic energy are given by:

$$U^{flap/lag} = \frac{1}{2}\int_{eR}^{R} EI^{flap/lag}(r)(w''^{flap/lag}(r,t))^2\,\mathrm{d}r + \frac{1}{2}K^{flap/lag}(w'^{flap/lag}(eR,t))^2 \tag{3.13a}$$

$$T^{flap/lag} = \frac{1}{2}\int_{eR}^{R} \rho A(r)(\dot{w}^{flap/lag}(r,t))^2\,\mathrm{d}r \tag{3.13b}$$

The term $\dfrac{1}{2}K^{flap/lag}(w'^{flap/lag}(eR,t))^2$ has been included in Eq. (3.13a) in order to account for the added strain energy in the system due to the existence of a discrete spring with

$K^{flap/lag}$ stiffness at the blade hinge location ($r = eR$) for the case of a spring-hinged articulated rotor. For a hingeless or a freely-hinged articulated rotor, the specific term can be removed from the analysis since effectively $K^{flap/lag} = 0$. Substituting Eqs. (3.11a, 3.11b) in Eqs. (3.13a, 3.13b) results in the following expressions:

$$U^{flap/lag} = \frac{1}{2}\sum_{i=1}^{N}\sum_{j=1}^{N} k_{i,j}^{flap/lag} q_i^{flap/lag}(t) q_j^{flap/lag}(t) + \frac{1}{2}\sum_{i=1}^{N}\sum_{j=1}^{N} f_{i,j}^{flap/lag} q_i^{flap/lag}(t) q_j^{flap/lag}(t) \tag{3.14a}$$

$$T^{flap/lag} = \frac{1}{2}\sum_{i=1}^{N}\sum_{j=1}^{N} m_{i,j}^{flap/lag} \dot{q}_i^{flap/lag}(t) \dot{q}_j^{flap/lag}(t) \tag{3.14b}$$

The inter-modal coupling coefficients within Eqs. (3.14a, 3.14b) are defined as follows:

$$m_{i,j}^{flap/lag} = \int_{eR}^{R} \rho A(r) \phi_i^{flap/lag}(r) \phi_j^{flap/lag}(r)\,\mathrm{d}r \tag{3.15a}$$

$$k_{i,j}^{flap/lag} = \int_{eR}^{R} EI^{flap/lag}(r) \phi_i^{''flap/lag}(r) \phi_j^{''flap/lag}(r)\,\mathrm{d}r \tag{3.15b}$$

$$f_{i,j}^{flap/lag} = K^{flap/lag} \phi_i^{'flap/lag}(eR) \phi_j^{'flap/lag}(eR) \tag{3.15c}$$

The terms $m_{i,j}^{flap/lag}$, $k_{i,j}^{flap/lag}$ and $f_{i,j}^{flap/lag}$ are the inertial, elastic and hub-spring inter-modal coupling coefficients respectively between the i^{th} and j^{th} assumed modes of motion for flapwise and lagwise bending. As previously mentioned, the coupling coefficient $f_{i,j}^{flap/lag}$ is non-zero only for an articulated rotor with a discretely defined hub spring. Equations (3.14a, 3.14b) essentially express the blade's strain and kinetic energy as functions of time-dependent generalized coordinates.

The next step is to obtain closed form expressions for the virtual work done by the centrifugal force acting on the rotating blade for flap and lag motion. Figures 3.1, a) & b) illustrate the kinematics of a beam element of mass $dm = \rho A(r)dr$ and local radius r for the flap and lag degrees of freedom respectively. The centrifugal force is directed outwards and away from the center of rotation. Figure 3.1, a) shows that for the case of flapwise bending, the external centrifugal force component dF acts only in the direction of the X – axis, hence $dF = dF_x$. Therefore dF produces work only when the beam element is displaced on the X – axis ($u^{flap}(r,t)$). For the case of lagwise bending, Fig. 3.1, b) demonstrates that there are force components on both X and Y axes (dF_x & dF_y respectively with $dF = \sqrt{dF_x^2 + dF_y^2}$). Thus, work is done when the beam element is displaced on both dimensions ($u^{lag}(r,t)$ and $w^{lag}(r,t)$ correspondingly).

The virtual work done by the centrifugal force on the entire blade due to the time-dependent elementary displacements $\delta u^{flap}(r,t)$, $\delta u^{lag}(r,t)$ and $\delta w^{lag}(r,t)$ of all individual

beam elements, is given by the following expressions for the flap and lag degrees of freedom:

$$\Delta W^{flap} = \int_{eR}^{R} \delta u^{flap}(r,t)\, \mathrm{d}F_x^{flap} \tag{3.16a}$$

$$\Delta W^{lag} = \int_{eR}^{R} \delta u^{lag}(r,t)\, \mathrm{d}F_x^{lag} + \int_{eR}^{R} \delta w^{lag}(r,t)\, \mathrm{d}F_y \tag{3.16b}$$

where $dF_x^{flap/lag}$ are the time-dependent X – axis centrifugal force components for the flap and lag case respectively. It is noted that, a nonlinear term proportional to $\frac{(\delta w^{lag}(r,t))^2}{2}$ has been omitted in Eq. (3.16b). Expressing Eqs. (3.16a, 3.16b) in terms of generalized coordinates gives:

$$\Delta W^{flap} = \sum_{i=1}^{N} Q_i^{flap} \delta q_i^{flap} \tag{3.17a}$$

$$\Delta W^{lag} = \sum_{i=1}^{N} Q_i^{lag} \delta q_i^{lag} \tag{3.17b}$$

where Q_i^{flap}, Q_i^{lag} are the generalized external forces corresponding to the generalized coordinates q_i^{flap} and q_i^{lag} respectively. These are defined as:

$$Q_i^{flap} = \int_{eR}^{R} \frac{\partial u^{flap}(r,t)}{\partial q_i^{flap}} \mathrm{d}F_x^{flap}, \qquad i = 1, ...N \tag{3.18a}$$

$$Q_i^{lag} = \int_{eR}^{R} \frac{\partial u^{lag}(r,t)}{\partial q_i^{lag}} \mathrm{d}F_x^{lag} + \int_{eR}^{R} \frac{\partial w^{lag}(r,t)}{\partial q_i^{lag}} \mathrm{d}F_y, \qquad i = 1, ...N \tag{3.18b}$$

It can be shown from Figs. 3.1 a) & b) that:

$$dF_x^{flap} = \rho A(r) \Omega^2 (eR + (r - eR)\cos\beta(r,t)) dr \tag{3.19a}$$

$$dF_x^{lag} = \rho A(r) \Omega^2 (eR + (r - eR)\cos\zeta(r,t)) dr \tag{3.19b}$$

$$dF_y = \rho A(r) \Omega^2 D \sin\left(\arcsin\frac{w^{lag}(r,t)}{D}\right) dr \tag{3.19c}$$

$$dF_z = 0 \tag{3.19d}$$

where Ω is the nominal rotorspeed in rad/sec and D is the distance of beam element dm from the rotation axis as shown in Fig. 3.1, b). The values $\beta(r,t) = \arcsin\frac{w^{flap}(r,t)}{r - eR}$ and $\zeta(r,t) = \arcsin\frac{w^{lag}(r,t)}{r - eR}$ are the effective beam element flap and lag angles respectively. Having assumed small displacements with regards to w^{flap} and w^{lag}, it can be considered that $\cos\beta(r,t) \approx 1$ and $\cos\zeta(r,t) \approx 1$. Equations (3.19a−3.19c) therefore give:

$$dF_x \equiv dF_x^{flap} = dF_x^{lag} \approx \rho A(r) \Omega^2 r dr \tag{3.20a}$$

$$dF_y = \rho A(r) \Omega^2 w^{lag}(r,t) dr \tag{3.20b}$$

It is noted that no approximation is made with regards to dF_y.

Having obtained closed form approximations for the differential centrifugal force components dF_x and dF_y, what remains in order to acquire expressions for the generalized forces given by Eqs. (3.18a, 3.18b), is the designation of $\frac{\partial u^{flap}(r,t)}{\partial q_i^{flap}(t)}$, $\frac{\partial u^{lag}(r,t)}{\partial q_i^{lag}(t)}$ and $\frac{\partial w^{lag}(r,t)}{\partial q_i^{lag}(t)}$, $i = 1, ...N$. Figure 3.2 presents the elementary dislocations during flapwise bending for a straight-line beam element of infinitesimal length dr. It is illustrated that for a first spatial derivative of transverse displacement equal to $w^{'}(r,t)$, there is an inboard total dislocation du within the infinitesimal radial distance dr. The components of du along the X and Z axes are defined as du_x and du_z respectively. It can be shown from Fig. 3.2 that:

$$du = dr(\sqrt{1 + w^{'}(r,t)^2} - 1) \tag{3.21a}$$

$$du_x = du \cos w^{'}(r,t) \tag{3.21b}$$

$$du_z = du \sin w^{'}(r,t) \tag{3.21c}$$

The dislocation component du_x is of interest both for flap and lag bending motion since there are centrifugal force components on the X – axis for both cases. Expanding Eq. (3.21a) using a McLaurin series up to the first term gives:

$$du \approx \frac{1}{2} w^{'}(r,t)^2 dr \tag{3.22}$$

Assuming small $w^{'}(r,t)$, Eq. (3.21b) leads to $du_x \approx du$. A similar analysis can be conducted for the lag degree of freedom yielding similar expressions for du and du_x. Integration of Eq. (3.22) from the beam root/hinge location ($r = eR$) up until the local beam element radius r, provides the total displacement of a beam element on the X – axis for flap and lag bending motion respectively:

$$u^{flap/lag}(r,t) = -\frac{1}{2} \int_{eR}^{r} w^{'flap/lag}(\xi,t)^2 \mathrm{d}\xi \tag{3.23}$$

where ξ is an independent integration variable. The negative sign has been added in front of the RHS of Eq. (3.23) to signify the inboard nature of the dislocation for both degrees of freedom. This convention essentially leads to negative X – axis differential displacement for positive $w^{'}(r,t)$ and vice-versa.

The terms u^{flap} and u^{lag} can now be expressed as functions of generalized coordinates. Substitution of Eqs. (3.11a, 3.11b) into Eq. (3.23) leads to the following expression:

$$u^{flap/lag}(r,t) = -\frac{1}{2} \sum_{i=1}^{N} \sum_{j=1}^{N} a_{i,j}^{flap/lag}(r) q_i^{flap/lag}(t) q_j^{flap/lag}(t) \tag{3.24}$$

where the parameters $a_{i,j}^{flap}(r)$ and $a_{i,j}^{lag}(r)$ are defined as follows:

$$a_{i,j}^{flap/lag}(r) = \int_{eR}^{r} \phi_i^{'flap/lag}(\xi)\phi_j^{'flap/lag}(\xi)\mathrm{d}\xi \tag{3.25}$$

Derivation of Eqs. (3.24, 3.11b) with respect to their i^{th} generalized coordinate ($q_i^{flap}(t)$ and $q_i^{lag}(t)$ for flap and lag motion in that order) gives:

$$\frac{\partial u^{flap}(r,t)}{\partial q_i^{flap}(t)} = -\sum_{j=1}^{N} a_{i,j}^{flap}(r) q_j^{flap}(t) \tag{3.26a}$$

$$\frac{\partial u^{lag}(r,t)}{\partial q_i^{lag}(t)} = -\sum_{j=1}^{N} a_{i,j}^{lag}(r) q_j^{lag}(t) \tag{3.26b}$$

$$\frac{\partial w^{lag}(r,t)}{\partial q_i^{lag}(t)} = \phi_i^{lag}(r) \tag{3.26c}$$

for $i = 1, ...N$. Combining Eqs. (3.26a, 3.26b, 3.26c) and Eqs. (3.18a, 3.18b) results in closed form expressions for the generalized external forces as functions of generalized coordinates:

$$Q_i^{flap/lag} = -\sum_{j=1}^{N} I_{i,j}^{flap/lag} q_j^{flap/lag}(t), \qquad i = 1, ...N \tag{3.27}$$

$I_{i,j}^{flap}$ and $I_{i,j}^{lag}$ are the effective centrifugal stiffening inter-modal coupling coefficients for flap and lag bending respectively which are defined as follows:

$$I_{i,j}^{flap} = \int_{eR}^{R} \rho A(r)\Omega^2 r a_{i,j}^{flap}(r)\mathrm{d}r \tag{3.28a}$$

$$I_{i,j}^{lag} = \int_{eR}^{R} \rho A(r)\Omega^2 r a_{i,j}^{lag}(r)\mathrm{d}r - \int_{eR}^{R} \rho A(r)\Omega^2 \phi_i^{lag}(r)\phi_j^{lag}(r)\mathrm{d}r \tag{3.28b}$$

Substituting the acquired expressions for strain and kinetic energy from Eqs. (3.14a, 3.14b) along with the generalized force expressions from Eq. (3.27) into Eq. (3.12) results in the following systems of ODEs describing flap and lag motion respectively:

$$\sum_{j=1}^{N} m_{i,j}^{flap/lag} \ddot{q}_j^{flap/lag}(t) + \sum_{j=1}^{N} (k_{i,j}^{flap/lag} + f_{i,j}^{flap/lag} + I_{i,j}^{flap/lag}) q_j^{flap/lag}(t) = 0, \qquad i = 1, ...N \tag{3.29}$$

Assuming periodic motion, we can consider a potential solution for the i^{th} generalized flap/lag coordinate of the form: $q_i^{flap/lag} = \bar{q}_i^{flap/lag} \sin(\omega_i^{flap/lag} t + \psi_i^{flap/lag})$. Substituting the aforementioned expression in Eq. (3.29) results in the following systems of equations:

$$\sum_{j=1}^{N} (G_{i,j}^{flap/lag} - (\omega_i^{flap/lag})^2 m_{i,j}^{flap/lag}) \bar{q}_j^{flap/lag} = 0, \qquad i = 1, ...N \tag{3.30}$$

where $\omega_i^{flap/lag}$ is the natural frequency of the i^{th} bending mode for flap and lag motion in that order. $G_{i,j}^{flap/lag} = k_{i,j}^{flap/lag} + f_{i,j}^{flap/lag} + I_{i,j}^{flap/lag}$, is the overall effective stiffness coupling coefficient between the i^{th} and j^{th} assumed modes of flap/lag bending motion including elastic, hub-spring as well as centrifugal stiffening effects. Eq. (3.30) essentially describes the formulated eigenproblem whose solution leads to the determination of the system's N first natural frequencies ($\omega_i^{flap/lag}$, $i = 1, ...N$) and mode shapes for flap and lag motion in that order. Arranging Eq. (3.30) in matrix notation leads to the following expression:

$$[A_{Lagrange}^{flap/lag}]\{\bar{q}^{flap/lag}\} = 0 \tag{3.31}$$

where $\{\bar{q}^{flap}\} = [\bar{q}_1^{flap},\ \bar{q}_2^{flap}, ...\bar{q}_N^{flap}]^T$, $\{\bar{q}^{lag}\} = [\bar{q}_1^{lag},\ \bar{q}_2^{lag}, ...\bar{q}_N^{lag}]^T$ and $[A_{Lagrange}^{flap}]$, $[A_{Lagrange}^{lag}]$ are square symmetric matrices of size N.

In order for Eq. (3.31) to have non-trivial solutions, the following condition needs to apply:

$$\det A_{Lagrange}^{flap/lag} = 0 \tag{3.32}$$

Equation (3.32) is another transcendental equation that can be evaluated numerically. This can be achieved through marching within the ω_i^{flap} and ω_i^{lag} domains respectively until the first N values of $\omega_i^{flap/lag}$, $i = 1, ...N$ that satisfy Eq. (3.32) are obtained. The vectors $\{\bar{q}^{flap}\}_i$, $\{\bar{q}^{lag}\}_i$, $i = 1, ...N$ are essentially eigenvectors of matrices $[A_{Lagrange}^{flap}]$ & $[A_{Lagrange}^{lag}]$ and are associated with $\omega_i^{flap/lag}$ respectively. Due to the nature of Eq. (3.32), the eigenvector length cannot be readily determined and a separate condition is required. A normalization condition is deployed in order to alleviate this non-uniqueness which is expressed as:

$$\{\bar{q}^{flap/lag}\}_i^T [M]^{flap/lag} \{\bar{q}^{flap/lag}\}_i = 1, \qquad (i = 1, ...N) \tag{3.33}$$

where $[M]^{flap}$ and $[M]^{lag}$ are square symmetric matrices of size N which contain the inertial inter-modal coupling coefficients $m_{i,j}^{flap}$ and $m_{i,j}^{lag}$, $i, j = 1, ...N$ respectively. It can be shown that deployment of Eq. (3.33) is equivalent to using the following condition:

$$\{\bar{q}^{flap/lag}\}_i^T [G]^{flap/lag} \{\bar{q}^{flap/lag}\}_i = (\omega_i^{flap/lag})^2, \qquad (i = 1, ...N) \tag{3.34}$$

where $[G]^{flap}$ and $[G]^{lag}$ are square symmetric matrices of size N which contain the overall effective stiffness inter-modal coupling coefficients $G_{i,j}^{flap}$ and $G_{i,j}^{lag}$, $i, j = 1, ...N$ respectively.

Since $[A_{Lagrange}^{flap}]$ and $[A_{Lagrange}^{lag}]$ are square symmetric matrices, their eigenvectors are orthogonal with one another. The eigenvector orthogonality condition is given by:

$$\{\bar{q}^{flap/lag}\}_i^T [M]^{flap/lag} \{\bar{q}^{flap/lag}\}_j = 0, \qquad i \neq j, \quad i, j = 1, ...N \tag{3.35}$$

The final N first mode shapes of the non-uniform rotating blade for flap and lag bending motion are provided as the dot products of the assumed mode shape vectors and the normalized eigenvectors of $[A^{flap}_{Lagrange}]$ and $[A^{lag}_{Lagrange}]$ matrices respectively. This procedure gives:

$$X_i^{flap/lag}(r) = \{\Phi^{flap/lag}(r)\} \cdot \{\bar{q}^{flap/lag}\}_i^T, \qquad i = 1, ...N \tag{3.36}$$

where $\{\Phi^{flap}(r)\} = [\phi_j^{flap}(r),\ j = 1, ...N]^T$ and $\{\Phi^{lag}(r)\} = [\phi_j^{lag}(r),\ j = 1, ...N]^T$ are the assumed mode shape vectors for flapwise and lagwise bending correspondingly.

Appendix B shows that the orthogonality between the acquired eigenvectors of matrices $[A^{flap}_{Lagrange}]$ and $[A^{lag}_{Lagrange}]$ due to their symmetric nature, also leads to the orthogonality of the acquired mode shapes given by Eq. (3.36). Therefore it applies that:

$$\int_{eR}^{R} \rho A(r) X_i^{flap/lag}(r) X_j^{flap/lag}(r) \mathrm{d}r = 0, \qquad i \neq j, \qquad i, j = 1, ...N \tag{3.37}$$

It is also demonstrated that deployment of the normalization condition expressed by Eq. (3.33) is equivalent to the condition applied for the normalization of the assumed deformation functions using Eq. (3.9) which gives:

$$\int_{eR}^{R} \rho A(r) (X_i^{flap/lag}(r))^2 \mathrm{d}r = 1, \qquad i = 1, ...N \tag{3.38}$$

3.3 Results & Discussion

3.3.1 Lagrangian approximation error

In order to evaluate the influence of the linearization assumption ($\frac{\partial T^{flap/lag}}{\partial q_i^{flap/lag}} \approx 0$) on the proposed method's accuracy, a comparative evaluation has been waged between the exact Bernoulli–Euler beam theory and the approximate Lagrangian formulation. Modal characteristics obtained from the application of the former (Appendix A) have been deployed as assumed deformation functions in the later. Figure 3.3 presents the Lagrangian method's relative error ε in the predicted frequency parameter β for the 10 first bending modes of a uniform non-rotating structure. The relative error ε is defined as:

$$\varepsilon = \frac{|\beta_{Lagrange} - \beta_{Bernoulli}|}{\beta_{Bernoulli}} \tag{3.39}$$

Results are presented for boundary conditions corresponding to a hingeless (Fig. 3.3, a)) and a spring-hinged articulated rotor blade (Fig. 3.3, b)). The influence of the total number of deployed assumed deformation functions on each mode's relative error ε is shown for both configurations.

It is observed from Fig. 3.3 that ε never exceeds a value of 7.6×10^{-5} and 3×10^{-5} for hingeless and spring-hinged articulated blade boundary conditions respectively. For the case of a hingeless rotor blade, Fig. 3.3, a) shows that ε is of the same order of magnitude for all modes, decreasing slightly with increasing mode number, with the exception of the 10^{th} mode where a small increase is observed. A small variation of ε with the number of assumed functions deployed in the formation of the Lagrangian eigenproblem is also observed for all modes. It is noted however that the overall range of this increase reaches approximately 2×10^{-7} per mode for a variation of up to 12 assumed modes, which can be considered negligible.

For the case of a spring-hinged articulated rotor blade, Fig. 3.3, b demonstrates the much larger difference in ε between mode shapes reaching roughly two orders of magnitude. A logarithmic scale is used for clarity. Again, there is but an infinitesimal variation of ε with the number of deployed assumed functions for each mode. It can be noticed that ε decreases rapidly with increasing mode number, which is partially due to the also increasing non-dimensionalizing head in Eq. (3.39). This is a sign of excellent convergence characteristics and consistent absolute error well within the user-imposed tolerance for the numerical solution of Eq. (3.31).

There is virtually no difference between the mode shapes obtained by the Lagrangian formulation and Bernoulli–Euler theory regarding both sets of boundary conditions. Further comparisons will therefore not be carried. It can thus be concluded that the linearization assumption for the Lagrangian equation is justifiable and does not result in significant errors for the relevant sets of boundary conditions. The ability of the Lagrangian approximation to numerically re-produce analytically derived results with very good levels of accuracy has also been demonstrated.

3.3.2 Numerical performance

In order to evaluate the numerical performance of the developed approach, an articulated and a hingeless small-scale generic helicopter rotor blade model have been analyzed. The small-scale models have been extensively described in Refs. [31, 32] respectively and thus further elaboration regarding their configuration shall be omitted. Simulations have been performed for values of rotorspeed corresponding to $\Omega = 69\, rad/sec\, (660\, rpm)$ and $\Omega = 105\, rad/sec\, (1000\, rpm)$ for the articulated and hingeless rotor blade models respectively.

Figures 3.4, 3.5 present the influence of the number of assumed deformation functions on the first five normalized flap/lag modal frequencies for the articulated and the hingeless rotor model respectively. The relatively quick convergence of each modal frequency to a definite value can be observed for both models. It is noted that the predicted first flap/lag modal frequencies are relatively uninfluenced by the number of assumed functions and that a definite value is obtained with the use of only two Bernoulli–Euler modes. A

similar observation can be made with regards to the second flap/lag frequencies where convergence has been achieved with the use of three and four modes for the cases of the articulated and the hingeless rotor blade respectively.

It is noticed that the lower modal frequencies converge fairly quickly to a constant value while a larger number of assumed modes is required for convergence to be achieved for frequencies corresponding to higher modes. This behavior is more pronounced in the higher lag modal frequencies which are inherently higher in comparison to the frequencies of the corresponding flap modes due to the significantly increased lag bending stiffness of the blades. A higher number of assumed modes associated with higher frequency content is therefore required to accurately capture the frequencies of the "stiffer" lag bending modes.

It is also highlighted that, convergence is achieved with a relatively smaller number of assumed functions for each mode of the articulated rotor model in comparison to the hingeless model. This is due to the fact that the hingeless rotor model incorporates very large steps of flap/lag stiffness as well as mass per unit length at the blade root location. These variations in conjunction with the corresponding boundary conditions, essentially deem the actual mode shapes at the root significantly different to the deployed assumed functions. The Lagrangian formulation must therefore be refined through the inclusion of higher order/more complex modal functions in order to accurately approximate the actual mode shapes at the blade root position and therefore obtain more accurate estimates of the corresponding natural frequencies.

It can thus be concluded that the proposed method possesses very good numerical behavior. Convergence is obtained for all required mode shapes with the deployment of a relatively small number of assumed deformation functions. Since the assumed functions are analytically derived from Bernoulli–Euler beam theory, there is no theoretical limit in their maximum obtainable number. It is noted that the proposed approach has not demonstrated any numerical instabilities or potential divergence during the course of this work.

3.3.3 Comparison with experiment and finite element analysis

Following the evaluation of the numerical behavior, several comparisons with experimental measurements as well as finite element analysis results have been waged for both rotor blade models mentioned above. The method's performance in predicting flap/lag natural frequencies and mode shapes is assessed for wide rotorspeed range.

Figure 3.6 presents the calculated resonance chart for the small-scale articulated rotor blade model described in Ref. [31]. Experimentally measured as well as FEA derived flap/lag frequencies extracted from Ref. [31] have been superimposed upon the resonance chart in Figs. 3.6, a) and b) respectively. The solid and broken curves represent Lagrangian

method predictions (Lagr.) while the markers signify experimental measurements or FEA results depending on indication. It is noted that the experiments reported Ref. [31] have not been conducted in vacuum conditions and therefore aerodynamic interference effects are essentially present in the measurements. It can be observed from Fig. 3.6, a) that the correlation between the rotating-blade frequencies obtained from the Lagrangian formulation and the experimentally measured ones can generally be considered as very good over the entire rotorspeed range. It is noted that the first flap and lag modes of motion are essentially rigid body modes for which Ref. [31] contains no data. Agreement is best with regards to the second flap and lag and well as the third flap frequencies. A larger discrepancy is noted with respect to the fourth flap mode frequency.

Figure 3.6, b) presents a comparison of the current numerical approach with results obtained from the MSC/NASTRAN finite element computer code for the specific articulated rotor model. Since Ref. [31] contains no data with regards to the rigid body modes, the superimposed data for the first flap and lag modes have been calculated based on Euler's extended dynamical equations (Ref. [25]). The agreement between the Lagrangian formulation and the FEA results is excellent over the entire range of rotorspeeds for which calculations have been carried out and for all flap/lag modes. The authors of Ref. [31] have attributed the relatively large discrepancy between experiment and FEA regarding the fourth flap mode frequency to inaccurate flapping stiffness data. This data has been used in the Lagrangian formulation presented in this chapter which essentially justifies the relative error in the predicted fourth flap mode frequency observed in Fig. 3.6, a) as well.

The corresponding calculated normalized mode shapes of flap and lag motion for the small-scale articulated rotor model are presented in Figs. 3.7, a) and b) respectively. Unfortunately Ref. [31] contains no data with respect to the measured or the FEA derived mode shapes so further comparisons for the particular model have not been carried out.

Figure 3.8 presents the calculated resonance chart for the small-scale hingeless rotor blade model described in Ref. [32] with the solid and broken lines signifying Lagrangian predictions (Lagr.). Figs. 3.8, a) and b) compare the calculated modal frequencies with experimental measurements and FEA results respectively extracted from Ref. [33]. It is noted that, contrary to the experimental measurements presented in Ref. [31], the measurements reported in Ref. [33] have been conducted in vacuum conditions. They are therefore not contaminated by any aerodynamically induced excitation. A limited number of data points is available in Ref. [33] regarding the measured natural frequencies and therefore Fig. 3.8, a) presents comparisons only for these points. It can be shown that the correlation between the predictions of the Lagrangian formulation and the measurements is very good for non-rotating conditions ($\Omega = 0\, rad/sec$) with respect to all modes presented. At high-speed rotating conditions however ($\Omega = 105\, rad/sec\, (1000\, rpm)$), it appears that there is a relatively small discrepancy between the predictions and the

measurements regarding all modes compared.

A potential source for the particular discrepancies at high-speed rotating conditions may be due to a combination of the linearization assumption requiring small values of $w^{'}(r,t)$ in Eq. (3.21b), the normalization condition of the Bernoulli–Euler functions (Eq.(3.9)) and the small-scale nature of the particular rotor configuration. Equation (3.9), which is used for the normalization the assumed functions, implies a generalized mass equal to 1 for each mode. This may be an overestimation, considering the small-scale nature of the rotor blade under consideration, leading to large assumed modal amplitudes for the assumed functions. This essentially results to the breakdown of the linearization assumption requiring small displacements for the derivation of Eqs.(3.20a, 3.20b) which describe the centrifugal loading on a beam element. Deployment of a more refined normalization condition for the assumed functions at small-scale conditions may in fact alleviate this discrepancy. Figure 3.8, b) presents a comparison of the present numerical approach with results obtained from the nonlinear finite element computer code described in Refs. [34,35]. A very good correlation can once again be noted for all modal frequencies analyzed. The correlations appear to be stronger for non-rotating conditions due to the reasons elaborated above.

Figures 3.9, 3.10 present the normalized calculated mode shapes for the small-scale hingeless rotor blade model described in Ref. [32] for non-rotating conditions ($\Omega = 0\ rad/sec$). Comparisons with the experimental and FEA results reported in Ref. [33] are included in Figs. 3.9 and 3.10 respectively. The solid and broken lines correspond to predictions while the markers signify experimentally measured values/FEA results. It can be observed from Fig. 3.9 that there is a very good agreement between the predicted and measured mode shapes regarding both flap and lag bending motion. A small discrepancy is observed at approximately 60% of blade radius for the second flap mode. Fig. 3.10 illustrates the excellent agreement between the mode shape predictions of the Lagrangian approach and the FEA results with respect to both flap and lag degrees of freedom.

Figures 3.11, 3.12 present the normalized calculated mode shapes for high-speed rotating conditions ($\Omega = 105\ rad/sec\ (1000\ rpm)$). Comparisons with experiment and FEA are provided in Figs. 3.11 and 3.12 respectively. Figure 3.11 demonstrates that there is a good agreement between experiment and simulation with the exception of the first flap mode. A similar behavior is observed in Fig. 3.12 where excellent agreement is exhibited between the Lagrangian approach and FEA results for all modes presented apart from the first flap mode. The results of Ref. [33] suggest that the specific mode shape of the particular rotor configuration is highly influenced by the effects of centrifugal stiffening at high-speed rotating conditions, while the rest of the mode shapes remain relatively unchanged. The current Lagrangian approach suggests that the particular mode shape is not influenced as much as suggested by the findings of Ref. [33]. At this point it is noted that, a radical alteration in a single mode shape while keeping the remaining ones

unchanged essentially results in a violation of the orthogonality condition expressed by Eq.(3.37)

3.4 Conclusions

A computationally efficient numerical method targeting the rapid estimation of the uncoupled natural vibration characteristics of helicopter rotor blades has been described. Lagrange's equation of motion along with Bernoulli–Euler beam theory have been utilized in order to derive an integrated approach applicable to rotating blades with nonuniform stiffness and mass per unit length properties. Readily implementable closed form expressions for the simulation of hingeless, freely-hinged and spring-hinged articulated rotor blades have been offered. Comparisons have been waged with experimental measurements and results from finite element analysis for a hingeless and an articulated small-scale helicopter rotor model.

It has been shown that the proposed methodology is capable of numerically re-producing analytically derived modal frequencies with great accuracy. Excellent numerical behavior is exhibited for all modes with no instabilities and definite convergence characteristics using a relatively small number of assumed deformation functions. Very good, in some cases excellent, agreement has been demonstrated for the predicted flap/lag natural frequencies with experiments and FEA results regarding both small-scale rotor models. Very good agreement has also been indicated with regards to the predicted mode shapes of the small-scale hingeless rotor model with the exception of the first flap mode at very high-speed rotating conditions. The acquired results are highly encouraging especially considering the proposed method's computational efficiency as well as the associated ease of implementation.

Although only the cases of flapwise and lagwise bending have been elaborated within the context of this work, the proposed approach can also be extrapolated to the case of torsional vibration. Application of a more refined condition for the normalization of the Bernoulli–Euler functions may improve the prediction accuracy at high-speed rotating conditions. Application of the proposed method results in the modal content required for a comprehensive rotor aeroelasticity analysis in the time domain without the need of a computationally expensive finite element simulation or a multi-body dynamics formulation.

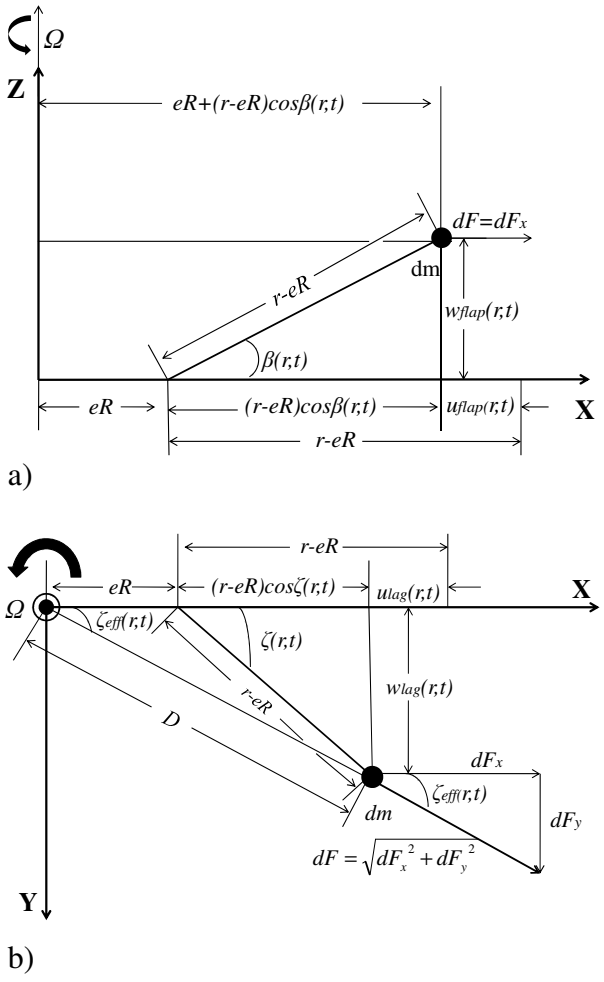

Figure 3.1: Beam element kinematics: a) Flap bending motion, b) Lag bending motion

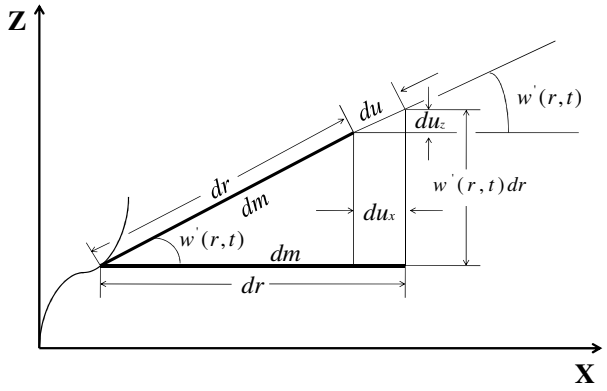

Figure 3.2: Elementary dislocations of a beam element for flap bending motion

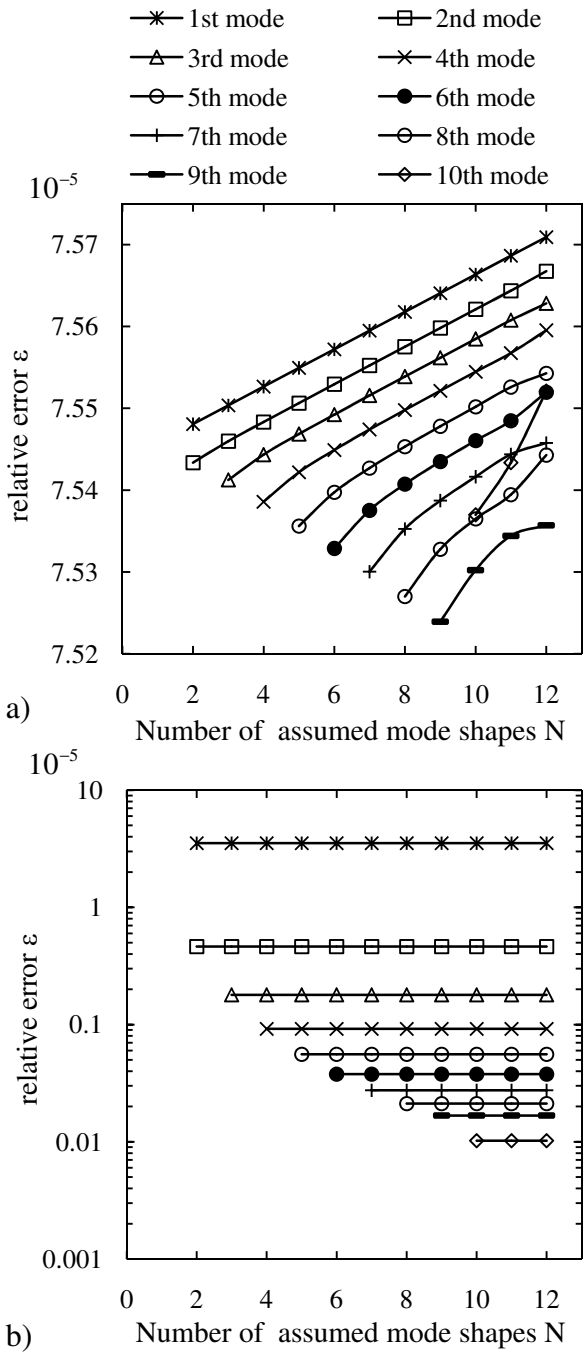

Figure 3.3: Frequency parameter relative error: a) Hingeless blade boundary conditions, b) Spring-hinged articulated blade boundary conditions

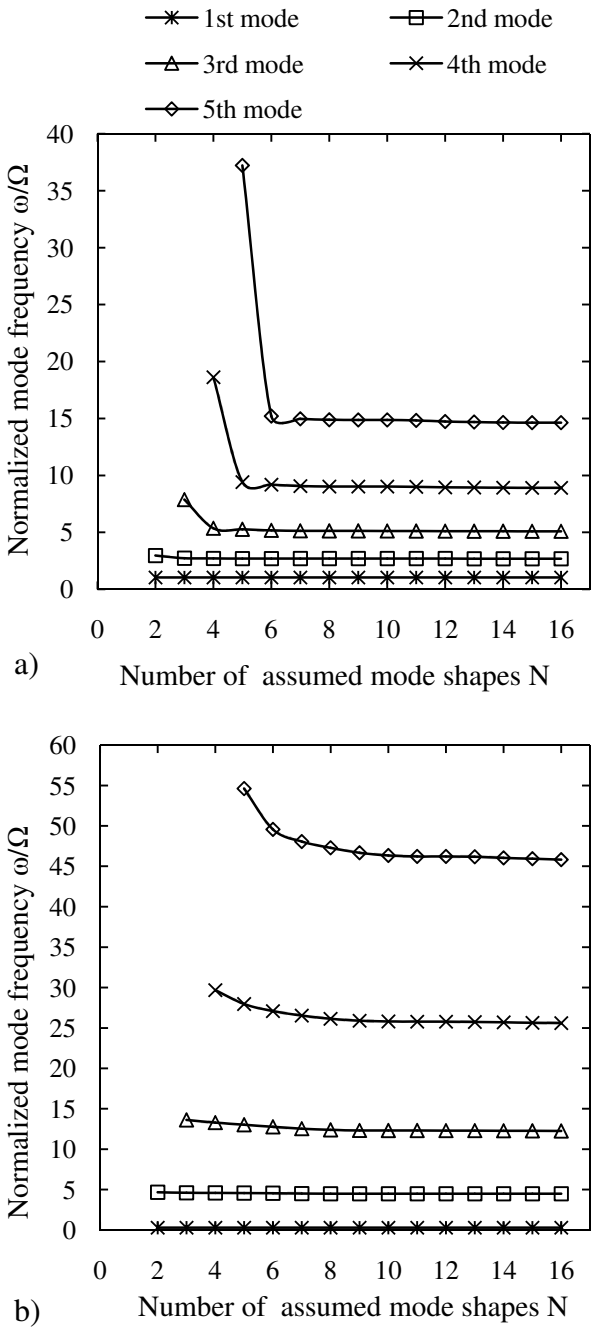

Figure 3.4: Influence of number of assumed deformation functions on the normalized modal frequencies of the articulated rotor blade model described in Ref. [31], $\Omega = 69\,rad/sec\,(660\,rpm)$: a) Flap modes, b) Lag modes

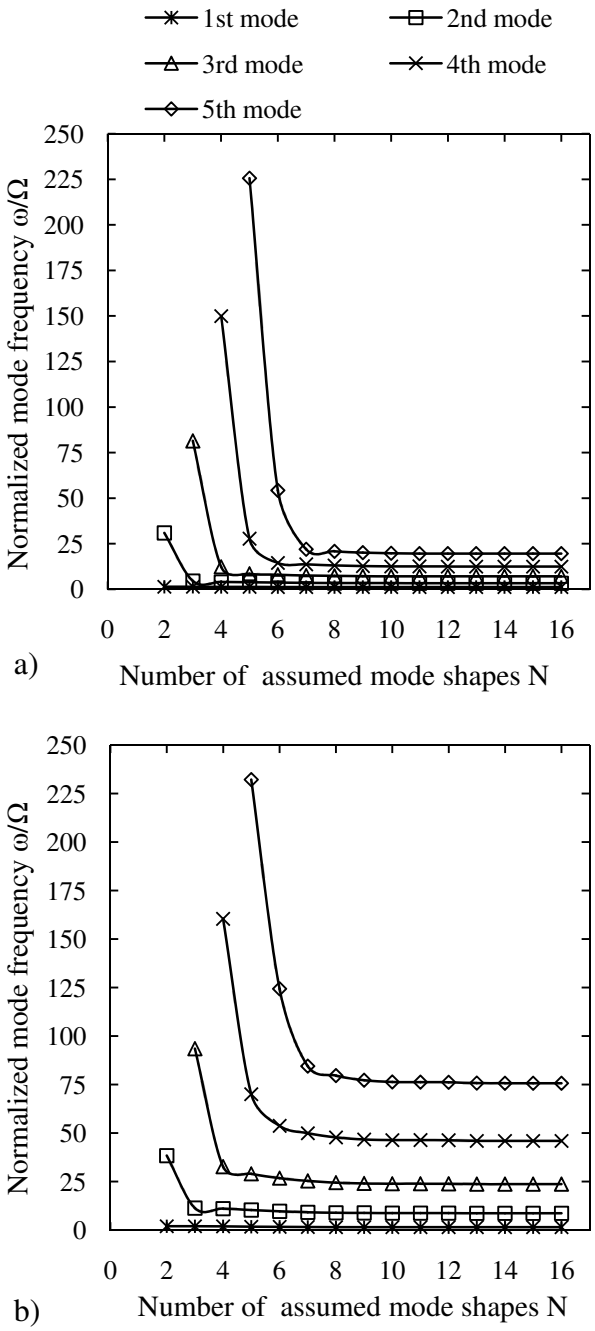

Figure 3.5: Influence of number of assumed deformation functions on the normalized modal frequencies of the hingeless rotor blade model described in Ref. [32], $\Omega = 105\,rad/sec\,(1000\,rpm)$: a) Flap modes, b) Lag modes

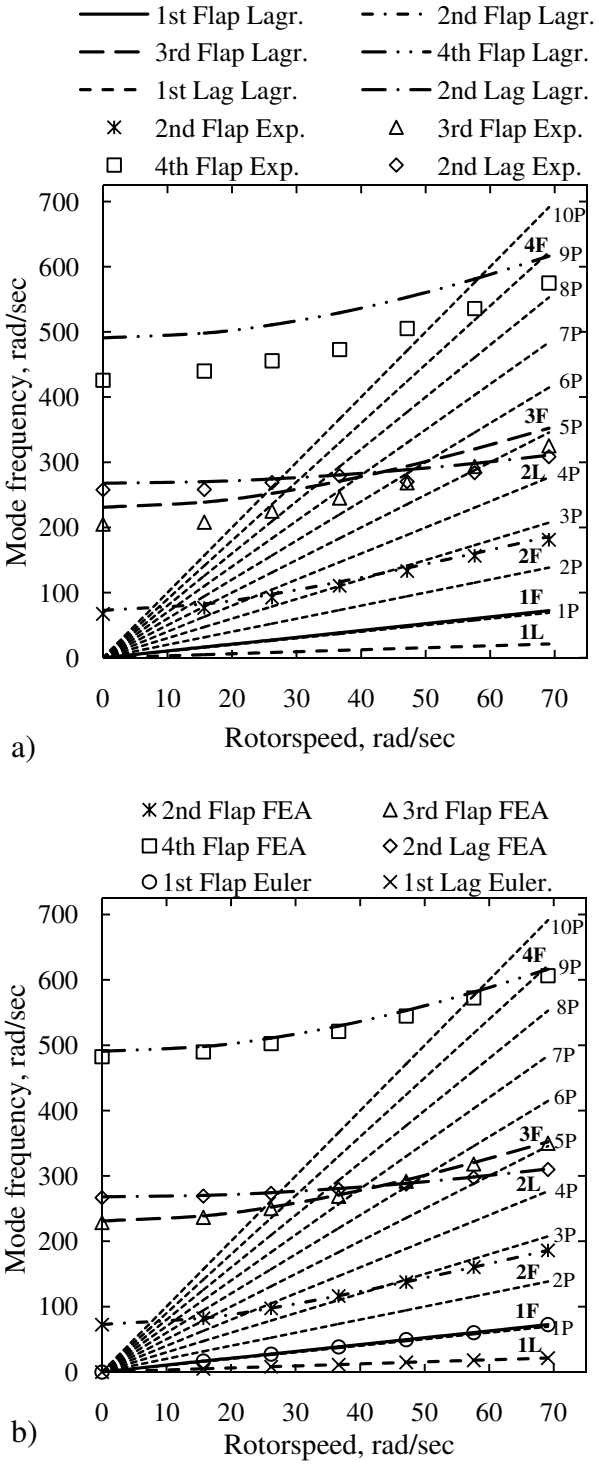

Figure 3.6: Resonance chart calculated for the articulated rotor blade model described in Ref. [31], comparison with: a) Experiment, b) Finite element analysis

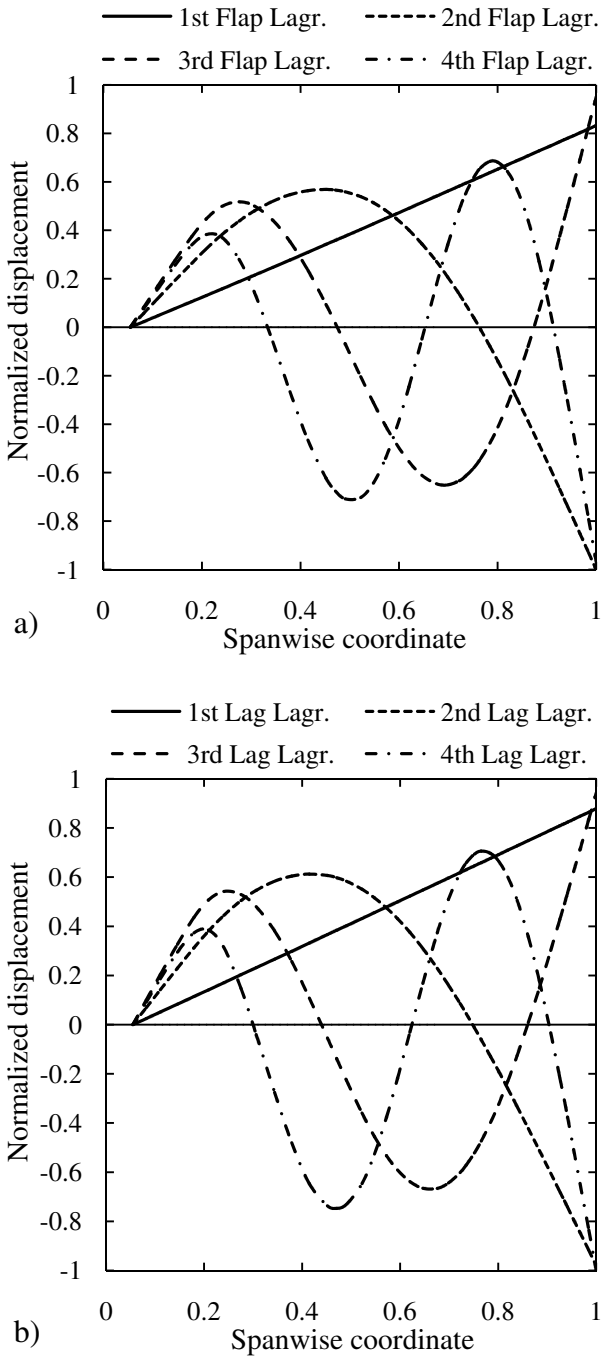

Figure 3.7: Normalized mode shapes calculated for the articulated rotor blade model described in Ref. [31], $\Omega = 69\, rad/sec\, (660\, rpm)$: a) Flap modes, b) Lag modes

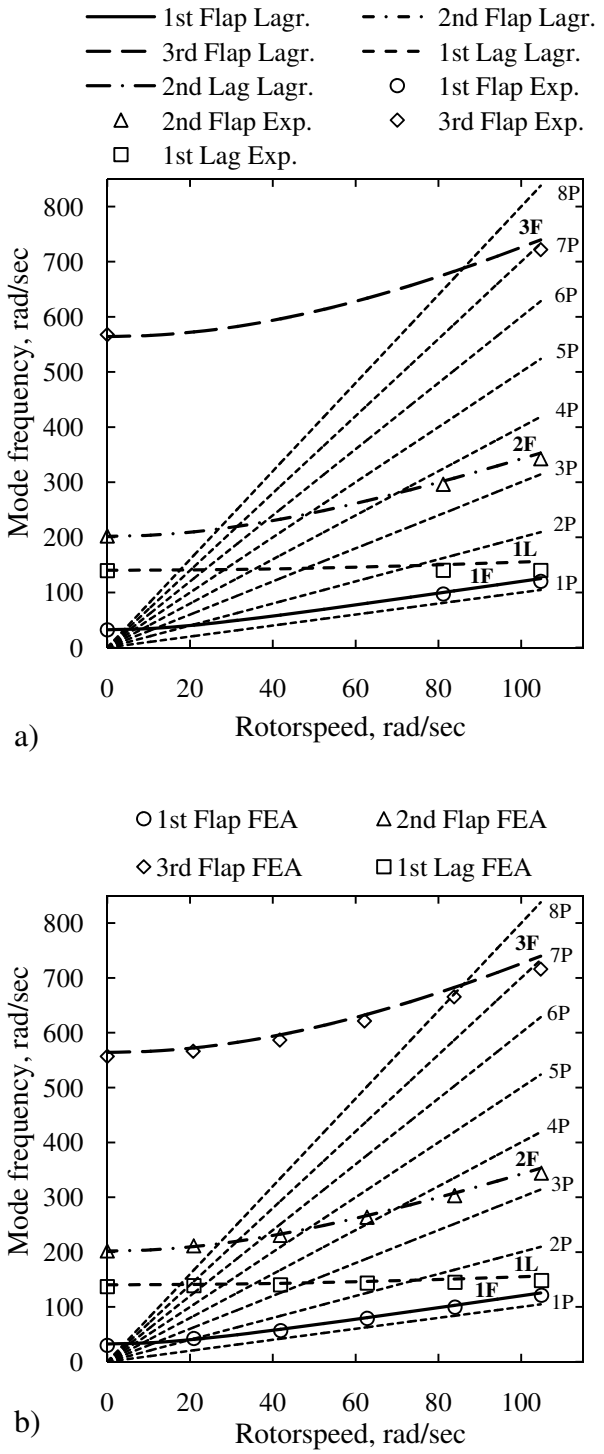

Figure 3.8: Resonance chart calculated for the hingeless rotor blade model described in Ref. [32], comparison with results from Ref. [33]: a) Experiment, b) Finite element analysis

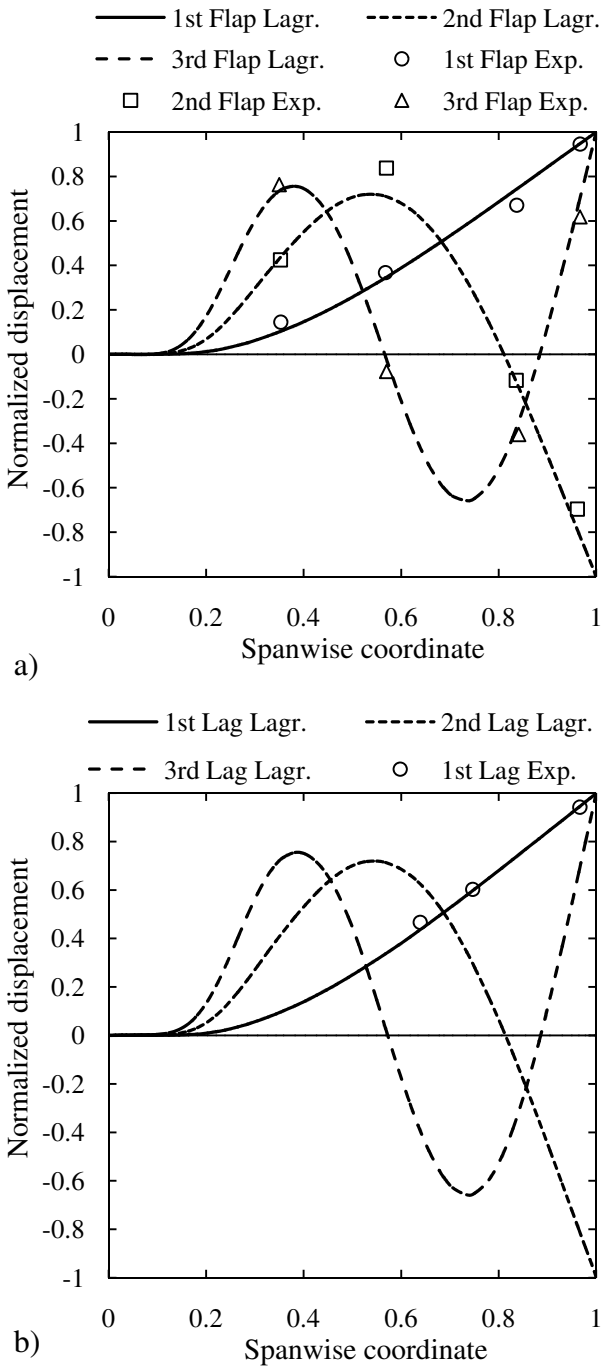

Figure 3.9: Normalized mode shapes calculated for the hingeless rotor blade model described in Ref. [32], $\Omega = 0\, rad/sec$ – comparison with experimental measurements from Ref. [33]: a) Flap modes, b) Lag modes

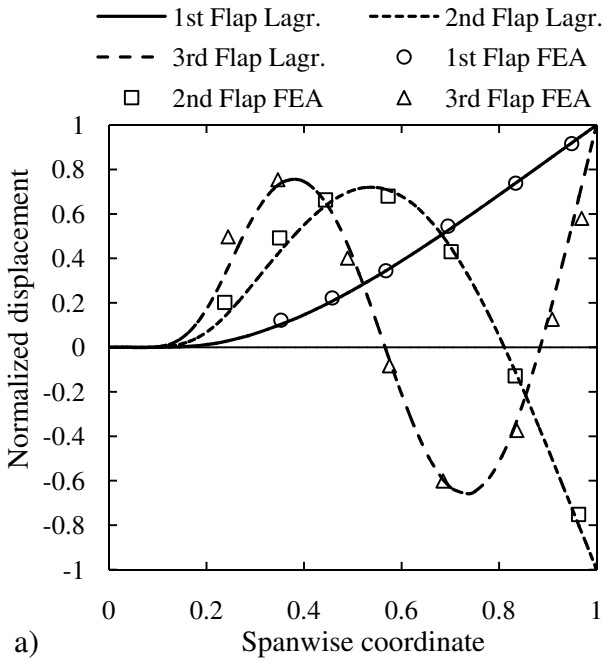

Figure 3.10: Normalized mode shapes calculated for the hingeless rotor blade model described in Ref. [32], $\Omega = 0\, rad/sec$ – comparison with finite element analysis results from Ref. [33]: a) Flap modes, b) Lag modes

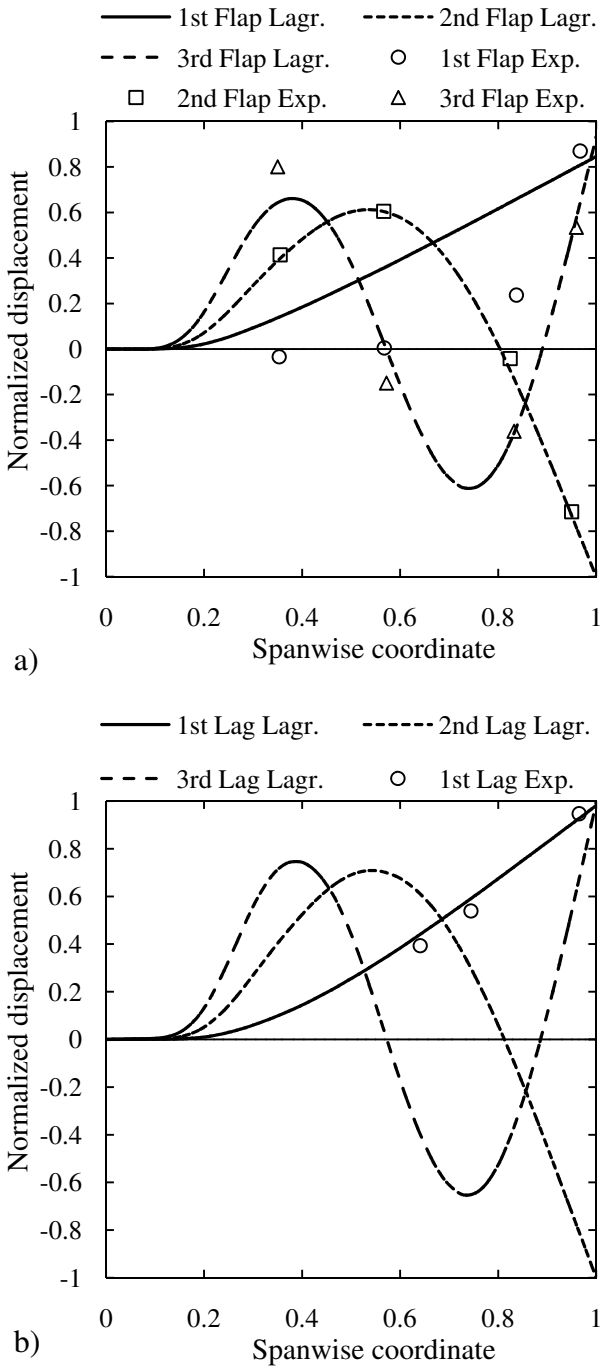

Figure 3.11: Normalized mode shapes calculated for the hingeless rotor blade model described in Ref. [32], $\Omega = 105\ rad/sec\ (1000\ rpm)$ – comparison with experimental measurements from Ref. [33]: a) Flap modes, b) Lag modes

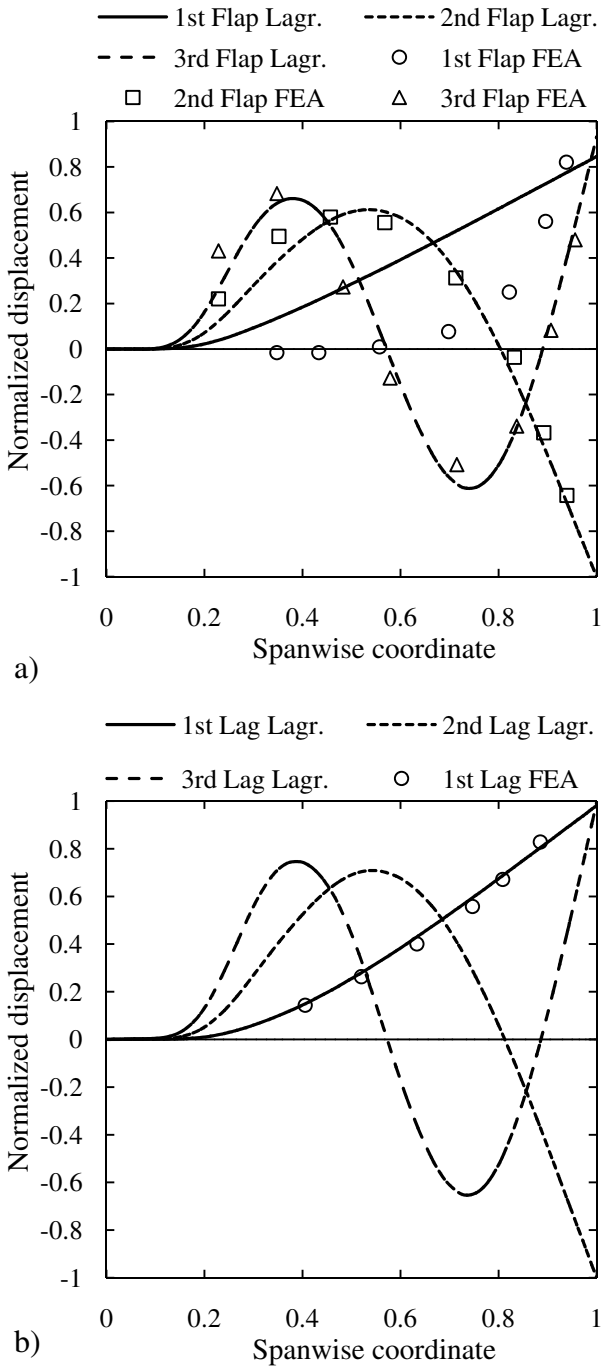

Figure 3.12: Normalized mode shapes calculated for the hingeless rotor blade model described in Ref. [32], $\Omega = 105\,rad/sec\,(1000\,rpm)$ – comparison with finite element analysis results from Ref. [33]: a) Flap modes, b) Lag modes

Chapter 4

Rotor Blade Flexibility Simulation for Helicopter Aeroelasticity and Flight Dynamics Applications

4.1 Introduction – Literature

As established in the 3^{rd} chapter of this Thesis, in order to cater for precise estimates of the unsteady main rotor forces and moments within helicopter flight dynamics simulation, it is necessary to adapt an approach treating each rotor blade as an individual entity. This not only allows for inclusion of more detailed blade dynamics models, but also for the implementation of improved inflow and blade aerodynamics models.

As elaborated within chapter 3, initial versions of individual–blade rotor formulations would essentially treat each blade as a rigid body. Combinations of hinge offsets and springs were used in order to account for the effective hub stiffness of hingeless rotor blades. Such models include the "Genhel" rotor model which was originally developed by Howlett in Ref. [36] for the UH-60 Blackhawk. The "Genhel" model was subsequently improved as shown in Refs. [18,37–39]. Other individual–rigid–blade rotor models include those due to Curtiss, Chaimovich, Miller, Talbot and Padfield as described in Refs. [40–44] respectively.

The development of more sophisticated rotor inflow (Ref. [45]) and blade aerodynamics models (Ref. [46]) has essentially led to the requirement of more advanced rotor dynamics models in order to keep up with the level of simulation fidelity. Brown *et al.* (Ref. [8]) performed a comparative evaluation between a first order finite state dynamic inflow model (Refs. [47–49]) and a formulation that solves the vorticity transport equation on a computational mesh enclosing the helicopter (Ref. [45]). Both inflow models were coupled dynamically with a rigid–blade rotor model and a fuselage dynamics model.

The effectiveness of the inflow models was assessed in terms of their quality of prediction of trimmed rotor blade flap, lag and feather angles, airframe attitudes, cross coupling derivatives, response to control inputs and airframe vibration characteristics. Brown *et al.* noted that the inclusion of real flow-field effects is an important factor with regards to extending the bandwidth over which flight dynamic models are valid. Despite that however, they concluded that in order for an improvement in the overall level of flight dynamics simulation fidelity to be achieved, advances in both rotor dynamics as well as inflow models need to be catered for simultaneously. Hence, an integrated jump in complexity of several aspects of the flight dynamics model is required. It was therefore understood that the classical rigid blade model was essentially acting as a bottleneck with regards to overall level of simulation fidelity.

With regards to a hingeless rotor, treating the blade as a rigid body is essentially an approximation to the motion of the elastic blade and specifically to the first cantilever flap and lag modes. A real rotor blade responds to the exerted aerodynamic and inertial loads by deforming in all of its modes. The magnitude of the contribution of higher modes to the rotating hub moment is directly related to the character of the external (aerodynamic and inertial) forcing. Shupe (Refs. [50, 51]) examined the effects of the second flap bending mode of a hingeless blade on the transmitted hub moment for a wide range of flight conditions. He supported the argument that the more pronounced the radial nonlinearity in the one-per-rev harmonic forcing, the greater will be the contribution of the higher modes. Thus, he concluded that the inclusion of the influence of higher order modes in flight dynamics simulation is essential for the correct hub moment prediction of hingeless rotors, especially in high-speed flight.

Lewis (Ref. [14]) used a multi-body dynamics formulation in order to investigate the effect of blade flexibility on the dynamics of the UH-60 articulated rotor and compared his results with flight test data. He concluded that for articulated rotor helicopters, the effect of blade flexibility is quite small in hover and increases slightly with increasing speed. Sturisky (Ref. [15]) however reports, that for the articulated rotor of the AH-64, the inclusion of higher order inflow dynamics coupled with a flexible blade model, may substantially improve the prediction accuracy of the off-axis rotor response to control inputs.

Turnour *et al.* (Ref. [16]) presented a methodology targeting the inclusion of coupled flap–lag–torsion dynamics of elastic rotor blades in flight dynamics applications. They presented a thorough treatment of the blade's inertial loads that had not been dealt with in previous references. Their method included the coupling of the elastic rotor model used in Ref. [17] with the fuselage equations of the "UM-Genhel" flight dynamics model (Ref. [18]) plus a finite-state induced flow model (Ref [10]). The integrated model was subsequently deployed for the purpose of evaluating the influence of blade flexibility on the frequency response characteristics of an articulated rotor helicopter in hover and forward

flight. Turnour *et al.* concluded from their results that, for the articulated rotor under investigation, the inclusion of blade flexibility along with higher order inflow dynamics does not improve the prediction of the off-axis rotor response to control inputs.

Colin *et al.* (Ref. [52]) described an integrated non-real-time flight dynamics simulation model which included the effects of blade flexibility with coupled flap–lag–torsion degrees of freedom and a free wake inflow formulation. A baseline flight mechanics model, described in Ref. [39], was coupled with the flexible blade model from Ref. [16] and a relaxation-type free wake model given in Ref. [53]. Colin *et al.* used the integrated model to investigate the effects of inflow and blade dynamics modeling on the accuracy of the predicted free-flight response of the BO-105 helicopter in a near hover maneuvering conditions. They arrived at the conclusion that neither free wake nor flexible blade models are required in order to obtain accurate prediction of the on-axis rotor response. However, for the given hingeless rotor system, accurate prediction of the off-axis rotor response requires sophisticated modeling and thus both free wake and flexible blade models must be used.

In light of what has been described in the aforementioned references, it is understood that the effect of blade flexibility on the main rotor response characteristics is rather pronounced for hingeless rotor systems and relatively moderate for articulated rotors. At this point Brown's *et al.* (Ref. [8]) conclusion shall be referred to once again: In order for an improvement in the overall level of flight dynamics modeling fidelity to be achieved, advances in both rotor dynamics as well as inflow and aerodynamics models need to be catered for simultaneously. It is therefore difficult to assess advances in rotor wake and blade aerodynamics models in the context of achieved simulation fidelity for flight dynamics, without catering for equivalent improvements in rotor dynamics models.

This chapter describes a comprehensive methodology targeting the simulation of rotor blade flexibility for helicopter flight dynamics and aeroelasticity applications. The modal characteristics obtained using a minimum potential energy Lagrangian approach are utilized. Each rotor blade is treated as a continuous system of nonuniform mass and stiffness properties. An ample treatment of the blade's three-dimensional kinematics in the time domain is offered. The nonlinear acceleration terms associated with large deflections and hub-wind angular motions are thoroughly retained. A stable, 2^{nd} order accurate, backward difference scheme, previously used successfully in the context of time-accurate free-wake analysis (Ref. [9]), is deployed for the approximation of the motion derivatives. Inertial coupling between flap, lag torsion is taken into account through proper treatment of the nonlinear acceleration terms. The process of aerodynamic and inertial loads integration is thoroughly discussed. Integral expressions are provided describing the overall forces and moments exerted by the main rotor in the hub-wind axes system. The model is compatible with every inflow and blade element aerodynamics theory that can operate in the time domain. It is readily available for implementation in existing codes utilizing

the hub-wind reference system without any change in the offered expressions.

The described rotor model is coupled with a finite state wake model (Ref [10]) and an unsteady nonlinear blade element aerodynamics model (Ref. [11]). The time-dependent response of the rotor blades to aerodynamic and inertial loads is calculated using a 5^{th} order accurate numerical evaluation scheme of the convolution integral. The integrated approach is deployed in order to investigate the unsteady structural loads of a full-scale, pre-coned hingeless rotor. An extensive comparative evaluation has been waged between predicted flapwise and chordwise blade bending moments and wind tunnel/flight test measurements.

It is shown that, the structured numerical approach is successful in predicting the low-frequency components of oscillatory flapwise and chordwise blade moments. The importance of including higher deformation modes for the accurate prediction of bending moments at the blade's mid-span position is demonstrated. Simulation results suggest that flapwise bending moment at the blade mid-span position comprises predominantly oscillatory loading associated with the 2^{nd} and 3^{rd} elastic modes, while chordwise moment consists mostly of 1P loading. The overall acquired results indicate the good predictive capabilities of the presented rotor model, considering its simplicity, generality, ease of implementation and computational efficiency.

4.2 Methodology

4.2.1 Natural vibration characteristics of helicopter rotor blades

The minimum potential energy approach based on Lagrange's equation of motion described in the 3^{rd} chapter of this Thesis, is utilized in order to obtain the natural vibration characteristics of the main rotor blades for flap and lag blade motion. It is noted that, neither inertial nor elastic coupling between flap/lag bending has been taken into account during the formation of the Lagrangian eigenproblem. The flap and lag degrees of freedom are essentially treated separately during the modal analysis.

Although elastically uncoupled flap and lag blade motion is considered within the present chapter, the modal characteristics of any employed theory can be used with any level of coupling considered. Blade torsion can also be included in the analysis. The approach presented in this chapter, maintains the inertial coupling between flap, lag and torsion through proper treatment of the inertial blade loads.

4.2.2 Treatment of three-dimensional rotor blade kinematics

Having obtained the necessary modal content with respect to the nonuniform rotating blades, the dynamic response of the integrated rotor system to any pilot control inputs or

externally imposed excitation can be estimated. In order to capture the true aeroelastic response of the main rotor, it is necessary that the time-dependent aerodynamic as well as inertial loads exerted on the rotor blades are accurately predicted. The helicopter may be pitching, rolling, climbing or turning. The velocity and acceleration terms associated with the motion of the helicopter and the deformation of the elastic blade need to be catered for. Therefore, an effective treatment of the rotor blade's nonlinear, three-dimensional kinematics is required. The treatment proposed in this chapter is based on the theory of rigid body kinematics with relative motion.

Figures 4.1 a), b) and c) illustrate the reference systems used for the description of the elastic blade's three-dimensional kinematics. The present formulation places each beam element $p(r,t)$ of radius r on the blade's mean elastic axis (Fig. 4.1, a)). Each element $p(r,t)$ is treated as a material object with mass $dm = \rho A(r)dr$ whose center gravity is offset from the blade's elastic axis according to user specification. A global non-rotating reference frame O which is aligned with the main rotor shaft is defined. The O frame's origin is located at the center of the main rotor hub and has unit vectors $\tilde{e}_x$, $\tilde{e}_y$, $\tilde{e}_z$ as shown in Fig. 4.1, a). The O system's unit vectors are specified relative to the hub-wind axes system as follows:

$$\begin{Bmatrix} \tilde{e}_x \\ \tilde{e}_y \\ \tilde{e}_z \end{Bmatrix} = [HW] \begin{Bmatrix} \tilde{e}_x^{hw} \\ \tilde{e}_y^{hw} \\ \tilde{e}_z^{hw} \end{Bmatrix} \tag{4.1}$$

where $[HW]$ is the transformation matrix between the hub-wind axes system and the non-rotating reference frame O. It is defined as:

$$[HW] = \begin{bmatrix} -1 & 0 & 0 \\ 0 & 1 & 0 \\ 0 & 0 & -1 \end{bmatrix} \tag{4.2}$$

where $\tilde{e}_x^{hw}$, $\tilde{e}_y^{hw}$, $\tilde{e}_z^{hw}$ are the corresponding unit vectors of the hub-wind axes system (Ref. [7]). The translational as well as angular velocity and acceleration components on the O reference frame axes due to the motion of the helicopter are shown in Fig. 4.1, a) and are classified in vector notation below:

$$\tilde{u}_o = [u_o \quad v_o \quad w_o]^T \tag{4.3a}$$

$$\tilde{\dot{u}}_o = [\dot{u}_o \quad \dot{v}_o \quad \dot{w}_o]^T \tag{4.3b}$$

$$\tilde{\omega}_o = [p_o \quad q_o \quad r_o]^T \tag{4.3c}$$

$$\tilde{\dot{\omega}}_o = [\dot{p}_o \quad \dot{q}_o \quad \dot{r}_o]^T \tag{4.3d}$$

A rotating reference system A_i, $i = 1, ...N_b$ aligned with the time-dependent blade root/hinge positioning is defined for each of the N_b rotor blades as shown in Fig. 4.1. The

origin of A_i is located at the i^{th} blade root/hinge position. The position vector of the A_i origin expressed in the non-rotating reference frame O is given by:

$$\tilde{r}_{A_i/O} = \begin{Bmatrix} eR\cos\psi_i(t) \\ eR\sin\psi_i(t) \\ 0 \end{Bmatrix} \tag{4.4}$$

It is noted that, $\psi_i(t)$ is the azimuth angle corresponding to the root/hinge of the i^{th} blade at time t (Fig. 4.1, a)) and e is the blade root/hinge offset distance from the center of rotation as a fraction of rotor blade radius R. Assuming rotor pre-cone, pre-sweep and collective pitch angles β_{pre}, ζ_{pre} and θ_0 respectively (Fig. 4.1, b)), a transformation matrix $[A_i]$ is defined as:

$$[A_i] = [\Theta_0][B_{pre}][Z_{pre}][\Psi_i] \tag{4.5}$$

with

$$[\Theta_0] = \begin{bmatrix} 1 & 0 & 0 \\ 0 & \cos\theta_0 & \sin\theta_0 \\ 0 & -\sin\theta_0 & \cos\theta_0 \end{bmatrix} \tag{4.6a}$$

$$[B_{pre}] = \begin{bmatrix} \cos\beta_{pre} & 0 & \sin\beta_{pre} \\ 0 & 1 & 0 \\ -\sin\beta_{pre} & 0 & \cos\beta_{pre} \end{bmatrix} \tag{4.6b}$$

$$[Z_{pre}] = \begin{bmatrix} \cos\zeta_{pre} & -\sin\zeta_{pre} & 0 \\ \sin\zeta_{pre} & \cos\zeta_{pre} & 0 \\ 0 & 0 & 1 \end{bmatrix} \tag{4.6c}$$

$$[\Psi_i] = \begin{bmatrix} \cos\psi_i(t) & \sin\psi_i(t) & 0 \\ -\sin\psi_i(t) & \cos\psi_i(t) & 0 \\ 0 & 0 & 1 \end{bmatrix} \tag{4.6d}$$

Application of $[A_i]$ to any vector expressed in O, will yield the corresponding expression of the same vector in A_i. Note that only collective pitch θ_0 has been applied towards the alignment of A_i with the blade root positioning. The effects of cyclic pitch along with blade twist will be individually accounted for within A_i. The absolute angular velocity and acceleration vectors of the origin of A_i expressed in O are given by:

$$\tilde{\omega}_{A_i/O} = [p_o \quad q_o \quad r_o + \Omega]^T \tag{4.7a}$$

$$\tilde{\dot{\omega}}_{A_i/O} = [\dot{p}_o \quad \dot{r}_o \quad \dot{q}_o + \dot{\Omega}]^T \tag{4.7b}$$

where Ω is the shaft rotorspeed. The absolute linear velocity and acceleration vectors of the origin of A_i expressed in O can therefore be written as:

$$\tilde{u}_{A_i/O} = \tilde{u}_o + \tilde{\omega}_{A_i/O} \times \tilde{r}_{A_i/O} \tag{4.8a}$$

$$\tilde{a}_{A_i/O} = \tilde{\dot{u}}_o + \tilde{\omega}_{A_i/O} \times (\tilde{\omega}_{A_i/O} \times \tilde{r}_{A_i/O}) + \tilde{\dot{\omega}}_{A_i/O} \times \tilde{r}_{A_i/O} \tag{4.8b}$$

The position vector of each beam element $p(r,t)$ relative to the origin of and expressed in the rotating A_i reference system (Fig. 4.1, c)) is given by:

$$\tilde{r}_{p/A_i}^{A_i} = \begin{Bmatrix} (r-eR)\cos\beta(r,t)\cos\zeta(r,t) \\ -(r-eR)\sin\zeta(r,t) \\ (r-eR)\sin\beta(r,t) \end{Bmatrix} \tag{4.9}$$

where $\beta(r,t)$ and $\zeta(r,t)$ are the element equivalent flap and lag angles respectively defined in A_i as shown in Fig. 4.1, c). They are defined as:

$$\beta(r,t) = \arcsin\frac{w^{flap}(r,t)}{r-eR} \tag{4.10a}$$

$$\zeta(r,t) = \arcsin\frac{w^{lag}(r,t)}{r-eR} \tag{4.10b}$$

where $w^{flap/lag}(r,t)$ is the time-dependent blade transverse displacement as regards flap and lag motion respectively. The negative sign of the second element of $\tilde{r}_{p/A_i}^{A_i}$ has been included due to the convention regarding $\zeta(r,t)$ being positive for backwards blade transverse displacement $w^{lag}(r,t)$ as shown in Fig. 4.1, c). The first and second derivatives of Eqs. (4.10a, 4.10b) lead to the respective angular velocity and acceleration components of beam element $p(r,t)$ expressed in A_i:

$$\dot{\beta}(r,t) = \frac{1}{\sqrt{1-(\frac{w^{flap}(r,t)}{r-eR})^2}}\frac{\dot{w}^{flap}(r,t)}{r-eR} \tag{4.11}$$

$$\ddot{\beta}(r,t) = (1-(\frac{w^{flap}(r,t)}{r-eR})^2)^{-3/2}(\frac{\dot{w}^{flap}(r,t)}{r-eR})^2(\frac{w^{flap}(r,t)}{r-eR})+(1-(\frac{w^{flap}(r,t)}{r-eR})^2)^{-1/2}(\frac{\ddot{w}^{flap}(r,t)}{r-eR}) \tag{4.12}$$

Similar expressions to Eqs. (4.11, 4.12) can be used for the determination of $\dot{\zeta}(r,t)$ and $\ddot{\zeta}(r,t)$ respectively.

The total angular velocity and acceleration vectors of beam element $p(r,t)$ including the blade motion due to cyclic pitch, can be expressed in the rotating A_i reference frame as:

$$\tilde{\omega}_{p/A_i}^{A_i} = \begin{Bmatrix} \dot{\theta}_c(eR,t) \\ -\dot{\beta}(r,t) \\ -\dot{\zeta}(r,t) \end{Bmatrix} \tag{4.13a}$$

$$\tilde{\dot{\omega}}_{p/A_i}^{A_i} = \begin{Bmatrix} \ddot{\theta}_c(eR,t) \\ -\ddot{\beta}(r,t) \\ -\ddot{\zeta}(r,t) \end{Bmatrix} \tag{4.13b}$$

for the case that cyclic pitch is applied inboard of the blade root/hinge location and:

$$\tilde{\omega}^{A_i}_{p/A_i} = \begin{Bmatrix} \cos\beta(eR,t)\cos\zeta(eR,t)\dot{\theta}_c(eR,t) \\ -\sin\zeta(eR,t)\cos\beta(eR,t)\dot{\theta}_c(eR,t) - \dot{\beta}(r,t) \\ \sin\beta(eR,t)\dot{\theta}_c(eR,t) - \dot{\zeta}(r,t) \end{Bmatrix} \tag{4.14a}$$

$$\tilde{\dot{\omega}}^{A_i}_{p/A_i} = \begin{Bmatrix} \cos\beta(eR,t)\cos\zeta(eR,t)\ddot{\theta}_c(eR,t) \\ -\sin\zeta(eR,t)\cos\beta(eR,t)\ddot{\theta}_c(eR,t) - \ddot{\beta}(r,t) \\ \sin\beta(eR,t)\ddot{\theta}_c(eR,t) - \ddot{\zeta}(r,t) \end{Bmatrix} \tag{4.14b}$$

for outboard blade pitch application. $\theta_c(eR,t)$ is the applied cyclic pitch angle at the blade root/hinge position eR at time t. Equations (4.13a, 4.13b) are suitable for hingeless rotor blades where there are no hinges involved, while Eqs. (4.14a, 4.14b) are well-suited for articulated rotor blades where pitch is applied outboard of the flap/lag hinge location. The negative signs of $\dot{\beta}(r,t)$, $\ddot{\beta}(r,t)$, $\dot{\zeta}(r,t)$, $\ddot{\zeta}(r,t)$ have been included in the vector elements of Eqs. (4.13a – 4.14b) in order for them to comply with the positive axes notation used for the A_i frame of reference as shown in Fig. 4.1, c).

The evaluation of Eqs. (4.11, 4.12) requires the determination of the first and second derivatives of $w^{flap}(r,t)$ and $w^{lag}(r,t)$ with respect to time. The applicability of the presented methodology in the time domain necessitates the numerical discretization of the blade motion in time. A 2^{nd} order backward difference approximation scheme, previously used successfully in the context of time-accurate free wake analysis (Ref. [9]), is deployed for the evaluation of the temporal derivatives of interest. The numerical differentiation scheme can be written as follows:

$$\frac{\partial w^{flap/lag}(r,t+\Delta t/2)}{\partial t} \approx \frac{3w^{flap/lag}(r,t+\Delta t) - w^{flap/lag}(r,t) - 3w^{flap/lag}(r,t-\Delta t) + w^{flap/lag}(r,t-2\Delta t)}{4\Delta t} \tag{4.15}$$

where Δt is the employed time-step during the time-marching procedure. A linearized analysis has been waged on the stability characteristics of Eq. (4.15) in Ref. [9] where it has been shown that it is stable with positive damping.

Equation (4.15) provides the first temporal derivatives of $w^{flap/lag}$ at the time instant corresponding to $t + \Delta t/2$. The present numerical approach requires knowledge of both first and second temporal derivatives of blade displacement at identical time instants. Application of Eq. (4.15) on the first temporal derivatives of $w^{flap/lag}$ taken at $t + \Delta t/2$, $t - \Delta t/2$, $t - 3\Delta t/2$ etc., essentially provides the second temporal derivative of displacement at time $= t$. The finite difference approximation of Eq. (4.15) is therefore modified by assuming $w^{flap/lag}(r,t+\Delta t/2) = \dfrac{w^{flap/lag}(r,t) + w^{flap/lag}(r,t+\Delta t)}{2}$ in order to provide the first temporal derivative at the time instant corresponding to time $= t$ as well. The

nature of the modified and the original numerical differentiation schemes are illustrated in Fig. 4.2. The modified algorithm gives:

$$\begin{aligned}&\frac{\partial w^{flap/lag}(r,t)}{\partial t} \approx \\ &\frac{3w^{flap/lag}(r,t+\Delta t)+2w^{flap/lag}(r,t)}{8\Delta t}+ \\ &\frac{-4w^{flap/lag}(r,t-\Delta t)-2w^{flap/lag}(r,t-2\Delta t)+w^{flap/lag}(r,t-3\Delta t)}{8\Delta t}\end{aligned} \tag{4.16}$$

It can be shown that Eq. (4.16) is also second order accurate with respect to time. The second temporal derivatives of $w^{flap/lag}(r,t)$ are given by:

$$\begin{aligned}&\frac{\partial^2 w^{flap/lag}(r,t)}{\partial t^2} \approx \\ &\frac{3\dot{w}^{flap/lag}(r,t+\Delta t/2)-\dot{w}^{flap/lag}(r,t-\Delta t/2)}{4\Delta t}+ \\ &\frac{-3\dot{w}^{flap/lag}(r,t-3\Delta t/2)+\dot{w}^{flap/lag}(r,t-5\Delta t/2)}{4\Delta t}\end{aligned} \tag{4.17}$$

where the values of $\dot{w}^{flap/lag}$ in Eq. (4.17) can be evaluated at their respective time instants using the original algorithm given by Eq. (4.15).

The relative velocity and acceleration vectors of $p(r,t)$ relative to the origin of and expressed in the A_i rotating frame are:

$$\tilde{u}^{A_i}_{p/A_i} = \tilde{\omega}^{A_i}_{p/A_i} \times \tilde{r}^{A_i}_{p/A_i} \tag{4.18a}$$

$$\tilde{a}^{A_i}_{p/A_i} = \tilde{\omega}^{A_i}_{p/A_i} \times (\tilde{\omega}^{A_i}_{p/A_i} \times \tilde{r}^{A_i}_{p/A_i}) + \tilde{\dot{\omega}}^{A_i}_{p/A_i} \times \tilde{r}^{A_i}_{p/A_i} \tag{4.18b}$$

which along with $\tilde{r}^{A_i}_{p/A_i}$, they can be expressed in the global non-rotating O frame of reference using the following transformations:

$$\tilde{r}^{O}_{p/A_i} = [A_i]^{-1}\tilde{r}^{A_i}_{p/A_i} \tag{4.19a}$$

$$\tilde{u}^{O}_{p/A_i} = [A_i]^{-1}\tilde{u}^{A_i}_{p/A_i} \tag{4.19b}$$

$$\tilde{a}^{O}_{p/A_i} = [A_i]^{-1}\tilde{a}^{A_i}_{p/A_i} \tag{4.19c}$$

The absolute velocity and acceleration vectors of point $p(r,t)$ expressed in the global non-rotating reference frame O are therefore given by:

$$\tilde{u}^{O}_{p} = \tilde{u}_{A_i/O} + \tilde{u}^{O}_{p/A_i} + \tilde{\omega}_{A_i/O} \times \tilde{r}^{O}_{p/A_i} \tag{4.20a}$$

$$\tilde{a}^{O}_{p} = \tilde{a}_{A_i/O} + \tilde{a}^{O}_{p/A_i} + 2\tilde{\omega}_{A_i/O} \times \tilde{u}^{O}_{p/A_i} + \tilde{\dot{\omega}}_{A_i/O} \times \tilde{r}^{O}_{p/A_i} + \tilde{\omega}_{A_i/O} \times (\tilde{\omega}_{A_i/O} \times \tilde{r}^{O}_{p/A_i}) \tag{4.20b}$$

It is of interest to obtain the velocity and acceleration components expressed in a blade element fixed frame of reference. Figure 4.1, c) illustrates the local blade element frame of reference corresponding to point $p(r,t)$ of the i^{th} blade. The system's orientation is specified by unit vectors $\tilde{e}_x^b$, $\tilde{e}_y^b$ and $\tilde{e}_z^b$. The vector $\tilde{e}_x^b$ is taken so as to be coincident with the blade's deformed elastic axis, pointing radially outwards. The $\tilde{e}_y^b$ vector points towards the element's trailing edge and $\tilde{e}_z^b$ completes the orthogonal system. Conversion to a locally fixed reference frame, not only provides the local flow-field conditions which is necessary input for any aerodynamic theory, but the principle of superposition with respect to the aerodynamic and inertial loads can be employed within this system.

The global expressions given by Eqs. (4.20a, 4.20b) can be converted to the local blade element coordinate system using the following transformation:

$$\tilde{u}_p^b = [T_i^b]\{\tilde{u}_p^O\} \tag{4.21a}$$

$$\tilde{a}_p^b = [T_i^b]\{\tilde{a}_p^O\} \tag{4.21b}$$

The $[T_i^b]$ operator is a transformation matrix which relates any vector expressed in the global non-rotating reference frame O directly to the local blade element coordinate system b of point $p(r,t)$ located on the i^{th} blade. It is defined as the following sequence of rotations:

$$[T_i^b] = [\theta_c][\beta][\zeta][\theta_{tw}][\lambda][A_i] \tag{4.22}$$

where $[\lambda]$, $[\theta_{tw}]$, $[\zeta]$, $[\beta]$ and $[\theta_c]$ are rotation matrices corresponding to the blade element sweep, pre-twist, lag, flap and cyclic pitch angle at the hub respectively. They are essentially identified as:

$$[\lambda] = \begin{bmatrix} \cos\lambda(r) & -\sin\lambda(r) & 0 \\ \sin\lambda(r) & \cos\lambda(r) & 0 \\ 0 & 0 & 1 \end{bmatrix} \tag{4.23a}$$

$$[\theta_{tw}] = \begin{bmatrix} 1 & 0 & 0 \\ 0 & \cos\theta_{tw}(r) & \sin\theta_{tw}(r) \\ 0 & -\sin\theta_{tw}(r) & \cos\theta_{tw}(r) \end{bmatrix} \tag{4.23b}$$

$$[\zeta] = \begin{bmatrix} \cos\zeta(r,t) & -\sin\zeta(r,t) & 0 \\ \sin\zeta(r,t) & \cos\zeta(r,t) & 0 \\ 0 & 0 & 1 \end{bmatrix} \tag{4.23c}$$

$$[\beta] = \begin{bmatrix} \cos\beta(r,t) & 0 & \sin\beta(r,t) \\ 0 & 1 & 0 \\ -\sin\beta(r,t) & 0 & \cos\beta(r,t) \end{bmatrix} \tag{4.23d}$$

$$[\theta_c] = -\begin{bmatrix} -1 & 0 & 0 \\ 0 & \cos\theta_c(eR,t) & \sin\theta_c(eR,t) \\ 0 & -\sin\theta_c(eR,t) & \cos\theta_c(eR,t) \end{bmatrix} \tag{4.23e}$$

where $\lambda(r)$ and $\theta_{tw}(r)$ are the local blade element sweep and pre-twist angles respectively, while $\theta_c(eR,t)$ is the cyclic pitch angle at the hub. The angles $\theta_{tw}(r)$ and $\theta_c(eR,t)$ are considered positive for blade nose-up rotation while $\lambda(r)$ is taken as positive for backwards blade sweep. It is noted that, the cyclic pitch rotation matrix $[\theta_c]$ expressed by Eq. (4.23e), has been derived for the case that cyclic pitch is applied inboard of the flap/lag hinge. Equation (4.23e) is therefore suitable for hingeless blades where there are no hinges involved. Proper manipulation of Eq. (4.23e) is required for the case that cyclic pitch is applied about the flapped and lagged hinge, similar to the one used for the derivation of Eqs. (4.14a, 4.14b).

4.2.3 Unsteady rotor loads integration

Concerning the process of rotor loads integration, Eq. (4.21b) can be used for the evaluation of the element acceleration vector expressed in the local blade element coordinate system. Using the principle of superposition for the inertial and aerodynamic forces and moments within the locally fixed frame and subsequently converting them to the global non-rotating reference frame O gives:

$$d\tilde{f}_p^O = [T_i^b]^{-1}\{\tilde{f}_{aero}^b - \rho A(r)\tilde{a}_p^b\}dr \tag{4.24a}$$

$$d\tilde{m}_p^O = [T_i^b]^{-1}\{\tilde{m}_{aero}^b - \rho A(r)\{\tilde{r}_p^{b,offset} \times \tilde{a}_p^b\}\}dr \tag{4.24b}$$

where $\tilde{r}_p^{b,offset}$ is the airfoil center gravity offset vector from the blade elastic axis expressed in the local coordinate system. The vectors $\tilde{f}_{aero}^b$ and $\tilde{m}_{aero}^b$ are the blade element aerodynamic force and moment per unit length vectors respectively which can be obtained by any blade element aerodynamics theory. The total time-dependent forces and moments that the main rotor exerts on the aircraft fuselage can be expressed as the summation of the contributions of the individual rotor blades:

$$\tilde{F}_{rotor}^O(t) = \sum_{i=1}^{N_b} \tilde{F}_i^O(t) \tag{4.25a}$$

$$\tilde{T}_{rotor}^O(t) = \sum_{i=1}^{N_b} \tilde{T}_i^O(t) \tag{4.25b}$$

where

$$\tilde{F}_i^O(t) = \int_{eR}^{R} d\tilde{f}_p^O, \qquad i = 1, ...N_b \tag{4.26}$$

The overall moment that a rotor blade with a root connection (or hinge for a hinged blade) offset exercises about the origin of O can be divided in two components: a) The moment $\tilde{T}_{i,offset}^O(t)$ that the blade root/hinge applies about the origin O due to its offset

from the center of rotation and b) The moment that the blade exerts directly on its root/hinge $\tilde{T}^O_{i,root}(t)$ due to the root/hinge spring stiffness. This gives:

$$\tilde{T}^O_i(t) = \tilde{T}^O_{i,offset}(t) + \tilde{T}^O_{i,root}(t), \qquad i = 1, ...N_b \tag{4.27}$$

The calculation of $\tilde{T}^O_{i,offset}(t)$ is identical for all rotor blade configurations and the corresponding expression is given by:

$$\tilde{T}^O_{i,offset}(t) = \tilde{r}_{A_i/O} \times \tilde{F}^O_i(t), \qquad i = 1, ...N_b \tag{4.28}$$

For a hingeless rotor blade, the component $\tilde{T}^O_{i,root}(t)$ is due to the effective stiffness of the blade root connection and can be expressed as:

$$\tilde{T}^O_{i,root}(t) = \int_{eR}^{R} \tilde{r}^O_{p/A_i} \times \mathrm{d}\tilde{f}^O_p + \int_{eR}^{R} \mathrm{d}\tilde{m}^O_p, \qquad i = 1, ...N_b \tag{4.29}$$

For a spring-hinged articulated rotor, the blade moment vector components at the hinge about the flap/lag degrees of freedom are determined from the local flap/lag angles and the corresponding spring stiffness constants. For a freely-hinged articulated rotor, the blade cannot exert any moment at its hinge about the corresponding degree of freedom for which there is no spring involved.

The rotor force and moment vectors derived from Eqs. (4.25a, 4.25b) can be expressed in the hub-wind axes system using the following transformations:

$$\tilde{F}^{hw}_{rotor}(t) = [HW]^{-1}\tilde{F}^O_{rotor}(t) \tag{4.30a}$$

$$\tilde{T}^{hw}_{rotor}(t) = [HW]^{-1}\tilde{T}^O_{rotor}(t) \tag{4.30b}$$

It is noted that $[HW] = [HW]^{-1}$. Equations (4.30a, 4.30b) can be used directly by any helicopter flight dynamics application utilizing the hub-wind axes reference system as defined in Ref. [7] for the calculation of the unsteady three-dimensional rotor force and moment loads.

4.2.4 Integrated aeroelastic rotor – aircraft model

The numerical approach for the treatment of rotor blade flexibility presented in this chapter is coupled with the Peters – He finite state induced flow model (Refs. [10, 54]) and the Leishman – Beddoes unsteady nonlinear blade element aerodynamics model (Ref. [11]). Careful treatment of the induced flow terms arising from the shed wake circulation has been carried out so that they are not duplicated by both induced flow and unsteady aerodynamics models. The modal characteristics obtained from the Lagrangian approach described in the 3^{rd} chapter of this Thesis, are utilized. The dynamic response of the elastic blades to the imposed aerodynamic and inertial external loads is calculated using a 5^{th} order accurate numerical evaluation scheme of the convolution integral.

The aircraft fuselage is treated dynamically as a rigid body with six degrees of freedom (three translations and three rotations) using the inertial tensors given in Ref. [7]. Experimentally derived look-up tables from Ref. [7] are employed that describe the fuselage force and moment coefficients as functions of incidence and sideslip angles. Two-dimensional characteristics are utilized for the prediction of the aerodynamic behavior of the horizontal and vertical stabilizers. Steady state airfoil data along with a 1^{st} order dynamic inflow formulation (Refs. [47, 48, 55]) are used for the prediction of the tail-rotor performance. Rigid body dynamics are employed for the simulation of the dynamic behavior of the tail-rotor blades.

A globally convergent Newton–Raphson method is incorporated in order to obtain the required trim controls for either wind tunnel simulation with prescribed hub moments, or for a designated set of flight conditions. With respect to overall aircraft trim, the numerical scheme is applied towards the solution of a linearized version of Euler's equations of motion for rigid body kinematics (Ref. [7]). The trim linearization assumption dictates that the flight state vector derivatives are essentially zero. The main and tail rotors are marched simultaneously in time using the initial condition of nonexistent circulatory wake. The time-marching process continues until once-per-rev (1P) periodicity is achieved with respect to the main rotor mean induced flow. Having achieved flow periodicity, a finite series of main rotor rotations is carried out where the main rotor hub-wind forces and moments given by Eqs. (4.30a, 4.30b) are time-averaged in order to acquire mean representative values to be used for the trim procedure.

4.3 Results & Discussion

The integrated simulation model has been applied towards the investigation of the unsteady flapwise and chordwise bending moments of the full-scale, pre-coned hingeless rotor of the MBB Bo 105 helicopter. The rotor design characteristics have been extensively analyzed in Ref. [56]. Simulations have been performed for a wide range of advance ratios ($\mu = \dfrac{V}{\Omega R}$). A total number of 9 inflow harmonics are deployed for all simulation results presented in this chapter in order to capture the effect of higher harmonic loading on the inflow response. The radial inflow distribution polynomials used reach up to the 12^{th} power of non-dimensional rotor radius. A total of 6 flap and lag bending modes are employed for each degree of freedom. Rotor wake/fuselage aerodynamic interference effects are not accounted for throughout the computations presented in this chapter.

Extensive comparisons with experimental data from wind tunnel and flight test measurements reported in Ref. [12] have been carried out. Correlations have been waged for the unsteady blade structural loads as well as rotor trim control inputs. With reference to the unsteady blade loads predictions, the main rotor is numerically trimmed to produce

designated values of thrust and hub moments corresponding to a specific advance ratio and shaft angle relative to the free-stream flow. This is done in order for the simulated experiments to comply with the flight and wind tunnel testing procedures reported in Ref. [12]. Potential modeling uncertainties introduced in the aircraft trim process from the remaining helicopter components is thus eliminated. Trim control values are obtained through the numerical procedure described in section "Integrated aeroelastic rotor – aircraft model" of this chapter.

Predictions from CAMRAD/JA (Comprehensive Analytical Model of Rotorcraft Aerodynamics and Dynamics, Johnson Aeronautics – (Refs. [57], [58]) of unsteady blade loads corresponding to the wind tunnel test conditions, are included and compared with the present modeling approach. All CAMRAD/JA simulation results have been extracted from Ref. [12]. The corresponding structural formulation within CAMRAD/JA is based on engineering beam theory for rotating wings with large pitch and pre-twist angles. The rotor blade is modeled as a cantilever beam with a straight, undeformed elastic axis. Second-order lifting-line theory is deployed coupled with steady-state, two-dimensional airfoil characteristics for the blade aerodynamic response. Corrections are applied for unsteady and three-dimensional flow effects (Ref. [46]). A free-wake model is used in order to predict the rotor wake induced inflow (Ref. [59]).

4.3.1 Rotor blade modal analysis

Figure 4.3 presents the calculated rotor resonance chart for the full-scale Bo 105 helicopter rotor. Simulation results from Boeing–Vertol Y-71 (Ref. [60]) with regards to flap and lag bending frequencies at nominal rotorspeed are also included. The natural frequency predictions from Y-71 have been extracted from Ref. [56]. The solid and broken lines correspond to the Lagrangian method predictions (Lagr.) while the markers signify Y-71 calculations.

Very good agreement between the Lagrangian method and the simulations from Y-71 can be observed with respect to the predicted flap and lag resonant frequencies at nominal rotorspeed. The corresponding normalized mode shapes obtained from the Lagrangian approach are shown in Figs. 4.4 a) and b) for flap and lag motion respectively. The acquired modal characteristics are utilized within the remainder of this chapter for the approximation of the rotor blade's dynamic response to any aerodynamic or inertial excitation.

4.3.2 Comparison with wind tunnel experiments

Figures 4.5 – 4.8 present correlations between predictions made with the described rotor model and wind tunnel measurements of unsteady flapwise and chordwise bending moments for the full-scale hingeless rotor of the Bo 105 helicopter. Simulations performed

with CAMRAD/JA are also included. All wind tunnel measured data and CAMRAD/JA predictions have been extracted from Ref. [12]. The results presented in Figs. 4.5, 4.6 correspond to an advance ratio of $\mu = 0.197$ and a shaft angle of $a = -4.8°$ relative to the free-stream flow. Results included in Figs. 4.7, 4.8 are for an advance ratio of $\mu = 0.313$ and a shaft angle of $a = -9.6°$. The trim thrust and hub moment settings corresponding to the wind tunnel tests, used for the correlations presented in this chapter are summarized in Ref. [12].

Figures 4.5, a) and b) compare predictions made with the present numerical approach for the oscillatory components of flapwise bending moment, with wind tunnel measurements and CAMRAD/JA simulations. Results are presented for radial stations located at $r/R = 0.144$ and $r/R = 0.57$ respectively. Figure 4.5, a) demonstrates that for $r/R = 0.144$, the agreement between simulation and experiment regarding the 1P component of flap bending moment is very good. This is due to the fact that the hub moments have been prescribed by the trim procedure. Both CAMRAD/JA as well as the current simulation model predict more 2P and 3P oscillatory loading than measured in the wind tunnel. Figure 4.5, b) shows that for $r/R = 0.57$, the current model is indeed able to capture the basic waveform corresponding to oscillatory flap loading. Excellent agreement is exhibited between CAMRAD/JA and the present approach. However, it can be noticed that the wind tunnel measurements suggest an 8P oscillatory loading component that has not been captured by neither simulation approach.

Figures 4.6, a) and b) present the respective comparisons for the oscillatory components of chordwise bending moment considering the same trim conditions and radial locations as Fig. 4.5. Figure 4.6, a) illustrates that for $r/R = 0.144$, both numerical formulations capture the basic waveform of the chordwise loading. Neither CAMRAD/JA nor the present formulation have succeeded in capturing the 8P oscillatory component measured in the wind tunnel. Figure 4.6, b) shows that for the blade mid-span location, $r/R = 0.57$, neither CAMRAD/JA nor the present model have accurately predicted the qualitative nature of the chordwise bending moment. Good agreement is exhibited between CAMRAD/JA and the current modeling approach. Certain differences between the two methods in the predicted magnitude of higher frequency oscillatory loading can be noticed. This may be due to a difference in the source of airfoil data utilized by the present approach concerning the aerodynamic response in terms of drag coefficients at higher angles of attack.

Figures 4.7, a) and b) present predictions made with the current rotor model regarding the oscillatory component of flapwise bending moment at $r/R = 0.144$ and $r/R = 0.57$ respectively. Comparisons are waged with wind tunnel measurements and simulations performed with CAMRAD/JA. Figure 4.7, a) demonstrates that for $r/R = 0.144$ the present modeling approach agrees well with both CAMRAD/JA and wind tunnel measurements concerning the 1P moment moment which is essentially prescribed by the trim proce-

dure. Both simulation models predict less 2P moment compared to the data measured in the wind tunnel. Figure 4.7, b) shows that with respect to the blade mid-span location ($r/R = 0.57$) the present modeling approach agrees very well with CAMRAD/JA. Both simulation models succeed in capturing the nature of the bending moment waveform. It is noted that both approaches seem to underpredict the 2P and 3P oscillatory components.

Figures 4.8, a) and b) present the respective comparisons of oscillatory chordwise bending moment for the same trim conditions and radial locations as Fig. 4.7. Figure 4.8, a) shows that for $r/R = 0.144$, the correlation between the current model predictions, CAMRAD/JA simulations and wind tunnel measured data is fair in the sense that the overall oscillatory magnitude was fairly accurately captured. The 2P bending moment component measured in the wind tunnel was not captured accurately by neither CAMRAD/JA nor the present numerical formulation. Good agreement is exhibited however between CAMRAD/JA and the described rotor model predominantly on the retreating path of the blade ($180° - 360°$). Figure 4.8, b) demonstrates that at the blade mid-span location ($r/R = 0.57$) there is a poor correlation considering both simulation models and the wind tunnel measured data. Good agreement can be observed between predictions made with the present model and CAMRAD/JA. Both modeling approaches seem to predict similar oscillatory chordwise loading waveforms for the specific radial location.

4.3.3 Comparison with flight tests – Main rotor trim controls

Before proceeding to the comparisons of predicted flapwise and chordwise bending loads with flight test measurements, it is essential that the overall trim process is validated with experimental data in terms of trim controls. The reason is that, good predictive ability of trim control angles indicates the sound estimation of the aeroelastic rotor response to 1P harmonic excitation. It is noted that, the fuselage/empennage aerodynamic behavior is estimated based on experimentally derived look-up tables. Thus, the modeling uncertainties introduced in the required rotor hub moments for trim are relatively limited. This is a prerequisite for the sound comparison of in-flight oscillatory bending loads since the 1P moment component at the rotor hub needs to be fairly accurately estimated.

Figures 4.9, 4.10 present rotor trim controls and power requirement predictions acquired from trim simulations performed for the Bo 105 helicopter using the helicopter model described in section "Integrated aeroelastic rotor – aircraft model" of this chapter. Results are presented as functions of advance ratio from hover ($\mu = 0$) to high-speed flight ($\mu = 0.36$). Comparisons with flight test data and simulation results using FEA and free-wake modeling extracted from Refs. [61] and [62] respectively, have also been included for validation purposes.

Figures 4.9, a) and b) present trim values of main rotor power requirement and collective pitch angle respectively. Very good correlation between the integrated model pre-

dictions and flight test data can be observed regarding both trim outputs, especially for low values of advance ratio. The agreement is not as good however with respect to higher advance ratios for neither trim outputs. This trend may once again be an indication of a deficiency in the deployed airfoil data at high Mach numbers. Very good correlation can be observed between predictions made with the present approach and the one described in Ref. [62] regarding higher values of advance ratio for which flight test data are not available. The collective pitch angle correlation between the two simulation models is excellent for $\mu \geq 0.15$, where the flow-field in the vicinity of the main rotor is dominated by free-stream conditions.

Figures 4.10, a) and b) present trim values of lateral (θ_{1s}) and longitudinal (θ_{1c}) cyclic pitch angles respectively. Good agreement is observed between the current model predictions and flight test data for both cyclic control inputs within the entire range of advance ratios. Rotor wake impingement on the horizontal stabilizer leads to underprediction of lateral cyclic pitch control angle (θ_{1s}) for $\mu \leq 0.02$. A noticeable deviation between the predicted and flight test measured longitudinal cyclic pitch angle (θ_{1c}) for $\mu \approx 0.05$ reveals the requirement for more sophisticated wake modeling with regards to the specific flight region. The strong influence of the wake roll-up on the induced flow distribution at the rotor tip path plane, regarding the transition region, is not accounted for by the Peters – He inflow model. This deficiency essentially leads to the underprediction of θ_{1c} at lower advance ratios as observed in Fig. 4.10, b). It is shown that the simulation model from Ref. [62] which incorporates a free-wake approach, can capture the required increase in θ_{1c} for $\mu \approx 0.05$.

The overall predictive accuracy of the integrated aeroelastic rotor – aircraft model in terms of trim controls is considered acceptable in order for comparisons of oscillatory blade bending moments predictions to be carried out. This conclusion is valid for advance ratios above $\mu = 0.1$ where the wake roll-up effect is much less pronounced and the Peters – He inflow model can be used with confidence in the context of aeroelasticity analysis.

4.3.4 Comparison with flight tests – Rotor blade bending moments

Figures 4.11 – 4.16 present correlations between predictions made with the described rotor model and flight test data of unsteady flapwise and chordwise bending moments extracted from Ref. [12]. Results are presented for straight and level flight and for three advance ratios: $\mu = 0.197$, $\mu = 0.225$ and $\mu = 0.306$. In order to maintain consistency with the available experimental data, comparisons of flapwise and chordwise bending moments are waged at different mid-span radial locations. Flapwise bending moment results at mid-span correspond to $r/R = 0.57$ while the respective chordwise bending moments are presented for $r/R = 0.45$. Both flap and chord bending moment predictions at the hub

are extracted for $r/R = 0.144$. Simulation results are presented for 1, 3 and 6 employed modes of elastically uncoupled flap/lag bending motion.

Figures 4.11 – 4.13 demonstrate the effect of number of incorporated mode shapes on the predictive qualities of oscillatory flapwise bending moment for $\mu = 0.197$, $\mu = 0.225$ and $\mu = 0.306$ respectively. Results are presented for $r/R = 0.144$ in Figs. 4.11 – 4.13, a) and for $r/R = 0.57$ in Figs. 4.11 – 4.13, b).

Figures 4.11 – 4.13, a) show that for $r/R = 0.144$ and each value of μ, the azimuthal distribution of flapwise bending moment converges to a specific waveform with the inclusion of up to 3 flap/lag bending modes. There is no noticeable difference between simulations performed using 3 and 6 flap/lag modes for none of the values of advance ratio that results are presented for. The converged waveform agrees well with the flight test data considering all flight conditions. It can be noticed that, for the specific radial location and for the two lower values of advance ratio, the flapwise bending moment comprises primarily 1P oscillatory loading. This is evident from the fact that, simulations performed with a single flap/lag mode are able to approximate the basic loading waveform. This behavior however breaks down for higher flight speeds ($\mu = 0.306$) where the contribution of the 2^{nd} and 3^{rd} bending modes becomes much more pronounced due to the radial nonlinearity in the aerodynamic forcing. This observation is in agreement with Shupe's conclusion (Refs. [50, 51]) regarding the contribution of the second flap bending mode to the produced hub moments in high-speed flight. Comparisons with flight test data suggest that, the 2P and 3P oscillatory moment components appear to have been fairly accurately captured by the simulation for all investigated flight conditions.

With respect to the radial location corresponding to $r/R = 0.57$, Figs. 4.11 – 4.13, b) show that, a number of up to 6 flap/lag mode shapes is required in order to obtain a converged waveform of oscillatory flapwise bending moment for all values of advance ratio presented. A noticeable difference is observed between loading waveforms employing 3 and 6 flap/lag modes. It is important to note that, simulations performed using a single flap/lag mode shape essentially predict almost zero oscillatory moment at the blade mid-span location. This is a strong indication that, flap bending moment at the mid-span is predominantly composed of oscillatory loading components associated with the 2^{nd} and 3^{rd} elastic flap modes. This conclusion is valid for all values of advance ratio for which results are presented in this chapter. Good agreement is observed between the predicted bending moment waveform calculated using 6 flap/lag modes and the fight test data for all flight conditions.

Figures 4.14 – 4.16 demonstrate the effect of number of deployed mode shapes on the predictive qualities of oscillatory chordwise bending moment for $\mu = 0.197$, $\mu = 0.225$ and $\mu = 0.306$ respectively. Results are presented for $r/R = 0.144$ in Figs. 4.14 – 4.16, a) and for $r/R = 0.45$ in Figs. 4.14 – 4.16, b).

Figures 4.14 – 4.16, a) show that, the basic waveform of chordwise bending moment

at $r/R = 0.144$ is well captured using a single flap/lag bending mode for all three values of advance ratio. The inclusion of higher harmonic content makes very little difference in the predicted oscillatory loading. It is noted that, the calculated waveform comprises predominantly 1P loading for all values of μ. Refinement with inclusion of higher modal content offers slight improvement on the predictive qualities for the specific radial location. Comparisons with flight test data suggest very good agreement with regards to 1P and 2P moment components. Flight test measurements also suggest an oscillatory component of 8P frequency which is not captured by the simulation, not even with the inclusion of 6 flap/lag bending modes.

As regards the radial location corresponding to $r/R = 0.45$, Figures 4.14 – 4.16, b) illustrate that the inclusion of higher modal content is important for obtaining a converged loading waveform. This conclusion is valid for all values of μ for which results are presented. Although good agreement is observed considering the 1P component of oscillatory moment between flight test data and simulation, there is a rather poor correlation with respect to higher harmonic loading content. It is however noted that the overall character of chordwise bending moment at the blade mid-span comprises mainly 1P loading as opposed to higher harmonic content. This is in contrast with the predictions corresponding to the flapwise bending moment at the blade's mid-span where the higher frequency oscillatory loading is predominant.

4.4 Conclusions

A numerical approach for the simulation of rotor blade flexibility in helicopter flight dynamics and aeroelasticity applications has been offered. A comprehensive treatment of the elastic blade's three-dimensional kinematics in the time domain has been described. The nonlinear acceleration terms due to large deflections and hub-wind angular motions have been thoroughly retained. A stable, 2^{nd} order accurate, numerical differentiation scheme has been successfully deployed for the approximation of the derivatives of motion. Integral expressions have been provided describing the overall forces and moments exerted by the elastic blades on the rotor hub. The proposed model is compatible with every inflow and blade element aerodynamics theory that can operate in the time domain. It is readily available for implementation in existing codes utilizing the hub-wind reference frame without any change in the offered expressions.

The described formulation has been coupled with the Peters – He induced flow model and the Leishman – Beddoes blade element aerodynamics model. The integrated approach has been deployed in order to investigate the unsteady structural loads of the full-scale, pre-coned hingeless rotor of the MBB Bo 105 helicopter. Extensive comparisons have been waged with data from wind tunnel experiments, flight tests and CAMRAD/JA simulations for a wide range of advance ratios.

It has been shown that, the present numerical approach has been successful in predicting the low-frequency components of oscillatory flapwise and chordwise blade moments as measured in the wind-tunnel. The current method has been unable to accurately predict the higher frequency oscillatory loading components. Good correlation has been demonstrated between flap/chord bending moment predictions made with the current rotor model and CAMRAD/JA.

Accurate predictive qualities have been exhibited with regards to the required main rotor trim control angles and power requirements and for straight and level flight. The absence of rotor wake roll-up effects in the Peters – He inflow model are responsible for the small underprediction of longitudinal cyclic (θ_{1c}) at very low advance ratios ($\mu \approx 0.05$).

Good correlation has been observed between flapwise bending moment predictions made with the present rotor model and flight test data for all advance ratios. Good predictive qualities have been demonstrated with regards to chordwise bending moments at the rotor hub. The importance of including higher modal content, reaching up to the 6^{th} flap/lag bending mode, on the predictive accuracy of oscillatory loading with respect to radially outwards locations, has been displayed. The present modeling approach agrees with Shupe's conclusion (Refs. [50, 51]) on the contribution of the second flap bending mode to the produced hub moments in high-speed flight. The simulations carried out suggest that, flapwise bending moment at the blade mid-span position is predominantly composed of oscillatory loading associated with the 2^{nd} and 3^{rd} elastic modes, while chordwise moment comprises mostly 1P loading. Both flapwise and chordwise bending moments at the rotor hub consist primarily of 1P oscillatory loading.

A general review of the obtained results indicates the very good predictive capacity of the described numerical approach, considering its simplicity, generality, ease of implementation and computational efficiency.

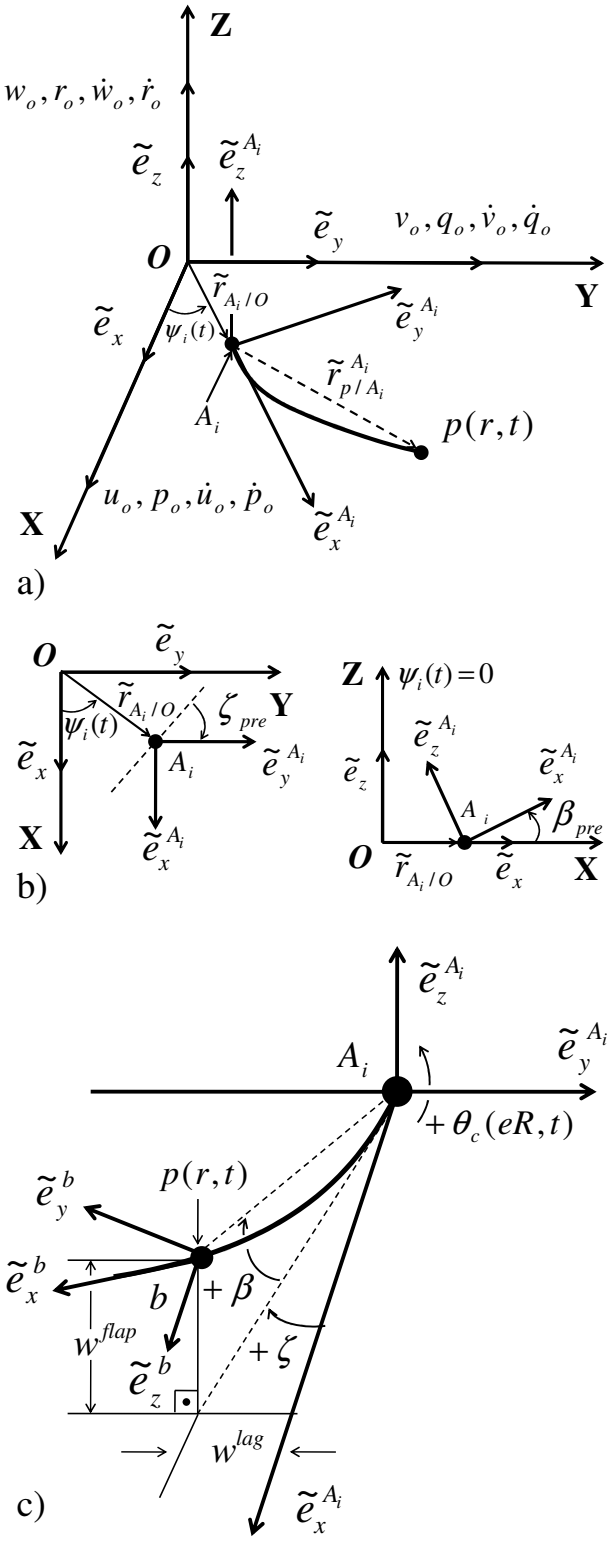

Figure 4.1: Reference systems for elastic blade kinematics: a) Global non-rotating reference system O, b) Hinge pre-sweep and pre-cone angles definition c) Rotating and blade element reference frames (A_i and b respectively)

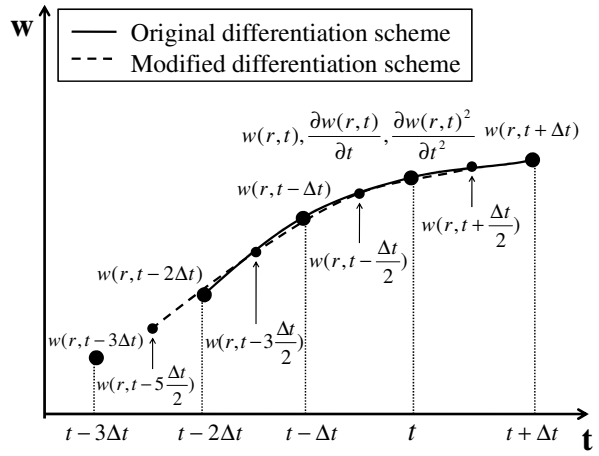

Figure 4.2: Graphical illustration of the deployed numerical differentiation schemes

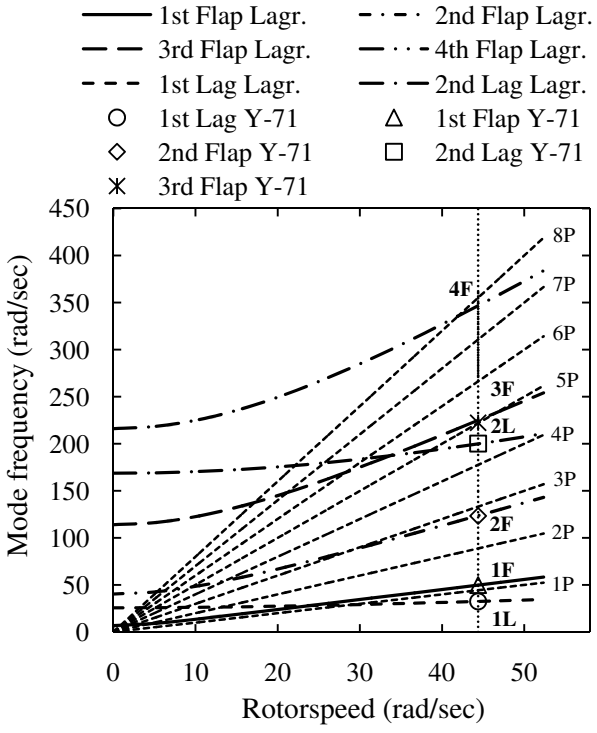

Figure 4.3: Resonance chart calculated for the MBB Bo 105 helicopter main rotor – Comparison with Boeing–Vertol Y-71 calculations reported in Ref. [56]

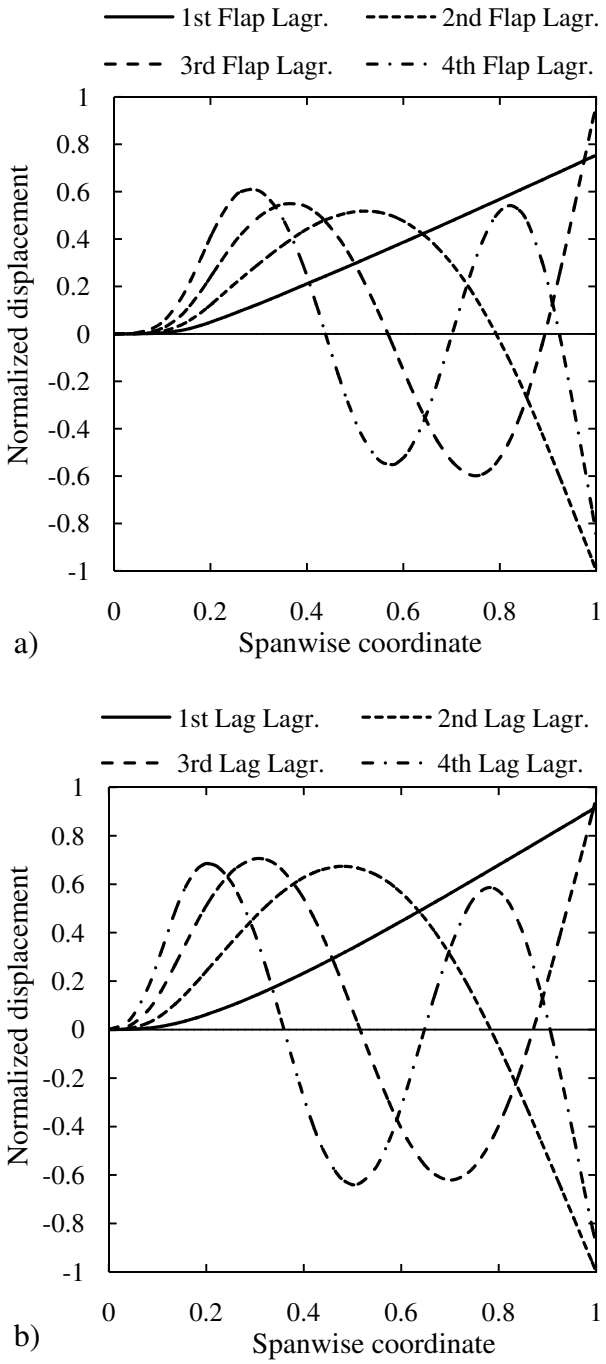

Figure 4.4: Normalized mode shapes calculated for the MBB Bo 105 helicopter hingeless rotor: a) Flap modes, b) Lag modes

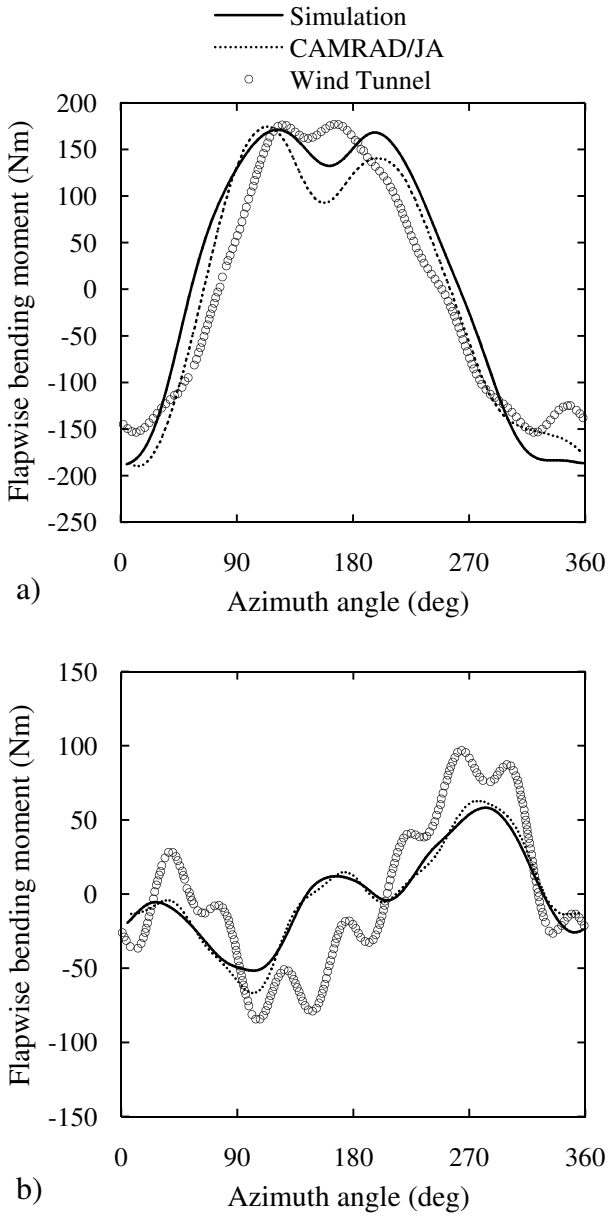

Figure 4.5: Oscillatory flapwise bending moment for $\mu = 0.197$, $a = -4.8°$ – comparison with wind tunnel experiments and CAMRAD/JA simulations from Ref. [12]: a) r/R=0.144, b) r/R=0.57

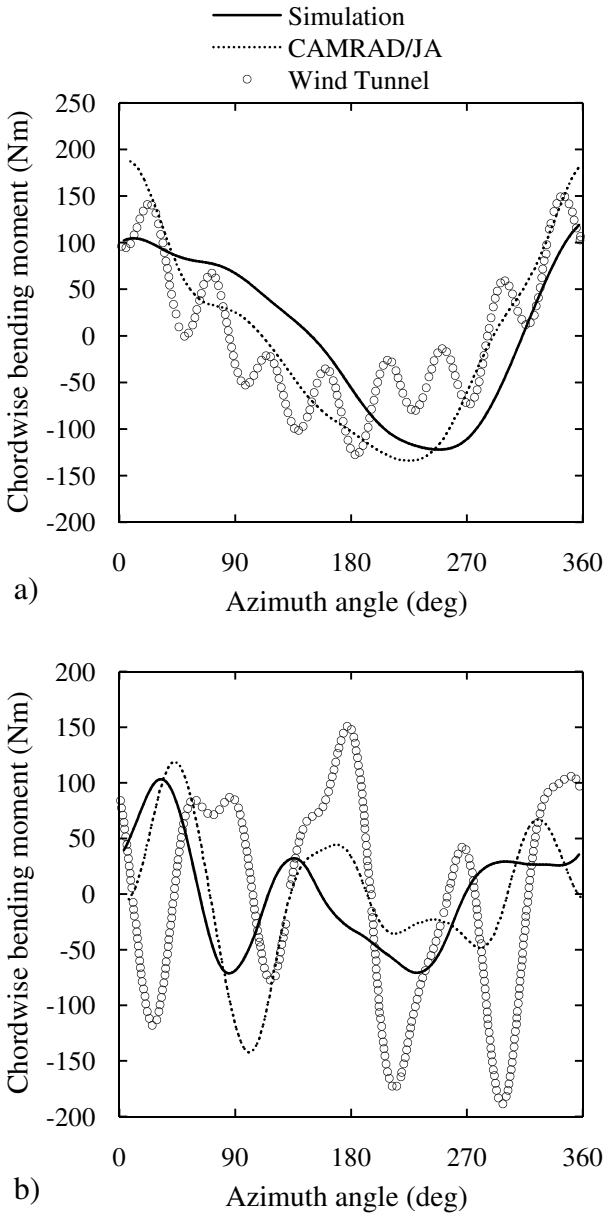

Figure 4.6: Oscillatory chordwise bending moment for $\mu = 0.197$, $a = -4.8°$ – comparison with wind tunnel experiments and CAMRAD /JA simulations from Ref. [12]: a) r/R=0.144, b) r/R=0.57

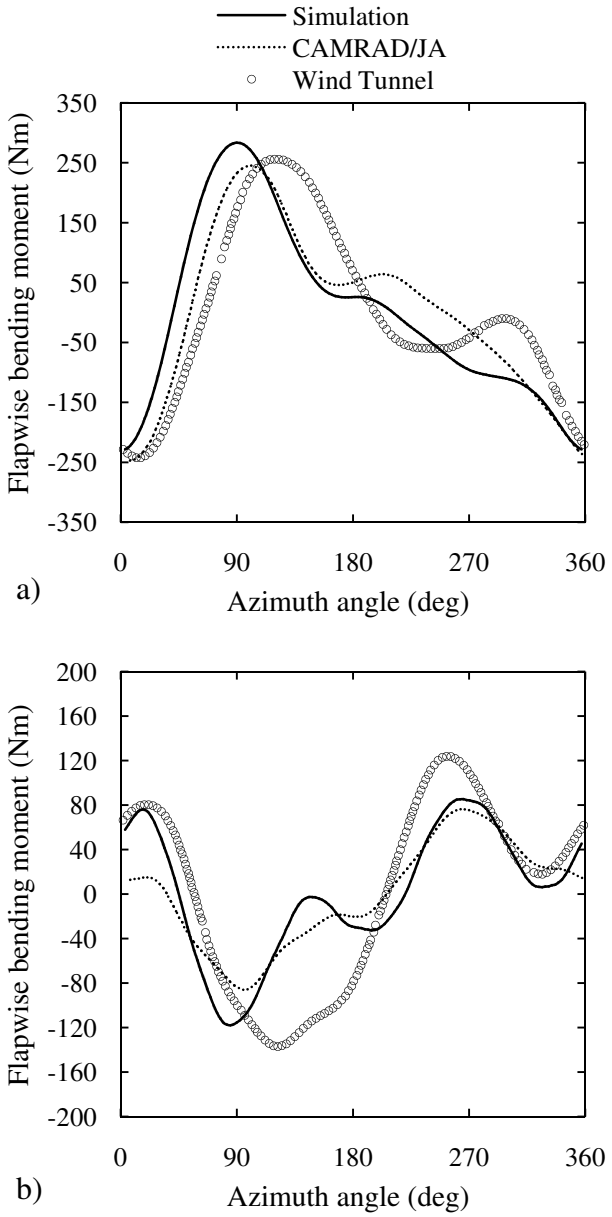

Figure 4.7: Oscillatory flapwise bending moment for $\mu = 0.313$, $a = -9.6°$ – comparison with wind tunnel experiments and CAMRAD/JA simulations from Ref. [12]: a) r/R=0.144, b) r/R=0.57

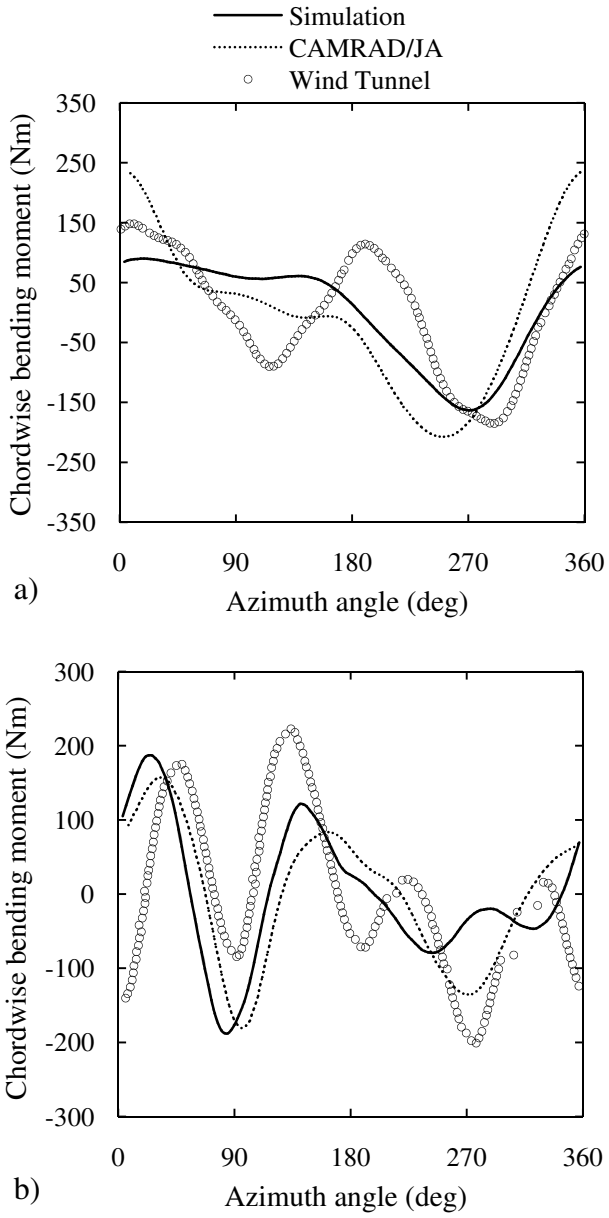

Figure 4.8: Oscillatory chordwise bending moment for $\mu = 0.313$, $a = -9.6°$ – comparison with wind tunnel experiments and CAMRAD/JA simulations from Ref. [12]: a) r/R=0.144, b) r/R=0.57

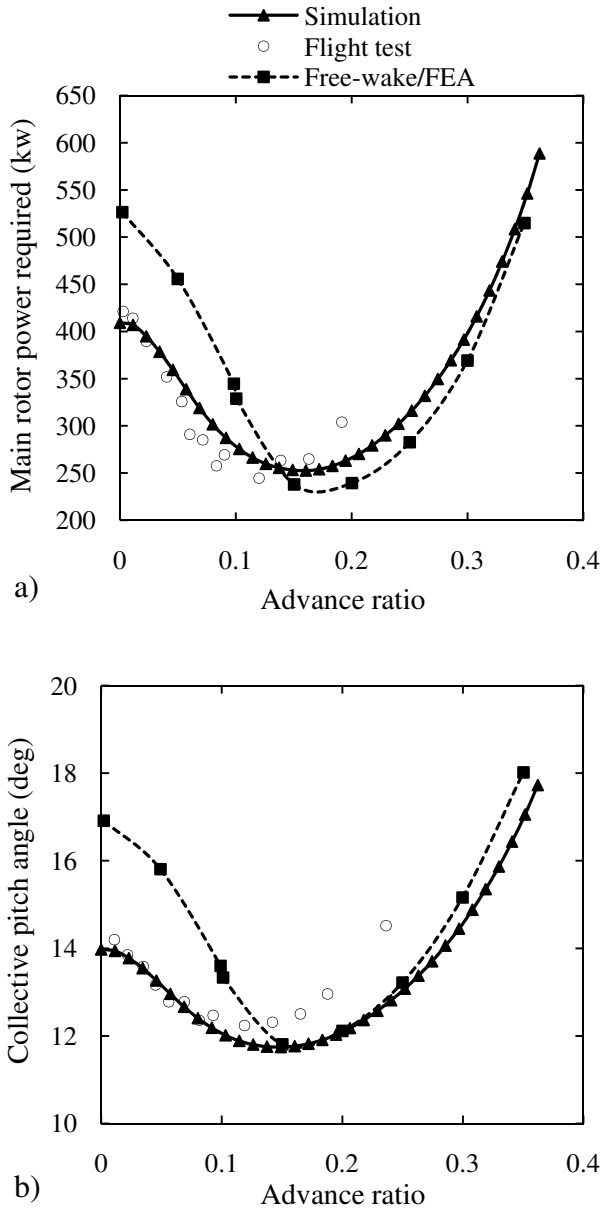

Figure 4.9: Trim results for the MBB Bo 105 helicopter – comparison with flight test data and free-wake/FEA simulation results extracted from Ref. [62]: a) Rotor power required, b) Collective pitch angle θ_0

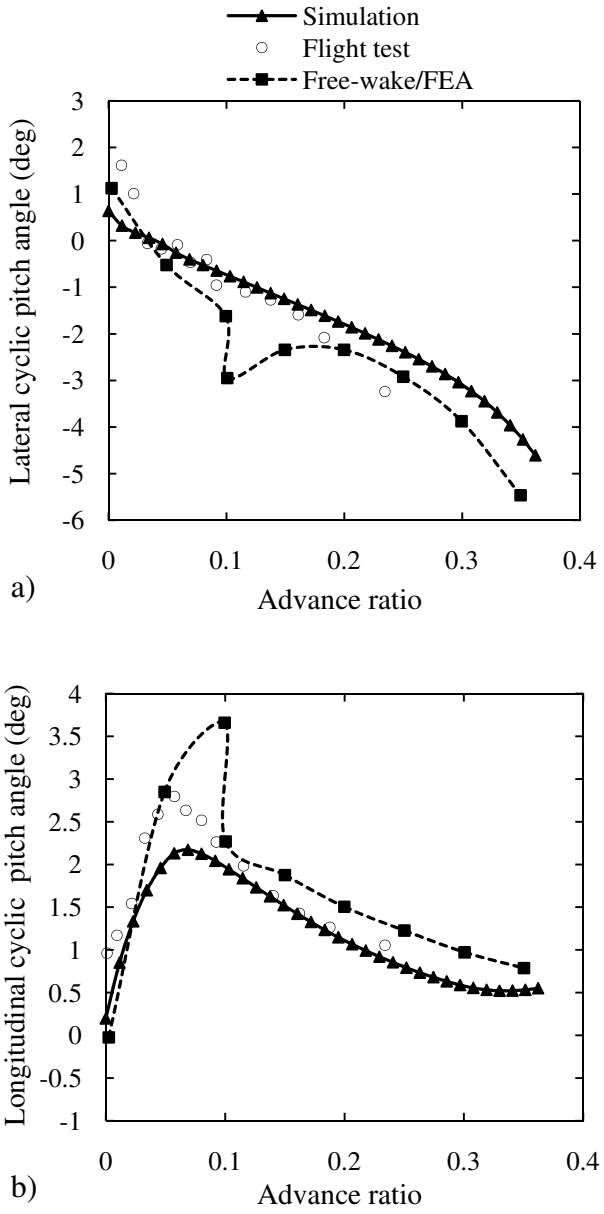

Figure 4.10: Trim results for the MBB Bo 105 helicopter – comparison with flight test data and free-wake/FEA simulation results extracted from Ref. [62]: a) Lateral cyclic pitch angle θ_{1s}, b) Longitudinal cyclic pitch angle θ_{1c}

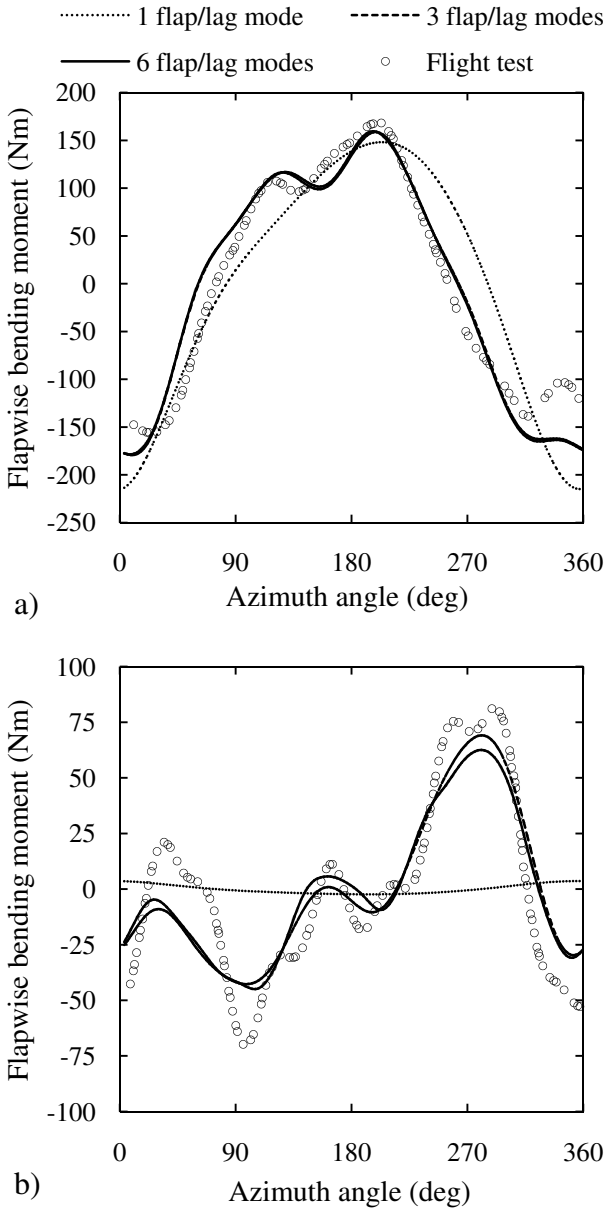

Figure 4.11: Effect of number of used flap/lag bending modes on the predicted oscillatory flapwise bending moment for $\mu = 0.197$ – comparison with flight test data reported in Ref. [12]: a) r/R=0.144, b) r/R=0.57

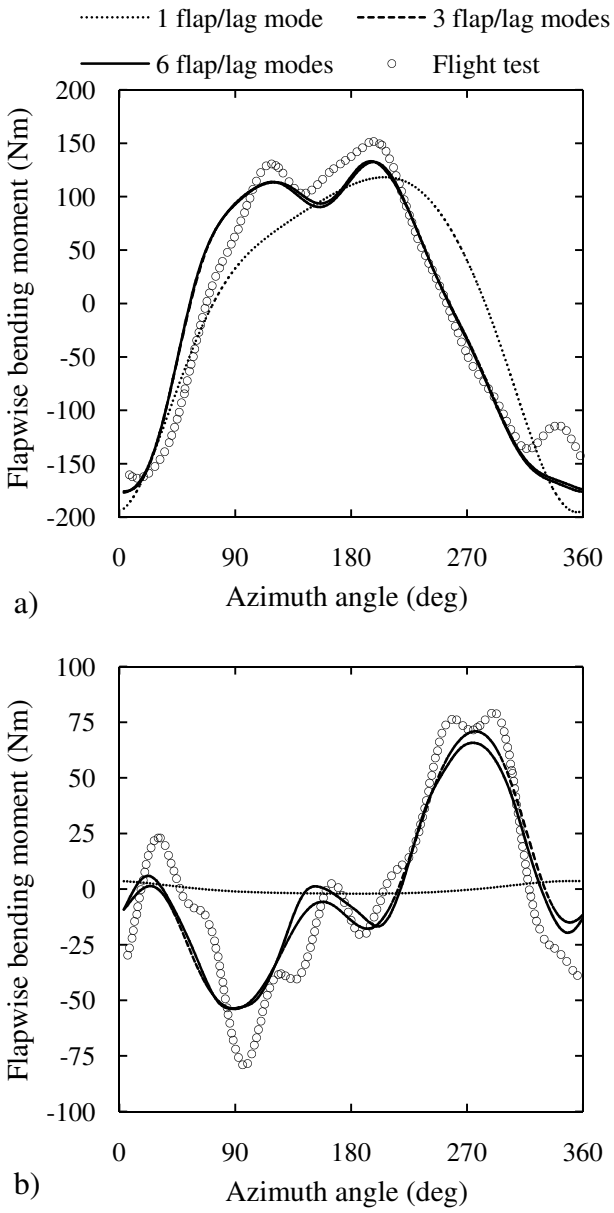

Figure 4.12: Effect of number of used flap/lag bending modes on the predicted oscillatory flapwise bending moment for $\mu = 0.225$ – comparison with flight test data reported in Ref. [12]: a) r/R=0.144, b) r/R=0.57

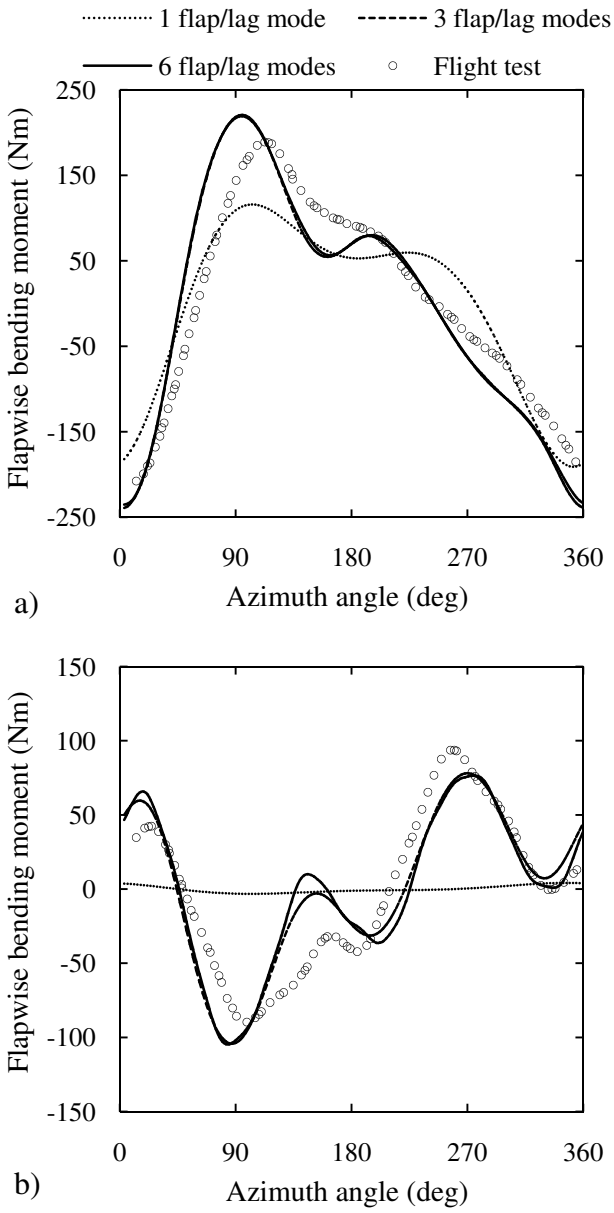

Figure 4.13: Effect of number of used flap/lag bending modes on the predicted oscillatory flapwise bending moment for $\mu = 0.306$ – comparison with flight test data reported in Ref. [12]: a) r/R=0.144, b) r/R=0.57

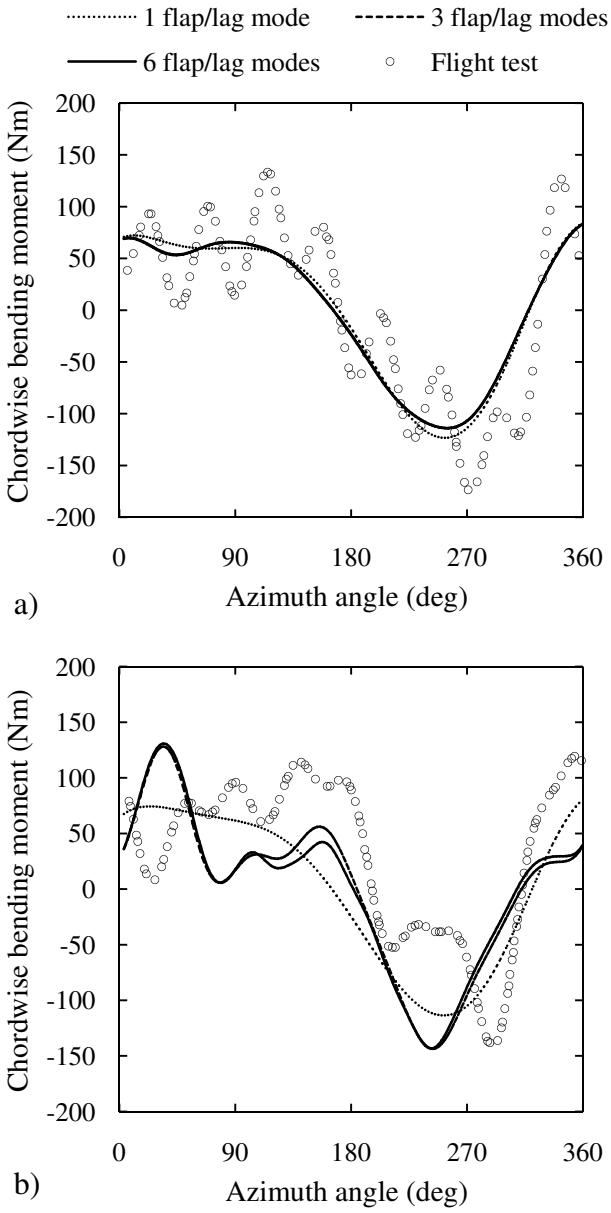

Figure 4.14: Effect of number of used flap/lag bending modes on the predicted oscillatory chordwise bending moment for $\mu = 0.197$ – comparison with flight test data reported in Ref. [12]: a) r/R=0.144, b) r/R=0.45

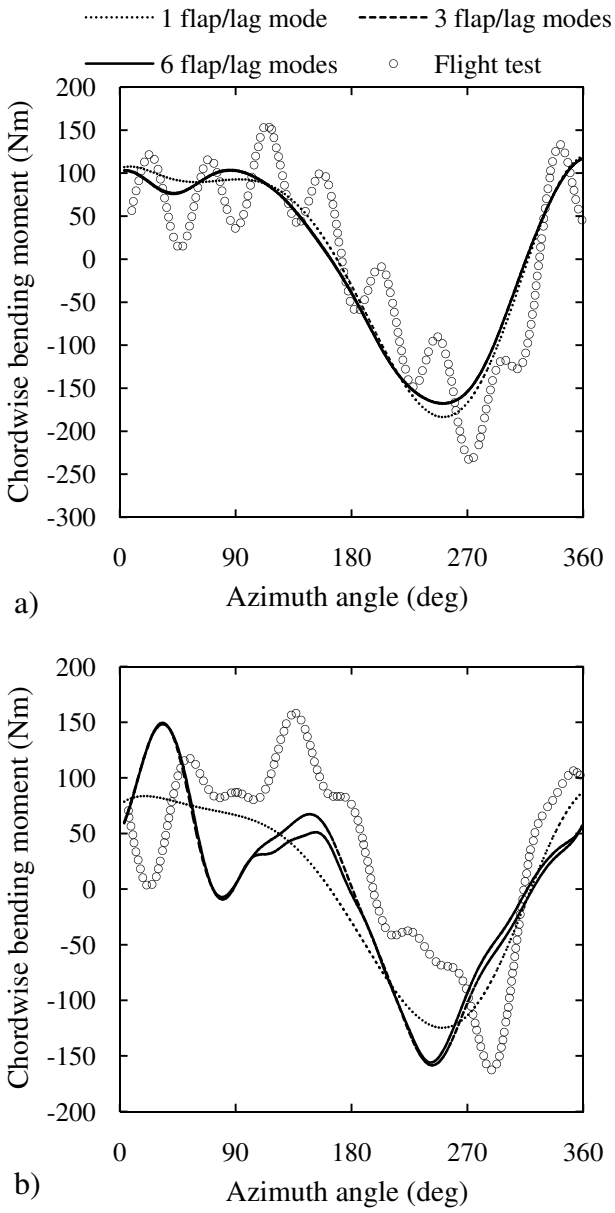

Figure 4.15: Effect of number of used flap/lag bending modes on the predicted oscillatory chordwise bending moment for $\mu = 0.225$ – comparison with flight test data reported in Ref. [12]: a) r/R=0.144, b) r/R=0.45

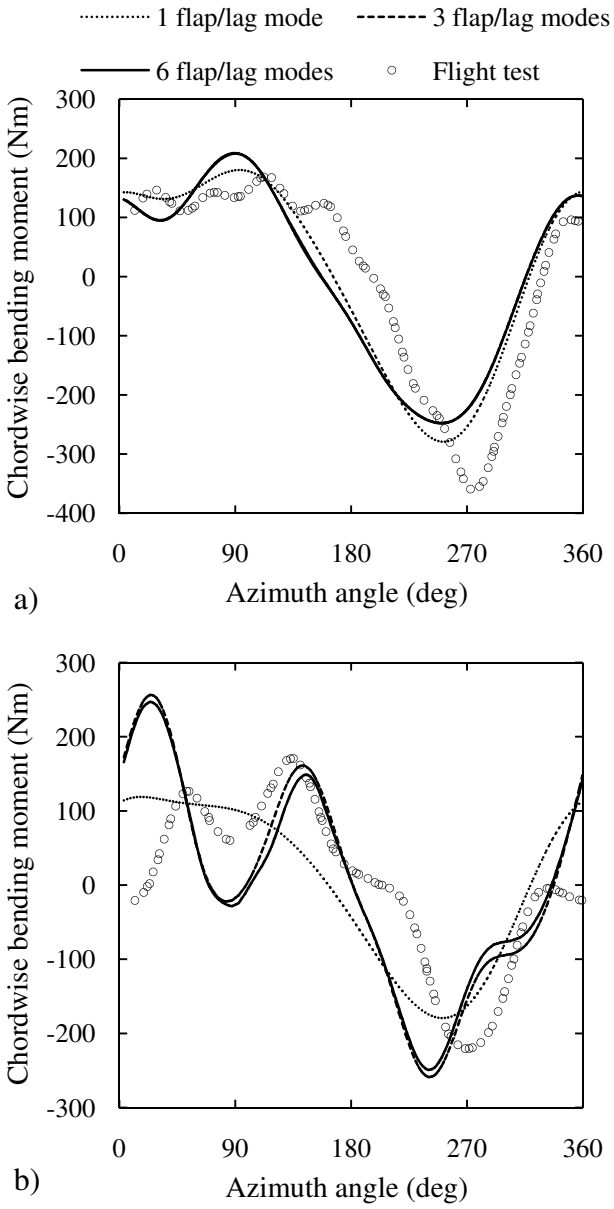

Figure 4.16: Effect of number of used flap/lag bending modes on the predicted oscillatory chordwise bending moment for $\mu = 0.306$ – comparison with flight test data reported in Ref. [12]: a) r/R=0.144, b) r/R=0.45

Chapter 5

Effects of Fuselage Induced Velocity Perturbations on the Aeroelastic Response of a Hingeless Helicopter Rotor

5.1 Introduction – Literature

As elaborated within the 3^{rd} chapter of this Thesis, obtaining reliable estimates of the produced rotor hub forces and moments for any set of imposed flight conditions, is a prerequisite for flight dynamics simulation. This not only requires sophisticated blade dynamics models, but also equally advanced rotor inflow as well as blade aerodynamics models. The overall rotor performance, as well as unsteady hub loads, are strong functions of the encountered flow-field conditions. It is thus understood that, proper assessment of the aeroelastic behavior of the main rotor requires that the surrounding complex flow-field is accurately predicted.

In order to understand the flow-field within which the helicopter main rotor is operating during flight, it is essential that the individual contributing components affecting the surrounding flow are identified and modeled at an acceptable level of detail. The fidelity of the approach may depend on application requirements. Investigations focusing on the underlying physics of the three-dimensional rotor inflow, may require a sophisticated modeling approach. This may possibly include the employment of a free-wake vortex filament method, vorticity transport simulation or maybe even a viscous CFD analysis. The associated computational cost may then be considered acceptable for the designated application. Cost-effective flight dynamics simulation on the other hand, may deem this related computational overhead prohibitive and thus, a more simplistic, but much less

computationally expensive modeling approach may be desired.

5.1.1 Rotor wake modeling

The rotor wake is the major contributing factor affecting the helicopter's induced flow-field. Significant work has been done to date on modeling the induced flow arising from the rotor wake at various levels of simulation fidelity. Currently available rotor wake models consist, among others, of finite state induced flow models, vortex filament methods and vorticity transport formulations.

Some of the finite state induced flow models developed over the years are based on the potential flow functions derived by Prandtl. Prandtl was able with the use of ellipsoidal coordinates, to obtain closed-form expressions for the potential flow functions corresponding to a control volume which includes an arbitrary pressure discontinuity across a circular disc. Mangler and Squire (Ref. [63]) were able to apply Prandtl's functions in the form of steady actuator disc theory in order to obtain the rotor induced flow-field in forward flight. In doing so, they assumed that the rotor blade loads were spread evenly along the rotor azimuth angle. Pitt and Peters (Refs. [47, 48]) extended Mangler and Squire's work and came up with an unsteady dynamic-inflow theory. Within Pitt's model, the induced flow is expressed arimuthally by a Fourier series whose coefficients are determined by the solution of a set of 1^{st} order Ordinary Differential Equations (ODEs). Peters and He (Refs. [10,54]) extrapolated Pitt's work by including higher harmonic inflow content along with more refined expressions for the radial inflow distribution using Legendre polynomial functions. They were thus able to derive an entirely closed form generalized dynamic wake model, capable of providing time-accurate estimates of the main rotor inflow. Further elaboration on finite state induced flow modeling as well as on the current "state of the art" is given in Refs. [64–67].

The current hierarchy of vortex filament based wake models ranges from relatively simple "prescribed" wake models to more sophisticated and computationally expensive "free" wake models. Both formulations require knowledge of the wake geometry, which is essentially composed of individual trailed and shed vortex filaments. Application of the Biot–Savart law and integration over the entire wake geometry, results in the wake induced flow-field. Prescribed wake modeling (Refs. [68, 69]) is based on the classical "rigid" wake model. Distortion functions are applied based on physical arguments or empirical observations. Thus, the wake geometry is essentially considered known a-priori. Free-wake models (Refs. [70, 71]) solve for the wake geometry directly and therefore experimental data is not required for their formulation. Free-wake methodologies are generally divided into two broad sections depending on the applied boundary and initial conditions as well as their corresponding solution methods: time-marching and relaxation based models.

Relaxation models have currently reached a state of good numerical stability prop-

erties along with relatively reduced computational overheard (Ref. [53]). They are not however capable of providing unsteady, time-accurate estimates of the main rotor inflow response since periodicity is enforced as a boundary condition. Time-marching models provide a more physically accurate representation of the main rotor wake but they have been susceptible to numerical instabilities as well as time-step sensitivity (Ref. [53]). Recent developments in time-marching free-wake methods have been able to address these issues and significantly improve on their numerical performance (Ref. [9, 72, 73]). It is however noted that, free-wake vortex methods are in general accompanied by a relatively large computational overhead which may be prohibitive depending on the designated application requirements.

More recent advancements in the field of rotor wake modeling include the development of induced flow models based on the numerical solution of the unsteady fluid-dynamics equations governing the generation and convection of vorticity. Brown (Ref. [45]) presented a numerical formulation based on the solution of the Navier–Stokes equations in vorticity conservation form, for the calculation of the unsteady aerodynamic environment surrounding a helicopter rotor system. The formulation was compared with experimental data for an isolated helicopter rotor for a case where strong rotor–wake interactions was present with favorable results.

The inflow model selected for this study is the popular Peters and He finite state induced flow model (Refs. [10, 54]) due to it's proven applicability in aeroelasticity applications. The model is able to provide the unsteady induced flow over any designated location on the rotor plane, which makes it suitable for the present analysis. Considerable flexibility is offered in terms of defined simulation fidelity for relatively small computational requirements.

5.1.2 Main rotor–fuselage interaction

Although the rotor wake is the main contributor to the rotor flow-field conditions, the aircraft fuselage may also serve to alter the flow pattern at the vicinity of the rotor plane. Current design trends dictate for helicopters to be increasingly more compact in order to raise attainable airspeed and consequently reduce operational costs (Ref. [74]). This trend essentially leads to the main rotor being closer to the fuselage surface, thus increasing the effective aerodynamic interaction between the two components. During flight, the presence of the fuselage affects the surrounding rotor flow-field in two discrete ways: the induced velocity perturbation due to its presence in the free-stream, and the velocity perturbations due to the rotor wake distortion it causes (Ref. [13]). The former effect can be captured with potential flow theory. The later component is more complex and a rather sophisticated approach is required in order to model it properly.

Several studies are reported in the literature where the effects of fuselage induced

flow on rotor performance have been investigated experimentally and analytically. Crimi and Trenka (Ref. [75]) developed a methodology based on potential flow theory for the simultaneous modeling of rotor wake and fuselage induced flow effects. Their goal was to predict the combined downwash at the rotor plane. Keys (Ref. [76]) deployed a source–panel method in order to investigate the effects of fuselage induced velocity perturbations on the rotor blade angle of attack during flight. Johnson and Yamauchi (Ref. [77]) attempted to assess the fuselage aerodynamic interference effects on the main rotor loads using a generic – axisymmetric fuselage geometry.

The literature contains an adequate amount of references where the flow around an isolated helicopter fuselage was studied independently from the rotor system. Berry and Althoff (Ref. [13]) followed a numerical and experimental approach in an effort to assess the flow-field properties in the vicinity of the experimental ROBIN (ROtor Body INteractions) fuselage (Ref. [78]). Their methodology incorporated the deployment of a potential flow source–panel code which was used to predict the steady-state induced velocity perturbations around the isolated fuselage taking into account only free-stream conditions. Perturbation velocities were computed and compared with experimental measurements made with a laser velocimeter at the rotor plane (rotor removed). Their numerical approach was found to agree well with the measurements, with the exception of the vicinity of the rotor hub where flow separation was suggested by the measured data.

Ghee *et al.* (Ref. [79]) performed an experimental investigation in an effort to evaluate the rotor wake geometry and quantify the induced flow behind a scaled-down model helicopter rotor in forward flight. Extensive wake measurement data was taken around the ROBIN fuselage shape. Berry and Bettschart (Ref. [74]) worked on a complete nonlinear rotor–fuselage interaction analysis for the Dauphine helicopter. A comparative evaluation was waged between three analytical methods and experimental data with regards to the flow-field conditions in the vicinity of the rotor–fuselage system. Good results were obtained with regards to steady-state flow-field predictions. The unsteady features of the flow were not accurately captured by none of the deployed analytical approaches.

Lorber and Egolf (Ref. [80]) described a computational method for the treatment of the unsteady helicopter rotor–fuselage interaction. Their approach included the use of a modified lifting line/prescribed wake rotor analysis coupled with a source–panel fuselage model. They were however not able to validate the primary outcome of their analysis with regards to the vibratory fuselage loads due to lack of experimental data. Renaud *et al.* (Ref. [81]) compared the performance of three different viscous flow solvers in terms of predicting the flow around the vicinity of the isolated fuselage as well as for the coupled rotor–fuselage system of the Dauphin 365N helicopter. Lee *et al.* (Ref. [82]) developed a three-dimensional inviscid flow solver based on an unstructured mesh. Their tool was subsequently deployed for the evaluation of the unsteady flow-field in the vicinity of the UH-60 helicopter using the ROBIN fuselage geometry.

At this point it is noted that, none of the aforementioned references has explored the effects of fuselage aerodynamic interference on the main rotor aeroelastic response and the corresponding implications in terms of helicopter trim parameters. The associated interference effects on the predictive qualities of rotor blade flap and chord bending moments has not been covered in the existing literature. Furthermore, the viability of modeling the interaction effects and including them through a standardized method within a computationally efficient flight dynamics simulation environment, has not been demonstrated.

The purpose of this work is to perform a 1^{st} order identification of the primary effects associated with fuselage induced velocity perturbations, on the predicted trim parameters and the unsteady rotor blade loads. A three-dimensional, potential flow source–panel method has been implemented. The scheme is based on the principle of constant internal potential and is capable of estimating the overall flow-field anywhere within the three-dimensional domain. It is deployed in order to predict the induced velocity perturbations arising from the existence of a generic rotorcraft fuselage body in free-stream conditions and within the rotor wake. The panel method is coupled with the aeroelastic rotor aircraft model described in section "Integrated aeroelastic rotor – aircraft model" of chapter 4 within this Thesis. The fuselage induced velocity perturbations are superimposed on the rotor tip path plane inflow. The rotor aeroelastic response and the fuselage induced potential flow are solved simultaneously due to their implicit coupling through the rotor wake.

Results are presented in terms of three-dimensional induced velocity perturbations on the rotor tip path plane for a scaled-down, isolated fuselage model. A comparative evaluation has been waged between simulation results and flow-field measurements conducted at the NASA Langley subsonic wind tunnel. Good agreement is shown between the induced velocity perturbations predicted by the developed potential flow method and the experimentally derived measurements, with the exception of the vicinity close to the rotor hub. Predictions of unsteady blade flapwise/chordwise bending moments and trim parameters are presented for advance ratios ranging from hover to high-speed flight for a hingeless rotor helicopter, modeled after the MBB Bo 105. Simulations have been performed with and without accounting for the fuselage induced flow perturbations on the main rotor tip path plane. Numerical results suggest that, steady-state aerodynamic interference effects can significantly influence the off-axis trim control control angle whereas the remaining trim parameters remain relatively unaffected. It is shown that, the inclusion of steady-state fuselage aerodynamic interference effects offers little improvement on the overall predictive qualities of oscillatory blade bending moments. The feasibility of including the interaction effects through the deployment of a standardized potential flow based method in a computationally efficient, helicopter flight dynamics simulation environment is exhibited.

5.2 Methodology

The mathematical modeling approach employed for the analysis presented in this chapter can be regarded as an effective combination of a steady-state potential flow method coupled with an unsteady aeroelastic rotor model. The coupling is based on the assumption that the fuselage induced velocity perturbations on the main rotor tip-path plane, can be superimposed on the overall rotor inflow. The effect of wake distortion due to impingement on the fuselage body, on the wake induced rotor inflow is neglected. The modified trailed-wake circulatory loading due to the fuselage perturbations affecting the flow-field in the main rotor vicinity, is accounted for. A time-averaged, rotor induced flow profile is superimposed upon the free-stream conditions encountered by the potential flow fuselage model, for the flight conditions where wake impingement on the fuselage occurs.

5.2.1 Steady-state potential flow method

Consider a three-dimensional body with solid boundaries defined by a surface S_b, immersed within a control volume with free-stream conditions $\tilde{V}_\infty = [U_\infty\, V_\infty\, W_\infty]^T$. The governing equation for the velocity potential corresponding to inviscid, incompressible and irrotational flow is given by:

$$\nabla^2 \Phi_{total}(x, y, z) = 0 \tag{5.1}$$

where $\Phi_{total}(x, y, z)$ is the total velocity potential comprising of free-stream and induced components. The general solution for Eq. (5.1) can be structured numerically by placing an appropriate distribution of source and doublet flow singularities along the solid body surface S_b (Ref. [83]). The induced, free-stream and total potentials at a point $P(x, y, z)$ located within the flow-field are then given by:

$$\Phi_i(x, y, z) = -\frac{1}{4\pi} \int_{S_b} \{\sigma(\frac{1}{r}) - \mu \tilde{n} \cdot \nabla(\frac{1}{r})\}\, \mathrm{d}S \tag{5.2a}$$

$$\Phi_\infty(x, y, z) = U_\infty x + V_\infty y + W_\infty z \tag{5.2b}$$

$$\Phi_{total}(x, y, z) = \Phi_i(x, y, z) + \Phi_\infty(x, y, z) \tag{5.2c}$$

where σ and μ are the source and doublet strengths per unit area respectively, r is the effective geometric distance of the source/doublet from the evaluation point $P(x, y, z)$ and $\tilde{n}$ is a unit vector perpendicular to dS pointing towards the direction of the potential jump (Ref. [83]).

Imposing the non-penetration condition $\dfrac{\partial \Phi_{total}}{\partial \tilde{n}} = 0$ along the solid body surface, essentially results indirectly to the derivation of the *Dirichlet* boundary condition which dictates constant internal potential within the region enclosed by S_b:

$$\Phi^{int.}_{total} = (\Phi_i + \Phi_\infty)_{body} = c \tag{5.3}$$

where c is an arbitrary constant. Substituting Eq.(5.2a) into Eq.(5.3) and subsequently making use of the identity $\tilde{n} \cdot \nabla f = \dfrac{\partial f}{\partial \tilde{n}}$, where f is a scalar function, gives:

$$\Phi_{total}^{int} = \frac{1}{4\pi} \int_{S_b} \mu \frac{\partial}{\partial \tilde{n}} (\frac{1}{r}) \mathrm{d}S - \frac{1}{4\pi} \int_{S_b} \sigma (\frac{1}{r}) \mathrm{d}S + \Phi_\infty = c \tag{5.4}$$

It is noted that the present formulation is designated for the estimation of the induced velocity perturbations of a helicopter fuselage which is assumed to produce zero circulatory lift. Therefore, no shed wake effects have been included in the formulation of Eq.(5.4). Setting $c = \Phi_\infty$ in Eq. (5.4) gives:

$$\frac{1}{4\pi} \int_{S_b} \mu \frac{\partial}{\partial \tilde{n}} (\frac{1}{r}) \mathrm{d}S - \frac{1}{4\pi} \int_{S_b} \sigma (\frac{1}{r}) \mathrm{d}S = 0 \tag{5.5}$$

Reference [83] shows that, application of the non-penetration condition $\dfrac{\partial \Phi_{total}}{\partial \tilde{n}} = 0$ along the solid body boundaries defined by S_b essentially leads to:

$$\sigma = \tilde{n} \cdot \tilde{V}_\infty \tag{5.6}$$

Equation (5.6) expresses the boundary condition used in the present numerical approach for the determination of the source strength per unit area distribution along the fuselage geometry defined by $\tilde{n}$.

Having assumed that the helicopter fuselage is a bluff body with no circulatory loading and no shed wake, the surrounding flow will only be affected by the associated geometry thickness effects. Thus, using only source singularities along the fuselage geometry, the equation for the induced potential becomes:

$$\Phi_i(x, y, z) = -\frac{1}{4\pi} \int_{S_b} \sigma (\frac{1}{r}) \, \mathrm{d}S \tag{5.7}$$

Therefore, the problem can be considered uniquely defined through application of Eq. (5.6) in terms of determining the distribution of source strength per unit area over the region defined by S_b. Subsequent evaluation of Eq. (5.7), yields the induced potential for any set of coordinates (x, y, z) anywhere within the flow-field.

Discretizing the body geometry into N_p quadrilateral, planar panels of constant source strength σ_j, $j = 1, ...N$ per unit area, leads to the following numerical expression for the analytical form of Eq. (5.7):

$$\Phi_i(x, y, z) = \sum_{j=1}^{N_p} B_j \sigma_j = 0 \tag{5.8}$$

The coefficient B_j essentially describes the influence of the j^{th} source–panel element at point $P(x, y, z)$ and is defined as follows:

$$B_j = -\frac{1}{4\pi} \int_{S_j} (\frac{1}{r}) \mathrm{d}S, \qquad j = 1, ...N \tag{5.9}$$

where S_j is the surface area of the j^{th} panel and r is the geometric distance of point $P(x, y, z)$ from the differential surface element dS. Hess and Smith (Ref. [84]) have provided closed form expressions for the estimation of the induced potential of quadrilateral planar elements with constant source strength and designated end-point coordinates. The complete equations are rather lengthy and have also been provided in (Ref. [83]), hence further elaboration will be omitted. The coordinates of $P(x, y, z)$ can be transformed to the reference frame defined by the planar coordinates of the j^{th} panel. This enables the employment of the Hess and Smith expressions (Ref. [84]) for the evaluation of the integral in the RHS of Eq. (5.9). The velocity perturbations can be subsequently evaluated by estimating the spatial gradient of the induced potential at point $P(x, y, z)$:

$$\tilde{v} = \nabla \Phi_i \tag{5.10}$$

where $\tilde{v} = [u\ v\ w]^T$ is the perturbation velocity vector.

The potential flow method described above is applied to the geometry of the ROBIN helicopter fuselage (Fig. 5.1) in order to predict the steady-state induced velocity perturbations at the main rotor tip-path plane. The ROBIN geometry has been described in (Refs. [13,78]), thus further elaboration will be omitted. Due to the fact that the deployed boundary condition (Eq. (5.6)) readily defines the required source strength distribution, there is no need for a numerical solution. This deems the described numerical procedure very robust and computationally efficient as well as easy to implement and apply in existing flight dynamics simulation codes.

5.2.2 Integration with aeroelastic rotor model

The panel method described in section "Steady-state potential flow method" of this chapter, is coupled with the aeroelastic rotor aircraft model described in section "Integrated aeroelastic rotor – aircraft model" of chapter 4 within this Thesis. The numerical approach employed in this study, makes use of the assumption that the fuselage induced velocity perturbations can be superimposed on the main rotor inflow. The implications of rotor wake distortion due impingement on the aircraft fuselage are not catered for. The effect of an altered time-history of circulatory blade loading due to the fuselage perturbation influence, is thoroughly captured implicitly through the formulation of the Peters – He inflow model.

For the range of flight conditions that wake impingement on the fuselage occurs, a time-averaged induced velocity profile over the rotor disc is considered. This velocity

profile is superimposed upon the free-stream components encountered by the discretized fuselage panel model. The superposition is applied at the appropriate panel locations depending on the wake skew angle relative to the fuselage. Larger wake skew angles dictate that the wake does not impinge on the fuselage, and therefore only free-stream components related to flight speed are accounted for.

5.3 Results & Discussion

5.3.1 Fuselage induced velocity perturbations

Figure 5.1, a) illustrates the fuselage geometry used for the computations of induced velocity perturbations throughout the work presented in this chapter. Extensive comparisons with experimental data extracted from (Ref. [13]) are waged regarding the induced flow-field conditions at the imaginary rotor plane for the isolated fuselage. It is noted that the fuselage geometry used for the experiments in Ref. [13] includes a slender portion of the rotor shaft including the rotor hub. The aforementioned geometry components are not modeled in the present analysis.

Results are presented for a free-stream velocity of $|\tilde{V}_\infty|= 28.65\, m/sec$ with a fuselage incidence of $a_f = -0.5°$ nose down. The imaginary rotor tip path plane incidence is $a_s = -3°$. The exact test conditions have been described in Ref. [13]. The rotor plane position relative to the fuselage body is illustrated in Figs. 5.1, b) and c). All dimensions are provided as functions of an effective rotor blade radius $R = 1.014\, m$ which corresponds to the scale of the experimental model. One longitudinal (at $Y = 0\, m$) and 2 lateral reference lines (at $X = 0\, m$ and $X = 1.4\, m$ respectively) are defined along the rotor plane, as shown in Fig. 5.1, b), for which the computed variations of velocity perturbations are compared with experimentally measured values.

Figures 5.2 – 5.4 present qualitative comparisons between predicted and measured values of normalized induced velocity perturbations ($\bar{u}$, $\bar{v}$, $\bar{w}$) on the main rotor plane. The normalized perturbation velocities are defined as follows:

$$\bar{u} = \frac{u \cos a_s - w \sin a_s}{|\tilde{V}_\infty|} \tag{5.11a}$$

$$\bar{v} = \frac{v}{|\tilde{V}_\infty|} \tag{5.11b}$$

$$\bar{w} = \frac{w \cos a_s + u \sin a_s}{|\tilde{V}_\infty|} \tag{5.11c}$$

It is noted that good qualitative correlation is exhibited for all perturbation components between simulations carried out and the measured data. Figures 5.2, a) and b) show a strong value of $\bar{u}$ directly over the imaginary rotor head. Figures 5.3, a) and b) indicate a

pattern where the flow is influenced by the initial lateral divergence around the fuselage geometry and subsequent convergence as the fuselage thickness goes to zero at the tail. Figures 5.4, a) and b) reveal a strong up-wash starting at the leading edge of the rotor disc, followed by a down-wash ending at the disc trailing edge.

Figures 5.5, a) and b) present comparisons between simulations and experimental data for the longitudinal variations of $\bar{u}$ and $\bar{w}$ velocity perturbations respectively. Results are presented for the reference line corresponding to $Y = 0\,m$ as shown in Fig. 5.1, b). Good agreement can be observed for both velocity perturbations away from the vicinity close to the imaginary rotor hub ($X = 0\,m$). A small underprediction of $\bar{u}$ close to the rotor disc leading edge can be noted. Larger deviations are noticed with regards to predicted values of $\bar{w}$ and experimental data close to the rotor hub location which are attributed to the absence of the rotor shaft and hub components in the modeled geometry (Fig. 5.1, a)). Deviations observed aft of the rotor hub are also due to a large amount of unmodeled separated flow behind the specific region.

Figures 5.6 – 5.8 present comparisons between predictions and experimentally measured values of the lateral variations of induced flow perturbations $\bar{u}$, $\bar{v}$ and $\bar{w}$ respectively. Results are presented for the reference lines corresponding to $X = 0\,m$ (Figs. 5.6 – 5.8, a)) and $X = 1.4\,m$ (Figs. 5.6 – 5.8, b)). A consistent underprediction of $\bar{u}$ close to the rotor disc leading edge ($X = 0\,m$) is observed in Fig. 5.6, a), although the perturbation gradient is accurately captured. Better predictive qualities are exhibited in Fig. 5.6, b) with regards to the position close to the disc trailing edge ($X = 1.4\,m$), apart from the vicinity behind the rotor hub ($Y = 0\,m$). Figures 5.7, a) and b) show that the nature of $\bar{v}$ perturbation is well predicted for both longitudinal locations, although simulations suggest steeper lateral inflow gradients for both longitudinal reference lines. Very good prediction of $\bar{w}$ is demonstrated for both longitudinal coordinates in Figs. 5.8, a) and b). The relatively larger deviation of the predicted values of $\bar{w}$ compared to the measurements for the vicinity close to $Y = 0\,m$, is attributed to the absence of rotor hub modeling in the fuselage geometry.

It is noted that, the perturbation component predominantly affecting the aerodynamic forces exerted on the rotor blades, is the one normal to the rotor tip-path plane ($\bar{w}$). The remaining perturbations which essentially influence the tangential velocity encountered by the blades, are rather insignificant compared to the rotational and free-stream components, particularly for radially outwards locations. The normal perturbation component induced by the fuselage can be of considerable magnitude, compared to the rotor wake induced flow, especially with regards to high-speed flight where the latter is drastically reduced. It has been shown in Figs. 5.5, b) and Fig. 5.8 that the behavior of $\bar{w}$ is fairly accurately captured away from the vicinity close to the rotor hub. Thus, the described numerical approach can be used with confidence in order to assess the effect of fuselage induced velocity perturbations on the aeroelastic rotor response.

5.3.2 Effect of fuselage interference on main rotor trim

Figures 5.9 – 5.12 present results acquired from trim simulations performed for the MBB Bo 105 helicopter using the aerodynamically and dynamically coupled fuselage–rotor model described in section "Integration with aeroelastic rotor model" of this chapter. The natural vibration characteristics for the rotor blades, presented in section "Rotor blade modal analysis" of chapter 4 within this Thesis, are utilized for the calculations presented within this chapter as well. Results are presented as functions of advance ratio $\bar{\mu} = \frac{V_{flight}}{\Omega R}$ from hover ($\bar{\mu} = 0$) to high speed flight ($\bar{\mu} = 0.36$). Simulations have been performed with the inclusion of fuselage aerodynamic interference effects as well as without.

It is once again noted that a total number of 9 inflow harmonics are deployed within the Peters – He inflow formulation (Refs. [10, 54]) with regards to all simulation results presented in this chapter. This is done in order to capture the effect of higher harmonic loading on the inflow response. The radial inflow distribution polynomials used reach up to the 12^{th} power of non-dimensional rotor radius. A total of 6 flap/lag bending modes are employed for each degree of freedom respectively. Measured data from flight tests extracted from (Ref. [61]) have been included. Simulation results reported in (Ref. [62]), obtained using a relaxation-type free-wake formulation along with a Finite Element Analysis (FEA) based aeroelastic rotor model are also included for comparison purposes.

It is emphasized that, the geometry deployed for the fuselage aerodynamic interference prediction, is actually different to the one employed for the Bo 105 helicopter. Reference [13] has shown that the effect of specifying a detailed fuselage geometry on the induced flow-field predictive qualities using a similar potential flow panel approach, is only pronounced in the vicinity close to the rotor hub. Radially outwards locations have been found to be relatively unaffected by the modeling detail in terms of exactly specified geometry. The rotor hub vicinity however, is of very little significance with respect to the overall blade aerodynamic loading. This is due to the blade's root-cutout distance ($0.21R$ for the Bo 105) and the very low dynamic heads encountered by the blade elements located radially inwards. These aspects designate the flow-field conditions in the vicinity affected by the nuances of the modeled fuselage geometry, irrelevant to the overall aerodynamically induced excitation on the rotor blades.

Figures 5.9, a) and b) present trim values of main rotor power requirement P_{rotor} and collective pitch angle θ_0 respectively, as functions of advance ratio. The good correlation between flight test data and simulations performed with the described aeroelastic rotor – aircraft model for both trim outputs, is once again noted. The relatively large deviation between flight tests and simulations, with respect to the collective pitch angle at higher values of advance ratio, has been previously attributed to a deficiency in the deployed airfoil data (4^{th}, chapter, section "Comparison with flight tests – Main rotor trim controls").

There is no noticeable difference in neither trim outputs between simulations performed with the inclusion of fuselage interference effects and without.

Figures 5.10, a) and b) present trim variations of lateral (θ_{1s}) and longitudinal (θ_{1c}) cyclic pitch control inputs respectively. It can be observed from Fig. 5.10, a) that, fuselage aerodynamic interference affects only very slightly the predicted values of θ_{1s}. The induced velocity perturbation component $\bar{w}$ is predominantly responsible for affecting the rotor blade's incidence through the interference effects. Figures 5.4, a) and b) show that, the $\bar{w}$ perturbation distribution on the rotor disc is axisymmetric with respect to the disc longitudinal centerline ($Y = 0\,m$). This flow feature is directly related to the axissymetric properties of the fuselage geometry. It is therefore understood that no once-per-rev aerodynamic excitation is induced in a sinusoidal fashion by the helicopter fuselage on the main rotor blades. During trim flight however, the rotor tip path plane is tilted laterally to compensate for the rolling moments exerted by the tailrotor, thus essentially producing a small lateral bias of the fuselage induced velocity perturbations. A finite compensation is therefore required by the lateral cyclic control input θ_{1s} as indicated in Fig. 5.9, a) which tends to increase with flight speed.

It is emphasized that, good agreement is observed between simulations performed with the present numerical approach and flight test data for intermediate values of advance ratio. The relatively large deviation for $\bar{\mu} \leq 0.05$ has been previously attributed to rotor induced flow impingement on the horizontal stabilizer which is underestimated in the deployed aircraft model (Chapter 4, section "Comparison with flight tests – Main rotor trim controls").

Figure 5.10, b) demonstrates that the predicted values of longitudinal cyclic pitch angle (θ_{1c}) are significantly influenced by the fuselage interference effects, especially concerning high speed flight conditions. This is due to the fact that the distribution of the fuselage induced flow component $\bar{w}$ is highly asymmetrical with respect to the disc lateral centerline ($X \approx 0.7\,m$). An effective once-per-rev cosinusoidal harmonic excitation, is therefore exerted on the rotor blades. The large longitudinal fuselage induced inflow gradients normal to the rotor disc (Fig. 5.5, b)), are essentially compensated for by increased values of θ_{1c}, particularly in high speed flight. The simulations carried out suggest that the required trim value of θ_{1c} when considering fuselage interference effects, can be up to 75% increased relative to the case where aerodynamic interaction effects are neglected.

It is noted that, good predictive qualities are exhibited by the simulations carried out for $\bar{\mu} \geq 0.1$. The underestimation of θ_{1c} for $\bar{\mu} \approx 0.05$ has been discussed in chapter 4, and has been attributed to the rotor wake roll-up effect which is not accounted for by the Peters – He inflow model. Better correlation is observed between experimental data and simulations performed with the inclusion of fuselage aerodynamic interference effects, particularly for higher values of advance ratio where fuselage induced flow effects become more pronounced.

Figures 5.11, a) and b) present trim values of fuselage pitch Θ and roll Φ attitude angles respectively. Figure 5.11, a) shows that the effect of fuselage aerodynamic interference on the fuselage pitch attitude angle Θ is negligible. A relatively small increase in the fuselage roll attitude angle Φ is observed in Fig. 5.11, b) for intermediate values of advance ratio, when accounting for the fuselage induced velocity perturbations relative to the baseline case. Good agreement is noticed in Fig. 5.11, a) on Θ between simulations performed with the present numerical approach and the one described in Ref. [62]. The deviations observed between flight test data and results obtained with both helicopter models for $\bar{\mu} \leq 0.1$, are once again attributed to the underpredicted effect of main rotor downwash impingement on the horizontal stabilizer.

Figures 5.12, a) and b) present trim values of longitudinal and lateral rotor flapping angles (β_{1c} and β_{1s} respectively). An increasing deviation of β_{1c} between simulations performed with and without fuselage aerodynamic interference effects can be observed with increasing advance ratio. No observable difference is noted with respect to the lateral flapping angle β_{1s}.

5.3.3 Effect of fuselage interference on unsteady blade loads

Figures 5.13 – 5.18 present correlations between predictions made with the present aeroelastic rotor model and flight test data of unsteady flapwise and chordwise bending moments extracted from Ref. [12]. It is noted that only the oscillatory components are presented. Simulations have been carried out with the inclusion of fuselage aerodynamic interference effects as well as without. The flight conditions along with the test procedures, have been extensively described in section "Comparison with flight tests – Rotor blade bending moments" of chapter 4 within this Thesis, thus further elaboration shall be omitted in this chapter.

Figures 5.13 – 5.15 demonstrate the effect of fuselage aerodynamic interference on the predictive qualities of oscillatory flapwise bending moment for $\bar{\mu} = 0.197$, $\bar{\mu} = 0.225$ and $\bar{\mu} = 0.306$ respectively. Results are presented for $r/R = 0.144$ in Figs. 5.13 – 5.15, a) and for $r/R = 0.57$ in Figs. 5.13 – 5.15, b).

Figures 5.13 – 5.15, a) show that for $r/R = 0.144$, the inclusion of fuselage aerodynamic interference effects offers little improvement on the overall predictive qualities of oscillatory flapwise bending moment. Subtle alterations of the higher frequency components can be observed in the predicted loading waveforms for the specific radial location. Figures 5.13 – 5.14, a) show that for $\bar{\mu} = 0.197$ and $\bar{\mu} = 0.225$, inclusion of fuselage induced velocity perturbations, affects predominantly the prediction of 2P oscillatory loading. Figures 5.13 – 5.15, b) demonstrate that for $r/R = 0.57$, accounting for fuselage aerodynamic interference results in very similar oscillatory loading waveforms. It can be noted that for $\bar{\mu} = 0.197$ and $\bar{\mu} = 0.225$, inclusion of aerodynamic interference effects seems to improve

the predictive quality of 3P oscillatory loading.

Figures 5.16 – 5.18 demonstrate the effect of fuselage aerodynamic interference on the prediction of oscillatory chordwise bending moment for $\mu = 0.197$, $\mu = 0.225$ and $\mu = 0.306$ respectively. Results are presented for $r/R = 0.144$ in Figs. 5.12 – 5.14, a) and for $r/R = 0.45$ in Figs. 5.12 – 5.14, b).

Figures 5.16 – 5.18, a) show that the basic waveform of chordwise bending moment at $r/R = 0.144$, is well captured by the simulations including fuselage interference effects as well as by those that do not. Although the 8P oscillatory loading as measured during flight tests was not captured by neither approach, it can be noticed that, inclusion of fuselage interference effects improves the approximation of the lower frequency components of the measured loading waveform. This observation is valid for all three values of advance ratio that results are presented for. As regards the radial location corresponding to $r/R = 0.45$, Figures 5.16 – 5.18, b) illustrate that inclusion of fuselage interference effects introduces a slight improvement on the approximation of the lower frequency components of chordwise loading in terms of approximating the measured data.

5.4 Conclusions

A three-dimensional, potential flow source–panel method has been implemented and presented. The method has been deployed for the prediction of the induced velocity perturbations arising from the existence of a small-scale, generic helicopter fuselage in a free-stream. The panel scheme has been coupled with an integrated helicopter flight dynamics formulation solving for the aeroelastic behavior of the main rotor. The effects of fuselage aerodynamic interference on the associated trim parameters as well as unsteady structural loads, have been investigated for the hingeless rotor configuration of the MBB Bo 105 helicopter. Extensive comparisons have been waged with flight test data regarding rotor trim power requirements, swash plate control inputs as well as fuselage attitude and rotor flapping angles. Correlations of oscillatory flapwise and chordwise bending moment predictions with measured data from flight tests have been presented for three advance ratios. The feasibility of including fuselage aerodynamic interference effects through a standardized potential flow method in a computationally inexpensive, helicopter flight dynamics simulation environment has been demonstrated.

A comparative evaluation has been waged between source–panel simulation results and flow-field measurements conducted at the NASA Langley subsonic wind tunnel. Good agreement has been found between potential flow predictions and experimentally measured values with regards to the induced flow components at the imaginary tip-path plane of the main rotor. Larger deviations have been found within the vicinity close to the rotor hub which have been attributed to the absence of the rotor shaft and hub components in the modeled fuselage geometry.

It has been shown that the laterally asymmetrical distribution of the fuselage induced normal perturbation component, exerts a once-per-rev cosinusoidal excitation on the rotor blades which needs to be compensated for by the respective cyclic pitch control input. The simulations carried out, suggest that the corresponding longitudinal cyclic pitch θ_{1c} increase can reach up to 75% in high speed flight, compared to the case where fuselage interference effects are neglected. Good agreement of θ_{1c} trim predictions catering for fuselage interference effects has been shown with flight test data for $\bar{\mu} \geq 0.2$. It has thus been concluded, that accurate estimation of θ_{1c} at high speed flight trim conditions, requires that the steady-state fuselage interference effects are accounted for. It has been shown that main rotor power requirements, remaining trim control angles, flapping angles and fuselage attitude angles are relatively unaffected by the aerodynamic interference.

It has been demonstrated that the inclusion of steady-state fuselage induced perturbations on the main rotor inflow, offers little improvement on the overall predictive qualities of oscillatory flapwise bending moment. Simulations performed suggest that the interaction effects influence predominantly the 2P oscillatory loading components at the blade root. With regards to the blade mid-span location, it has been found that the principal influence of steady-state aerodynamic interference effects is on the 3P bending moment component. A small improvement due to the inclusion of fuselage steady-state induced flow, in the predictive accuracy of the 2P oscillatory component of chordwise root bending moment, has been observed for lower values of advance ratio.

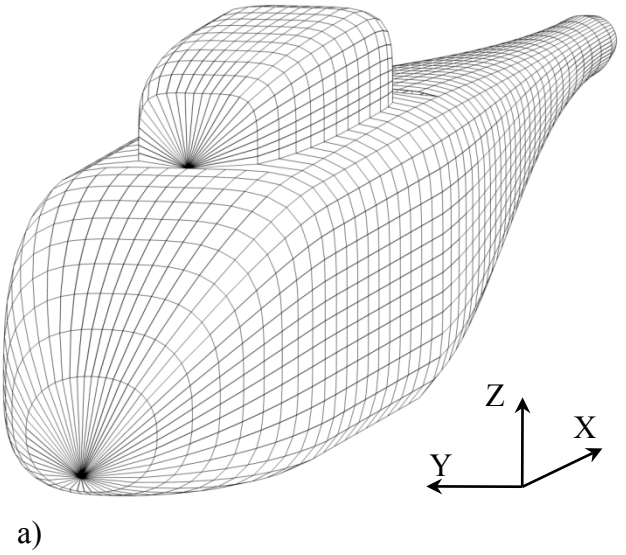

a)

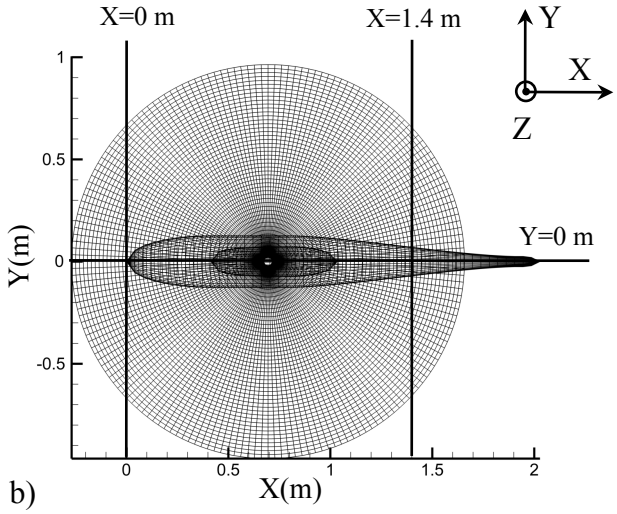

b)

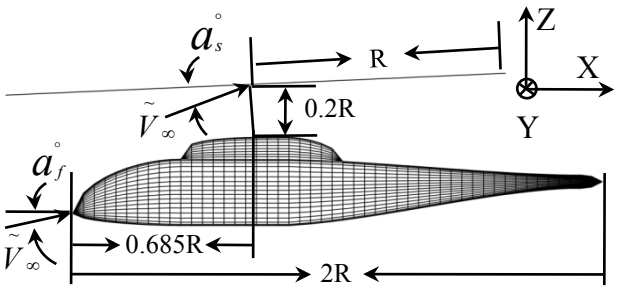

c)

Figure 5.1: ROBIN fuselage geometry: a) Three-dimensional panel model – Global reference system, b) Comparison lines location on rotor disc ($X = 0\,m$, $X = 1.4\,m$ and $Y = 0\,m$), c) Definition of rotor shaft and fuselage incidence angles (a_s & a_f) respectively

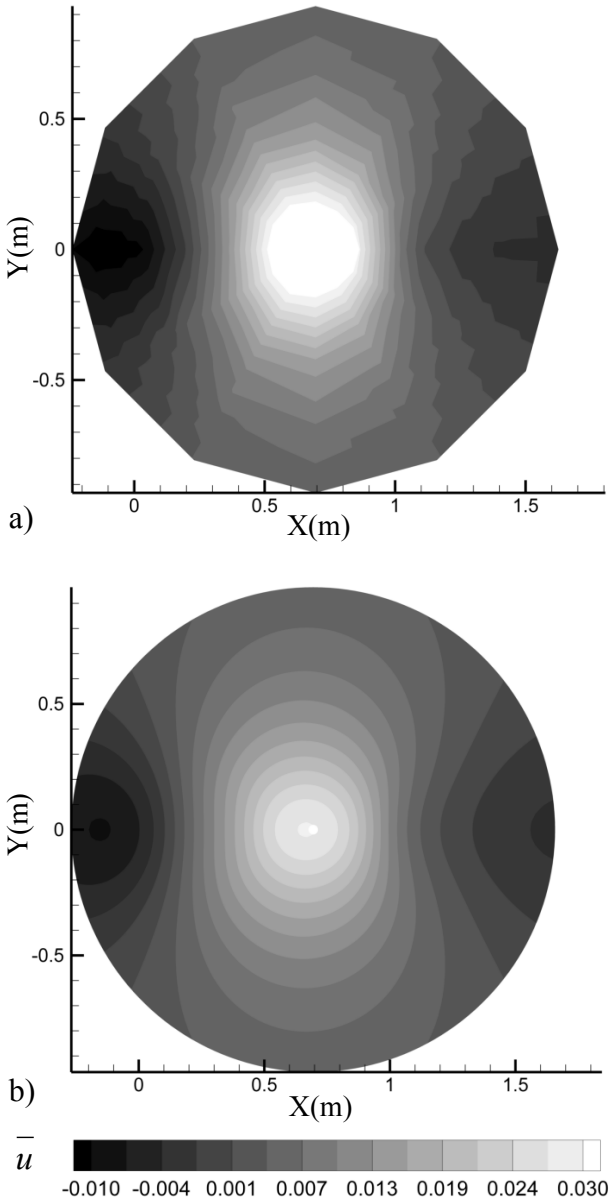

Figure 5.2: Longitudinal induced velocity perturbation component tangential to the main rotor disc, $\bar{u}$: a) Measurements reported in Ref. [13], b) Simulation

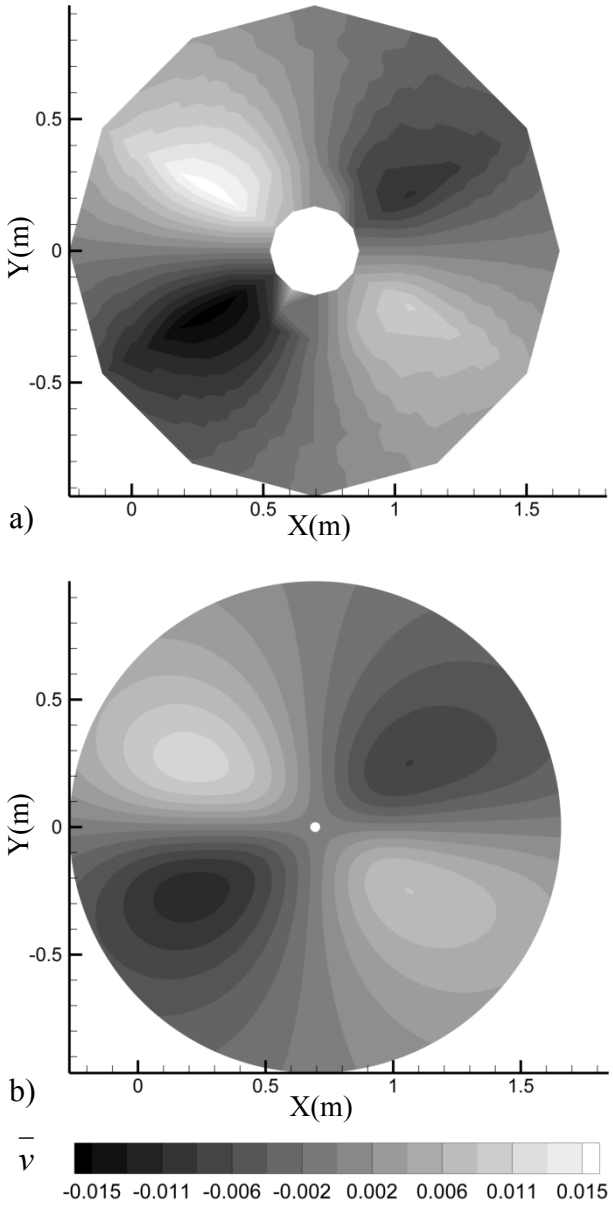

Figure 5.3: Lateral induced velocity perturbation component tangential to the main rotor disc, $\bar{v}$: a) Measurements Ref. [13], b) Simulation

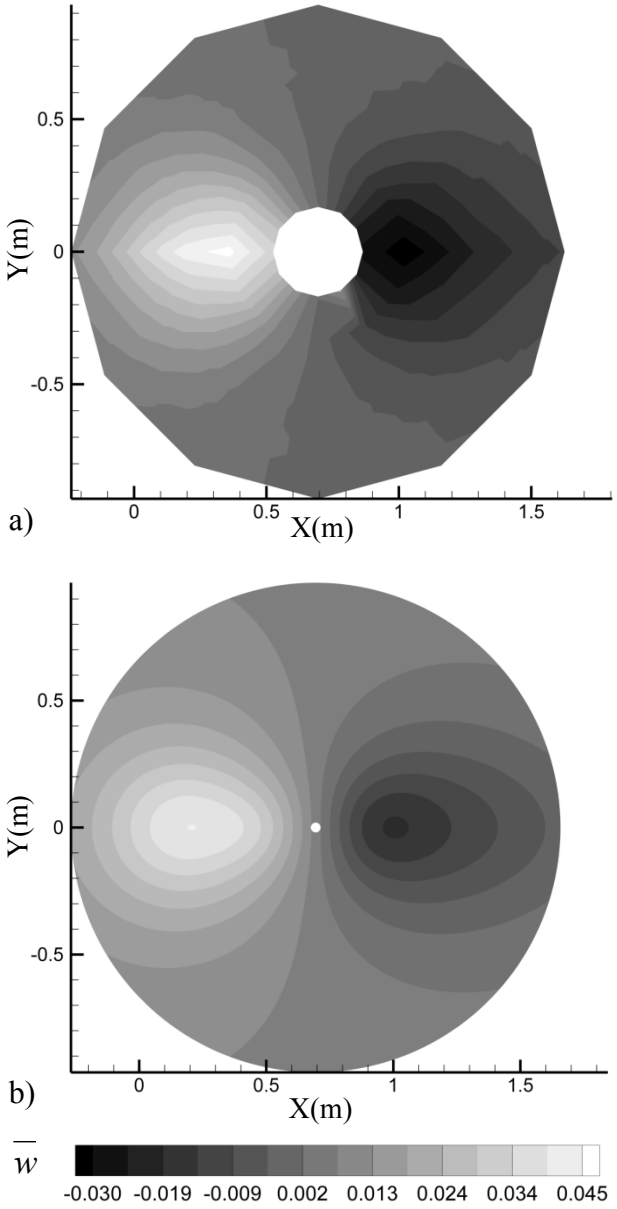

Figure 5.4: Induced velocity perturbation component normal to the rotor disc, $\bar{w}$: a) Measurements reported in Ref. [13], b) Simulation

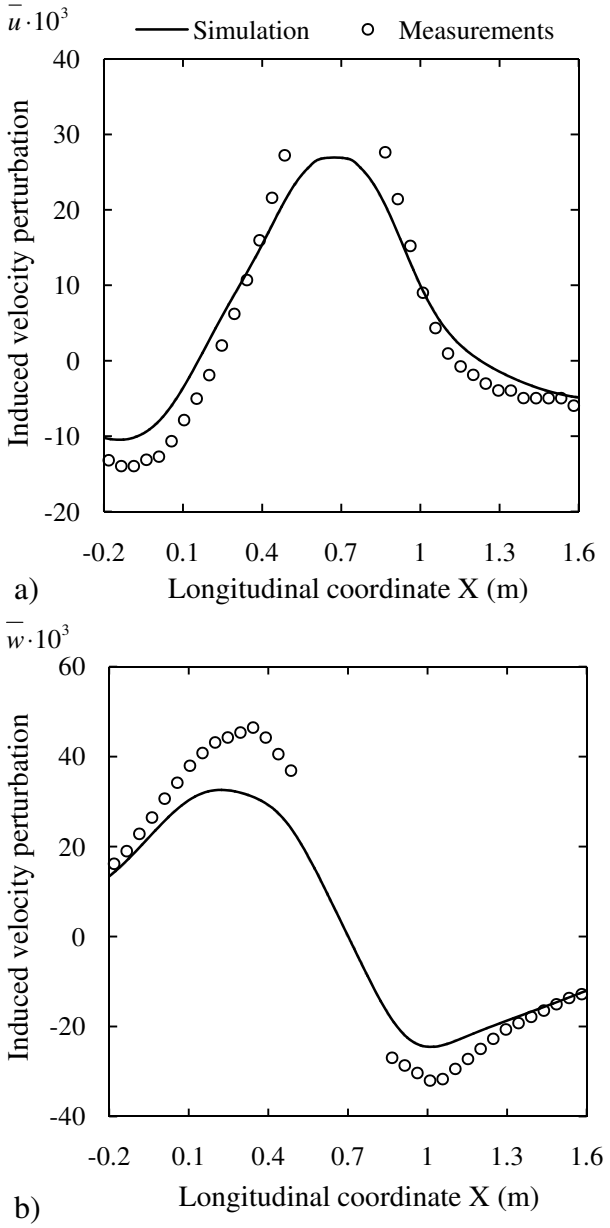

Figure 5.5: Longitudinal variation of induced velocity perturbations for $Y = 0\,m$ – Comparison with measured data reported in Ref. [13]: a) Tangential component $\bar{u}$, b) Normal component $\bar{w}$

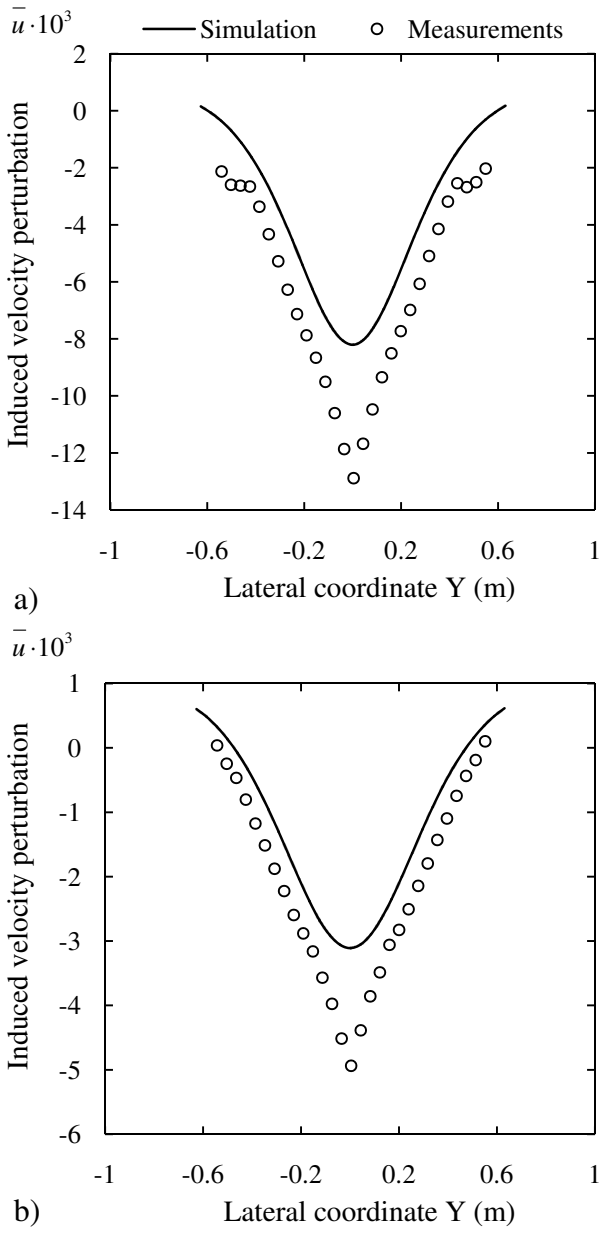

Figure 5.6: Lateral variation of induced velocity perturbation component $\bar{u}$ – Comparison with measured data reported in Ref. [13]: a) $X = 0\,m$, b) $X = 1.4\,m$

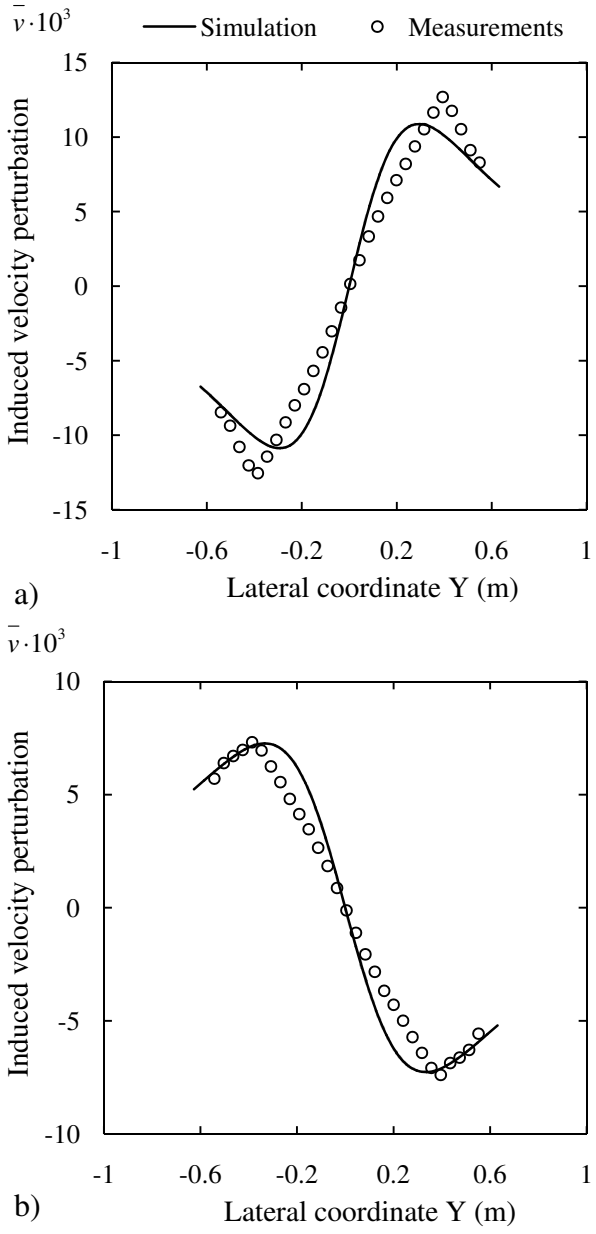

Figure 5.7: Lateral variation of induced velocity perturbation component $\bar{v}$ – Comparison with measured data reported in Ref. [13]: a) $X = 0\,m$, b) $X = 1.4\,m$

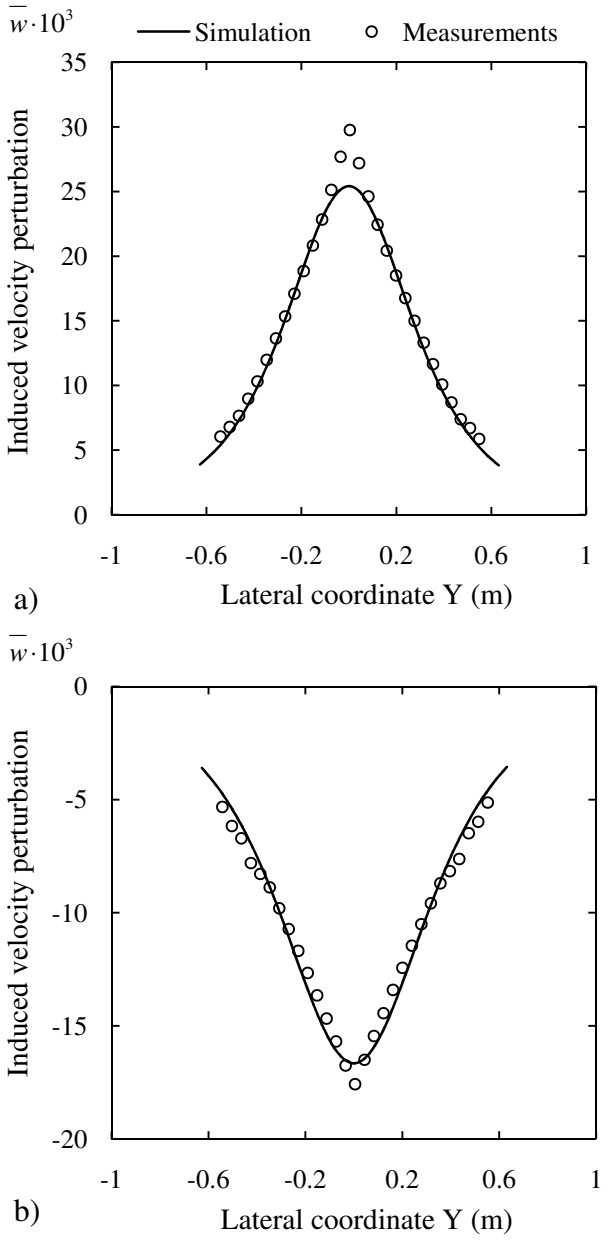

Figure 5.8: Lateral variation of induced velocity perturbation component $\bar{w}$ – Comparison with measured data reported in Ref. [13]: a) $X = 0\,m$, b) $X = 1.4\,m$

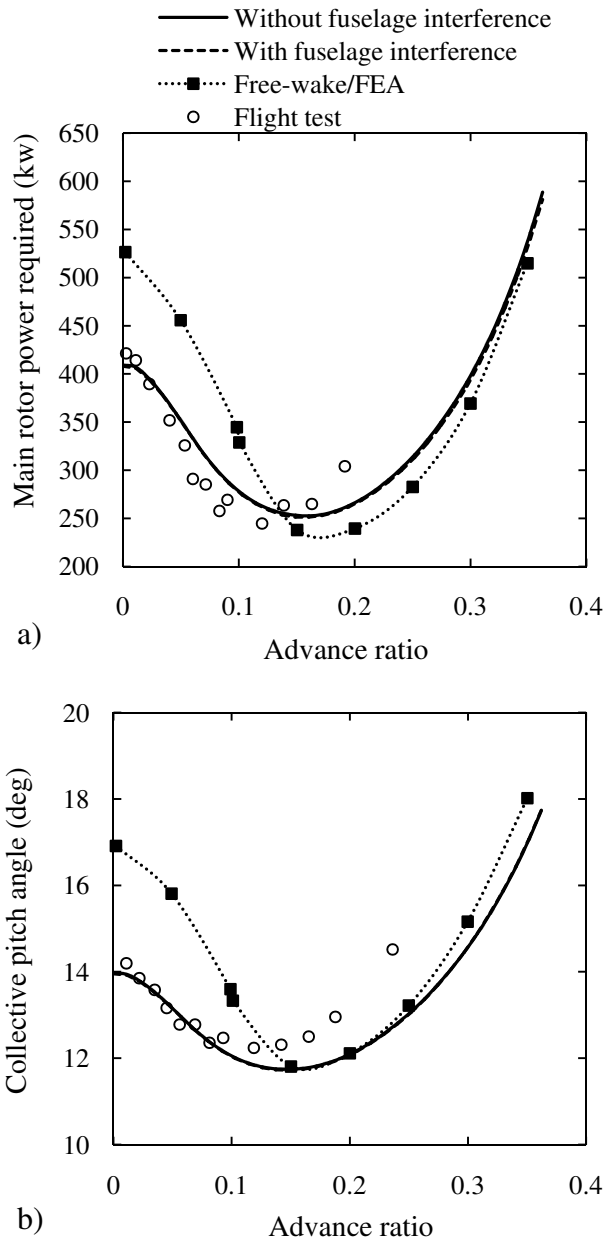

Figure 5.9: Effect of fuselage induced flow perturbations on the MBB Bo 105 helicopter trim, comparison with flight test data (Ref. [61]) and free-wake/FEA results (Ref. [62]): a) Main rotor power required P_{rotor}, b) Collective pitch angle θ_0

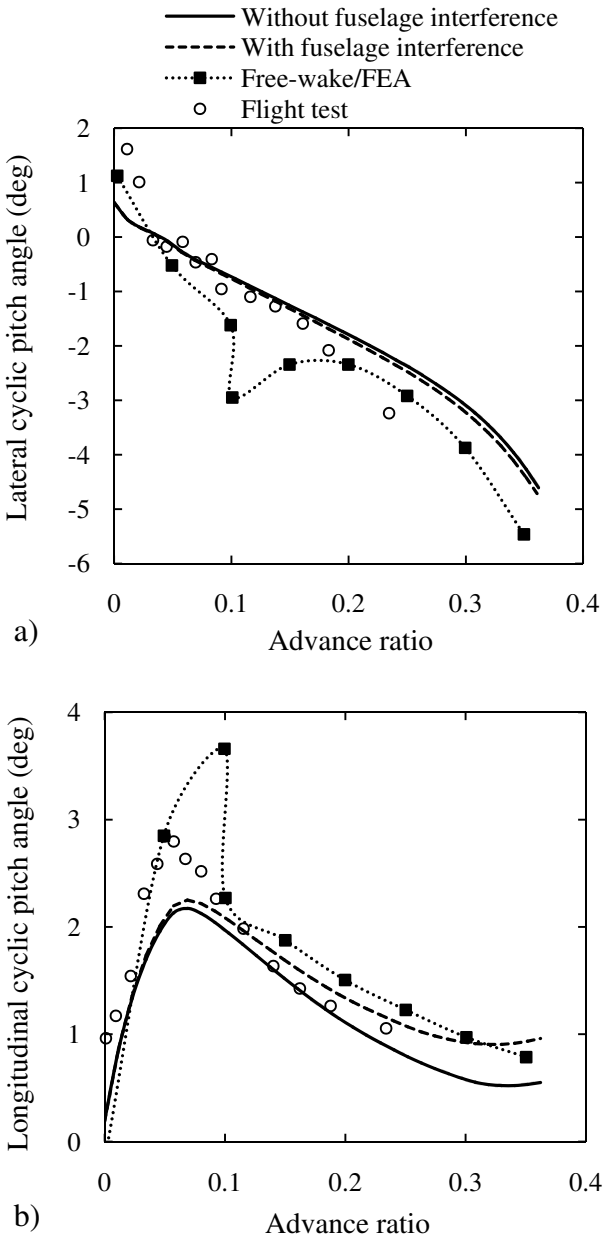

Figure 5.10: Effect of fuselage induced flow perturbations on the MBB Bo 105 helicopter trim, comparison with flight test data (Ref. [61]) and free-wake/FEA results (Ref. [62]): a) Lateral cyclic pitch angle θ_{1s}, b) Longitudinal cyclic pitch angle θ_{1c}

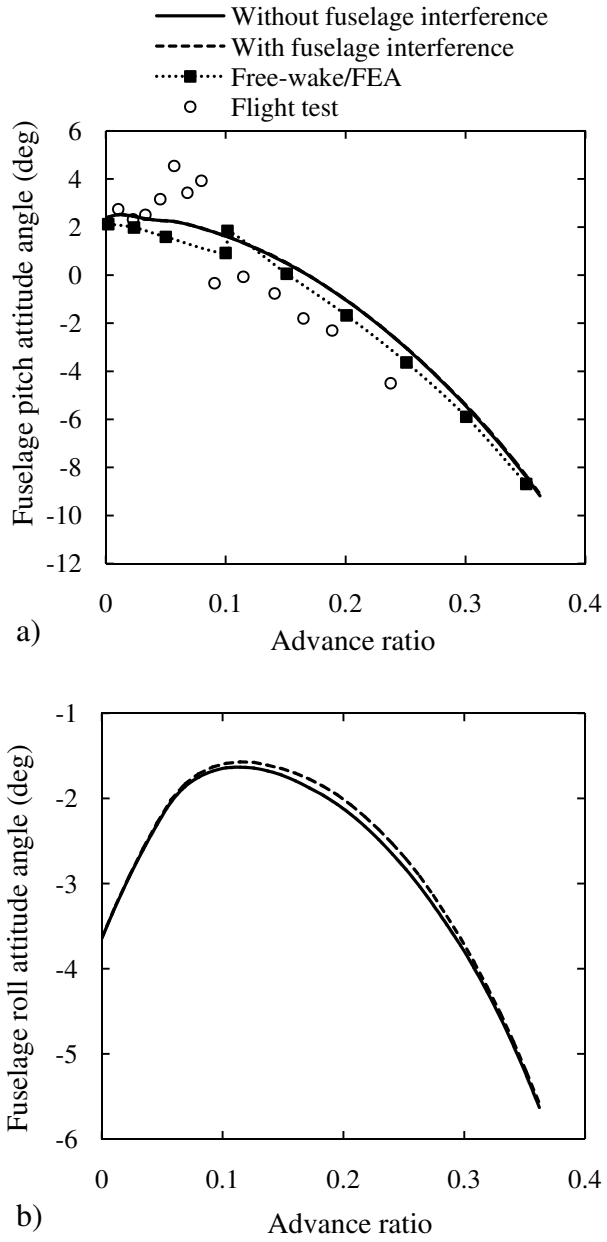

Figure 5.11: Effect of fuselage induced flow perturbations on the MBB Bo 105 helicopter trim, comparison with flight test data (Ref. [61]) and free-wake/FEA results (Ref. [62]): a) Fuselage pitch attitude angle Θ, b) Fuselage roll attitude angle Φ

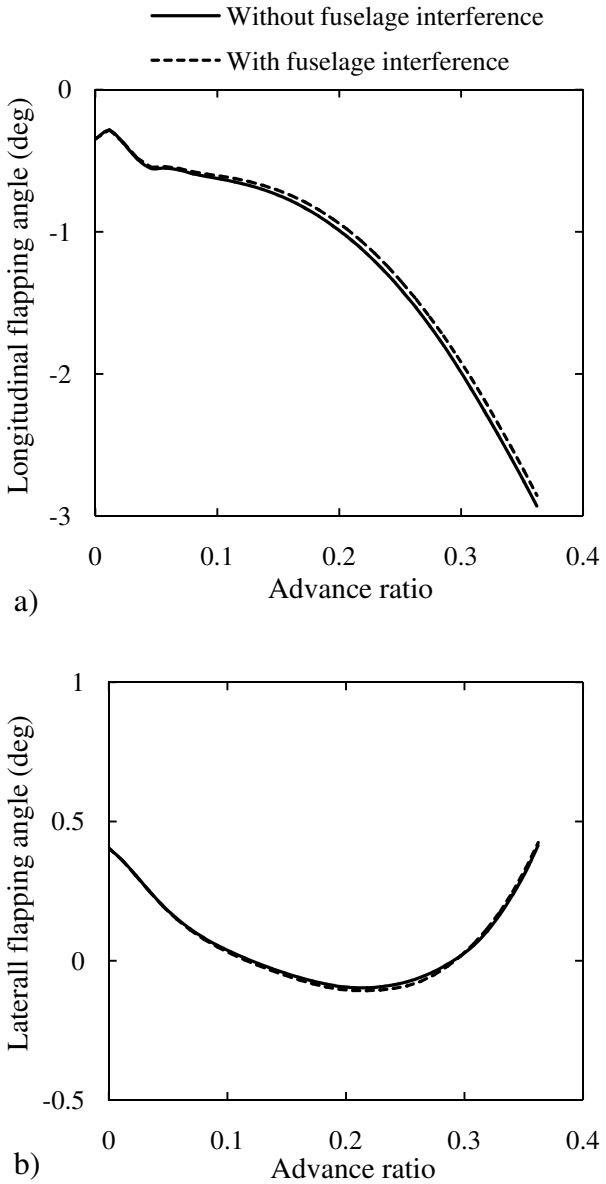

Figure 5.12: Effect of fuselage induced flow perturbations on the MBB Bo 105 helicopter trim: a) Main rotor longitudinal flapping angle β_{1c}, b) Main rotor lateral flapping angle β_{1s}

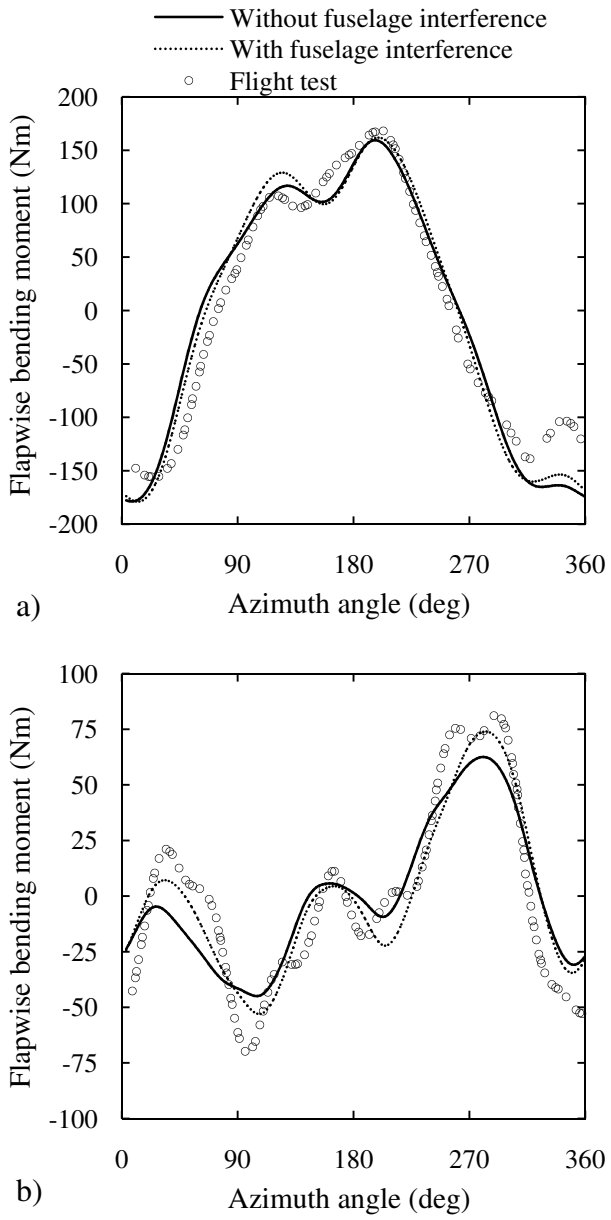

Figure 5.13: Effect of fuselage induced flow perturbations on the predicted oscillatory flapwise bending moment for $\bar{\mu} = 0.197$, $a_s = -4.0°$ – comparison with flight test data from Ref. [12]: a) r/R=0.144, b) r/R=0.57

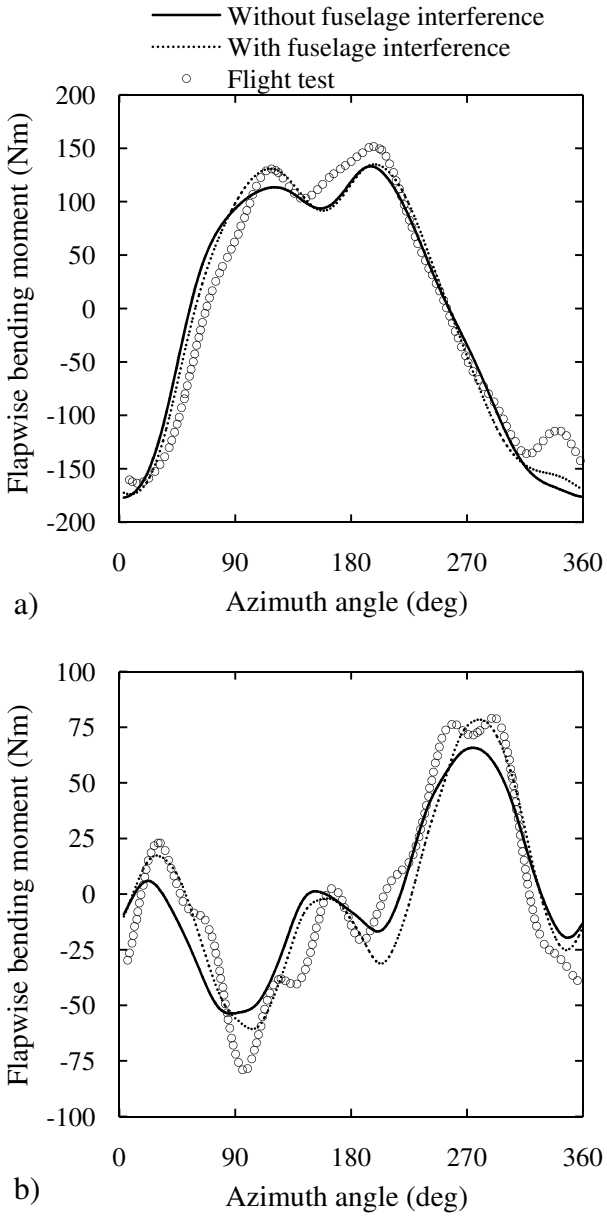

Figure 5.14: Effect of fuselage induced flow perturbations on the predicted oscillatory flapwise bending moment for $\bar{\mu} = 0.225$, $a_s = -4.8°$ – comparison with flight test data from Ref. [12]: a) r/R=0.144, b) r/R=0.57

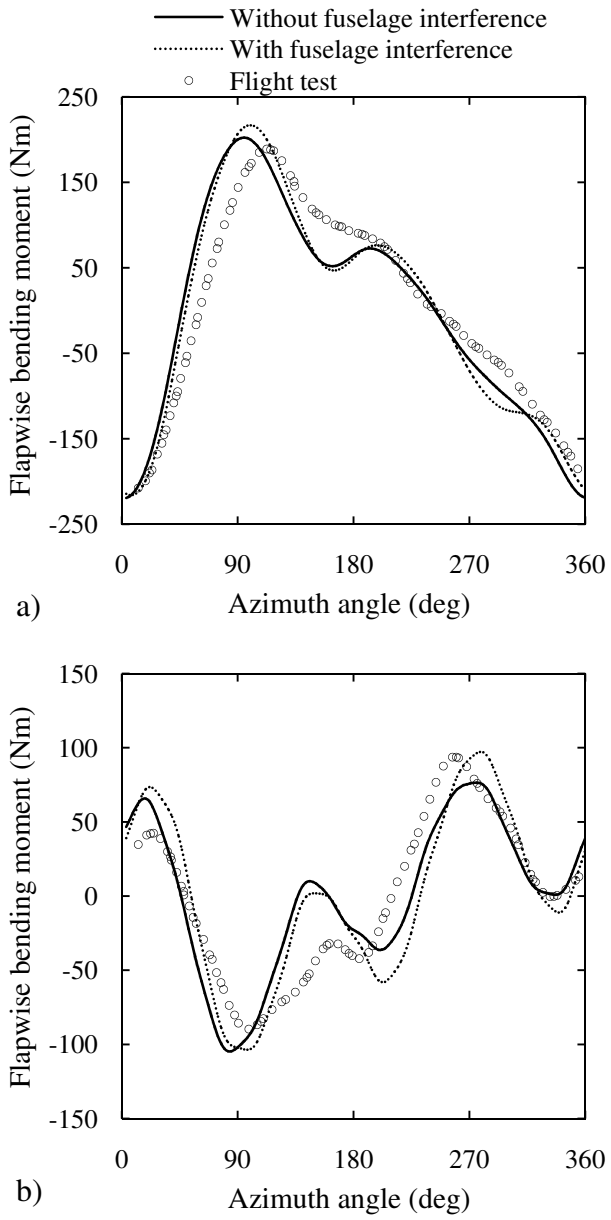

Figure 5.15: Effect of fuselage induced flow perturbations on the predicted oscillatory flapwise bending moment for $\bar{\mu} = 0.306$, $a_s = -7.7°$ – comparison with flight test data from Ref. [12]: a) r/R=0.144, b) r/R=0.57

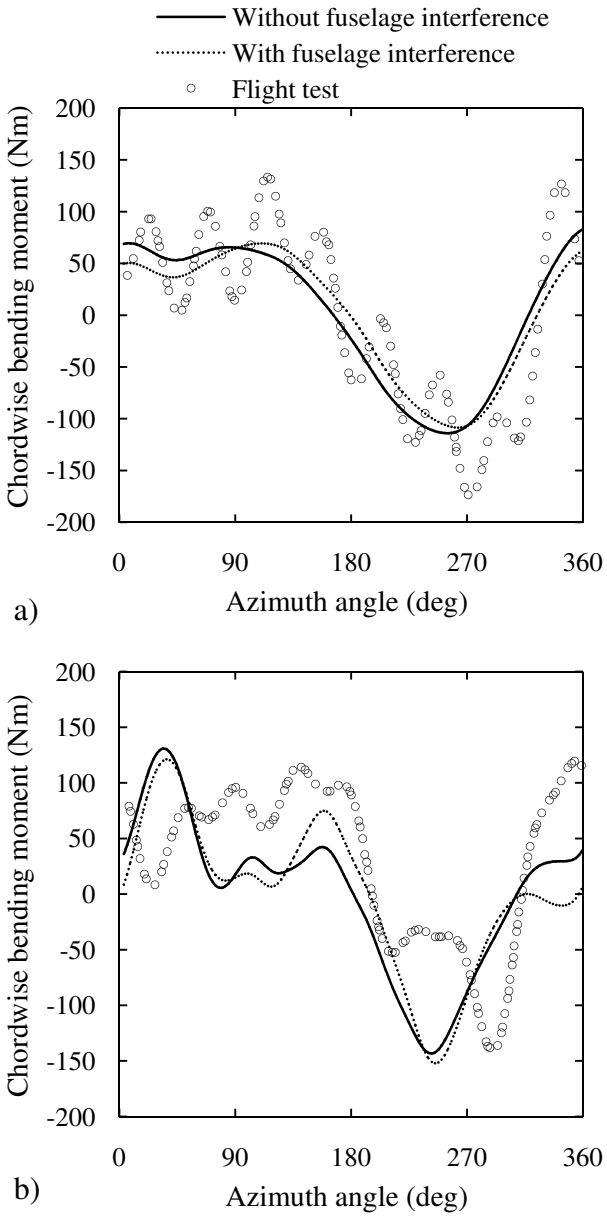

Figure 5.16: Effect of fuselage induced flow perturbations on the predicted oscillatory chordwise bending moment for $\bar{\mu} = 0.197$, $a_s = -4.0°$ – comparison with flight test data from Ref. [12]: a) r/R=0.144, b) r/R=0.45

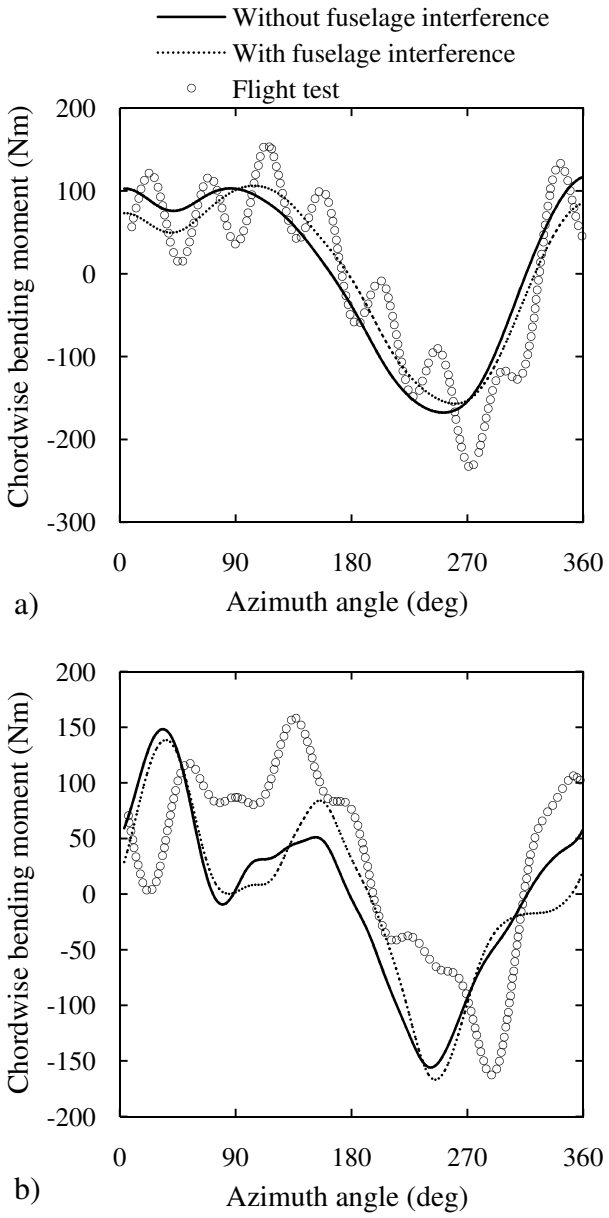

Figure 5.17: Effect of fuselage induced flow perturbations on the predicted oscillatory chordwise bending moment for $\bar{\mu} = 0.225$, $a_s = -4.8°$ – comparison with flight test data from Ref. [12]: a) r/R=0.144, b) r/R=0.45

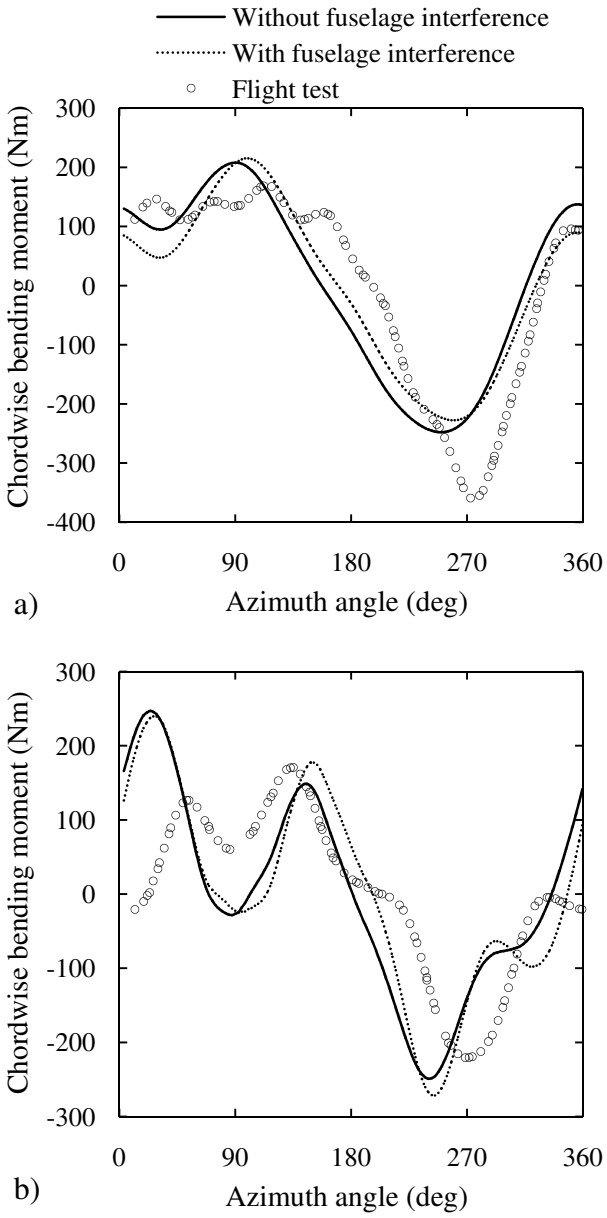

Figure 5.18: Effect of fuselage induced flow perturbations on the predicted oscillatory chordwise bending moment for $\bar{\mu} = 0.306$, $a_s = -7.7°$ – comparison with flight test data from Ref. [12]: a) r/R=0.144, b) r/R=0.45

Chapter 6

Helicopter Mission Performance Simulation using an Unsteady Aeroelastic Rotor Model

6.1 Introduction – Literature

As elaborated within the 1^{st} chapter of this Thesis, the Advisory Council for Aeronautics Research in Europe (ACARE), in an attempt to control the environmental impact of civil aviation, has set a number of objectives to be achieved by 2020. These include, among others, 50% reduction in CO_2 emissions through drastic reduction of overall fuel consumption. It has been argued however within Chapter 1 that, although the investigation of conceptual designs may not address the realization of the relatively short-termed ACARE goals, it is an effective means towards managing the environmental impact of civil aviation within larger time-scales. Therefore, the potential of incorporating conceptual–optimised aircraft designs has to be thoroughly explored. The response of the rotary-wing community needs to be a dynamic one, considering the substantial rotorcraft traffic growth that is expected over the next decade (Ref. 2)

This essentially gives birth to a fundamental requirement for a rotorcraft design assessment approach. The overall method has to be able to provide accurate estimates of total fuel consumption with regards to any designated operation in order to address the aspect of fuel economy. Considering the context of multidisciplinary rotorcraft optimisation, both comprehensiveness as well as computational efficiency are deemed as prerequisites of the employed modeling approach. As elaborated within the 1^{st} chapter of this Thesis, key design variables, which might influence the performance of a helicopter–engine system within a designated type of operation, have to be readily identifiable by the deployed formulation. An advanced level of simulation fidelity is therefore required, so that the

behavior of the associated performance trade-off between designs optimised in a multidisciplinary manner, is fairly accurately captured. The associated computational overhead however, has to be maintained within an acceptable limit thus constituting the employed approach applicable for iterative optimisation process. It is therefore understood that, an efficient compromise between modeling fidelity and computational efficiency has to be sought for.

Goulos *et al.* (Ref. [1]) described an integrated simulation framework for helicopter mission analysis based on the flight performance methodology developed in Ref. [85]. The overall approach was subsequently deployed for the optimisation of a climb profile for a generic, twin-engine medium helicopter modeled after the Eurocopter AS 332. The rather crude approximation of rotorcraft flight mechanics within the method described in Ref. [85], designated the overall approach insufficient for the task of rotorcraft design evaluation/assessment, and thus the method was abandoned.

D'Ippolito *et al.* (Ref. [2]) presented an integrated methodology for the simulation of a twin-engine light rotorcraft within a Category A take-off maneuver. Their mathematical approach included the use of the EUROPA rotorcraft code (Refs. [86], [87]) and the engine performance simulation tool GSP (Refs. [88], [89]). Goulos *et al.* (Ref. [3]) subsequently extrapolated this methodology towards the simulation and multidisciplinary optimisation of complete, three-dimensional rotorcraft operations for fuel burn, chemical emissions and ground noise impact. The EUROPA code essentially utilizes steady-state nonlinear blade element aerodynamics within a disc-like representation of the rotor disc based on rigid body dynamics. Thus, the simulation approach deployed in Refs. [2], [3] essentially belongs to the 1^{st} level of Padfield's three-fold hierarchy of simulation models (Ref. [7]). This constitutes the overall approach, inapplicable towards the task of rotor design which among others may require reasonably accurate estimates of rotor blade structural loads during flight.

In appreciation of the fundamental requirement for a simulation methodology capable of assessing rotorcraft designs within complete three-dimensional operations, a comprehensive mission analysis approach utilizing the unsteady aeroelastic rotor model described and validated in the previous chapters of this Thesis, has been developed. The proposed method is capable of assessing the helicopter's main rotor behavior at the 3^{rd} level of Padfield's hierarchical paradigm of simulation models, while simultaneously complying with the associated requirements for computational efficiency. The approach is therefore applicable to the task of rotor design and can be utilized for the investigation of conceptual configurations. The overall methodology is based upon a numerical procedure combining the individual mathematical formulations, described in the preceding chapters of this Thesis. The individual mathematical theories have been shown to effectively address the tasks of rotor blade structural analysis, treatment of main rotor blade flexibility and nonlinear flight dynamics helicopter trim with rapid execution. Within this chap-

ter, the development of a three-dimensional flight path definition method as well as the implementation of an engine performance simulation tool is also described.

The integrated methodology is applied towards the analysis of two generic helicopter operations: a Search & Rescue (SAR) and an Oil & Gas (OAG) mission. The deployed configuration model is based on the popular Aérospatiale SA 330 twin-engine medium helicopter. Extensive comparisons with flight test data on main rotor trim controls, power requirement and unsteady blade structural loads have been waged. The time-variations of various engine performance parameters during flight are presented and analyzed. The simulations carried out suggest that for the typical range of operating conditions encountered by modern twin-engine medium civil helicopters, the effect of operational altitude on fuel consumption is predominantly influenced by the corresponding effects induced on the engine rather than on airframe–rotor performance. It is shown that, thorough identification of the most power-demanding conditions within a complete helicopter operation, cannot be properly addressed without catering for an accurate prediction of the aircraft's time-dependent All Up Mass (AUM) during flight. The potential to deploy a level 3 simulation modeling approach for the evaluation of helicopter–engine integrated systems within complete, three-dimensional missions is demonstrated.

6.2 Methodology

The integrated modeling approach employed for the simulation of complete rotorcraft operations, comprises a finite series of consecutive analyses, each applicable to a different aspect of rotorcraft flight dynamics and performance. The developed simulation framework comprises the Lagrangian rotor blade modal analysis presented in chapter 3, a flight path profile analysis based on the World Geodetic System dated in 1984 (WGS 84), the nonlinear trim procedure solving for the aeroelastic behavior of the main rotor blades presented in chapter 4 and an engine off-design performance analysis (Ref. [90]). The individual modeling methodologies are combined within an elaborate integral procedure, essentially solving for the unknown initial aircraft AUM. It is noted that the initial AUM essentially comprises the helicopter's Operational Empty Weight (OEW), the unknown required mission on-board fuel supplies (F), and any necessary payload–equipment. The helicopter's OEW plus the necessary payload–equipment weight, constitute the Operational Weight (OW). The required on-board fuel supplies corresponding to the designated operation, are acquired though a fixed-point type of iteration with respect to the overall mission fuel consumption. The individual modeling methodologies are described within this section of this chapter.

6.2.1 WGS 84 flight path model

The task of simulating effectively "real world" rotorcraft mission profiles requires three-dimensional treatment (latitude, longitude, altitude) of the rotorcraft operational trajectory. For that reason, a flight path definition tool has been developed which allows for specification of a wide variety of "real world" rotorcraft operations. A complete mission is structured in terms of individual pre-defined mission task elements (MTEs). Each MTE represents a standardized helicopter procedure which is tailored according to the designated operation specifications. Examples of MTEs include idle, hover, vertical climb/descent, straight and level flight (cruise), climbing turns, take-off/landing maneuvers etc. The corresponding specification parameters may comprise climb/descent/turn rates, flight speed, flight altitude etc.

The nature of the described implementation requires an effective approach for the translation of coordinates defined in a global geographical system (latitude–longitude) to the Cartesian level. Higher order polynomial expressions have been structured, describing the mathematical correspondence of a single minute of latitude/longitude to Cartesian length in meters. The offered expressions have been derived based on the global representation employed by WGS 84 (Ref. [91]), it being the standard coordinate frame of reference considering earth geography definition. The derived polynomials are provided in 6^{th} decimal accuracy below

$$d_{lat}^{min}(x_{lat}^{\circ}) = 1.597401E-11(x_{lat}^{\circ})^6 - 5.368544E-07(x_{lat}^{\circ})^4 - 6.766806E-13(x_{lat}^{\circ})^3 + 5.606089E-03(x_{lat}^{\circ})^2 + 3.330305E-09x_{lat}^{\circ} + 1.842911E+03 \tag{6.1}$$

$$d_{long}^{min}(x_{lat}^{\circ}) = -4.682085E-11(x_{lat}^{\circ})^6 + 6.766856E-06(x_{lat}^{\circ})^4 - 2.955679E-13(x_{lat}^{\circ})^3 - 2.807881E-01(x_{lat}^{\circ})^2 + 1.439889E-09x_{lat}^{\circ} + 1.855346E+03 \tag{6.2}$$

where x_{lat}° is the latitudinal coordinate in degrees and d_{lat}^{min}, d_{long}^{min} is the Cartesian length in meters, corresponding to a minute of latitude and longitude respectively. It can be noticed from Eqs. (6.1, 6.2) that d_{lat}^{min} and d_{long}^{min} are only functions of x_{lat}°. The variations of d_{lat}^{min} and d_{long}^{min} with x_{lat}° expressed by Eqs. (6.1, 6.2), are illustrated in Figs. 6.1, a) and b) respectively. The expressions provided by Eqs. (6.1, 6.2) are utilized within the present numerical approach for the translation of coordinates from the global to the Cartesian system and vice-versa.

6.2.2 Engine performance simulation

The engine performance model (TURBOMATCH) used for the present work has been developed and refined at Cranfield University over a number of decades (Ref. [90]). Tur-

bomatch is based on zero-dimensional aero-thermodynamic analysis employing discrete component maps. The employed method essentially solves for the mass and energy balance between the various engine components. Turbomatch has been previously deployed in several studies available in the literature for the prediction of design and off-design performance of gas turbine engines (Refs. [92], [93]). For the scope of the present analysis, the engine is assumed to be operating exclusively at steady-state off-design conditions.

6.2.3 Mission breakdown

Figure 6.2 presents a flow-chart which demonstrates the numerical procedure employed for the simulation of complete rotorcraft operations. The overall process involves the break-down of each designated MTE, into discrete segments with a pre-defined time-step Δt. The helicopter is assumed to be operating in trim and the engine in steady-state off-design during each segment of duration Δt. This assumption is valid, considering that the primary focus of the structured numerical approach is the estimation of the total mission fuel consumption.

Figure 6.2 shows that the mission analysis process is initiated ($n = 1$) with a user-defined guess as regards the overall mission fuel consumption. The initial rotorcraft AUM is subsequently determined based on that initial guess of the on-board fuel supplies. Depending on the mission definition and the corresponding segment time-point t, the flight path model determines the helicopter flight conditions in terms of altitude, flight speed, flight path angle and turn rate. The nonlinear rotorcraft trim model subsequently trims the helicopter, thus determining among others, the engine shaft power requirements. The engine performance model subsequently establishes the engine operating point based on the power requirements and the corresponding inlet conditions. Therefore, the engine fuel flow is determined among other off-design performance parameters. The time-dependent fuel consumption corresponding to time-point t, is calculated by applying a numerical time integration scheme over the mission segments corresponding to $0 \leq \tau \leq t$. This value is subtracted from the initial AUM at time t in order to simulate the helicopter's gradual weight reduction during the course of the mission. The helicopter's spatial location is also updated based on the flight conditions dictated by the flight path model.

Having completed a first-pass ($n = 1$) along the entire mission, the estimated value of total fuel consumption (F_n) is compared with the initial fuel burn guess (F_1). If the obtained error is within a user-defined tolerance, the process is halted. In the case that the acquired error exceeds the defined tolerance, the rotorcraft initial AUM is updated based on the calculated total mission fuel consumption F_n. The overall process is re-iterated in a fixed-point manner until the following convergence criterion is met

$$\left| \frac{F_n}{F_{n-1}} - 1 \right| \leq \epsilon \tag{6.3}$$

where n and ϵ signify the mission fuel burn iteration index and numerical error tolerance respectively.

6.3 Results & Discussion

The aircraft selected for the case study presented in this chapter, has been modeled after the Aérospatiale SA 330 Puma. The SA 330 is a twin-engine medium helicopter equipped with two Turbomeca Turmo IVC turboshaft engines rated at 1163 kW maximum contingency power. Table 6.1 presents the main rotorcraft design parameters. The Turmo IVC engine is equipped with a single-spool gas generator including a single-stage axial followed by a centrifugal compressor. The engine configuration is outlined in Table 6.2. The maximum contingency power setting has been selected as the design point for the respective Turbomatch model. The model has been matched at design point conditions with public domain data in terms of Specific Fuel Consumption (SFC) with an accuracy of 0.3%.

The configuration of the SA 330 as well as its performance characteristics have been extensively documented and analyzed in Refs. [94], [7], thus further elaborations shall be omitted. A detailed decription of the Turbomeca Turmo engine family can be found in Ref. [95].

6.3.1 Rotor blade modal analysis

Figure 6.3 presents the calculated rotor resonance chart for the full-scale, articulated rotor of the SA 330 helicopter using the Lagrangian approach presented in Ref. [96]. The specific articulated rotor design has been extensively described in Ref. [94], thus further discussion on the rotor configuration shall be omitted. Simulation results from CAMRAD (Refs. [57], [58]) with regards to flap and lag bending frequencies at nominal rotorspeed are also included. The natural frequency predictions made with CAMRAD have been extracted from Ref. [94]. The solid and broken lines correspond to the Lagrangian method predictions (Lagr.) while the markers signify CAMRAD calculations.

Good agreement between the Lagrangian method and CAMRAD simulations can be observed with respect to the predicted flap (1F – 3F) and lag resonant (1L – 2L) frequencies at nominal rotorspeed ($\Omega = 27\, rad/sec$). The corresponding normalized mode shapes obtained from the Lagrangian approach are shown in Figs. 6.4, a) and b) for flap and lag motion respectively. The acquired modal characteristics are utilized within the remainder of this chapter for the approximation of the blade's dynamic response to any aerodynamic or inertial blade excitation.

6.3.2 Helicopter flight dynamics trim analysis

Figures 6.5, 6.6 present trim controls and power requirement predictions for the main rotor based on simulations performed for the SA 330 helicopter for straight and level flight. The corresponding rotorcraft design parameters are provided in Table 6.1. The numerical formulation described in section "Integrated aeroelastic rotor – aircraft model" within chapter 4, has been utilized in order to obtain trim solutions based on the unsteady, aeroelastic behavior of the articulated rotor. Results are presented as functions of advance ratio $\mu = \frac{V}{\Omega R}$ from hover ($\mu = 0$) to high-speed flight ($\mu \approx 0.4$). Comparisons with flight test data extracted from Ref. [94] have also been included for validation purposes.

Figures 6.5, a) and b) present trim values of main rotor power requirement P_{rotor} and collective pitch angle θ_0 respectively. Good correlation between the integrated model predictions and flight test data can be observed regarding both trim outputs. Agreement is best for $\mu \geq 0.15$ where the flow-field in the vicinity of the main rotor begins to be dominated by the free-stream component. Small discrepancies between predictions and experimental data are noted with respect to $\mu \leq 0.15$ considering both trim outputs. This indicates a potential overestimation of the induced losses at low-speed flight conditions.

Figures 6.6, a) and b) present trim values of lateral (θ_{1s}) and longitudinal (θ_{1c}) cyclic pitch angles respectively. Fair agreement is observed between the deployed model predictions and flight test data considering both cyclic control inputs within the entire range of advance ratios. The performed simulations suggest that rotor wake impingement on the horizontal stabilizer occurs for $\mu \geq 0.15$ leading to large positive pitching moments. The control system thus compensates with a corresponding decrease in the lateral cyclic pitch control angle θ_{1s}. The flight test data suggest that rotor wake impingement interaction begins for lower advance ratios ($\mu \geq 0.1$), since no corresponding increase is observed in θ_{1s} for $\mu \geq 0.1$. A noticeable deviation between the predicted and measured longitudinal cyclic pitch angle (θ_{1c}) for $\mu \leq 0.15$ reveals the requirement for more sophisticated wake modeling with regards to the transitional flight region ($0 \leq \mu \leq 0.15$). The strong influence of the wake roll-up on the main rotor induced flow within the transition region, is not accounted for by the Peters – He inflow model which essentially models a prescribed, cylindrical wake. This deficiency leads to the underprediction of θ_{1c} at lower advance ratios as observed in Fig. 6.6, b).

6.3.3 Unsteady rotor blade structural loads prediction

Figures 6.7 – 6.9 present correlations between predictions made with the present aeroelastic rotor model and flight test measurements of unsteady flapwise and chordwise bending moments for the full-scale articulated rotor of the SA 330 helicopter. Results are presented for $\mu = 0.307$ and $\mu = 0.321$. The simulations correspond to trim solutions obtained for

the respective values of advance ratio using the trim model described in section "Integrated aeroelastic rotor – aircraft model" of chapter 4. Comparisons of flapwise bending moment are presented for two blade radial locations corresponding to $r/R = 0.35$ and $r/R = 0.55$ respectively. Chordwise bending moment correlations are presented for $r/R = 0.73$. The presented flight test data have been extracted from from Ref. [94].

Figures 6.7 – 6.8 present simulations and measurements of unsteady blade flapwise bending moment for $\mu = 0.307$ and $\mu = 0.321$ respectively. Results are presented for $r/R = 0.35$ (Figs. 6.7, a) & b)) and $r/R = 0.55$ (Figs. 6.8, a) & b)). Good correlation can be observed between predictions and flight tests with respect to both radial locations and both values of advance ratio. Agreement is best for $\mu = 0.307$ where the behavior of 3P and 4P oscillatory loading is accurately predicted, both in terms of magnitude and phase considering both radial locations.

Figures 6.9, a) and b) present correlations between simulations and measurements of unsteady blade flapwise bending moment for $\mu = 0.307$ and $\mu = 0.321$ respectively. Results are presented for $r/R = 0.73$. The agreement can be considered fair in the sense that the overall magnitude of the oscillatory waveform has been captured by the modeling approach. The higher frequency components of the waveform do not appear to have been accurately predicted. The larger discrepancies with regards to the predictions of chordwise bending moment compared to the flap bending case, are attributed to insufficiently accurate aerofoil data with respect to drag coefficients for higher values of Mach number.

A similarity between flapwise and chordwise bending moment waveforms is noted. This is due to the coupling between flap/chord moments and flap/lag bending motion. The coupling occurs through the application of collective and cyclic pitch. As the pitched blade essentially flaps upwards, a deformation component is accounted for as chordwise deformation as well. The same applies for flap bending moment.

6.3.4 Engine performance trim analysis

Figures 6.10 – 6.11 present the respective engine performance parameters as functions of advance ratio. The operating conditions correspond to the flight dynamics trim analysis presented in the respective section of this chapter. Results are presented for atmospheric conditions of zero ISA deviation, at an absolute altitude of 100 m. The intake mach number M_{intake} is essentially defined by the designated advance ratio μ.

It is shown that, all of the presented engine performance parameters, essentially follow the classic "bucket-shape" curve which is dictated by the power requirement of the main rotor as shown in Fig. 6.5, a). It is noted that the tail-rotor power requirements, which are included in the produced engine shaft power (Fig. 6.10, a)), follow a similar "bucket-shape" curve. They are however relatively small compared to P_{rotor} (10% at hover, reducing to 5% approximately in forward flight), which makes the engine shaft power function P_{engine}

(Fig. 6.10, a)) look very similar to the main rotor power function P_{rotor} (Fig. 6.5, a)).

It is noted that a small ram compression effect on engine performance is present in the results presented in Figs. 6.10 – 6.11. It is shown in Fig. 6.10, a), that the required engine shaft power P_{engine} is roughly 500 kW for $\mu = 0$ as well as for $\mu \approx 0.32$. The latter value of μ corresponds to $M_{intake} \approx 0.2$ which essentially leads to an increase of inlet total pressure of the order of 2.7% due to ram compression. The predicted change in maximum engine pressure is around 0.5% upwards. The overall pressure ratio produced by the compressors however, is reduced by approximately 2.1% leading to a corresponding decrease in compressor work. It is noted that ram temperature rise may increase the compressor work for a given pressure ratio. With regards to the designated operating conditions and engine configuration however, the former effect is predominant leading to a reduction to the power absorbed from the gas generator turbine for compression. The effects described above lead to a combined rise in engine thermal efficiency of the order of 1.44%.

The corresponding increase in air mass flow W due to ram compression is of the order of 0.94%. The aforementioned effects of ram compression at the intake, essentially lead to a reduction in engine fuel flow and SFC of the order of 1.5% for $\mu = 0.32$ in comparison to the hovering case ($\mu = 0$) while maintaining identical power output P_{engine}.

6.3.5 Helicopter mission analysis

Two generic, three-dimensional missions, representative of modern twin-engine medium helicopter operations have been defined: a search & rescue (SAR) and an oil & gas (OAG) mission. The incorporated operational procedures in terms of geographical location selection, deployed airspeed, altitude, climb/descent rates and idle times have been defined in collaboration with the European Helicopter Operator's Committee (EHOC). The geographical representation of the missions is illustrated in Figs. 6.12, a) and b) in terms of global coordinates.

The SAR mission schedule assumes that the helicopter takes-off from Stockholm Arlanda airport in Sweden and subsequently travels towards a designated location above the Baltic Sea. The helicopter is then assumed to engage in a search pattern in order to trace and pick up citizens in distress from a location corresponding to an assumed naval incident. After successfully locating the citizens in distress, the helicopter SAR crew picks them up while the helicopter is hovering over the imaginary incident zone. The patients are then transported to Högbergsgatan hospital where the helicopter lands on the respective helipad where it drops-off the patients and subsequently returns to Stockholm Arlanda airport. The OAG mission schedule assumes that the helicopter takes-off from De Kooy airfield in Den Helder, Netherlands, while carrying a specified payload. The helicopter subsequently travels towards a designated offshore oil/gas platform (oil rig 1)

located in the North Sea where it lands and drops-off the on-board payload. The helicopter then travels towards a second offshore oil/gas platform (oil rig 2) where it picks-up another useful payload and subsequently returns to the original De Kooy airfield in Den Helder.

The implemented operational procedures are outlined in Tables 6.3, 6.4 for the SAR and OAG mission respectively. A time-step Δt of 5 *secs* is used for the each individual mission segment. All coordinated turns are executed with a turn rate of $5°/sec$, with the exception of fine tuning the helicopter's orientation where the turn rate is defined based on the orientation error and the mission time-step Δt. During idle operation, the overall helicopter power requirements are assumed to be equal to 20% of maximum contingency engine shaft power.

Figures 6.13, 6.14 present the time variations of the helicopter's AGL altitude and flight speed for the SAR and OAG mission respectively. The variations presented are essentially based on the incorporated operational procedures outlined in Tables 6.3, 6.4. As regards the SAR mission, Fig. 6.13 shows that the helicopter spends almost half of the mission time engaged in the SAR pattern where the deployed flight speed and AGL altitude is $30\,m/sec$ and $60\,m$ respectively. With respect to the OAG operation, it can be observed that the overall mission comprises 3 cruise task elements. The second cuise element is a relatively short one, since the two oil rigs are located within a distance of only 8.6 km.

The performance of the integrated helicopter–engine system is assessed throughout the course of both missions using the integrated methodology described in section "Mission breakdown" of this chapter, applied to the Aérospatiale SA 330 configuration (Tables 6.1, 6.2). The total parameters in terms of range, time and fuel consumption are outlined in Table 6.5 for both missions. It is noted that, a comparison of the calculated mission range using the flight path model described in section "WGS 84 flight path model" with calculations performed using the virtual globe/geographical information program "Google earth", revealed a relative error of the order of 0.05% and 0.1% for the SAR and OAG missions respectively. This indicates the very good predictive qualities of the polynomial expressions provided by Eqs. (6.1, 6.2).

Figures 6.15 – 6.17 and 6.18 – 6.20 demonstrate the variation of various engine performance parameters as functions of mission time for the SAR and OAG missions respectively. The idle segments can be distinguished as conditions associated with low values of engine shaft power, fuel flow, and SOT but relatively high SFC. Climbing forward flight along with hover, are identified as the most demanding trim settings in terms of engine shaft power as shown in Figs. 6.15, 6.18, a).

For identical atmospheric conditions, the relationship in terms of rotor power requirement between hover and climbing forward flight, depends on the aircraft AUM. A large AUM, due to either on-board fuel supplies or useful payload, essentially requires higher

main rotor thrust settings. This results in increased rotor induced flow, hence induced losses. With respect to hovering conditions, the main rotor power requirement is essentially dominated by the induced losses. At higher values of advance ratio however, the rotor induced flow is significantly reduced and thus the additional induced losses associated with a larger aircraft AUM have a smaller impact on aircraft performance. Therefore, a large AUM may impose a more significant penalty on the rotor power requirement in hover, rather than climbing or forward flight, due to the associated reduction in mean induced flow.

This behavior is shown in Fig. 6.15, a) with respect to the SAR mission. The power requirement for hover is larger than for climbing forward flight as regards the first hover task element, where the aircraft AUM comprises, among others, the entire mission onboard fuel supplies. This is not the case however as regards the second and third hover task elements, within which the AUM has been significantly reduced due to the helicopter's fuel consumption. A similar behavior is observed for the OAG mission in Fig. 6.18, a). It is therefore understood that, thorough identification of the most power-demanding conditions within a complete rotorcraft operation, cannot be properly addressed without catering for an accurate prediction of the aircraft's time-dependent AUM during flight. This signifies the necessity for accurate estimation of the interrelationship between engine and helicopter performance throughout the course of the designated operation, due to their implicit coupling through the aircraft AUM. The significance of the numerical procedure presented in section "Mission breakdown" of this chapter, with respect to the accurate estimation of an initial aircraft AUM is also emphasized.

It is noted that, with the exception of the second hover task element of the SAR mission, hover takes place within an effective ground influence as regards both missions. The effective distance of the rotor disc from the ground during IGE hover, is roughly 80% of rotor radius. The respective reduction in mean induced inflow is around 11% (Ref. [97]), leading to a corresponding decrease in induced losses. Despite the beneficial ground effect however, Figs. 6.15, 6.18, a) show that hovering flight is still among the flight conditions with the highest power requirement for to both missions.

An interesting behavior is observed with respect to climbing/descending forward flight, as regards both designated operations. Figures 6.15, 6.18, a) show that during climb, there is a gradual increase in engine shaft power. This is due to the gradual decrease in air density, leading to increased induced flow through the main rotor disc with a corresponding rise in induced losses. This is not the case however with respect to fuel flow as shown in Figs. 6.15, 6.18, b). Fuel flow is actually shown to decrease with altitude, despite the rise in engine shaft power. This is attributed to the gradually decreasing ambient temperature which gives rise to an increased referred rotational speed $\frac{N_1}{\sqrt{T_1/T_0}}$, $N_1 = constant$, $T_0 = 288.15\ K$ (N_1 and T_1 being the LPC rotational speed and

inlet temperature respectively). This essentially leads to increased values of OPR and SOT (Figs. 6.16, 6.19, a)) which combine to increase the engine thermal efficiency and thus decrease the overall SFC (Figs. 6.16, 6.19, b)). Thus, the favorable altitude effect on engine thermal efficiency, dominates the penalizing influence on helicopter performance, leading to an overall reduction in required fuel flow. The reverse behavior is observed for descending forward flight.

It is interesting to note the magnitude of the helicopter's gradual weight reduction effect due to the associated fuel consumption, on the on the engine shaft power requirement as well as on the various engine performance parameters presented for both missions. This essentially indicates once again the importance of accurately estimating the initial aircraft AUM. This aspect is especially significant for long-range missions where the large weight of the on-board fuel supplies can influence the calculation of the overall mission fuel consumption considerably. It is understood that, overestimation of the on-board fuel supplies may lead to a penalty in fuel consumption, while underestimation may render the designated mission unfeasible. It can thus concluded that, correct prediction of the overall mission fuel consumption ahead of flight, is also a key parameter in addressing the aspect of mission fuel economy.

Figures 6.17, 6.20 present the LPC and HPC operating points during the course of SAR and OAG mission respectively. It is observed that both LPC and HPC operating points are located within a well-defined region of representative running lines for both operations. This is due to the fact that the engine essentially encounters a relatively low range of mach numbers ($0 \leq M_{intake} \leq 0.2$) within the operational envelope defined by a typical twin-engine medium helicopter mission. Therefore, the location of the operating points within the corresponding compressor map is predominantly affected by the engine shaft power. Thus, the LPC and HPC operating points within a generic helicopter mission are found to be closely spaced around the region defined by the typical engine running line for sea-level static conditions.

6.4 Conclusions

A comprehensive helicopter mission analysis approach utilizing an unsteady aeroelastic rotor model has been presented. The proposed method has been shown to be capable of performing flight dynamics assessments at the 3^{rd} level of Padfield's hierarchy of simulation models, while simultaneously catering for a reduced computational overhead. The approach is therefore applicable to the task of rotor design, and therefore to the investigation of conceptual configurations. The integrated approach has been successfully applied towards the performance analysis of a twin-engine medium helicopter, modeled after the Aérospatiale SA 330. Good agreement has been shown between predictions and flight test measurements with regards to main rotor trim controls, power requirements and unsteady

blade structural loads. The performance of the integrated helicopter–engine system within two generic helicopter missions, representative of modern twin-engine medium rotorcraft operations has been analyzed.

The simulations carried out suggest that, for the range of operating conditions encountered by modern twin-engine medium rotorcraft, the favorable altitude effect on engine thermal efficiency, dominates over the respective penalizing influence on helicopter performance. It has been argued that, thorough identification of the most power-demanding conditions within a complete helicopter operation, cannot be properly addressed without catering for an accurate prediction of the aircraft's time-dependent AUM during flight. It has been demonstrated that correct estimation of the overall mission fuel consumption ahead of flight, is a key parameter in addressing the aspect of mission fuel economy. The LPC and HPC operating points within a generic twin-engine medium helicopter mission, have been found to be closely spaced around the region defined by the typical engine running line for sea-level static conditions. The potential to deploy a level 3 simulation modeling approach using rapid estimation methods, for the evaluation of helicopter–engine integrated systems within complete three-dimensional missions, has been demonstrated.

Table 6.1: SA 330 rotorcraft model design parameters.

Design parameter	Value	Units
OEW	3536	kg
OW	5805	kg
Number of blades	4	–
Blade radius	7.53	m
Blade chord	0.54	m
Blade twist	0.14	rad
Rotorspeed	27	rad/sec

Table 6.2: Turbomeca Turmo IVC engine model parameters at design point.

Design parameter	Value	Units
Max contingency shaft power (P_{engine})	1163	kW
LPC pressure ratio (Single-stage axial)	1.2	–
HPC pressure ratio (Centrifugal)	4.83	–
Overall pressure ratio (OPR)	5.8	–
Air mass flow (W)	5.9	kg/sec
Stator outlet temperature (SOT)	1308	K
Combustor fuel to air ratio (FAR)	0.022	–
Specific fuel consumption (SFC)	$107.06 \cdot 10^{-9}$	kg/J

Table 6.3: SAR mission specification parameters.

MTE	Airspeed (m/sec)	Altitude AGL – final (m)	Climb rate (m/sec)
Idle (5 *mins*)	0	0	0
Hover IGE (1 *min*)	0	0	0
Climb	40	600	5
Cruise	60	600	0
Descent	50	60	-3.8
Search pattern – cruise	30	60	0
Hover IGE (2 *mins*)	0	60	0
Climb	40	600	5
Cruise	60	600	0
Descent	50	0	-3.8
Idle (1 *min*)	0	0	0
Hover (1 *min*)	0	0	0
Climb	40	600	5
Cruise	60	600	0
Descent	50	0	-3.8
Idle (1 *min*)	0	0	0

Table 6.4: OAG mission specification parameters.

MTE	Airspeed (m/sec)	Altitude AGL – final (m)	Climb rate (m/sec)
Idle (5 *mins*)	0	0	0
Hover IGE (1 *min*)	0	0	0
Climb	40	900	5
Cruise	60	900	0
Descent	50	0	-3.8
Idle (10 *mins*)	0	0	0
Hover IGE (1 *min*)	0	0	0
Climb	40	300	5
Cruise	50	300	0
Descent	50	0	-3.8
Idle (1 *min*)	0	0	0
Hover IGE (1 *min*)	0	0	0
Climb	40	900	5
Cruise	60	900	0
Descent	50	0	-3.8
Idle (1 *min*)	0	0	0

Table 6.5: Total mission parameters.

Mission parameter	SAR	OAG	Units
Range	370.1	206.8	km
Time	8660	4935	sec
Total fuel consumption	1022.2	551.1	kg

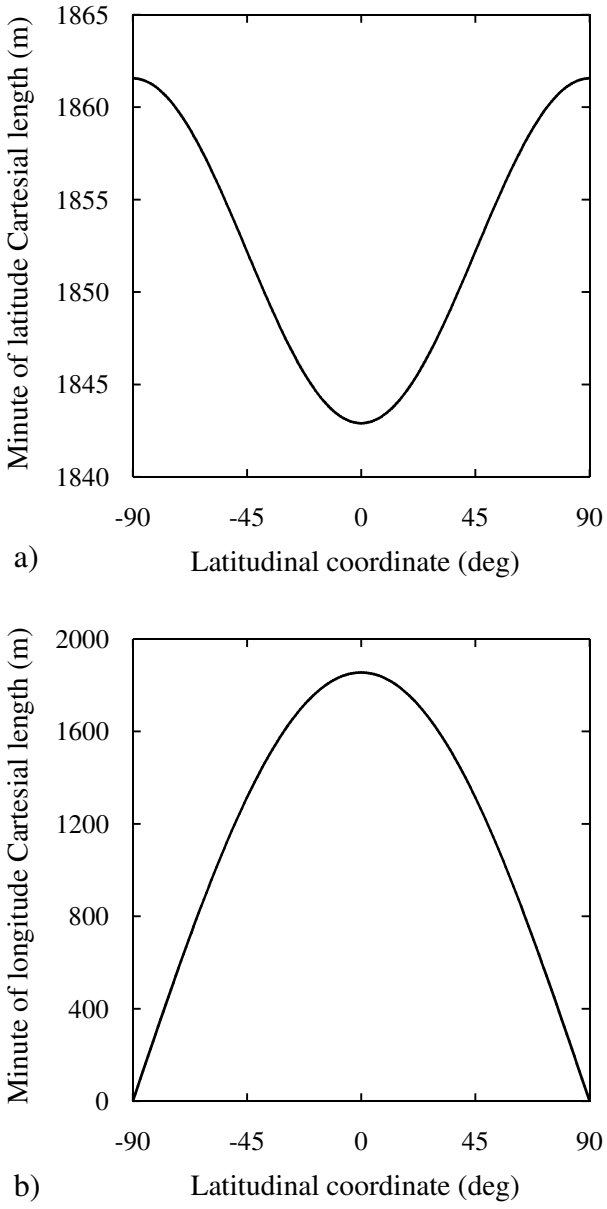

Figure 6.1: WGS 84 based polynomial variations: a) Cartesian distance corresponding to a minute of latitude d_{lat}^{min} as a function of the latitudinal coordinate x_{lat}°, b) Cartesian distance corresponding to a minute of longitude d_{long}^{min} as a function of the latitudinal coordinate x_{lat}°

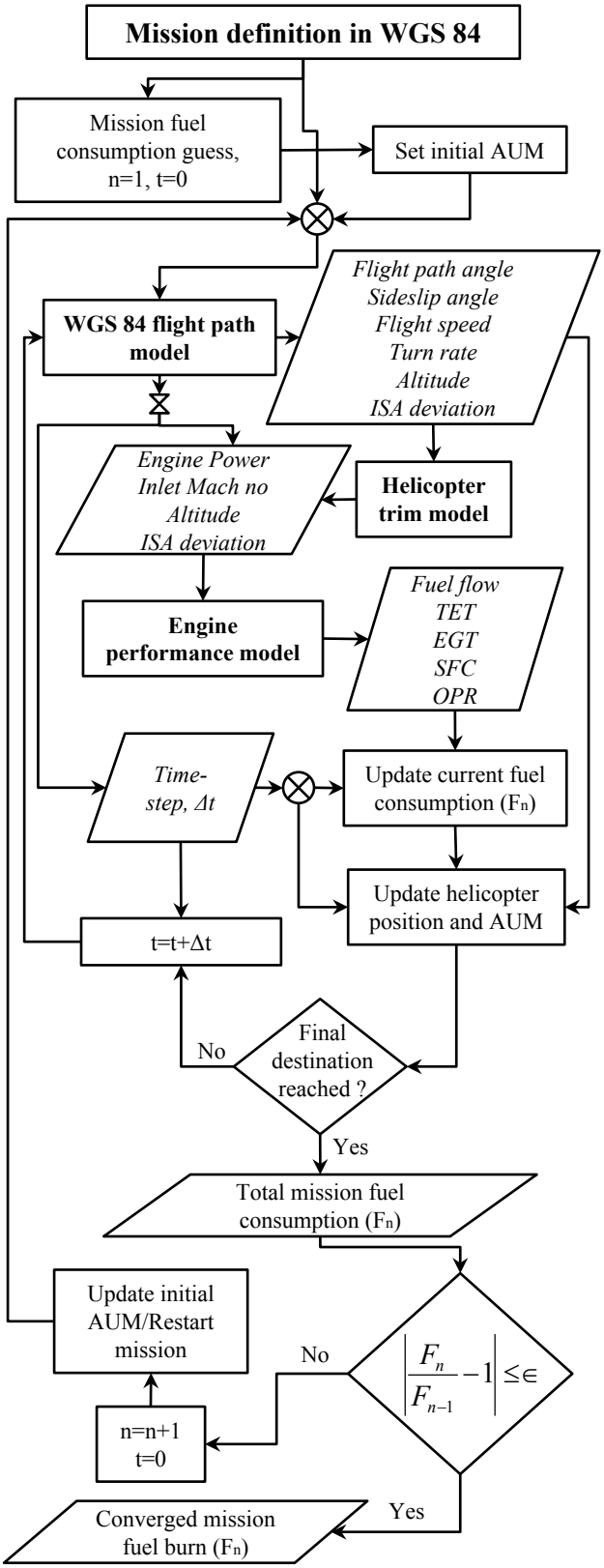

Figure 6.2: Integrated mission analysis numerical procedure flow-chart

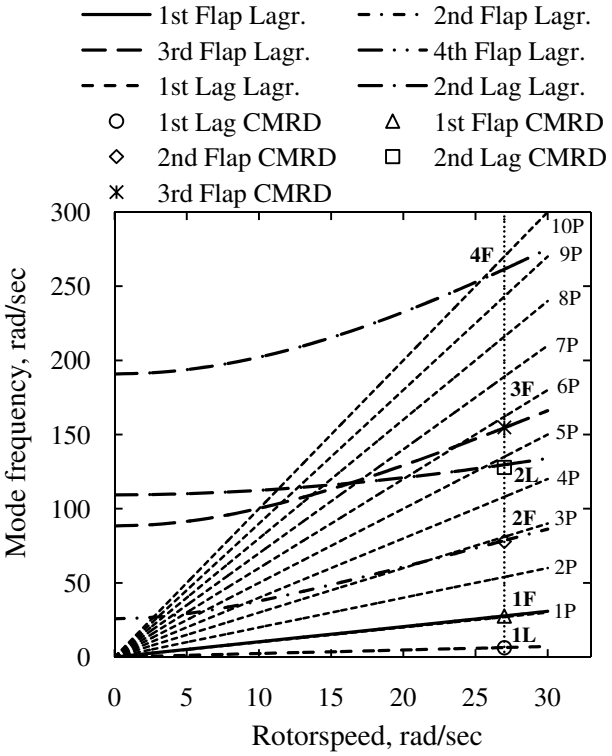

Figure 6.3: Resonance chart for the SA 330 helicopter main rotor – Comparison with CAMRAD results from Ref. [94]

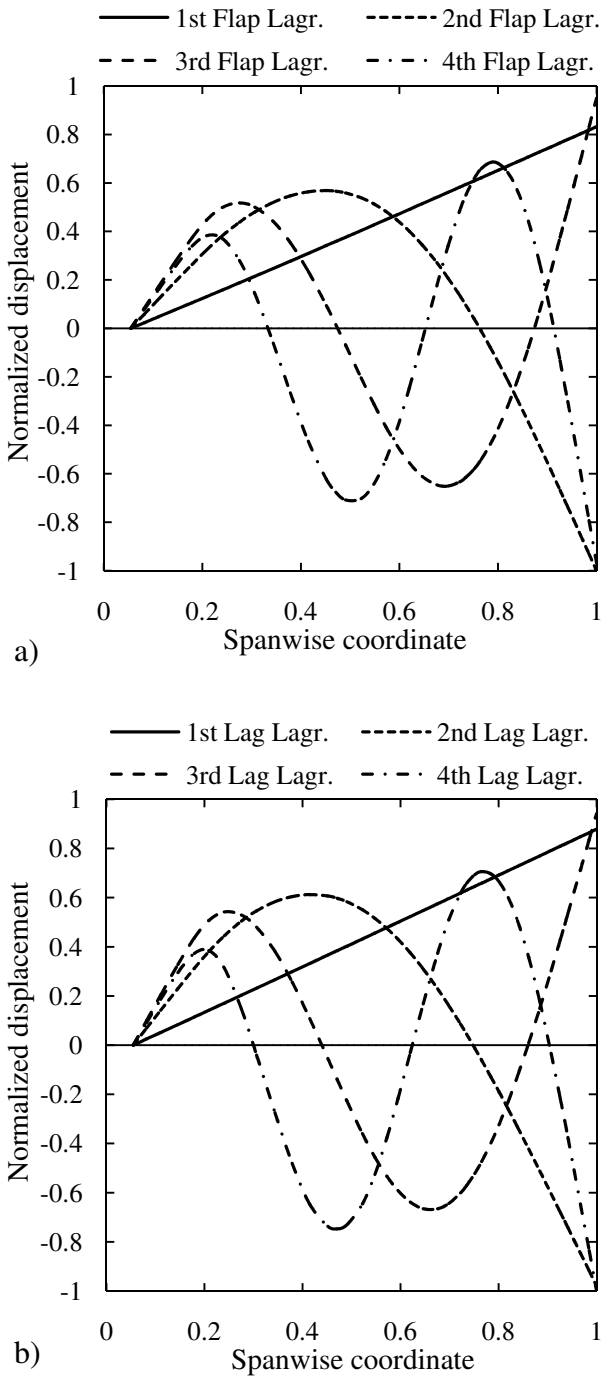

Figure 6.4: Normalized mode shapes for the SA 330 helicopter articulated rotor: a) Flap modes, b) Lag modes

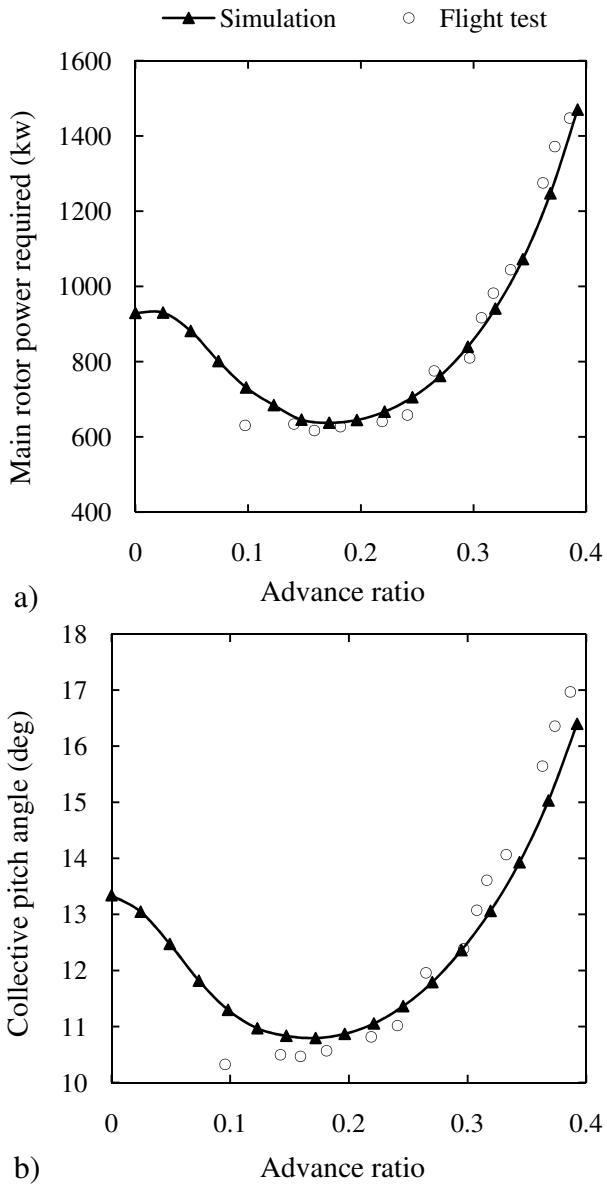

Figure 6.5: Flight dynamics trim results for the SA 330 helicopter – comparison with flight test data extracted from Ref. [94]: a) Main rotor power required P_{rotor}, b) Collective pitch angle θ_0

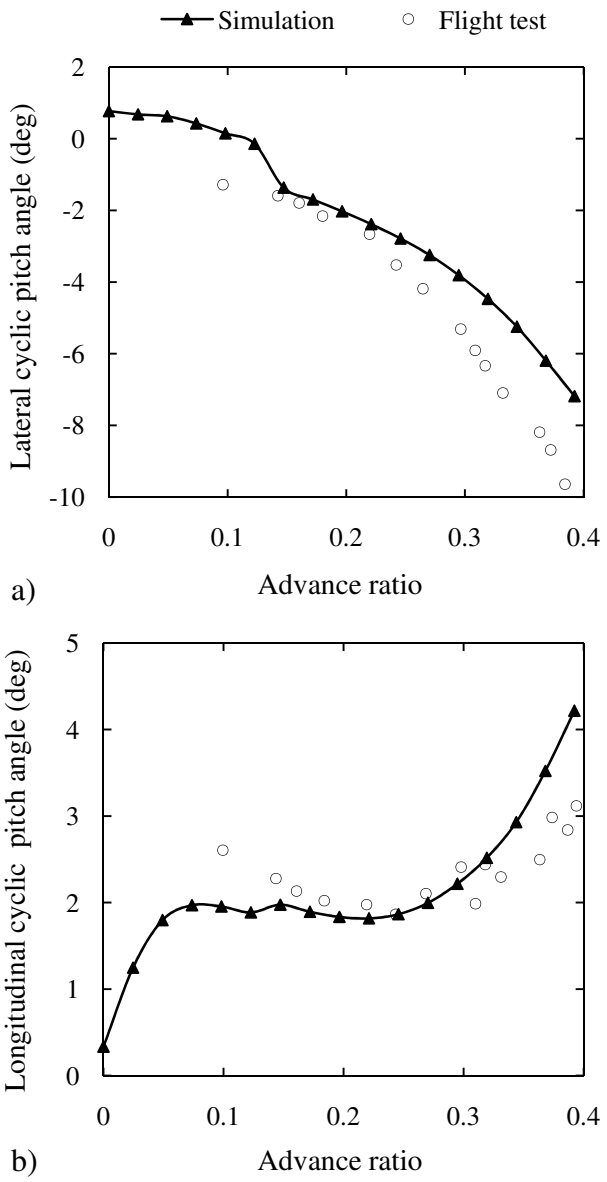

Figure 6.6: Flight dynamics trim results for the SA 330 helicopter – comparison with flight test data extracted from Ref. [94]: a) Lateral cyclic pitch angle θ_{1s}, b) Longitudinal cyclic pitch angle θ_{1c}

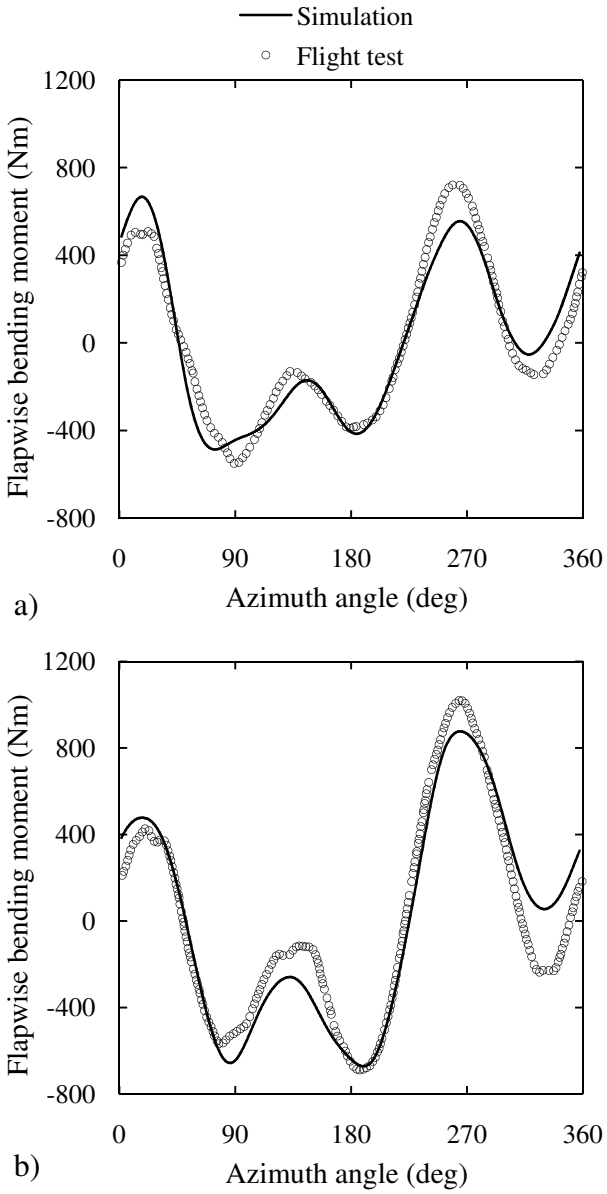

Figure 6.7: Unsteady flapwise blade bending moment for the SA 330 helicopter rotor, $\mu = 0.307$ – comparison with flight test data extracted from Ref. [94]: a) $r/R = 0.35$, b) $r/R = 0.55$

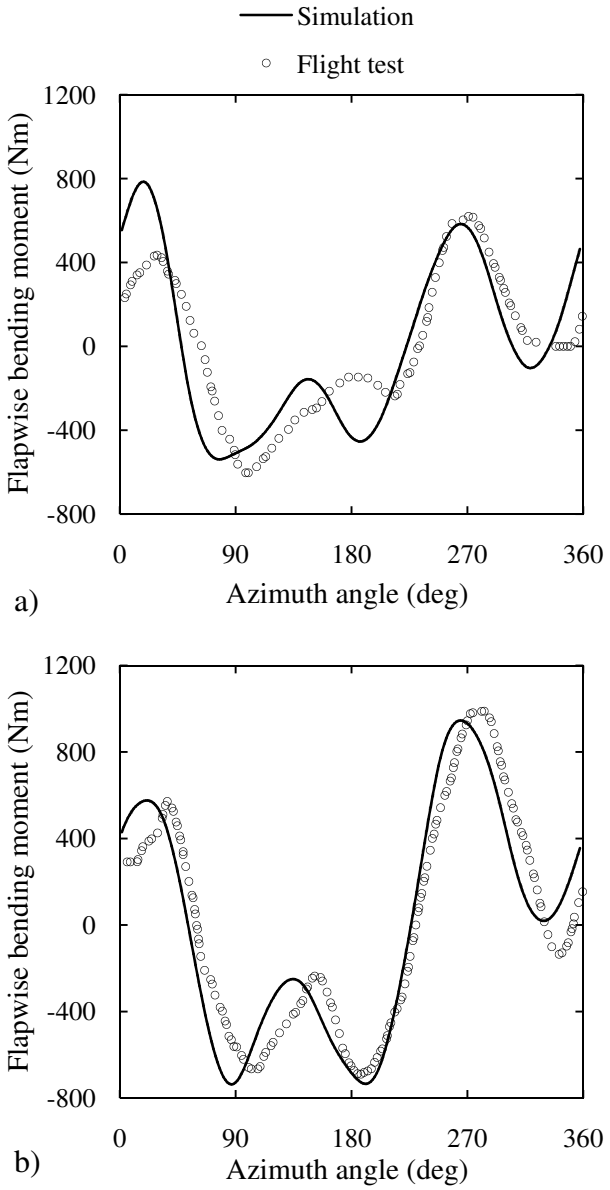

Figure 6.8: Unsteady flapwise blade bending moment for the SA 330 helicopter rotor, $\mu = 0.321$ – comparison with flight test data extracted from Ref. [94]: a) $r/R = 0.35$, b) $r/R = 0.55$

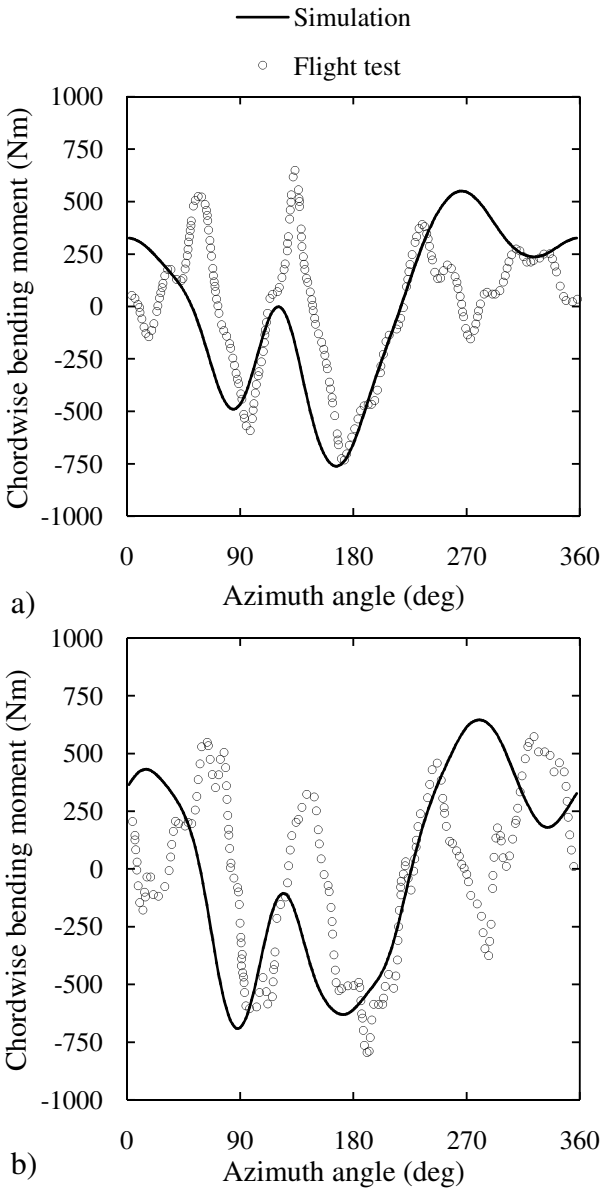

Figure 6.9: Unsteady chordwise blade bending moment for the SA 330 helicopter rotor, $r/R = 0.73$ – comparison with flight test data extracted from Ref. [94]: a) $\mu = 0.307$, b) $\mu = 0.321$

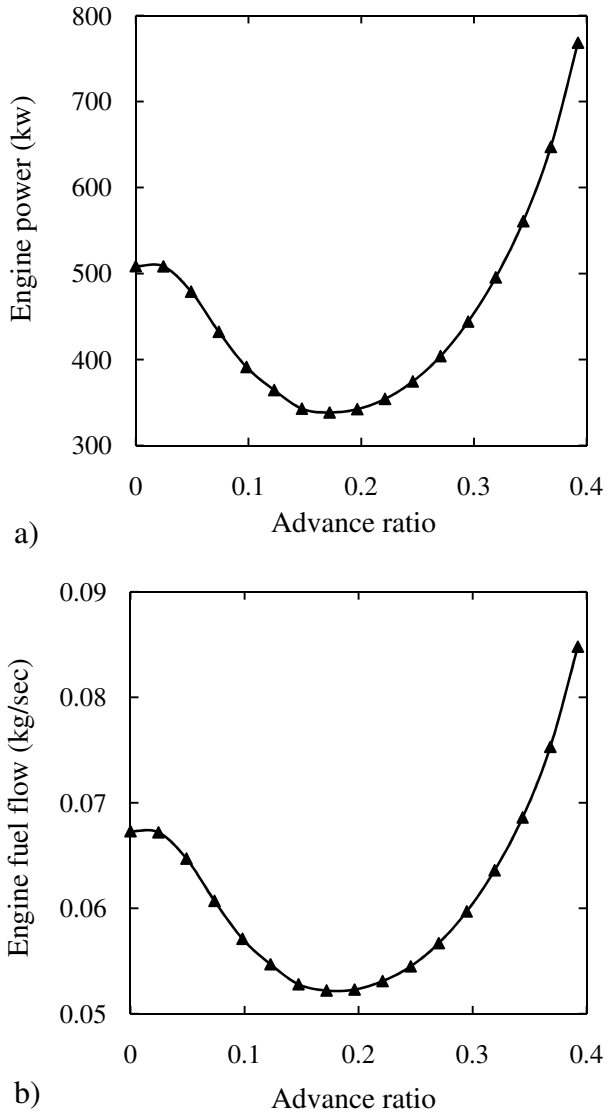

Figure 6.10: Engine performance trim results for the SA 330 helicopter: a) Shaft power P_{engine}, b) Fuel flow w_f

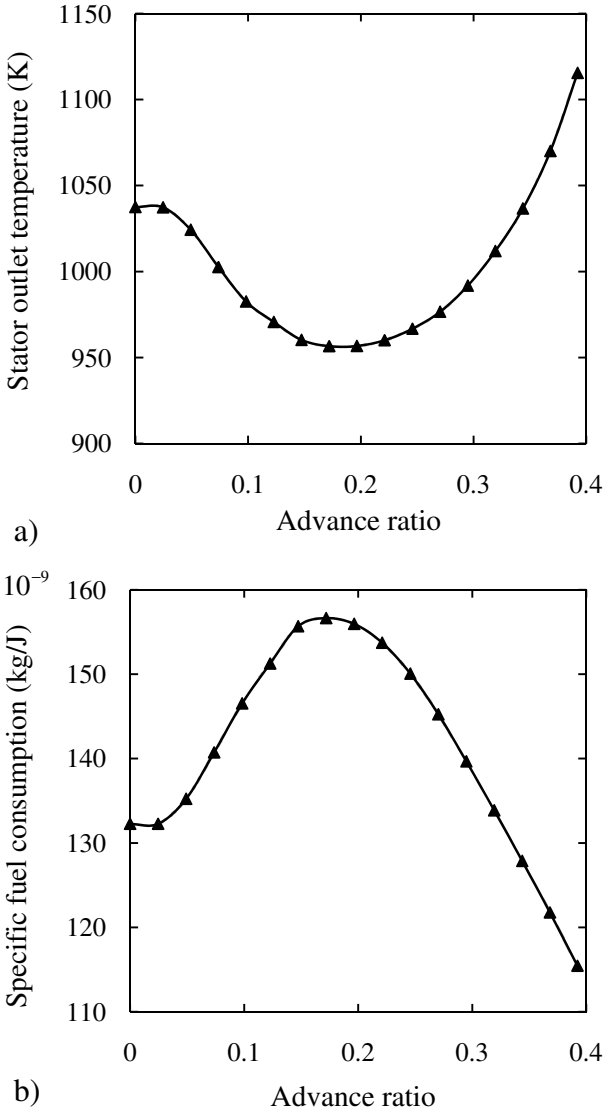

Figure 6.11: Engine performance trim results for the SA 330 helicopter: a) Stator outlet temperature (SOT), b) specific fuel consumption (SFC)

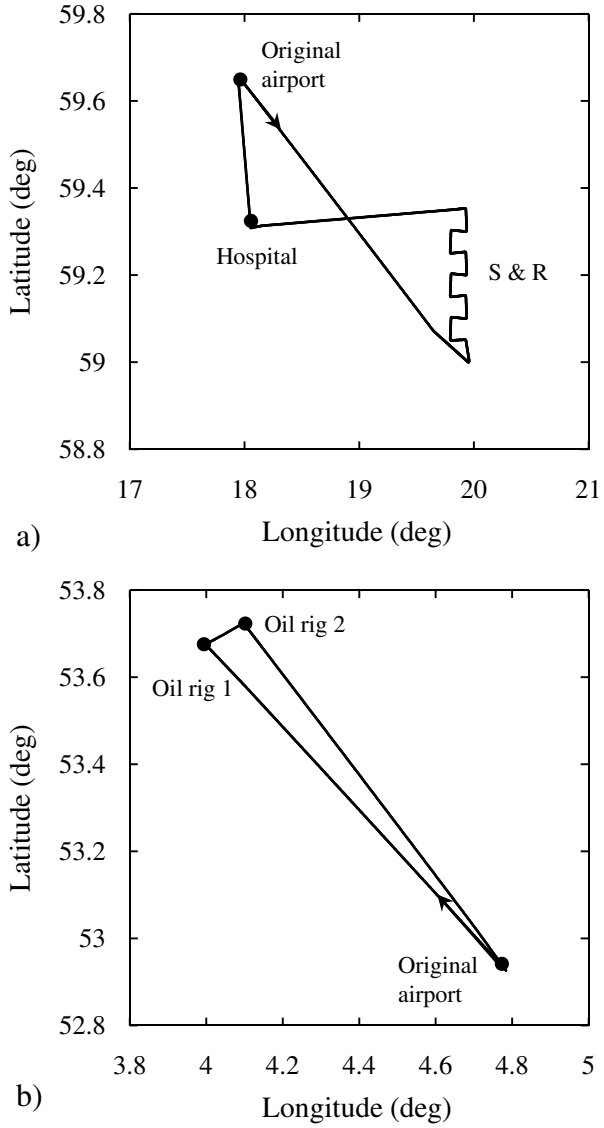

Figure 6.12: Geographical definition of investigated helicopter operations: a) SAR, b) OAG

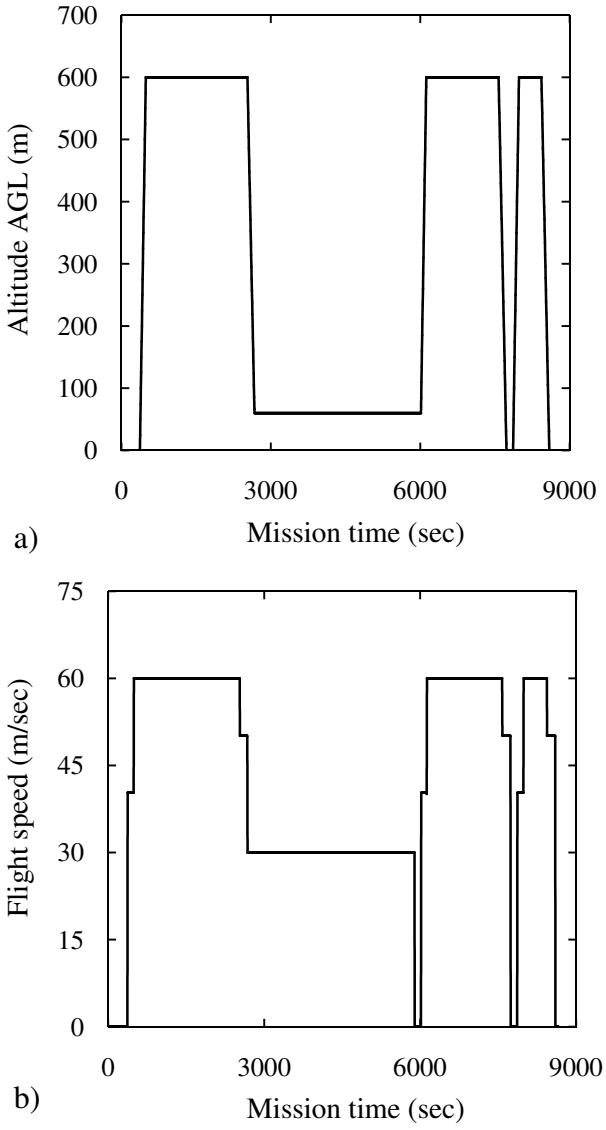

Figure 6.13: SAR mission: a) AGL altitude, b) Flight speed

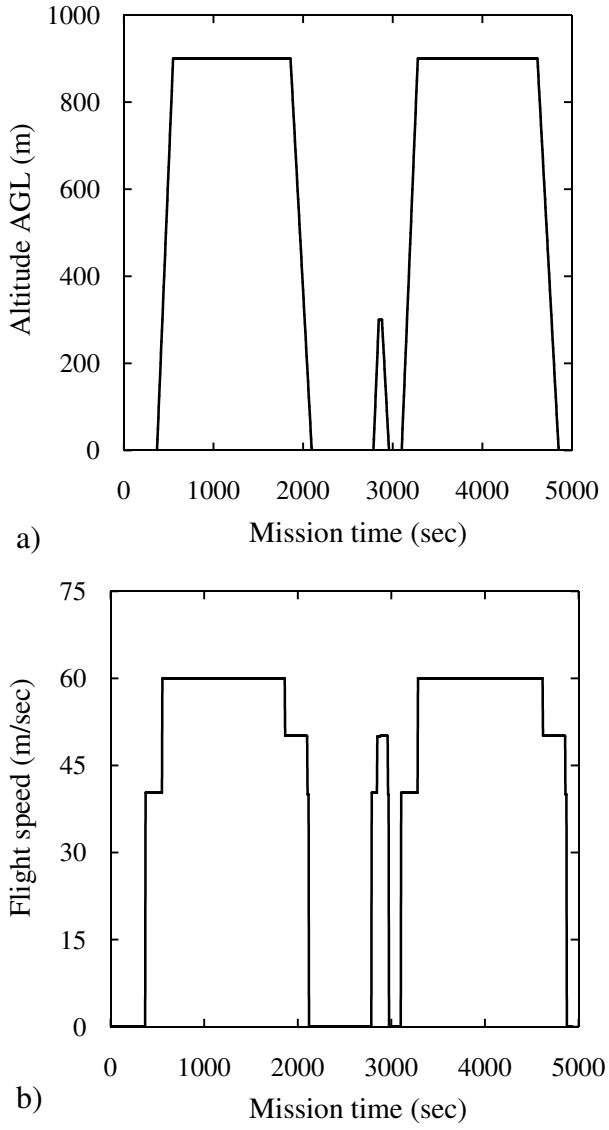

Figure 6.14: OAG: a) AGL altitude, b) Flight speed

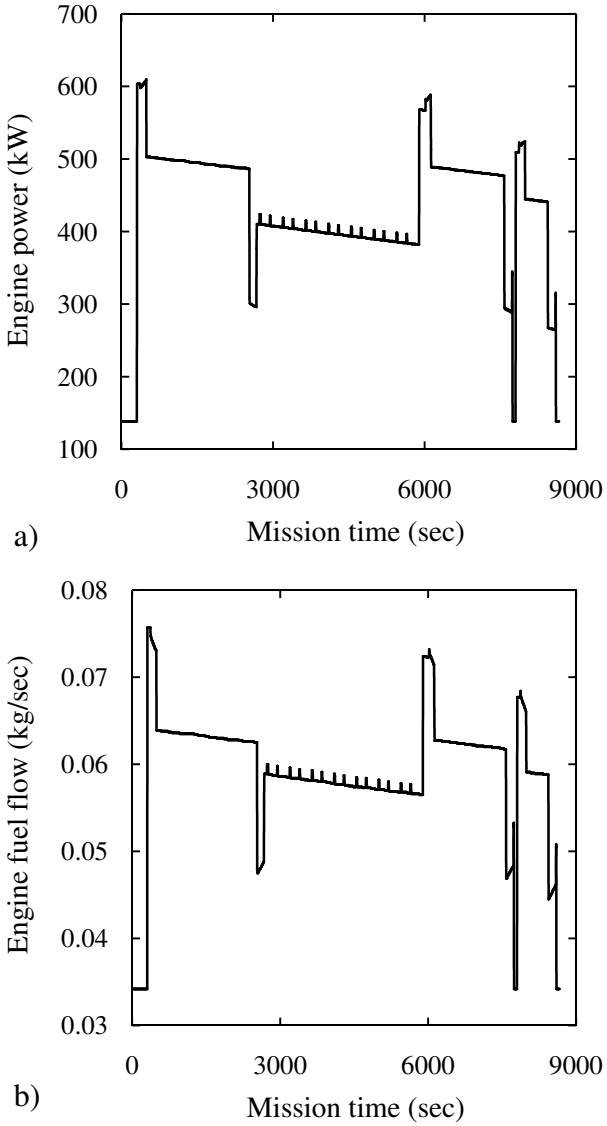

Figure 6.15: Engine performance parameters for the SAR mission: a) Shaft power P_{engine}, b) Fuel flow w_f

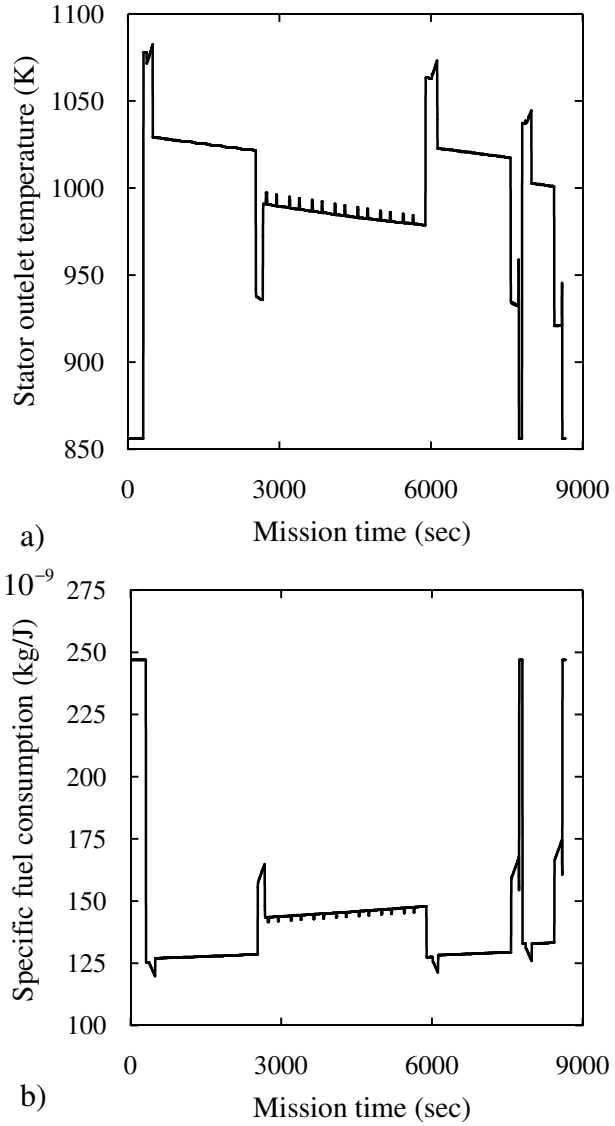

Figure 6.16: Engine performance parameters for the SAR mission: a) Stator outlet temperature SOT, b) Specific fuel consumption SFC

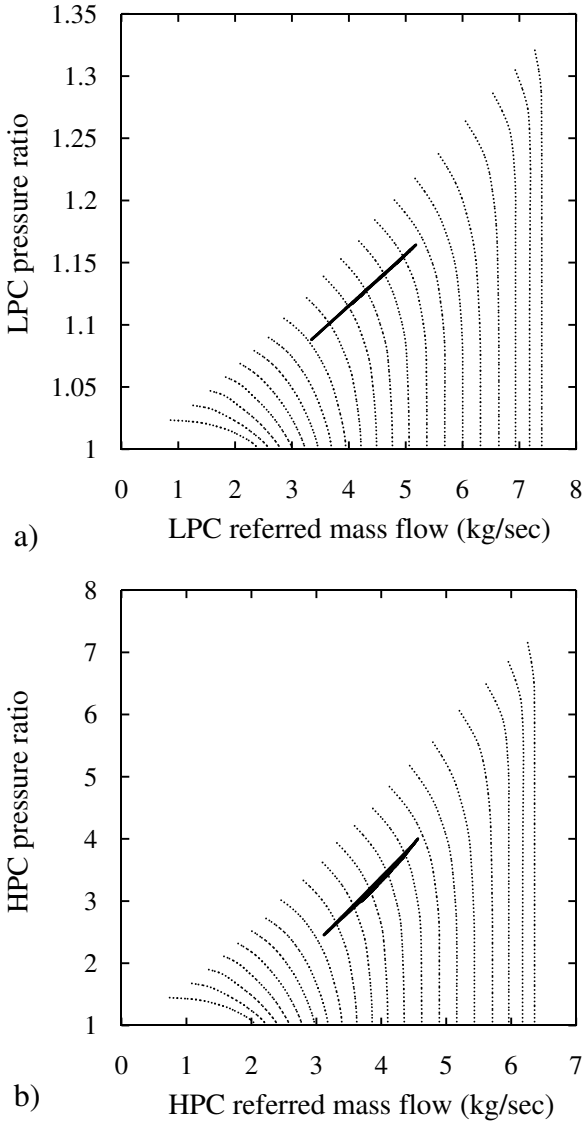

Figure 6.17: Engine performance parameters for the SAR mission: a) LPC running line, b) HPC running line

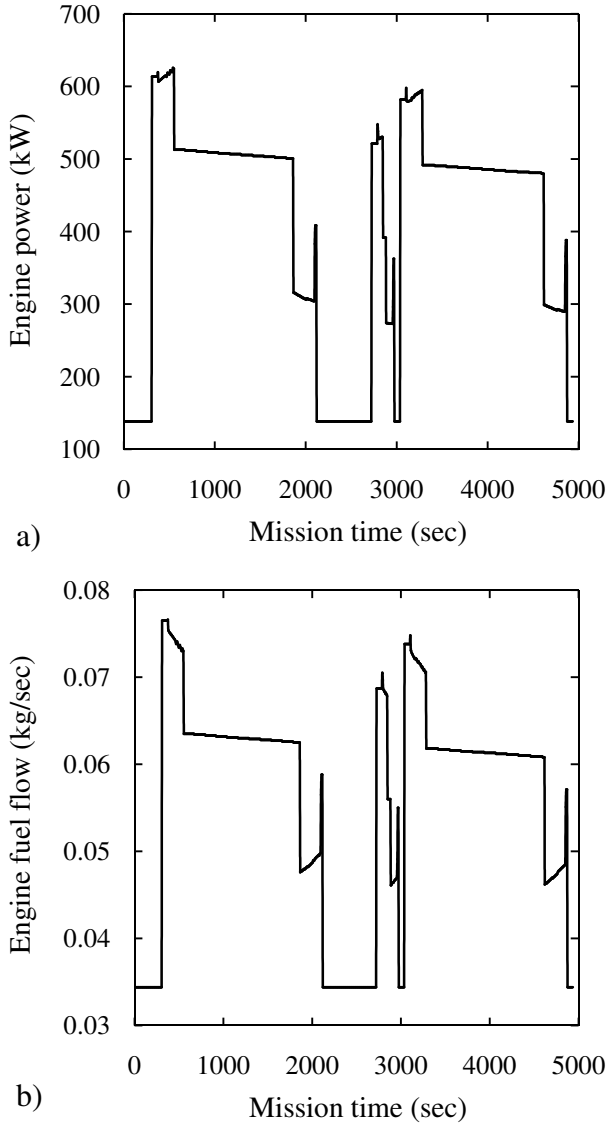

Figure 6.18: Engine performance parameters for the OAG mission: a) Shaft power P_{engine}, b) Fuel flow w_f

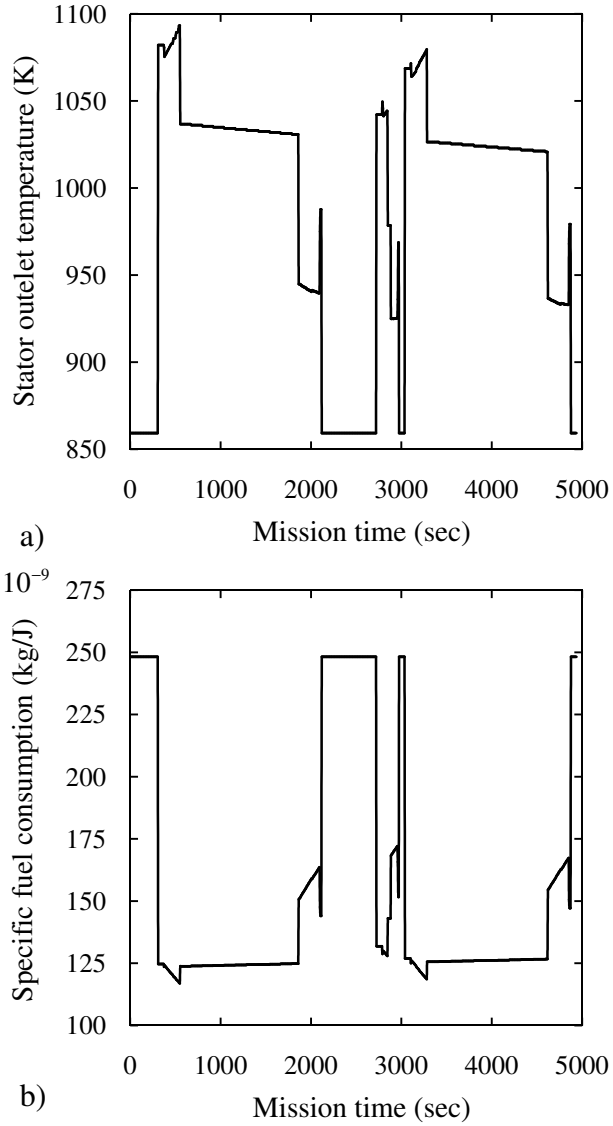

Figure 6.19: Engine performance parameters for the OAG mission: a) Stator outlet temperature SOT, b) Specific fuel consumption SFC

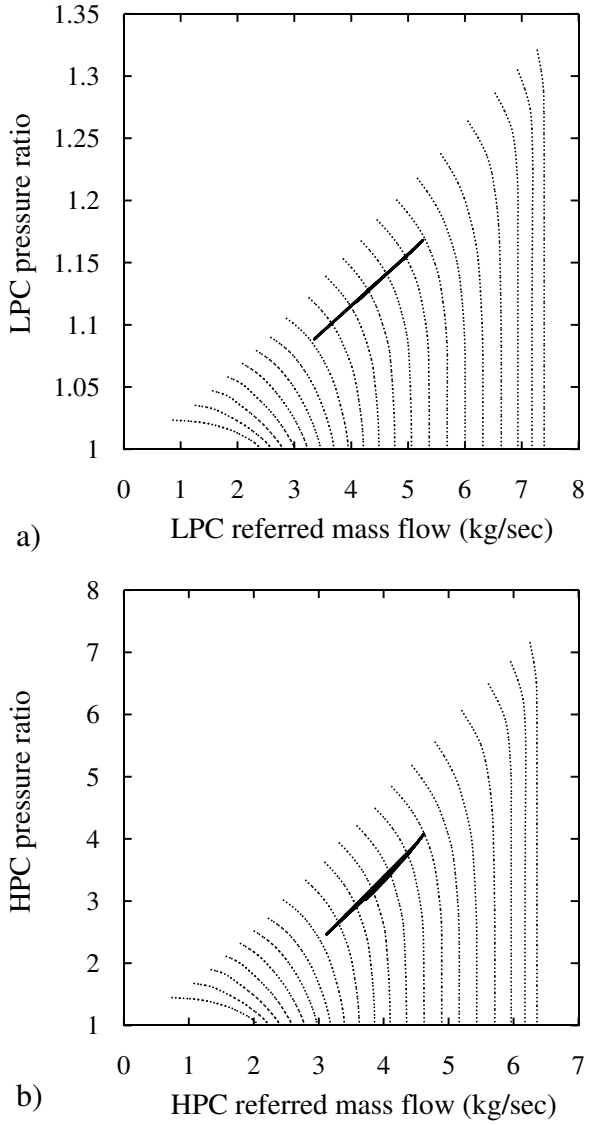

Figure 6.20: Engine performance parameters for the OAG mission: a) LPC running line, b) HPC running line

Chapter 7

An Integrated Approach for the Multidisciplinary Design of Optimum Rotorcraft Operations

7.1 Introduction – Literature

It has been discussed within the 1^{st} chapter of this Thesis that, current trends in civil aviation dictate continuously increasing demands on reducing fuel burn and environmental impact. ACARE has set a number of environmental goals which are to be achieved by 2020 which include, among others, reductions in carbon dioxide (CO_2) and nitrogen oxides (NO_x) emissions of the order of 50% and 80% respectively. With respect to civil rotorcraft aviation, a dynamic response is required, considering the anticipated rotorcraft traffic growth (Ref. 2). It has been argued within chapter 1 that, in order to effectively address the ACARE 2020 goals, emphasis needs to be placed towards the design and implementation of operational procedures leading to minimum required fuel burn and associated environmental impact.

Celis *et al.* (Ref. [98]) investigated and demonstrated the potential of global optimisation methods on the problem of aircraft trajectory optimisation for fuel burn and gaseous emissions. Their case study focused on the two-dimensional climb profile of a generic, twin-engine, single aisle, large transport aircraft. Their methodology included the use of steady state aircraft and engine performance models and genetic algorithms. Their optimisation results suggested an achievable reduction in fuel burn and CO_2 of the order of 6.7% relative to a sub-optimal generic baseline trajectory.

Goulos *et al.* (Ref. [99]) focused on the application of a hybrid optimisation strategy on the case study described in Ref. [98] using identical modeling methodology. They deployed a genetic algorithm in order to explore the global design space and finalized

the optimisation process with a local – gradient method. They were thus able to come up with optimised flight paths requiring 8% less fuel in comparison to the sub-optimal baseline trajectory used in Ref. [98]. Goulos *et al.* (Ref. [1]) extrapolated the methodology described in Ref. [99] to the problem of helicopter trajectory optimisation for fuel burn and gaseous emissions. They worked on the two-dimensional climb profile of a generic, twin engine, medium utility helicopter based on the configuration of the Eurocopter Super PUMA AS332. Their simulation methodology included the use of a steady state helicopter performance model described in Ref. [85]. Through their optimisation results they were able to identify flight paths requiring up to 6.5% less fuel compared to a sub-optimal baseline flight path.

D'Ippolito *et al.* (Ref. [2]) worked on the optimisation of a helicopter Category A take-off maneuver for fuel burn and ground noise impact. Their optimisation strategy included the use of a "Design of Experiment" (DOE) method coupled with "Response Surface Models" (RSMs). Their modeling methodology included transient performance for the helicopter flight mechanics while the engine was assumed to be operating under steady state off-design conditions. Their modeled helicopter configuration was based on the MBB Bo105. They were indeed able to identify a trajectory which minimized fuel burn, CO_2, NO_x and ground noise impact by applying a hybrid optimisation strategy similar to the one used in Refs. [1, 99].

It is noted that the work presented in the aforementioned references is limited to specific mission task elements and that the inherent individuality of a complete rotorcraft operation has not been recognized. Therefore, applicability towards complete 3-dimensional rotorcraft missions, where the trade-off between fuel burn, gaseous emissions and ground noise impact becomes a function of the operation type itself, has not been demonstrated. This work proposes an innovative methodology capable of designing 3-dimensional flight paths, optimum in terms of overall mission fuel burn, produced gaseous emissions and ground noise impact for complete rotorcraft missions. The proposed method recognizes that each rotorcraft operation is unique and is thus adjusted according to the mission specification.

An integrated tool capable of computing the performance of any defined rotorcraft configuration within any defined mission has been deployed. Two generic – baseline rotorcraft missions representative of current rotorcraft operations have been defined. The design space corresponding to the 3-dimensional trajectory definition has been thoroughly explored for the two missions with the application of a Latin Hypercube Design (LHD) method. RSMs for fuel burn, gaseous emissions and ground noise impact have been structured. A hybrid optimisation strategy has been applied and optimum flight paths have been obtained. A comparative evaluation has been carried out for the purpose of quantifying the corresponding trade-off arising from the deployment of flight paths optimised for different objectives. Multi-objective optimisations have been performed using the RSMs

in order to derive Pareto fronts for fuel burn and noise over designated populated zones. Interpolated models derived from the calculated Pareto fronts are subsequently deployed for the design of operations optimised in a multidisciplinary fashion.

The obtained results indicate that the proposed methodology shows promise in designing flight paths with significantly reduced fuel burn requirements, gaseous emissions, and ground noise impact. The obtainable reductions are found to be dependent on the operation type. It is demonstrated that the selection of optimal flight conditions during a mission task element cannot be achieved without catering for the individuality of the complete mission. Finally, it is shown that it is feasible to design operations simultaneously optimum for fuel burn and ground noise impact using a single design criterion: the respective trade-off between these two parameters that the designer is willing to accept.

7.2 Simulation Methodology

Due to the multi-disciplinary nature of the problem tackled in this work, an equivalently diverse and rigorous modeling capability is required. This capability has to be able to provide estimates of fuel burn, gaseous emissions, and ground noise impact for any designated rotorcraft operation. An integrated tool under the name *PhoeniX* (Platform Hosting Operational & Environmental Investigations for Rotorcraft) has been built. *Phoenix* consists of a rotorcraft flight mechanics code (EUROPA), an engine performance and gaseous emissions code (GSP) and a rotorcraft environmental noise analysis code (HELENA). The individual tools have been linked together using the process integration and simulation framework "Noesis Optimus" (Ref. [100]). A brief description of the individual codes is provided below:

7.2.1 European Rotorcraft Performance Analysis (EUROPA)

EUROPA (Ref. [86]) is designed to calculate helicopter steady state (trim) and dynamic (maneuver) performance. Maneuvers can be complex and can be evaluated with engine failure, different atmospheric conditions etc. EUROPA is ideally suited to calculate flight manual performance charts and to determine take-off and landing flight paths. Individual simulation models for vehicle, pilot, environment and control logic have been implemented. The code has been validated using flight test data for trim performance and dynamic response in Ref. [87]. For the purpose of this work, the main rotor modeling fidelity is set to be based on blade element integration using linear aerodynamics. The helicopter is handled dynamically during take-off and landing phases while it assumed to be operating in trim during cruise segments. Turns are calculated as semi-trimmed conditions with a defined roll angle equal to the required heading change, with a maximum value of 30°. The climb and descent rates are held constant to 1000 ft/min and 750 ft/min respectively.

7.2.2 Gas Turbine Simulation Program (GSP)

GSP (Ref. [88]) is a component stacking model capable of calculating both steady-state and transient gas turbine performance including secondary effects such as compressor bleed, turbine cooling and power off-take. The simulation is based on zero-dimensional modelling of the various thermodynamic processes occurring within the various engine components. The flow properties are thermodynamically averaged within cross-areas located at the various engine stations. The performance of individual engine components is simulated with the deployment of discrete maps corresponding to a range of operating conditions. Having defined the design point of the engine, the off-design performance can be acquired by the solution of a system of non-linear differential equations corresponding to mass, heat and power balance between the various engine components. Further information on GSP has been provided by Visser *et al.* in Ref. [101].

The chemical emissions formation estimation at design point is based on a single reactor model for NO_x and CO using ICAO engine emissions database interpolation. Semi-empirical ratio models based on the pollutants emission indices (EIs) at design point are deployed for the estimations at off-design conditions (Ref. [102]).

7.2.3 Helicopter Environmental Noise Analysis (HELENA)

The HELENA (Helicopter Environmental Noise Analysis) platform is able to derive helicopter noise footprints based on a pre-calculated rotorcraft trajectory over a chosen ground model. HELENA utilizes a representative database of noise hemispheres derived from measurements or calculations (CFD). HELENA caters for the inclusion of wind effects, distance (short and long), atmospheric absorption corrections, and ground reflection. HELENA has been validated with dedicated flight tests. It has been extensively analyzed in Ref. [103], thus further elaboration on the tool will be omitted.

Several noise metrics have been developed in the past in an effort to quantify the perceived "noisiness" of jet aircraft and rotorcraft by ground observers. The noise metric used in this work is the "Effective Perceived Noise Level" (EPNL). Further elaboration on noise scales can be found in Ref. [2]. Assumptions of flat terrain and zero wind speed are made for the purpose of this work.

7.2.4 Integration of tools

A schematic representation of the integrated tool architecture is illustrated in Fig. 7.1. The process starts by loading the rotorcraft and engine configuration data, along with the defined mission into the respective models. The defined mission profile is truncated into discrete segments based on user-defined time-step values. Different time-steps are employed for the dynamic mission task elements (dynamic time-step – dt) and the trimmed

flight conditions (static time-step – Δt). The initial All Up Mass (AUM) is equal to the sum of the Operational Empty Weight (OEW), the useful payload and the on-board fuel supplies. The amount of fuel required for a particular mission however, is unknown beforehand and therefore so is the AUM. Thus an initial guess is made regarding the weight of the on-board fuel supply.

For each time-step EUROPA calculates the engine power requirement, intake inlet conditions and updates the new space-wise position of the rotorcraft. The instantaneous values of fuselage roll, pitch and yaw attitude angles (Φ, Θ, Ψ respectively), main rotor and tail rotor thrust and attitude are saved for later use within HELENA. GSP subsequently establishes the off-design operating point of the engine that satisfies the rotorcraft power requirements. Thus the engine fuel flow and the emission indices of various pollutants can be established for the given time-step. During this process, the integral of fuel flow with respect to time is calculated implicitly from zero up to the current mission time. The calculated value is subsequently subtracted from the initial AUM in order to simulate the rotorcrafts gradual weight reduction due to the on-board fuel being burned. This process is then repeated for the next time-step and continues until the entire mission is complete. A total value of the overall fuel consumption is then acquired. This value is compared with the previous on-board fuel supply guess. The guess is then updated accordingly depending on the comparison result. The overall procedure is repeated until the residual error between the guessed and the calculated required fuel supplies is well within the limits of a user-defined tolerance. Having achieved convergence on the mission fuel burn, the corresponding values of the produced gaseous emissions can be obtained. The 3-dimensional trajectory and the time-dependent values of main/tail rotor thrust and attitude as well as the fuselage attitude angles are also acquired.

The noise propagation calculations are carried out by deploying HELENA through an external loop after the aforementioned procedure has converged. This is due to the fact that there is no implicit coupling (only explicit) between the emitted noise and the rotorcraft flight mechanics or the engine performance. HELENA estimates the noise propagation based on the calculated rotorcraft trajectory. The respective noise footprint for any specified ground location can then be acquired in terms of EPNL. This step completes the overall assessment of the designated rotorcraft mission in terms of fuel burn, gaseous emissions and ground noise impact.

7.3 Optimisation Strategy

The relatively complex nature of the problem tackled in this work in conjunction with the increased computational requirements of the aforementioned simulation methodology has deemed imperative the compilation of a robust and simultaneously cost-effective optimisation strategy. The available design space consists of the deployed mission cruise – loitering

altitude – airspeed as well as the longitude and latitude coordinates of the complete 3-dimensional flight paths (design inputs). Thus effectively, potential Air Traffic Control (ATC) constraints can be treated as design space limitations and not as optimisation constraints in the strictest sense of the term. This point will become clear in the "Case Study" section of this chapter. The overall optimisation strategy developed for the present analysis consists of two steps: the design space exploration – system approximation and the actual optimisation approach.

7.3.1 Design space exploration and system approximation

This step is divided in two main parts: the deployment of a DOE method in order to efficiently explore the available design space and the subsequent construction of RSMs based on the DOE results. In order to avoid a prohibitively large number of simulations associated with the process of iterative design, it has been decided to build RSMs that can accurately approximate the response of the simulation methodology. The RSMs are to be deployed subsequently for the optimisations instead of using actual simulations. The required computational time can thus be substantially reduced.

A DOE is a systematic approach to get the maximum amount of system information out of a given number of experiments. Out of the different kinds of DOE available in the literature (Ref. [104]) the LHD algorithm has been selected. The LHD method belongs to the category of random methods and thus various points in the computational space are selected randomly for evaluation. Complete randomness however can lead to a design space filled with clustered points which is unsatisfactory for sampling purposes. In statistical sampling, structured randomization is achieved through a Latin square. A Latin square is defined as a grid containing sample positions if and only if there is only one sample in each row and each column. A Latin Hypercube will generalize this idea in multiple dimensions by forcing only one sample on each axis-aligned hyper plane. Further elaboration regarding the LHD method is provided in Ref. [105].

An RSM can be viewed as a hyper-surface which essentially describes the relationship between design inputs and outputs. Having successfully completed the DOE approach, RSMs can be afterwards structured based on the DOE results in an effort to effectively approximate the system's response. For the purpose of this work, interpolation using Radial Basis Functions (RBF) has been the method of choice in order to construct the required RSMs. Information on the various RBF interpolation methods can be found in Ref. [106].

7.3.2 Optimisation approach

Having explored and efficiently approximated the system response, the search for optimum solutions can commence. The simulation computational requirements are no longer an

issue hence the optimisation approach can consist of multiple algorithms. The multi-disciplinary character of the problem requires a robust approach capable of performing single-objective as well as multi-objective optimisations.

The single-objective method has to be immune to the danger of being trapped between locally optimum solutions. Hence a global method is required. Global methods converge within a very small domain of potential globally optimum solutions. In order to find the absolute global optimum among these, a local optimisation method must be deployed. Thus a truly global optimum solution can be obtained. The global and local methods selected for the purpose of this work are "Self-Adaptive Evolution" (SAE) and "Non-Linear Programming by Quadratic Lagrangian" (NLPQL) respectively.

Self-Adaptive Evolution (SAE) is a Genetic Algorithm (GA) – evolutionary scheme. These schemes are nature-inspired and imitate biological mutation and natural selection in a simplified way with the purpose of finding the "fittest" solution to multi-dimensional technical problems (Ref. [107]). The main advantage of using evolutionary schemes in a multi-disciplinary context is that they do not require the calculation of the sensitivities between the design variables and the objective function. SAE is based on an iterative process utilizing populations (generations) of λ number of designs. The members χ_m^k of each generation k are created by recombination and mutation from a set of μ parent designs χ_p^k, where m and p are the member and parent indices respectively. Parent designs are essentially members selected from the previous generation. Members with better fitness have a larger probability of being selected. SAE is multi-recombinant scheme, meaning that multiple parents are selected in order to generate a single offspring. Each design is independently mutated according the following recombination scheme

$$\chi_{m,i}^k = \chi_{p,i}^k + \delta_m^k s_i^k \tag{7.1}$$

where i is the step direction, s_i^k is the random search direction and δ_m^k is a step length. The step length for each member is constructed on the basis of the μ parent designs as follows

$$\delta_m^k = \frac{1}{\rho} \sum_{j=1}^{\rho=\mu} \delta_{p,z_j(1,\mu)}^k \tag{7.2}$$

where $z_j(1,\mu)$ is a uniform distributed random integer ranging within $[1,\mu]$. Thus a generation of new members is consequently produced and their fitness is subsequently evaluated. The process is repeated until the generation step length is below a user-defined tolerance.

NLPQL is a gradient method that was originally introduced by Schittowski (Ref. [108]). NLPQL is in fact a Sequential Quadratic Programming (SQP) algorithm (Ref. [109]) with a distributed non-monotone line search strategy. NLPQL and SQP have been extensively analyzed in Ref. [110].

In order to analytically assess the trade-off between any two design outputs of interest, the Pareto front formation is essential. Thus the deployment of a multi-objective optimisation method is required. The method selected for this work is the Normal-Boundary Intersection Method (NBIM). NBIM uses a geometrically intuitive parametrization to produce an even spread of points on the Pareto surface, giving an accurate picture of the optimal system response. Further information on NBIM can be found in Ref. [111].

7.4 Case Study

In order to assess the potential and address the limitations of the methodology presented in this chapter, a case study has been prepared. A twin engine light rotorcraft model based on the configuration of the MBB Bo105 (now under Eurocopter) has been implemented in EUROPA. The specific rotorcraft is equipped with two Rolls-Royce Alison 250-C20B turboshaft engines. Thus the corresponding engine model has been developed and implemented in GSP. The design point of the engine is defined at take-off conditions. Indicative values corresponding to the rotorcraft configuration and engine design point cycle parameters are presented in Tables 7.1 and 7.2 respectively.

Two complete, sub-optimal, baseline missions representative of current twin engine light rotorcraft operations have been defined; a law enforcement/police mission and passenger transport/air taxi mission. The police mission assumes that the rotorcraft takes-off from Myttinge airport in Stockholm, Sweden. It then heads towards the city centre where it loiters in a circular fashion around two specified designated locations and subsequently returns to the original airport. The air taxi mission assumes that the rotorcraft takes off from Hanover, Germany airport and heads towards a designated location where it picks up 3 passengers. It subsequently travels towards a designated passenger drop-off location. The rotorcraft finally returns to the original airport. The detailed specification of both baseline missions in terms of individual mission task elements is provided in Tables 7.3 and 7.4.

A populated area has been designated in the vicinity of each mission for the purpose of assessing the ground noise impact. Each area is defined as a circular periphery with specified centre coordinates and radius. The ground noise impact for each mission is assessed in terms of the average EPNL at the corresponding area. The calculated mission design outputs in terms of fuel burn, CO_2, NO_x and EPNL are presented in Table 7.5 for both missions. The respective trajectories along with the EPNL noise contours over each mission's regional area are presented in Fig. 7.2. The locations of the designated populated areas have been annotated in the aforementioned figure for each mission.

Tables 7.6, 7.7 and Fig. 7.3 define the design space for the two missions in terms of variable bounds. Due to the fact that ground noise impact over a designated area is a design output, the mission design space has to be explored in a complete 3-dimensional

manner. Potential ways to achieve minimum ground noise impact may include the deployment of higher operational altitude, a different flight path route (keeping the same altitude) or any combination of the two. Thus in order to systematically explore the effect of all available options, it is required to schedule missions not only in terms of altitude and airspeed but also in terms of flight route.

To address the aforementioned point, each cruise task element is divided into 5 individual segments with 4 corresponding intermediate waypoints (Fig. 7.3) for both missions. The latitude (police mission) or longitude (passenger mission) coordinates of the respective waypoints can be treated as flight path design variables. The addition of those extra degrees of freedom in the design space allows for the 3-dimensional character of each mission to be thoroughly captured. Thus potentially optimum noise abatement procedures incorporating alterations in both route and operational altitude-airspeed can be designed.

It can now become clear that any potential location dependent ATC constraints essentially define the available mission design space in terms of variable bounds. Since the operational altitude – airspeed as well as the selected route are treated essentially as design inputs (and not design outputs), any performed optimisations can be executed without any constraints from ATC regulations. The symbol "[-]" in Tables 7.6 and 7.7 signifies the fact that the corresponding value is identical to the value located in the same column and one position above. This is essential in order to maintain a space-wise consistency in the 3-dimensional trajectory. The respective values are thus essentially defined by the same variable and they can be treated as such. Values listed in *italic characters* are held fixed. It is noted that climb and descent rates have remained fixed for the purpose of this work.

It is thus concluded that the design space of each mission as defined in Tables 7.6, 7.7 and Fig. 7.3 consists of a total of 14 variables. The optimisation objective is to acquire optimum combinations of design inputs leading to minimum overall fuel burn, gaseous emissions (CO_2 and NO_x) and EPNL over the respectively defined populated area and for both missions.

7.5 Results & Discussion

7.5.1 LHD and RSM approach

In order to accurately capture the character of each mission – system through the execution of the LHD method, a sufficient number of simulations must be carried out. A total of 600 simulations have been performed for both cases. Having successfully completed the LHD DOE, sufficient information about the interrelationship between certain design outputs can be obtained. Tables 7.8 and 7.9 present the principal linear correlation estimation regarding the defined design outputs for the police and passenger missions

respectively.

The principal linear correlation coefficients indicate the amount and type of average dependency between two specified design outputs. A correlation coefficient can range from -1 to 1. A positive and a negative non-zero value will indicate a direct and an indirect correlation respectively. A very strong correlation between fuel burn and CO_2 (1.000) is observed for both missions as expected. Thus any mission optimised for fuel burn will be optimised for CO_2 and vice versa. The rather strong correlation coefficient between fuel burn and NO_x for the passenger mission (0.964) indicates that the same principle can be applied for the NO_x. Regarding the police mission however, a rather lower correlation coefficient is observed (0.921). This indicates that the optimum solution for NO_x emission may be sub-optimum in terms of fuel burn – CO_2. Therefore optimisations for fuel burn – CO_2 and NO_x have to be performed separately. The conclusions above have been confirmed during the optimisation process as well. The even smaller linear correlation coefficients observed between fuel burn – gaseous emissions and EPNL dictate, as expected, that separate optimisations have to be performed for EPNL regarding both missions.

RSMs for fuel burn, CO_2, NO_x and EPNL have been structured using RBF interpolation based on the DOE results. The RSMs have been subsequently deployed for optimisation purposes. Figure 7.4 presents contours of fuel burn as a function of deployed airspeed for the first two cruise mission task elements and for both missions.

7.5.2 Single-objective optimisations

Having explored and successfully approximated the available design space, the optimisation process can commence. As suggested by the DOE results, three separate single-objective optimisations for fuel burn – CO_2, NO_x and EPNL respectively have been performed for the police mission. Only 2 single-objective optimisations for fuel burn – CO_2 – NO_x and EPNL respectively have been carried out for the passenger mission.

The single-objective optimisation approach has commenced with the execution of SAE. As previously discussed, SAE is a genetic algorithm that works iteratively in terms of marching through generations of experiments – simulations. The population of each generation is recommended to be set 5 to 6 times the number of variables. Since the design space for both missions consists of 14 variables, the population size has been set to 75 for both missions regarding every objective. Convergence is assumed to have been achieved when the step-length δ reaches a value below 10^{-2}. NLPQL has been subsequently deployed using the optimum solution acquired by SAE as a starting point. NLPQL is assumed to have converged when the norm of the quadratic Lagrangian reaches a value below 10^{-4}. The optimisation process for fuel burn is presented in Fig. 7.5 for both missions. It is shown that convergence has been achieved fairly quickly within

both SAE and NLPQL for both missions. The convergence criteria for SAE are satisfied within only 15 generations regarding both missions. The NLPQL convergence criteria are satisfied within 9 and 7 iterations for the police and passenger missions respectively. The different magnitudes in fuel burn reduction for SAE and NLPQL can also be observed. The additional decrease achieved by NLPQL is very small compared to the SAE reduction for both missions. This is an indication of the very good convergence properties of SAE with regards to the present application.

Having completed the single-objective optimisations, it is essential that the quality of the RSMs is checked. Thus, a separate simulation has been performed at each optimum acquired for each objective and for both missions. The optimum design outputs obtained from the simulations have been subsequently compared with the corresponding outputs acquired from the RSMs. The RSM relative error at the optimum designs is defined as follows:

$$RSM\ Rel.\ Error\ \% = 100 \times \frac{Quantity_{rsm} - Quantity_{sim}}{Quantity_{sim}} \tag{7.3}$$

Tables 7.10 and 7.11 present the RSM relative error at the respective optimums regarding all design outputs for the police and passenger mission respectively. The Root Mean Square (RMS) of the relative error at each design optimum is also included. As regards the police mission, it noted that the RSM has excellently captured the behavior of the fuel burn – CO_2 and EPNL optimums. Specifically the RMS relative error for all design outputs at the aforementioned optimums is of the order of 0.30% and 0.35% respectively. This is also an indication that the specific optimums are close to pre-calculated DOE experiments that have been used for RBF interpolation. With reference to the NO_x optimum, it can be noticed that the RMS relative error is of the order of 2.40%. This is an indication that the NO_x system behavior may have not been captured as accurately as the behavior of fuel burn – CO_2 and EPNL. As regards, the passenger mission RSM, Table 7.11 shows that the RMS relative error of all design outputs at the EPNL optimum is of the order of 0.04%. This also indicates that the optimum is very close to a pre-calculated DOE experiment. The RMS relative error calculated for the fuel burn – CO_2 – NO_x optimum is of the order of 2.14%. The large RMS relative error is highly influenced by the substantial NO_x error which is of the order of -3.59%. This indicates that the NO_x system behavior has not been captured as accurately as the rest of the design outputs for the passenger mission as well.

The RSMs may have not captured the NO_x system behavior as accurately as fuel burn – CO_2 due the highly non-linear nature of the specific design output in relation to the mission design variables. It is the author's view that more sophisticated interpolation methods such as the "Kriging method" (Ref. [112]) may improve the accuracy of the NO_x RSM. It is however noted that any potential error in the RSMs may only cause the optimisation process to deviate from the actual global optimums. The error does not

propagate in the trade-off analysis. This is due to the fact that the actual optimisation results are taken from direct simulations performed at the optimum points as suggested by the RSMs and not directly by the RSMs. Hence the RSMs are only used as drivers in the optimisation process with actual simulations giving the final results.

Tables 7.12 and 7.13 present the single-objective optimisation results. The optimised flight paths are compared in a quantitative manner with their respective baseline profiles. The corresponding relative trade-off for each design output is defined as follows:

$$Rel.\,Trade-off\% = 100 \times \frac{Quantity_1 - Quantity_2}{Quantity_2} \tag{7.4}$$

Figures 7.6 and 7.7 present the altitude and airspeed as functions of mission time for the optimum and baseline flight paths regarding the police and passenger mission respectively. It is noted that for the fuel burn and gaseous emissions optimisations, the intermediate waypoint coordinates have remained fixed. This is due to the fact that the baseline flight paths are defined in terms of the shortest route available (straight line paths). Thus it would be expected that any deviation from them would result in an increase of mission range, hence flight time and fuel burn – emissions.

As regards the police mission, Table 7.12 shows that a reduction in fuel burn – CO_2 of the order of 19.17% has been achieved relative to the baseline. The associated NO_x reduction is of the order of 25.00%. Comparing the respective altitude profiles in Fig. 7.6, a) it can be observed that the optimisation process suggests the deployment of higher cruise and loitering altitude relative to the baseline. With regards to the flight airspeed, Fig. 7.6, b) shows that the fuel burn – CO_2 optimised flight path incorporates lower cruise airspeed but much higher loitering airspeed. The final result is the quicker finalization of the mission resulting in a lower overall mission time.

As it is noted from Figs. 7.6, a) and b), the rotorcraft spends a significant amount of time loitering during the police mission. Thus, the selection of flight conditions within this mission task element is critical with regards to fuel burn – CO_2 minimization. Selecting a lower altitude may indeed result in lower main rotor induced losses but higher parasitic – fuselage drag for a given true airspeed and vice versa. The selection of lower airspeed relative to a baseline may either increase or decrease the overall engine fuel flow requirement depending on whether the baseline speed is on the ascending or the descending part of the rotorcraft power curve. The rotorcraft power curve however is very much a function of altitude as well as of the overall payload that the rotorcraft may be carrying. The payload is a function of the initial AUM and the fuel already consumed which depends on the mission. It is therefore understood that the problem of optimum flight conditions selection is highly non-linear and very much a function of the defined mission. Thus, it can be concluded that the selection of optimal flight conditions in terms of fuel burn for a given mission task element, cannot be established without catering for the individuality of the entire rotorcraft operation.

Table 7.12 shows that the NO_x can be further reduced up to 26.76%. The fact that the fuel burn – CO_2 optimum is not the same as the corresponding NO_x optimum has also been indicated by the earlier principal linear correlation analysis. Figure 7.6, a) suggests that the NO_x optimum flight path altitude profile is quite similar to the corresponding fuel burn optimum. Figure 7.6, b) suggests that the NO_x optimum flight path maintains a constant value of 80 knots for both cruise task elements as well as during the loitering procedure. The end result is a lower mission time in comparison to the baseline, but still higher compared to the fuel burn – CO_2 optimised flight path.

As regards the passenger mission, Table 7.13 shows that the achievable fuel burn reduction is of the order of 6.81% relative to the baseline mission. The corresponding NO_x reduction is of the order of 14.06%. The indications from the principal linear correlations analysis earlier in this chapter have been confirmed through the deployment of an additional optimisation for NO_x. The NO_x optimum solution has been found to be identical to the fuel burn – CO_2. Thus fuel burn, CO_2 and NO_x have indeed been minimized within a single optimisation. According to Fig. 7.7 the optimisation process suggests the deployment of lower cruise altitude and airspeed for the first two cruise task elements relative to the baseline mission. For the third cruise task element the use of higher airspeed and altitude is proposed.

The very large difference observed in the achievable fuel burn – gaseous emissions reduction between the two missions, is due to the incorporation of a highly sub-optimal loitering operation within the police mission. As previously explained, the selection of flight conditions within the specific mission task element has a tremendous impact on the overall mission fuel burn – CO_2. The baseline police mission assumes that during loitering the rotorcraft operates in two circular trajectories at an altitude of a 1000 ft and at 60 knots. These conditions are apparently highly sub-optimal leading to increased mission fuel burn and time. Having optimised the flight conditions during loitering, the overall mission fuel burn has tremendously improved. For the passenger mission, only the selection of flight condition during cruise is optimised (no loitering mission task element). Hence the corresponding fuel burn reduction is much lower. It can thus be concluded that the potential to achieve reductions in fuel burn and gaseous emissions is dependent on the type of operation.

Figure 7.8 presents the EPNL noise contours for the EPNL optimised missions. According to Tables 7.12 and 7.13 the EPNL over the respective populated areas has been reduced by 16.92% and 11.06% for the police and passenger mission respectively. Figures 7.6, 7.7 and 7.8 show that the implemented noise abatement procedures have been designed based on combinations of route selection and higher cruise altitude in comparison to the baseline missions. As regards the police mission, it can be noticed that the flight path within the first and second cruise mission task elements, has strongly deviated from the populated region. It is also noted from Fig. 7.6, a) that the altitude during cruise 1 has

been significantly increased compared to the baseline mission. A similar noise abatement approach has been designed for the passenger mission as well.

It can be observed that for the police mission, the EPNL reduction is accompanied with a fuel burn reduction of the order of 11.19% despite the obviously increased range of the mission. This is due to the significant influence of the loitering task element in the overall mission fuel burn. Figure 7.6 shows that the loitering altitude and airspeed for the EPNL optimum solution is quite close to the optimum values for fuel burn. Hence, the EPNL optimum for the particular mission also favors fuel economy due the implicit coupling through the loitering task element. As regards the passenger mission, the corresponding fuel burn increase for the EPNL optimum flight path is of the order of 3.75%. This is due to the increased range of the EPNL mission as shown in Fig. 7.8, b).

7.5.3 Multi-objective optimisations

The optimised flight paths presented and elaborated above have been derived while focusing only on a single objective, with no constraints on the related design outputs. The associated trade-off between the various parameters may be unacceptable for some cases or when the present methodology is extrapolated to different missions. It is thus realized that the optimum solution selection has to be based on the most effective compromise between the various design outputs of interest. Hence their interrelationship has to be understood in a quantitative manner. This problem can be thoroughly addressed with the deployment of a multi-objective optimisation – Pareto front finding method. As discussed previously, the selected method is NBIM (Ref. [111]). The approximation of the system response has been handled by the RSMs in an effort to reduce the required computational time.

Pareto fronts have been structured for the fuel burn and ground noise impact in an effort to systematically quantify the trade-off between them. The formation process is presented in Fig. 7.9 for both missions. The Pareto fronts are clearly visible. Sufficiently accurate models have been structured that can approximate the response on the Pareto fronts (Pareto models). The model formation process is based on RBF interpolation and is identical to the method used for the structure of the RSMs. The acquired Pareto models can be subsequently deployed in order to automatically design operations that comply with the fuel burn – EPNL trade-off that the designer is willing to accept.

Since the Pareto models are essentially based on the system approximation of the RSMs, it would be expected that the RSM associated error will have propagated in the Pareto models. It is therefore necessary that the quality of the Pareto model is checked. A specified point has been selected from the Pareto model of each mission (Fig. 7.9). Each point corresponds to a mission design which has been simultaneously optimised for fuel burn and ground noise impact. The sole variable that defines the multi-optimum design

on the Pareto front of each mission is the accepted fuel burn – ground noise impact trade-off. A separate simulation has been performed for the design corresponding to each point. The simulation design outputs for each of the points selected, along with the relative prediction errors of the Pareto models are presented in Tables 7.14 and 7.15 for the police and the passenger mission respectively.

As regards the police mission, table 7.14 shows that the Pareto model RMS relative error for all design outputs is of the order of 0.74%. Hence the corresponding design outputs have been rather accurately captured by the Pareto model. The selected point effectively corresponds to a mission design which simultaneously achieves reductions of the order of 14.38% and 10.64% for fuel burn and EPNL respectively relative to the baseline mission. Regarding the passenger mission, the Pareto model RMS relative error regarding all design outputs is of the order of 1.59%. The design that corresponds to the selected point is capable of achieving reductions of the order of 4.84% and 5.29% for fuel burn and EPNL respectively relative to the baseline mission.

The corresponding multi-optimised flight paths, along with the EPNL noise contours around their respective regional areas are presented in Fig. 7.10. As regards the police mission, it can is observed that the flight path deviates from the optimum straight line path during the first cruise task element. The purpose is to essentially avoid inflicting noise over the designated populated area. The second cruise task element however has remained identical to the fuel burn optimised one in terms of chosen route. It has therefore been kept a straight line. This is in order to avoid any further increase in mission range which would effectively penalize fuel burn even more. Although not presented in this chapter, the multi-optimum flight path is quite similar to the fuel burn optimised flight path in terms of operational altitude and airspeed. Regarding the passenger mission, it can be observed that a similar approach has been applied by the Pareto model. Further elaboration will be therefore omitted. In conclusion, it has been demonstrated that it is feasible to design optimal noise abatement procedures for a designated mission with minimum penalty in the overall mission fuel burn.

It is thus understood, that the proposed methodology enables the design of complete flight paths optimised for multiple objectives using a single design criterion: the respective trade-off that the designer is prepared to accept between fuel burn, gaseous emissions and ground noise impact over any designated area. Hence the individuality of the rotorcraft mission is once again implicitly recognized and catered for during the design process.

7.6 Conclusions

An innovative methodology capable of addressing the design of complete rotorcraft missions optimised for fuel burn, gaseous emissions and ground noise impact has been proposed. The method is based on the deployment of an integrated tool capable of computing

the flight dynamics, engine performance and emitted noise of any defined rotorcraft configuration within any designated mission. A robust and computationally efficient optimisation strategy has been developed, implemented and presented. The overall methodology has been applied to two different, generic – baseline rotorcraft missions representative of modern twin engine light rotorcraft operations.

The results obtained so far indicate that the proposed method shows promise in achieving substantial reductions in fuel burn, gaseous emissions and ground noise impact simultaneously for any rotorcraft mission. It has been shown that the deployment of DOE methods coupled with RSMs is an effective and efficient approach with regards to the specific application. The NO_x system behavior has been found difficult to capture accurately using simple RBF interpolation and higher order interpolation methods have been suggested. The obtainable reductions have been found to be dependent on the designated mission application. It has been shown that selection of optimal flight conditions during a mission task element cannot be addressed without catering for the individuality of the complete mission. Finally, it has been demonstrated that it is possible to design optimum flight paths in a multidisciplinary fashion using a single design input variable: the trade-off between fuel burn and ground noise impact that the designer is willing to accept.

Table 7.1: Rotorcraft configuration model parameters

Design parameter	Value	Units
OEW	2000	kg
Number of blades	4	–
Blade radius	4.91	m
Blade chord	0.27	m
Blade twist	8	degrees
Rotorspeed	424	rpm

Table 7.2: Engine model design point cycle parameters

Design parameter	Value	Units
Pressure ratio	7.2	–
Air mass flow	1.814	kg/sec
Combustor FAR	0.024	–
SOT	1547.96	K

Table 7.3: Baseline police mission specification

Mission Task Element	Airspeed (kts)	Altitude AGL – final (ft)	Climb rate (ft/min)
Take-off	65	1000	–
Climb	80	1500	1000
Cruise	120	1500	0
Descent	60	1000	-750
Loiter 1	60	1000	0
Cruise	60	1000	0
Loiter 2	60	1000	0
Climb	80	1500	1000
Cruise	120	1500	0
Descent	100	1000	-750
Land	35	0	–

Table 7.4: Baseline passenger mission specification

Mission Task Element	Airspeed (kts)	Altitude AGL – final (ft)	Climb rate (ft/min)
Take-off	65	1000	–
Climb	80	1500	1000
Cruise	120	1500	0
Descent	100	1000	-750
Land	35	0	–
Take-off	65	1000	–
Climb	80	1500	1000
Cruise	120	1500	0
Descent	100	1000	-750
Land	35	0	–
Take-off	65	1000	–
Climb	80	1200	1000
Cruise	120	1200	0
Descent	100	1000	-750
Land	35	0	–

Table 7.5: Baseline missions design outputs

Design output	Police mission	Passenger mission	Units
Mission time	5823	1840	sec
Mission range	193.29	43.77	km
Fuel burn	371.77	117.10	kg
CO_2	1178.73	371.30	kg
NO_x	1.02	0.32	kg
EPNL	68.38	76.34	db

Table 7.6: Bounds for operational design variables: Police mission

Mission Task Element	Airspeed (kts)	Altitude AGL – final (ft)
Take-off	*65*	*1000*
Climb	*80*	[1000-2000]
Cruise	[80-140]	[-]
Descent	[40-80]	[700-1500]
Loiter 1	[-]	[-]
Cruise	[-]	[-]
Loiter 2	[-]	[-]
Climb	*80*	[1000-2000]
Cruise	[80-140]	[-]
Descent	*100*	*1000*
Land	*35*	0

Table 7.7: Bounds for operational design variables: Passenger mission

Mission Task Element	Airspeed (kts)	Altitude AGL – final (ft)
Take-off	*65*	*1000*
Climb	*80*	[1000-2000]
Cruise	[100-140]	[-]
Descent	*100*	*1000*
Land	*35*	*0*
Take-off	*65*	*1000*
Climb	*80*	[1000-2000]
Cruise	[100-140]	[-]
Descent	*100*	*1000*
Land	*35*	*0*
Take-off	*65*	*1000*
Climb	*80*	[1000-1800]
Cruise	[100-140]	[-]
Descent	*100*	*1000*
Land	*35*	*0*

Table 7.8: Design outputs linear correlation coefficients estimation: Police mission

Design output	Fuel burn	CO_2	NO_x	EPNL
Fuel burn	1.000	1.000	0.921	0.110
CO_2	1.000	1.000	0.918	0.108
NO_x	0.921	0.918	1.000	0.151
EPNL	0.110	0.108	0.151	1.000

Table 7.9: Design outputs linear correlation coefficients estimation: Passenger mission

Design output	Fuel burn	CO_2	NO_x	EPNL
Fuel burn	1.000	1.000	0.964	-0.050
CO_2	1.000	1.000	0.959	-0.008
NO_x	0.964	0.959	1.000	-0.045
EPNL	-0.050	-0.045	-0.008	1.000

Table 7.10: RSM relative error of design outputs at optimum designs: Police mission

Design output/Optimum	Fuel burn	CO_2	NO_x	EPNL	RMS
Fuel burn – CO_2 opt.	0.04	0.05	0.13	-0.59	0.30
NO_x opt.	2.52	2.60	-2.67	1.70	2.40
EPNL opt.	0.38	0.38	0.46	0.00	0.35

Table 7.11: RSM relative error of design outputs at optimum designs: Passenger mission

Design output/Optimum	Fuel burn	CO_2	NO_x	EPNL	RMS
Fuel burn – CO_2 – NO_x opt.	1.08	1.18	-3.59	1.72	2.14
EPNL opt.	0.06	0.07	0.00	-0.02	0.04

Table 7.12: Design output trade-off analysis: Police mission

Flight path comparison	Fuel burn %	CO_2 %	NO_x %	EPNL %
Fuel – CO_2/Baseline	-19.17	-19.12	-25.00	-3.50
NO_x/Baseline	-18.99	-18.93	-26.76	-4.57
EPNL/Baseline	-11.19	-11.14	-16.47	-16.92

Table 7.13: Design output trade-off analysis: Passenger mission

Flight path comparison	Fuel burn %	CO_2 %	NO_x %	EPNL %
Fuel – CO_2 – NO_x/Baseline	-6.81	-6.75	-14.06	-3.68
EPNL/Baseline	3.75	3.68	7.18	-11.06

Table 7.14: Pareto model point design outputs: Police mission

Design output	Relative to baseline %	Pareto model relative error %
Fuel burn	-14.38	0.59
CO_2	-14.24	0.64
NO_x	-22.05	-0.63
EPNL	-10.64	1.13
	RMS rel. error:	**0.74**

Table 7.15: Pareto model point design outputs: Passenger mission

Design output	Relative to baseline %	Pareto model relative error %
Fuel burn	-4.84	-1.26
CO_2	-4.49	-1.18
NO_x	-14.06	-2.13
EPNL	-5.29	-1.65
	RMS rel. error:	**1.59**

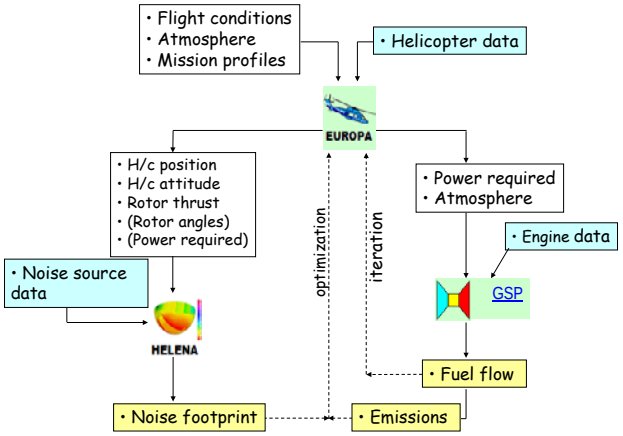

Figure 7.1: Integrated tool architecture

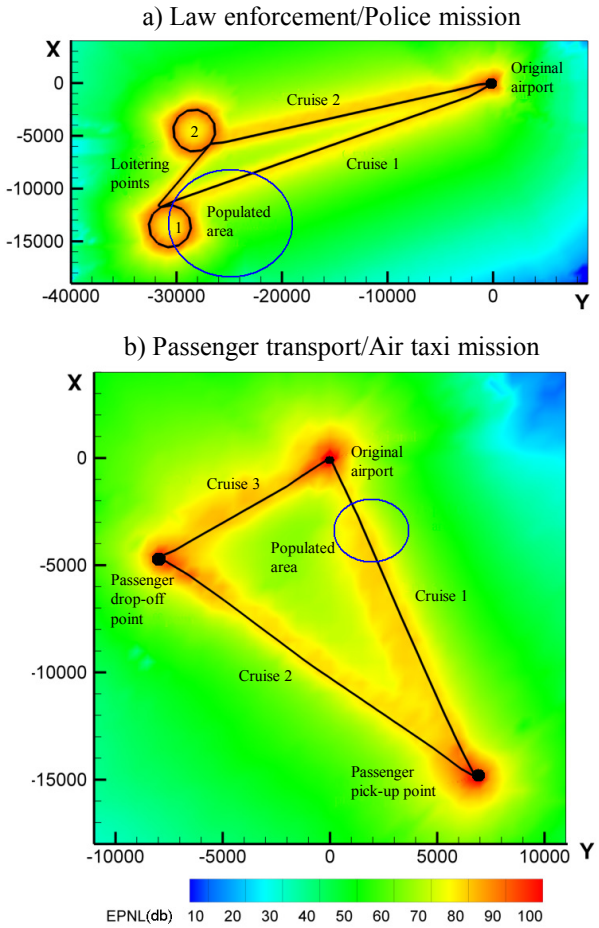

Figure 7.2: Baseline missions EPNL noise contours: a) Police mission, b) Passenger mission

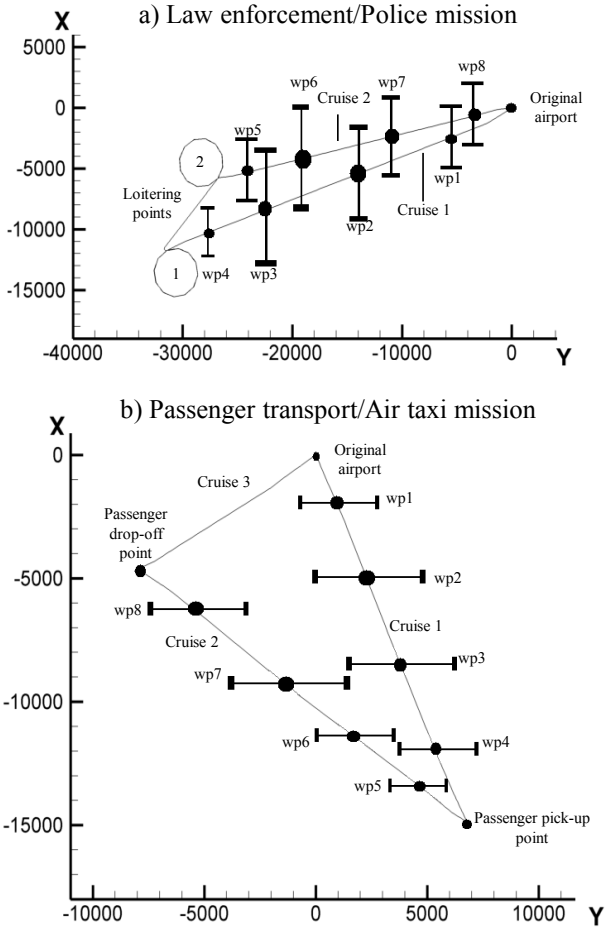

Figure 7.3: Route specification range of variables: a) Police mission, b) Passenger mission

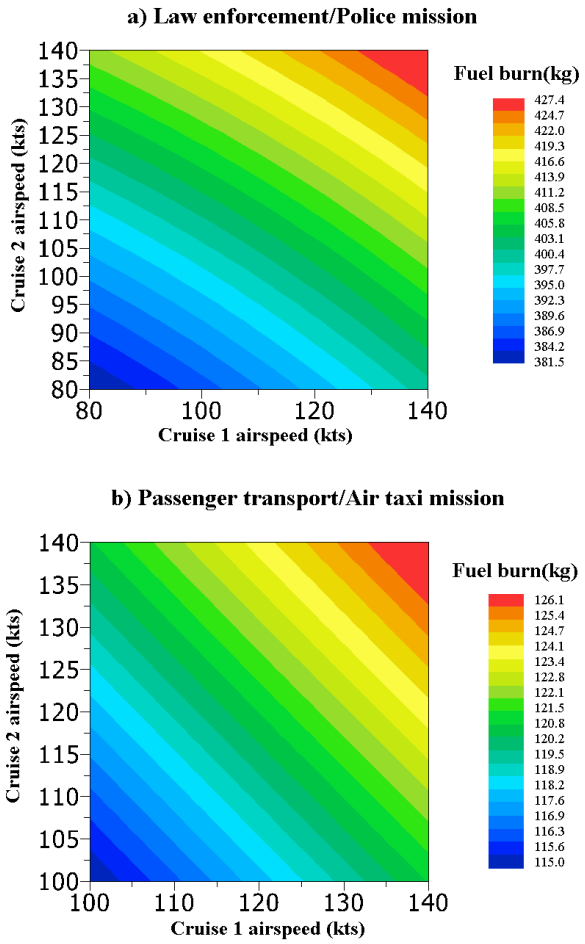

Figure 7.4: Structured RSMs for fuel burn: a) Police mission, b) Passenger mission

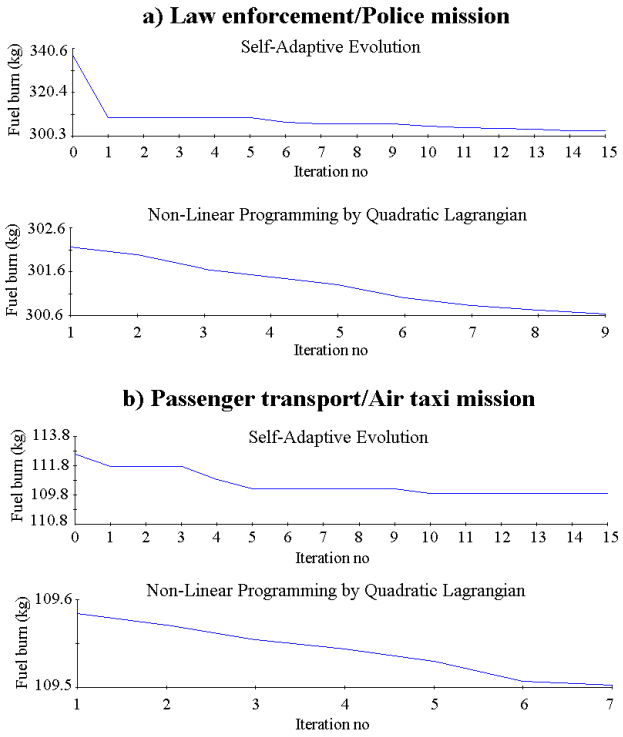

Figure 7.5: Optimisation process for fuel burn: a) Police mission, b) Passenger mission

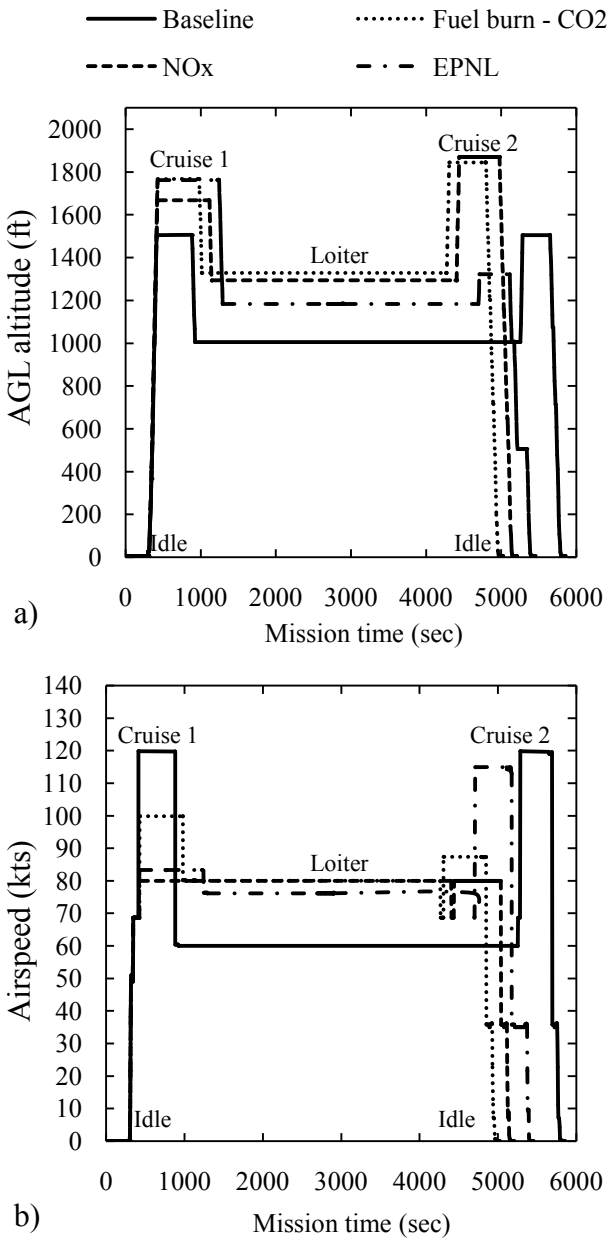

Figure 7.6: Optimum/Baseline flight paths comparison – police mission: a) Altitude, b) Airspeed

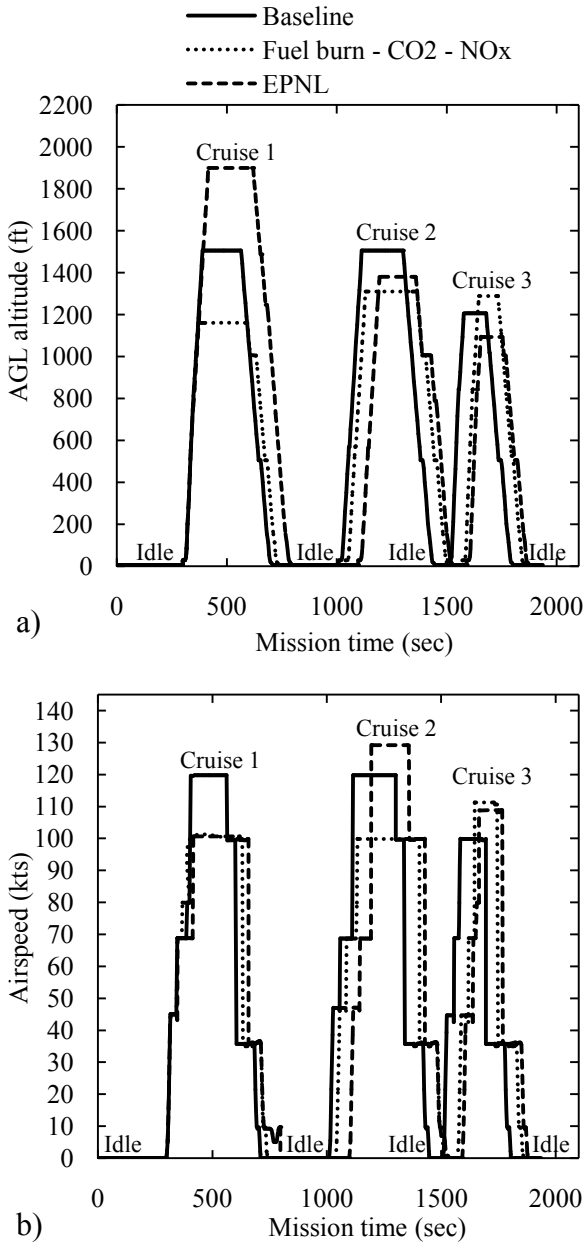

Figure 7.7: Optimum/Baseline flight paths comparison – passenger mission: a) Altitude, b) Airspeed

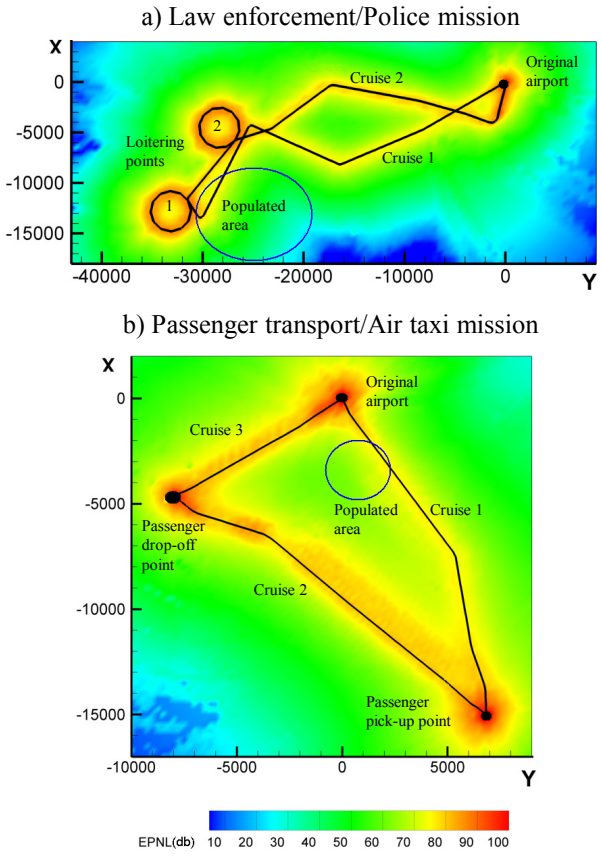

Figure 7.8: EPNL optimised missions noise contours: a) Police mission, b) Passenger mission

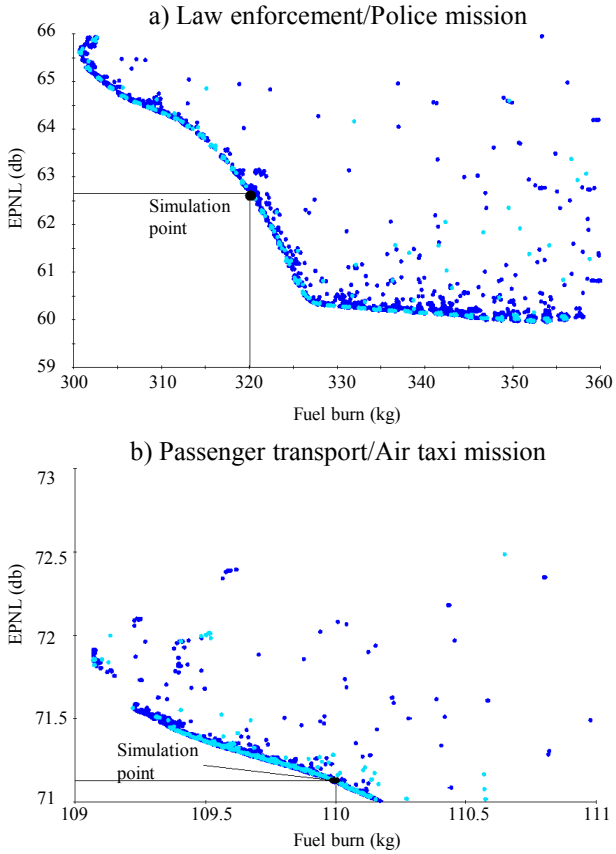

Figure 7.9: Pareto fronts for fuel burn and EPNL: a) Police mission, b) Passenger mission

a) Law enforcement/Police mission

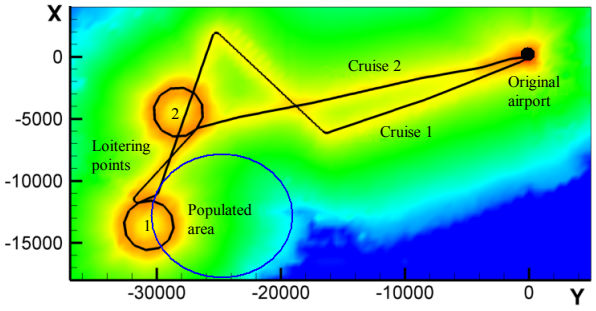

b) Passenger transport/Air taxi mission

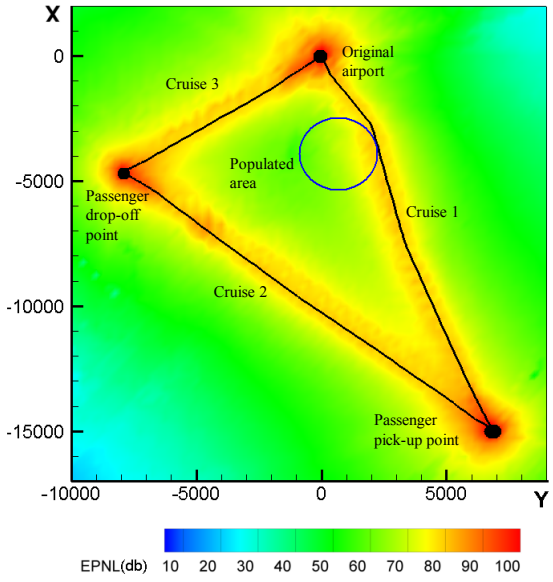

Figure 7.10: Fuel burn – EPNL optimised mission noise contours: a) Police mission, b) Passenger mission

Chapter 8

Conclusions

8.1 Context Overview

Due to the individuality of the research topics elaborated within the preceding chapters, each of them has been accompanied by a separate section discussing conclusions corresponding to the specialized material presented. This chapter recapitulates the most significant conclusions drawn and simultaneously attempts to assess the level of success in terms of addressing the objectives originally set to be achieved. Finally, the overall contribution to knowledge arising from the successful completion of this project is discussed and suggestions for future work are made.

A variety of research topics related to helicopter performance, flight dynamics and mission analysis has been tackled. This effort has been made in order to address the two fundamental requirements identified in the 1^{st} chapter with respect to managing the environmental impact of civil rotorcraft aviation. These essentially comprise:

- Requirement for a generic methodology applicable to existing helicopter configurations, capable of designing optimum operational procedures in terms of fuel burn, chemical emissions and ground noise impact.

- Requirement for a rotorcraft design assessment approach capable of estimating the overall fuel consumption with regards to a designated operation. The employed method has to approximate the 3^{rd} level of Padfield's hierarchical paradigm while simultaneously maintaining a reasonable computational overhead so as to be deployable in the context of multidisciplinary design.

As elaborated within chapter 1, the 1^{st} of the requirements mentioned above essentially constitutes a short-term approach towards reducing the environmental impact associated with rotorcraft operations. It can thus be regarded as a potential path towards addressing

the 2020 ACARE goals with respect to the rotorcraft section of civil aviation. It has also been analyzed that, as regards coming up with a longer-term solution, the potential implementation of conceptual rotorcraft designs has to be thoroughly investigated. This essentially requires a comprehensive performance assessment approach complying with the set of specifications outlined within the 2^{nd} of requirements stated above. It has therefore been concluded that, addressing the specific requirement is essential towards moving forward with the implementation of innovative rotorcraft designs for the purpose of satisfying fuel economy. Hence, it constitutes an effective means towards managing the long-term evolution of the environmental impact associated with civil rotorcraft aviation. For that reason, the majority of the content presented in this Thesis, has been focused towards the 2^{nd} of the requirements outlined above.

8.2 Achievement of Set Objectives

As discussed in chapter 1, in order to effectively address the identified requirements, two broad objectives were defined. These are essentially associated with the design of operational procedures and performance assessment of rotorcraft configurations respectively. The objectives set along with the undertaken actions and achieved results are discussed within this section of this chapter.

8.2.1 Design of optimal operational procedures

Objective

Development and application of a generic, computationally-efficient methodology, capable of optimising civil helicopter operations in a multidisciplinary manner, with respect to total mission fuel consumption and associated environmental impact. The approach needs to be able to cater for the inherent individuality of a complete helicopter operation and as such, it needs to be adaptable to the operational environment dictated by the mission specifications.

Tasks performed and conclusions drawn

An integrated approach applicable to the multidisciplinary design of three-dimensional rotorcraft missions optimised for fuel burn, gaseous emissions and ground noise impact has been structured. The method has been based on the deployment of an integrated tool capable of computing the flight dynamics, engine performance and emitted noise of any defined rotorcraft configuration within any designated mission. A robust and computationally inexpensive optimisation strategy has been developed and implemented.

Extensive application of the developed methodology has been presented for two different, generic – baseline rotorcraft missions representative of modern twin engine light rotorcraft operations. The conclusions drawn are outlined below:

- The developed approach shows promise in achieving considerable reductions in fuel burn, gaseous emissions and ground noise impact simultaneously as regards a wide range of rotorcraft mission.
- The reductions obtained have been found to be dependent on the designated mission application.
- It has been shown that, selection of optimal flight conditions during a mission task element cannot be properly addressed without catering for the individuality of the complete rotorcraft mission.
- It has been demonstrated that, it is possible to design optimum flight paths in a multidisciplinary fashion using a single design input variable: the trade-off between fuel burn and ground noise impact that the designer is willing to accept.

8.2.2 Development of a comprehensive rotorcraft performance assessment approach

Objective

Analytical and computational development of an integrated approach, capable of assessing the overall performance of integrated helicopter–engine systems belonging to the single main/tail rotor class, approximating the 3^{rd} level of Padfield's hierarchy of simulation models. The method has to be able to provide reasonably accurate estimates of various parameters related to rotorcraft flight dynamics, unsteady rotor blade structural loads and engine performance within three-dimensional missions. The associated computational overhead needs to remain within an acceptable level, so that the developed approach can be deployed in a multidisciplinary design process.

Tasks performed and conclusions drawn

The path that has been followed towards addressing the specific objective, has essentially revolved around breaking it down to a series of more specific goals. Each goal has been related to the development of a specialized analytical procedure applicable to an individual aspect of rotorcraft flight dynamics and performance. The numerical approach with regards to each method has been such as to achieve a good compromise between the

fidelity specifications dictated by the 3^{rd} level of Padfield's hierarcy of simulation models and the requirement of a relatively low computational overhead. This approach has been adopted in order for the overall methodology to be deployable within the context of mission analysis as well as within multidisciplinary optimisation, the reason being the accompanied large number of evaluation points.

The identified individual goals as regards the respective broad objective, along with the corresponding undertaken actions and achieved results are discussed below.

1. **Goal set:** *Development of an analytical procedure applicable to the rapid estimation of natural vibration characteristics of helicopter rotor blades*

   Approach followed: A computationally efficient numerical approach based on an effective coupling between Lagrange's equation of motion and Bernoulli–Euler beam theory has been developed. The method has been shown to be able to provide reasonably accurate estimates of the natural vibration characteristics of rotating helicopter blades with nonuniform stiffness and mass per unit length properties. The developed approach has been compared with experimental measurements and FEA results for two small-scale helicopter rotor models. The comparisons have lead to the following conclusions:

   - It has been shown that the method exhibits excellent numerical behavior with no instabilities and good convergence characteristics
   - The method has demonstrated very good, in some cases excellent, agreement with experiments and FEA results with regards to flap/lag natural frequencies.
   - Good agreement has been indicated with respect to the predicted mode shapes.

2. **Goal set:** *Development of a mathematical approach for the treatment of rotor blade flexibility in helicopter aeroelasticity applications*

   Approach followed: An analytical method for the simulation of rotor blade flexibility in helicopter flight dynamics and aeroelasticity applications has been offered. A stable, 2^{nd} order accurate, numerical differentiation scheme has been incorporated for the approximation of motion derivatives. Integral expressions have been provided describing the overall forces and moments exerted by the elastic blades on the rotor hub. The developed approach is compatible with every inflow and blade element aerodynamics theory that can operate in the time domain. It is readily available for implementation in existing codes utilizing the hub-wind reference frame without any change in the offered expressions.

   The analytical method method has been coupled with the Lagrangian formulation developed in chapter 3, the Peters – He induced flow model (Ref. [10]) and the

Leishman – Beddoes blade element aerodynamics model (Ref. [11]). The integrated approach has been deployed in order to investigate the unsteady structural loads of the full-scale, pre-coned hingeless rotor of the MBB Bo 105 helicopter. Extensive comparisons have been waged with data from wind tunnel experiments, flight tests and CAMRAD/JA simulations for a wide range of advance ratios. The following conclusions have been drawn based based on the comparison results:

- The developed numerical approach has been successful in predicting the low-frequency components of oscillatory flapwise and chordwise blade bending moments as measured in the wind-tunnel. Good correlation has been demonstrated between predictions made with the developed rotor model and CAMRAD/JA.
- Accurate predictive qualities have been exhibited with regards to the required main rotor trim control angles and power requirements and for straight and level flight.
- Good correlation has been observed between flapwise bending moment predictions made with the present rotor model and flight test data for all advance ratios. The effect of including higher modal content, reaching up to the 6^{th} flap/lag bending mode, on the predictive accuracy of oscillatory loading with respect to radially outwards locations, has been thoroughly investigated.
- Overall, the very good predictive capacity of the described numerical approach, especially considering its simplicity, generality, ease of implementation and computational efficiency, has been demonstrated.

3. **Goal set:** *Implementation of a computationally inexpensive methodology to account for in-flight aerodynamic rotor–fuselage interaction*

   Approach followed: A three-dimensional, incompressible, potential flow source–panel method has been described and implemented. The method has been deployed for the prediction of the induced velocity perturbations arising from the existence of a small-scale, generic helicopter fuselage in a free-stream. The panel scheme has been coupled with the integrated helicopter flight dynamics formulation solving for the aeroelastic behavior of the main rotor. A comparative evaluation has been waged between source–panel simulation results and flow-field measurements conducted at the NASA Langley subsonic wind tunnel. The effects of fuselage aerodynamic interference on helicopter trim as well as unsteady rotor blade structural loads, have been investigated for the hingeless rotor configuration of the MBB Bo 105 helicopter. Extensive comparisons have been presented with flight test data regarding rotor trim power requirements, swash plate control inputs as well as fuselage attitude and rotor flapping angles. The following conclusions have been drawn:

- Good agreement has been found between potential flow predictions and experimentally measured values with regards to the induced flow components at the imaginary tip-path plane of the main rotor for the case of an isolated fuselage in a free-stream.
- It has been suggested that, accurate estimation of longitudinal cyclic (θ_{1c}) at high speed flight trim conditions, requires that the steady-state rotor–fuselage interference effects are accounted for.
- It has been shown that main rotor power requirements, remaining trim control angles, flapping angles and fuselage attitude angles are relatively unaffected by the steady-state aerodynamic interference effects.
- It has been demonstrated that the inclusion of steady-state fuselage induced perturbations on the main rotor inflow, offers a small improvement on the overall predictive qualities of oscillatory flap/chord bending moments.

4. **Goal set:** *Comprehensive assessment of combined helicopter–engine designs within complete three-dimensional operations*

   Approach followed: A helicopter mission analysis approach utilizing the unsteady aeroelastic rotor model described in chapters 3–4, along with an in-house engine performance simulation tool, has been developed. The proposed method has been shown to be capable of performing flight dynamics simulation approximating the 3^{rd} level of Padfield's hierarchical paradigm of simulation models, while simultaneously catering for the required reduced computational overhead. The approach has therefore been shown to be applicable to the task of rotor design, and therefore to the performance investigation of conceptual configurations within complete rotorcraft missions. The integrated approach has been successfully applied towards the performance analysis of a twin-engine medium helicopter, modeled after the Aérospatiale SA 330. The performance of the integrated helicopter–engine system within two generic helicopter missions, representative of modern twin-engine medium rotorcraft operations has been analyzed. The following conclusions have been drawn:

   - For the range of operating conditions encountered by modern twin-engine medium rotorcraft, the favorable altitude effect on engine thermal efficiency, dominates over the respective penalizing influence on helicopter performance.
   - It has been argued that, thorough identification of the most power-demanding conditions within a complete helicopter operation, cannot be properly addressed without catering for an accurate prediction of the aircraft's time-dependent AUM during flight.

- The potential to deploy a level 3 simulation modeling approach using rapid estimation methods, for the evaluation of helicopter–engine integrated systems within three-dimensional missions, has been demonstrated.

It can therefore be concluded that, the objectives initially set out to be achieved with respect to the requirements elaborated within section "Objectives" of chapter 1, have been thoroughly addressed.

8.3 Contribution to Knowledge

The primary outcome to have risen from the successful completion of the undertaken project, is the computational development of a state of the art simulation framework encompassing all features and analytical procedures elaborated within chapters 3–6 of this thesis. This framework has been named "*HECTOR*" (HEliCopter Omni-disciplinary Research).

HECTOR is capable of analyzing the overall performance of any designated helicopter–engine integrated system, classified under the single-main/single-tail rotor class, within complete and realistically defined three-dimensional missions. Helicopter flight dynamics simulation is carried out with the incorporation of the previously described unsteady, three-dimensional aeroelastic rotor model. Rotor–fuselage aerodynamic interaction effects are accounted for through deployment of the potential flow approach elaborated within chapter 5. Simulations are therefore performed, within the entire mission phase, at a high level of fidelity, while simultaneously maintaining a relatively small computational overhead. *HECTOR* is able to provide reasonably accurate estimates of unsteady blade structural loads and associated trim parameters within each phase of a complete rotorcraft mission. Hence, it is fully capable of being deployed within the context of rotorcraft multidisciplinary design for the purpose of fuel economy within designated types of operations.

HECTOR is a standalone platform with no external dependencies. It has been developed exclusively in FORTRAN 90/95, comprising approximately 50,000 lines of code. The software architecture has been based on a fully modular layout, thus allowing the easy interchange of various simulation models with respect to blade aerodynamics, structural dynamics, rotor inflow, fuselage aerodynamics etc. Software modularity ensures the relatively effortless manipulation of the code structure for the purpose of modeling conceptual configurations such as tilt-rotor aircraft, inter-meshing/co-axial rotor aircraft etc. *HECTOR* is currently being used for rotorcraft-related research carried out within the context of various MSc, PhD and EngD projects at Cranfield University. All numerical results presented in chapters 3–6 of this Thesis have been produced with *HECTOR*, unless stated otherwise.

Further to the development of *HECTOR*, contribution has been made towards various rotorcraft-related research aspects throughout the process leading to the successful completion of this work. These are essentially associated with the subjects dealt with and elaborated within the respective chapters of this Thesis. These are outlined below:

- Analytical development of a computationally efficient numerical approach for the rapid estimation of natural vibration characteristics of helicopter rotor blades. The method's computational characteristics have been thoroughly investigated and closed form expressions have been offered for the immediate simulation of freely-hinged, spring-hinged and hingeless helicopter rotor blades. The developed approach has been extensively validated with existing numerical and experimental data from the public domain.

- Analytical development of a generic methodology targeting the treatment of rotor blade flexibility in helicopter aeroelasticity applications. The approach has been shown to be compatible with any rotor inflow and blade aerodynamics theory applicable in the time domain. Extensive validation has been waged with flight test data available in the public domain in terms of main rotor trim controls and unsteady rotor blade bending moments.

- Investigation of in-flight steady-state rotor–fuselage aerodynamic interference effects on various helicopter trim parameters and unsteady blade structural loads. A standardized method based on potential flow has been described, validated with experimental data, and proposed for implementation in various flight dynamics simulations codes in order to account for steady-state rotor–fuselage aerodynamic interaction effects.

- Development of an integrated methodology for the comprehensive assessment of combined helicopter–engine designs, within complete, three-dimensional operations. Closed form expressions have been offered for the immediate implementation of earth geography definition based on WGS 84 with very good levels of accuracy. The potential to deploy level-3 helicopter simulation models within the context of mission analysis has been demonstrated.

- Development and application of a generic, cost-efficient methodology, capable of optimising modern helicopter operations in a multidisciplinary manner, with respect to total mission fuel consumption and associated environmental impact. It has been argued that selection of optimum flight conditions within a designated mission phase, cannot be addressed without properly catering for the individuality of the complete operation. It has been shown that, it is feasible to design optimum operations using a single design variable: The respective trade-off between fuel burn and ground noise impact that the mission designer is willing to accept.

Furthermore, with respect to the work conducted for Clean Sky TE within the three-year period of the undertaken project, contribution has been made towards the development, beta-testing and debugging of *Phoenix*. As elaborated within Chapter 7, *Phoenix* has been structured based on an existing helicopter flight dynamics model (EUROPA, Ref. [86]), an engine performance simulation code (GSP, Ref. [88]) and a rotorcraft noise propagation model (HELENA, Ref. [103]). A second simulation framework has been developed utilizing *Phoenix*, capable of performing multidisciplinary design of optimum rotorcraft operations in terms of fuel consumption, produced chemical emissions and ground noise impact. The overall framework has been built using the process integration tool "Noesis Optimus" (Ref. [100]) and has been used to produce all numerical results presented in chapter 7. It has also been made available within Clean Sky TE for rotorcraft trajectory optimisation studies.

8.4 Future Work

Although only the cases of flapwise and lagwise bending have been elaborated within the context of this work, the proposed approach within chapter 3 can also be extrapolated to the case of torsional vibrations. Application of a more refined condition for the normalization of the Bernoulli–Euler functions may improve the predictive accuracy at high-speed rotating conditions with respect to the simulation of small-scale rotor models.

Although elastically uncoupled flap and lag blade motion has been considered within chapter 4, the modal characteristics of any employed theory can be used with any level of coupling considered. The effects of rotor blade torsional vibrations on the main rotor trim parameters and associated structural loads could be thoroughly investigated.

The aspects of flight dynamics related to helicopter stability and response could also be tackled using the analytical procedures developed within this Thesis. Both linear as well as non-linear models could be derived using the integrated aeroelastic rotor aircraft model described within chapters 3–5. This process is essential with respect to the optimisation of conceptual and existing helicopter designs. Comprehensive assessment of the stability and control characteristics of an optimised conceptual or even existing rotorcraft design, is a prerequisite for the purpose of achieving airworthiness certification.

Although the mission analysis approach described within chapter 6 does not cater for transient flight dynamics simulation, the developed methodology could also be extrapolated in order to cater for the simulation of transient rotorcraft take-off and landing maneuvers. This would essentially require numerical integration of Euler's non-linear differential equations for the kinematics of rigid bodies, applied to the helicopter fuselage. Implementation of transient engine performance simulation, could also lead to the detailed determination of aircraft control schedules leading to optimum take-off and landing maneuvers in terms of fuel consumption.

The NO_x system behavior has been found difficult to capture accurately within chapter 7 using simple RBF interpolation. This has been attributed to the highly non-linear nature of the NO_x design output with respect to the mission specification variables. Therefore the incorporation of higher-order interpolation methods is proposed for the structuring of RSMs as regards the specific design output. This process could also substantially improve the respective predicted accuracy of the associated RSMs corresponding to the remaining design outputs. The overall error within the deployed optimisation strategy could therefore be considerably reduced and thus, the accuracy of the overall methodology significantly improved.

References

[1] Goulos, I., Mohseni, M., Pachidis, V., d'Ippolito, R., and Stevens, J., "Simulation framework development for helicopter mission analysis," *Proceedings of ASME Turbo Expo 2010*, Vol. 3, 2010, pp. 843–852.

[2] d'Ippolito, R., Stevens, J., Pachidis, V., Berta, A., Goulos, I., and Rizzi, C., "A Multidisciplinary Simulation Framework for Optimization of Rotorcraft Operations and Environmental Impact," *2nd International Conference on Engineering Optimization*, 2012.

[3] Goulos, I., Pachidis, V., D'Ippolito, R., Stevens, J., and Smith, C., "An Integrated Approach for the Multidisciplinary Design of Optimum Rotorcraft Operations," *Journal of Engineering for Gas Turbines and Power*, Vol. 134(9), 2012.

[4] Clarke, J.-P., "The role of advanced air traffic management in reducing the impact of aircraft noise and enabling aviation growth," *Journal of Air Transport Management*, Vol. 9, 2003, pp. 161–165.

[5] Brooker, P., "Civil Aircraft Design Priorities: Air Quality? Climate Change? Noise?" *The Aeronautical Journal*, Vol. 110(1110), 2005, pp. 517–532.

[6] "Clean Sky Joint Technology Initiative (JTI) web-page," http://www.cleansky.eu/.

[7] Padfield, G. D., *Helicopter Flight Dynamics*, Blackwell Publishing, 2007.

[8] Brown, R. and Houston, S., "Comparison of Induced Velocity Models for Helicopter Flight Mechanics," *Journal of Aircraft*, Vol. 37, August 2000, pp. 623–629.

[9] Bhagwat, M. J. and Leishman, J. G., "Transient Rotor Inflow Using a Time-Accurate Free-Vortex Wake Model," *39th AIAA Aerospace Sciences Meeting & Exhibit*, 2001.

[10] Peters, D. A., Boyd, D. D., and He, C. J., "Finite-State Induced-Flow Model for Rotors in Hover and Forward Flight," *Journal of the American Helicopter Society*, Vol. 10(01), 1989, pp. 5–17.

[11] Leishman, J. G. and Beddoes, T., "A Semi-Empirical Model for Dynamic Stall," *Journal of the American Helicopter Society*, Vol. 34, No. 3, 1989, pp. 3–17.

[12] Peterson, R. L., Maier, T., Langer, H. J., and Trnapp, N., "Correlation of Wind Tunnel and Flight Test Results of a Full-Scale Hingeless Rotor," *American Helicopter Society Aeromechanics Specialists Conference*, January 19-21 1994.

[13] Berry, J. D. and Althoff, S. L., "Computing induced velocity perturbations due to a helicopter fuselage in a free stream," Tech. Rep. 4113, National Aeronautics and Space Administration, 1989.

[14] Lewis, W., "An Aeroelastic Model Structure Investigation for a Manned Real-time Rotorcraft Simulation," *47th American Helicopter Society International Annual Forum*, 1993.

[15] Sturisky, S. H. and Schrage, D. P., "System Identification Validation of an AH-64 Aeroelastic Simulation Model," *47th American Helicopter Society International Annual Forum*, 1993.

[16] Turnour, S. R. and Celi, R., "Modeling of Flexible Rotor Blades for Helicopter Flight Dynamics Applications," *Journal of the American Helicopter Society*, Vol. 41(1), January 1996, pp. 52–66.

[17] Spence, A. and Celi, R., "Coupled Rotor-Fuselage Dynamics in Turning Flight," *AIAA Dynamics Specialists Conference*, 1992.

[18] Kim, F. D., Celi, R., and Tischler, M. B., "Forward flight trim calculation and frequency response validation of a high-order helicopter simulation model," *47th Annual Forum of the American Helicopter Society*, Vol. 1, 1991, pp. 155–168.

[19] Houbolt, J. C. and Brooks, G. W., "Differential Equations of Motion for Combined Flapwise Bending, Chordwise Bending, and Torsion of Twisted Nonuniform Rotor Blades," Tech. Rep. TN-3905, National Advisory Committee for Aeronautics, 1957.

[20] Murthy, V. R., "Dynamic Characteristics of Rotor Blades," *Journal of Sound and Vibration*, Vol. 49(4), 1976, pp. 483–500.

[21] Murthy, V. R. and Nigam, N. C., "Dynamic Characteristics of Stiffened Rings by Transfer Matrix Approach," *Journal of Sound and Vibration*, Vol. 39(2), 1975, pp. 237–245.

[22] Hunter, W. F., "Integrating–Matrix Method for Determining The Natural Vibration Characteristics of Propeller Blades," Tech. Rep. TN-D-6064, Natioanal Aeronautics and Space Administration, 1970.

[23] Surace, G., Anghel, V., and Mares, C., "Coupled Bending-Bending-Torsion Vibration Analysis of Rotating Pretwisted Blades: An Integral Formulation and Numerical Examples," *Journal of Sound and Vibration*, Vol. 206(4), 1997, pp. 473–486.

[24] Bielawa, R., *Rotary Wing Structural Dynamics and Aeroelasticity*, AIAA education series, American Institute of Aeronautics and Astronautics, 2006.

[25] Done, G. and Balmford, D., *Bramwells Helicopter Dynamics*, Butterworth-Heinemann, 2001.

[26] Bisplinghoff, R. L., Ashley, H., and Halfman, R. L., *Aeroelasticity*, Dover Publications, 1996.

[27] Wilde, E. and Price, H., "A Theoretical Method for Calculating Flexure and Stresses in Helicopter Rotor Blades: Development of a Variational Procedure based on the Rayleigh-Ritz Method which Leads to a Rapid Estimation of the Flapwise Vibration Modes and Frequencies," *Aircraft Engineering and Aerospace Technology*, Vol. 37(2), 1965, pp. 45–54.

[28] A.Fasana and Marchesiello, S., "Rayleigh-Ritz Analysis of Sandwich Beams," *Journal of Sound and Vibration*, Vol. 241(4), 2001, pp. 643–652.

[29] Duncan, W., "Mechanical Admittances and Their Applications to Oscillation Problems," Tech. Rep. R. & M. 2000, Aeronautical Research Council, 1947.

[30] Duncan, W. J. and Lindsay, D. D., "Methods for Calculating the Frequencies of Overtones," Tech. Rep. R. & M. 1888, Great Britain Aeronautical Research Committee, 1939.

[31] Wilkie, W. K., Mirick, P. H., , and Langston, C. W., "Rotating Shake Test and Modal Analysis of a Model Helicopter Rotor Blade," Tech. Rep. NASA TM-4760, National Aeronautics and Space Administration, June 1997.

[32] Sharpe, D. L., "An Experimental Investigation of the Flap-Lag-Torsion Aeroelastic Stability of a Small-Scale Hingeless Helicopter Rotor in Hover," Tech. Rep. NASA TP-2546, National Aeronautics and Space Administration, January 1986.

[33] Srinivasan, A., Cutts, D., Shu, H., Sharpe, D., and Bauchau, O., "Structural Dynamics of a Helicopter Rotor Blade System," *Journal of the American Helicopter Society*, Vol. 35, No. 1, 1990, pp. 75–85.

[34] Bauchau, O. A. and Hong, C.-H., "Finite Element Approach to Rotor Blade Modeling," *Journal Of The American Helicopter Society*, Vol. 1(1), January 1987, pp. 60–67.

[35] Bauchau, O. and Hong, C., "NONLINEAR COMPOSITE BEAM THEORY." *Journal of Applied Mechanics, Transactions ASME*, Vol. 55, No. 1, 1988, pp. 156–163.

[36] Howlett, J. J., "UH-60A Black Hawk Engineering Simulation Program:Volume I– Mathematical Model," Tech. Rep. CR-166309, NASA, December 1981.

[37] Ballin, M. G., "Validation of a Real-Time Engineering Simulation of the UH-60A Helicopter," Tech. Rep. TM-88360, NASA, February 1987.

[38] Diftler, M. A., "UH-60A Helicopter Stability Augmentation Study," *14th European Rotorcraft Forum*, 1988.

[39] Kim, F. D., Celi, R., and Tischler, M. B., "High-Order State Space Simulation Models of Helicopter Flight Mechanics," *Journal of the American Helicopter Society*, Vol. 38(4), 1993, pp. 16–27.

[40] Curtiss, H. C. and Zhao, X., "A Linearized Model of Helicopter Dynamics Including Correlation with Flight Test," *2nd International Conference on Rotorcraft Basic Research*, 1988.

[41] Chaimovitz, M., Rosen, A., and Rand, O., "A Generic Harmonic Rotor Model for Helicopter Flight Simulation," *17th European Rotorcraft Forum*, 1991.

[42] Miller, D. and White, F., "Treatment of the Impact of Rotor-Fuselage Coupling on Helicopter Handling Qualities," *American Helicopter Society 43rd Annual Forum*, Vol. 2, 1987, pp. 631–644.

[43] Talbot, P. D., Tinling, B. E., Decker, W. A., and Chen, R. T. N., "A Mathematical Model of a Single Main Rotor Helicopter for Piloted Simulation," Tech. Rep. TM-84281, National Aeronautics and Space Administration, September 1982.

[44] Padfield, G., Thorne, R., Murray-Smith, D., Black, C., and Caldwell, A., "U.K. Research into System Identification for Helicopter Flight Mechanics," *Vertica*, Vol. 11(4), 1987, pp. 665–684.

[45] Brown, R., "Rotor Wake Modeling for Flight Dynamic Simulation of Helicopters," *AIAA journal*, Vol. 38, No. 1, 2000, pp. 57–63.

[46] Johnson, W., "Rotorcraft aerodynamics models for a comprehensive analysis," *American Helicopter Society Forum*, Vol. 1, 1998, pp. 71–93.

[47] Pitt., D. M. and Peters, D. A., "Theoretical Prediction of Dynamic Inflow Derivatives," *Vertica*, Vol. 5, No. 1, 1981, pp. 21–34.

[48] Peters, D. A. and HaQuang, N., "Dynamic Inflow for Practical Applications," *Journal of the American Helicopter Society*, Vol. 33(4), 1988, pp. 64–68.

[49] Gaonkar, G. and Peters, D. A., "A Review of Dynamic Inlfow Modeling for Rotorcraft Flight Dynamics," *Vertica*, Vol. 12(3), 1988, pp. 213–242.

[50] Shupe, N., "A Study on the Dynamic Motions of Hingeless Rotored Helicopters," Tech. Rep. TR ECOM-3323, US Army Electronics Command, August 1970.

[51] Curtiss, H. and Shupe, N., "A Stability and Control Theory for Hingeless Rotors," *27th Annual Forum of the American Helicopter Society*, 1971.

[52] Theodore, C. and Celi, R., "Helicopter Flight Dynamic Simulation with Refined Aerodynamics and Flexible Blade Modeling," *56th Annual Forum of the American Helicopter Society*, May 2-4, 2000.

[53] Bagai, A. and Leishman, J. G., "Rotor Free-Wake Modeling using a Pseudo-Implicit Technique - Including Comparisons with Experimental Data," *Journal Of The American Helicopter Society*, Vol. 40(3), 1995, pp. 29–41.

[54] Peters, D. A. and He, C. J., "Correlation of measured induced velocities with a finite-state wake model," *Journal of the American Helicopter Society*, Vol. 36, No. 3, 1991, pp. 59–70.

[55] Gaonkar, G. H. and Peters, D. A., "Effectiveness of Current Dynamic-Inflow Models in Hover and Forward Flight," *Journal Of The American Helicopter Society*, Vol. 31(2), 1986, pp. 47–57.

[56] Staley, J. A., "Validation of Rotorcraft Flight Simulation Program through Correlation with Flight Data for Soft-in-plane Hingeless Rotor," Tech. rep., Boeing - Vertol Company, 1976.

[57] Johnson, W., "A comprehensive Analytical Model of Rotorcraft Aerodynamics and Dynamics Vol. I: Theory Manual," Tech. rep., Johnson Aeronautics, 1988.

[58] Johnson, W., "A comprehensive Analytical Model of Rotorcraft Aerodynamics and Dynamics Vol. II: User Manual," Tech. rep., Johnson Aeronautics, 1988.

[59] Johnson, W., "General free wake geometry calculation for wings and rotors," *51st American Helicopter Society Annual Forum*, Vol. 1, 1995, pp. 137–153.

[60] Rinehart, S., "Computer Program Y-59 User's Report Program Documentation for Predicting Whirl Flutter, Free Vibration and Forced Response of a Prop-Rotor System," Tech. rep., Rochester Applied Sciences Associates, January 1971.

[61] Padfield, G. D., , McCallumand, A. T., Haverdings, H., Dequinand, A. M., Haddonand, D., Kampaand, K., Bassetand, P. M., and von Grunhagenand, W., "Predicting Rotorcraft Flying Qualities Through Simulation Modelling. A Review of Key Results from Garteur AG06," *Proceedings of the 21st Annual European Rotorcraft Forum*, August 1995.

[62] Colin, T. R., *Helicopter Flight Dynamics Simulation with Refined Aerodynamic Modeling*, Ph.D. thesis, University of Maryland, College Park, 2000.

[63] Mangler, K. W. and Squire, H. B., "The Induced Velocity Field of a Rotor," Tech. Rep. R. & M. No. 2642, Aeronautical Research Council, 1953.

[64] Peters, D., "How dynamic inflow survives in the competitive world of Rotorcraft aerodynamics the Alexander Nikolsky honorary lecture," *Journal of the American Helicopter Society*, Vol. 54, No. 1, 2009, pp. 1–15.

[65] Yu, K. and Peters, D., "Nonlinear state-space modeling of dynamic ground effect," *Journal of the American Helicopter Society*, Vol. 50, No. 3, 2005, pp. 259–268.

[66] Prasad, J., Zhao, J., and Peters, D., "Rotor Dynamic Wake Distortion Model for Helicopter Maneuvering Flight," *Journal of the American Helicopter Society*, Vol. 49, No. 4, 2004, pp. 414–424.

[67] Peters, D. A., Morillo, J. A., and Nelson, A. M., "New Developments in Dynamic Wake Modeling for Dynamics Applications," *Journal Of The American Helicopter Society*, Vol. 48(2), 2003, pp. 120–127.

[68] Landgrebe, A. J., "An Analytical Method for Predicting Rotor Wake Geometry," *Journal Of The American Helicopter Society*, Vol. 14(4), 1969, pp. 20–32.

[69] Landgrebe, A. J., "An Analytical and Experimental Investigation of Helicopter Rotor Hover Performance and Wake Geometry Characteristics," Tech. Rep. USAAM-RDL TR71-24, U.S. Army Air Mobility Research and Development Laboratory, June 1971.

[70] Leiper, D. C. A., "Free Wake Analysis. A method for the Prediction of Helicopter Rotor Hovering Performance," *Journal of the American Helicopter Society*, Vol. 15, No. 1, 1970, pp. 3–11.

[71] Sadler, S. G., "A method for predicting helicopter wake geometry, wake-induced flow and wake effects on blade airloads," *27th Annual National V/STOL Forum*, May 1971.

[72] Bhagwat, M. and Leishman, J., "Stability, consistency and convergence of time-marching free-vortex rotor wake algorithms," *Journal of the American Helicopter Society*, Vol. 46, No. 1, 2001, pp. 59–71.

[73] Leishman, J., Bhagwat, M., and Bagai, A., "Free-vortex filament methods for the analysis of helicopter rotor wakes," *Journal of Aircraft*, Vol. 39, No. 5, 2002, pp. 759–775.

[74] Berry, J. and Bettschart, N., "Rotor-Fuselage Interaction: Analysis and Validation with Experiment," *American Helicopter Society 53rd Annual Forum*, 1997.

[75] Crimi, P. and Trenka, A. R., "Theoretical prediction of the flow in the wake of a helicopter rotor: Addendum: Effects due to a fuselage in a constant, nonuniform flow," Tech. Rep. BB-199Y-S-3, Cornell Aeronautical Laboratory, 1966.

[76] Keys, C., "Rotary-wing Aerodynamics, Volume II - Performance Prediction of Helicopters," Tech. Rep. NASA CR-3083, National Aeronautics and Space Administration, 1979.

[77] Johnson, W. and Yamauchi, G. K., "Applications of an Analysis of Axisymmetric body Effects on Rotor Performance and Loads," *10th European Rotorcraft Forum*, 1984.

[78] Schweitzer, S., *Computational Simulation of Flow Around Helicopter Fuselages*, Master's thesis, The Pennsylvania State University, 1999.

[79] Ghee, T., Berry, J., Zori, L., and Elliot, J., "Wake Geometry Measurements and Analytical Calculations on a Small-Scale Rotor Model," Tech. Rep. NASA TP 3584, National Aeronautics and Space Administration, 1997.

[80] Lorber, P. F. and Egolf, T. A., "An Unsteady Helicopter Rotor-Fuselage Interaction Analysis," Tech. Rep. NASA CR-4178, National Aeronautics and Space Administration, 1988.

[81] Renaud, T., O'Brien, D., Smith, M., and Potsdam, M., "Evaluation of Isolated Fuselage and Rotor-Fuselage Interaction using CFD," *American Helicopter Society 60th Annual Forum*, 2004.

[82] Lee, B. S., Jung, M. S., and Kwon, O. J., "Numerical Simulation of Rotor-Fuselage Aerodynamic Interaction Using an Unstructured Overset Mesh Technique," *Journal of Aeronautical & Space Sciences*, Vol. 11(1), 2010, pp. 1–9.

[83] Katz, J. and Plotkin, A., *Low-Speed Aerodynamics*, Cambridge Aerospace Series, Cambridge University Press, 2001.

[84] Hess, J. L. and Smith, A. M. O., "Calculation of Non-Lifting Potential Flow About Arbitrary Three-Dimensional Bodies," Tech. Rep. Report No. E.S. 40622, Douglas Aircraft Co., Inc., 1962.

[85] Mohseni, M., *HELIX - Simulation Framework Development for Assessment of Rotorcraft Engines*, Ph.D. thesis, Cranfield University, 2011.

[86] Serr, C., Hamm, J., Toulmay, E., Polz, G., Langer, H. J., Simoni, M., andA. Russo, M. B., Vozella, A., Young, C., Stevens, J., Desopper, A., and Papillier, D., "Improved Methodology for Take-Off and Landing Operational Procedures - The RESPECT Programme," *25th European Rotorcraft Forum*, 1999.

[87] Serr, C., Polz, G., Hamm, J., Hughes, J., Simoni, M., Ragazzi, A., Desopper, A., Taghizad, A., Langer, H., Young, C., Russo, A., Vozella, A., and Stevens, J., "Rotorcraft Efficient and Safe Procedures for Critical Trajectories," *Air & Space Europe*, Vol. 3(3), 2001, pp. 266–270.

[88] Visser, W., "Gas Turbine Simulation at NLR," *Symposium on Simulation Technology*, 1995.

[89] Visser, W. and Broomhead, M., "GSP: A generic object-oriented gas turbine simulation environment," Tech. Rep. NLR-TP-2000-267, National Aerospace Laboratory NLR, 2000.

[90] Macmillan, W. L., *Development of a Module Type Computer Program for the Calculation of Gas Turbine Off Design Performance*, Ph.D. thesis, Department of Power and Propulsion, Cranfield University, 1974.

[91] European Organization for the Safety of Air Navigation (EUROCONTROL) and Institute of Geodesy and Navigation (IfEN), Brussels, Belgium, *WGS 84 IMPLEMENTATION MANUAL*, 1998.

[92] Li, Y. G., Marinai, L., Gatto, E. L., Pachidis, V., and Pilidis, P., "Multiple-Point Adaptive Performance Simulation Tuned to Aeroengine Test-Bed Data," *Journal of Propulsion and Power*, Vol. 25(3), 2009, pp. 635–641.

[93] Pachidis, V., Pilidis, P., Marinai, L., and Templalexis, I., "Towards a full two dimensional gas turbine performance simulator," *Aeronautical Journal*, Vol. 111(1121), 2007, pp. 433–442.

[94] Bousman, W. G., Young, C., Toulmay, F., Gilbert, N. E., Strawn, R. C., Miller, J. V., Costes, T. H. M. M., and Beaumier, P., "A Comparison of Lifting-Line and CFD Methods with Flight Test Data from a Research Puma Helicopter," Tech. Rep. TM-110421, National Aeronautics and Space Administration, October 1996.

[95] Gunston, B., *Jane's Aero-engines*, Jane's Information Group, 1996.

[96] Goulos, I., Pachidis, V., and Pilidis, P., "Lagrangian Formulation for the Rapid Estimation of Helicopter Rotor Blade Vibration Characteristics," *Article submitted to the Journal of the American Helicopter Society*, 2012.

[97] Cheeseman, I. C. and Bennet, W. E., "The effect of the Ground on a Helicopter Rotor in Forward Flight," Tech. Rep. R & M No 3021, Aeronautical Research Council, 1957.

[98] Celis, C., Long, R., Sethi, V., and Zammit-Mangion, D., "On Trajectory Optimization for Reducing the Impact of Commercial Aircraft Operations on the Environment," *19th ISABE Conference*, 7-11 September 2009.

[99] Goulos, I., C.Celis, Pachidis, V., d'Ippolito, R., and Stevens, J., "Simulation framework development for aircraft mission analysis," *Proceedings of ASME Turbo Expo 2010*, Vol. 1, 2010, pp. 341–351.

[100] Noesis Solutions, Leuven, Belgium, *OPTIMUS REV 8 - Manual*, November 2008.

[101] Visser, W. and Broomhead, M., "GSP, A Generic Object Oriented Gas Turbine Simulation Environment," *Procceedings of ASME Turbo Expo 2000*, 2000.

[102] Visser, W. and Kluiters, S., "Modeling the effects of operating conditions and alternative fuels on gas turbine performance and emissions," Tech. Rep. NLR-TP-98629, National Aerospace Laboratory NLR, 1998.

[103] Oosten, N. V., "HELENA, a new tool for helicopter noise footprint calculation," *IMAGINE Final Meeting*, Budapest, Hungary, October 25 2006.

[104] Lorenzen, T. and Anderson, V., *Design of Experiments: A No-Name Approach*, CRC Press, 1993.

[105] Olsson, A., Sandberg, G., and Dahlblom, O., "On Latin hypercube sampling for structural reliability analysis," *Structural Safety*, Vol. 25, No. 1, 2003, pp. 47 – 68.

[106] Wright, G. B., *Radial Basis Function Interpolation: Numerical and Analytical Development*, Ph.D. thesis, Department of Applied Mathematics, University of Colorado, 2003.

[107] Schwefel, H., *Numerical optimization of computer models*, Interdisciplinary systems research, Wiley, 1981.

[108] Schittkowski, K., "Theory, implementation and test of a nonlinear programming algorithm," *Optimization Methods in Structural Design*, 1983.

[109] Schittkowski, K., "On the convergence of a sequential quadratic programming method with an augmented Lagrangian search direction," *Optimization*, Vol. 14, 1983, pp. 197–216.

[110] Hock, W. and Schittkowski, K., "A comparative performance evaluation of 27 nonlinear programming codes," *Computing*, Vol. 30, 1983, pp. 335–358.

[111] Das, I. and Dennis, J. E., "Normal-Boundary Intersection: A New Method for Generating the Pareto Surface in Nonlinear Multicriteria Optimization Problems," *SIAM Journal on Optimization*, Vol. 8, 1998, pp. 631–657.

[112] Bayraktar, H. and Turalioglu, F., "A Kriging-based approach for locating a sampling site in the assessment of air quality," *Stochastic Environmental Research and Risk Assessment*, Vol. 19, 2005, pp. 301–305.

Appendix A

This appendix contains a comprehensive derivation of assumed deformation functions for flapwise and lagwise blade motion through the application of Bernoulli–Euler beam theory. The appropriate boundary conditions are applied for a hingeless, a freely-hinged and a spring-hinged articulated rotor blade. Closed form expressions are provided for the first N mode shapes as well as their first, second and third spatial derivatives. The presented functions are readily implementable in Lagrange's equation of motion for the approximation of the rotor blade's strain and kinetic energy.

The Bernoulli–Euler mode shape for a given frequency parameter β along with its first, second and third derivatives with respect to the modal ordinate x are given below

$$\Phi(x) = A\sin\beta x + B\cos\beta x + C\sinh\beta x + D\cosh\beta x \tag{A.1a}$$

$$\Phi^{'}(x) = A\beta\cos\beta x - B\beta\sin\beta x + C\beta\cosh\beta x + D\beta\sinh\beta x \tag{A.1b}$$

$$\Phi^{''}(x) = -A\beta^2\sin\beta x - B\beta^2\cos\beta x + C\beta^2\sinh\beta x + D\beta^2\cosh\beta x \tag{A.1c}$$

$$\Phi^{'''}(x) = -A\beta^3\cos\beta x + B\beta^3\sin\beta x + C\beta^3\cosh\beta x + D\beta^3\sinh\beta x \tag{A.1d}$$

The boundary conditions of the rotor blade can be applied on Eqs. (A.1a−A.1d). Any type of user-imposed boundary condition is applicable. This process leads to the formation of the matrix Eq. (3.7). Equation (3.8) provides the required condition in order for matrix Eq.(3.7) to have a non-trivial solution. Due to the nature of the coefficients contained in $[A_{Bernoulli}]$, Eq. (3.8) is a transcendental equation that can be evaluated numerically. This can be achieved through marching within the β domain until the required N first values of β that satisfy Eq. (3.8) are obtained. For each β solution of Eq. (3.8), a corresponding mode shape is obtained. This is achieved by setting the integration constant A within $\{x_{Bernoulli}\}$ equal to an arbitrary real value c. The matrix Eq. (3.7) is subsequently used to determine the remaining integration constants as functions of A. Equations (A.1a−A.1d) are then deployed in order to derive the corresponding mode shape along with its derivatives.

Until this stage, the modal amplitude is arbitrarily defined due to the selection of a random constant for A. The non-uniqueness of the amplitude of each acquired modal function is alleviated by deploying the normalization condition given by Eq. (3.9). A modal normalization parameter is derived based on Eq. (3.9) for each of the acquired

mode shapes which is given by

$$C_{norm,i} = \sqrt{\frac{1}{\int_0^l \rho A_{midspan} \Phi_i^2(x)\,\mathrm{d}x}}, \qquad i = 1, ...N \tag{A.2}$$

Equation (A.2) can be modified according to any imposed normalization condition. The acquired mode shapes, along with their first and second derivatives, can be readily normalized and transferred to the local beam radius r domain using the following equations

$$\phi_i^{flap/lag}(r) = C_{norm,i}\Phi_i(x + eR) \tag{A.3a}$$
$$\phi_i^{'flap/lag}(r) = C_{norm,i}\Phi_i^{'}(x + eR) \tag{A.3b}$$
$$\phi_i^{''flap/lag}(r) = C_{norm,i}\Phi_i^{''}(x + eR) \tag{A.3c}$$

for $i = 1, ...N$ and flapwise or lagwise bending respectively.

The specialized sub-cases for the aforementioned three different types of rotor blade configurations are described individually in the corresponding sections within this appendix.

Bernoulli–Euler Solution for a Hingeless Rotor Blade

The boundary conditions for a hingeless rotor blade at the hub and tip modal ordinate locations ($x = 0$ and $x = l$ respectively) are defined as follows

$$w(0,t) = 0 \Rightarrow \Phi(0) = 0 \tag{A.4a}$$
$$w^{'}(0,t) = 0 \Rightarrow \Phi^{'}(0) = 0 \tag{A.4b}$$
$$w^{''}(l,t) = 0 \Rightarrow \Phi^{''}(l) = 0 \tag{A.4c}$$
$$w^{'''}(l,t) = 0 \Rightarrow \Phi^{'''}(l) = 0 \tag{A.4d}$$

Combining Eqs. (A.4a−A.4d) and (A.1a−A.1d) leads to the formation of the following 2×2 system of equations

$$(\sin\beta l + \sinh\beta l)A + (\cos\beta l + \cosh\beta l)B = 0 \tag{A.5a}$$
$$(\cos\beta l + \cosh\beta l)A + (\sinh\beta l - \sin\beta l)B = 0 \tag{A.5b}$$

The integration constants C and D are found to be equal to zero. Arranging Eqs. (A.5a, A.5b) in the matrix notation of Eq. (3.7) leads to the following expressions for $[A_{Bernoulli}]$ and $\{x_{Bernoulli}\}$

$$[A_{Bernoulli}] = \begin{bmatrix} \sin\beta l + \sinh\beta l & \cos\beta l + \cosh\beta l \\ \cos\beta l + \cosh\beta l & \sinh\beta l - \sin\beta l \end{bmatrix} \tag{A.6a}$$

$$\{x_{Bernoulli}\} = [A \quad B]^T \tag{A.6b}$$

Substituting Eq. (A.6a) in Eq. (3.8) results in the following closed form expression

$$\cos\beta l \cosh\beta l + 1 = 0 \tag{A.7}$$

Equation (A.7) expresses the condition that β must satisfy in order for Eq. (3.7) to have a non-trivial solution. The ratio of the non-zero integration constants for a β value that satisfies Eq. (A.7) is given by

$$\frac{B}{A} = -\frac{\sin\beta l + \sinh\beta l + \cos\beta l + \cosh\beta l}{\cos\beta l + \cosh\beta l + \sinh\beta l - \sin\beta l} \tag{A.8}$$

Bernoulli–Euler Solution for a Freely-Hinged Articulated Rotor Blade

The boundary conditions for a freely-hinged rotor blade at the hub and tip modal ordinate locations ($x = 0$ and $x = l$ respectively) are given by

$$w(0,t) = 0 \Rightarrow \Phi(0) = 0 \tag{A.9a}$$
$$w''(0,t) = 0 \Rightarrow \Phi''(0) = 0 \tag{A.9b}$$
$$w''(l,t) = 0 \Rightarrow \Phi''(l) = 0 \tag{A.9c}$$
$$w'''(l,t) = 0 \Rightarrow \Phi'''(l) = 0 \tag{A.9d}$$

Combining Eqs. (A.9a−A.9d) and (A.1a−A.1d) leads to the formation of the following 2×2 system of equations

$$(-\beta^2 \sin\beta l)A + (\beta^2 \sinh\beta l)C \tag{A.10a}$$
$$(-\beta^3 \cos\beta l)A + (\beta^3 \cosh\beta l)C \tag{A.10b}$$

The integration constants B and D are found to be equal to zero. Arranging Eqs. (A.10a, A.10b) in the matrix notation of Eq. (3.7) leads to the following expressions for $[A_{Bernoulli}]$ and $\{x_{Bernoulli}\}$

$$[A_{Bernoulli}] = \begin{bmatrix} -\beta^2 \sin\beta l & \beta^2 \sinh\beta l \\ -\beta^3 \cos\beta l & \beta^3 \cosh\beta l \end{bmatrix} \tag{A.11a}$$

$$\{x_{Bernoulli}\} = [A \quad C]^T \tag{A.11b}$$

Substituting Eq. (A.11a) in Eq. (3.8) results in the following closed form expression

$$\sinh\beta l \cos\beta l - \sin\beta l \cosh\beta l = 0 \tag{A.12}$$

Equation (A.12) expresses the condition that β must satisfy in order for Eq. (3.7) to have a non-trivial solution. The ratio of the non-zero integration constants for a β value that satisfies Eq. (A.12) is given by

$$\frac{C}{A} = \frac{\sin\beta l + \cos\beta l}{\sinh\beta l + \cosh\beta l} \tag{A.13}$$

For the specific set of imposed boundary conditions, the Bernoulli–Euler beam has a rigid body mode of motion which corresponds to $\omega = \beta = 0$. Setting $\beta = 0$ in Eq. (3.4) results in the following

$$\Phi^{''''}(x) = 0 \tag{A.14a}$$
$$\Phi^{'''}(x) = a \tag{A.14b}$$
$$\Phi^{''}(x) = ax + b \tag{A.14c}$$
$$\Phi^{'}(x) = \frac{a}{2}x^2 + bx + c \tag{A.14d}$$
$$\Phi(x) = \frac{a}{6}x^3 + \frac{b}{2}x^2 + cx + d \tag{A.14e}$$

where a, b, c and d are real constants of integration. It can be shown by combining Eqs. (A.14b−A.14e) and Eqs. (A.9a−A.9d) that $a = b = d = 0$. The rigid body mode of motion can therefore be expressed as

$$\Phi(x) = Ax \tag{A.15}$$

where $A = c$ the only non-zero integration constant.

Bernoulli–Euler Solution for a Spring-Hinged Articulated Rotor Blade

The boundary conditions for a spring-hinged rotor blade at the hub and tip modal ordinate locations ($x = 0$ and $x = l$ respectively) are defined as follows

$$w(0,t) = 0 \Rightarrow \Phi(0) = 0 \tag{A.16a}$$
$$-EI_{midspan}w^{''}(0,t) = -Kw^{'}(0,t) \Rightarrow EI_{midspan}\Phi^{''}(0) = K\Phi^{'}(0) \tag{A.16b}$$
$$w^{''}(l,t) = 0 \Rightarrow \Phi^{''}(l) = 0 \tag{A.16c}$$
$$w^{'''}(l,t) = 0 \Rightarrow \Phi^{'''}(l) = 0 \tag{A.16d}$$

where $K = K^{flap}$ for flapwise bending and $K = K^{lag}$ for lagwise bending. Combining Eqs. (A.16a−A.16d) and (A.1a−A.1d) leads to the formation of the following 4×4 system of

equations

$$B + D = 0 \tag{A.17a}$$
$$KA + EI_{midspan}\beta B + KC - EI_{midspan}\beta D = 0 \tag{A.17b}$$
$$(-\beta^2 \sin \beta l)A + (-\beta^2 \cos \beta l)B + (\beta^2 \sinh \beta l)C + (\beta^2 \cosh \beta l)D = 0 \tag{A.17c}$$
$$(-\beta^3 \cos \beta l)A + (\beta^3 \sin \beta l)B + (\beta^3 \cosh \beta l)C + (\beta^3 \sinh \beta l)D = 0 \tag{A.17d}$$

Arranging Eqs. (A.17a, A.17d) in the matrix notation of Eq. (3.7) leads to the following expressions for $[A_{Bernoulli}]$ and $\{x_{Bernoulli}\}$

$$[A_{Bernoulli}] = \begin{bmatrix} 0 & 1 & 0 & 1 \\ K & EI_{midspan}\beta & K & -EI_{midspan}\beta \\ -\beta^2 \sin \beta l & -\beta^2 \cos \beta l & \beta^2 \sinh \beta l & \beta^2 \cosh \beta l \\ -\beta^3 \cos \beta l & \beta^3 \sin \beta l & \beta^3 \cosh \beta l & \beta^3 \sinh \beta l \end{bmatrix} \tag{A.18a}$$

$$\{x_{Bernoulli}\} = [A \quad B \quad C \quad D]^T \tag{A.18b}$$

The ratios of the integration constants contained in $\{x_{Bernoulli}\}$ for a β value that satisfies Eq. (3.8) is given by the following closed form expressions

$$B = \frac{-1 - \dfrac{\sin \beta l}{\sinh \beta l}}{\dfrac{\cos \beta l + \cosh \beta l}{\sinh \beta l} + \dfrac{2EI_{midspan}}{K}} A \tag{A.19a}$$
$$C = -\frac{2EI_{midspan}B + KA}{K} \tag{A.19b}$$
$$D = -B \tag{A.19c}$$

Appendix A

Appendix B

This appendix contains proof of orthogonality with regards to the flap and lag modes of motion obtained using the Lagrangian formulation presented in this paper. Due to the property of symmetry of the $[A^{flap/lag}_{Lagrange}]$ matrices, the following condition applies for their i^{th} and j^{th} eigenvectors

$$\{\bar{q}^{flap/lag}\}_i^T [M]^{flap/lag} \{\bar{q}^{flap/lag}\}_j = 0, \qquad i \neq j, \quad i,j = 1,...N \tag{B.1}$$

Expanding Eq. (B.1) results in the following

$$\sum_{k=1}^{N} \sum_{l=1}^{N} m_{l,k}^{flap/lag} \bar{q}_{i,l}^{flap/lag} \bar{q}_{j,k}^{flap/lag} = 0, \qquad i \neq j, \quad i,j = 1,...N \tag{B.2}$$

where $\bar{q}_{i,l}^{flap/lag}$ and $\bar{q}_{j,k}^{flap/lag}$ are the l^{th} and k^{th} elements of the eigenvectors $\{\bar{q}^{flap/lag}\}_i$ and $\{\bar{q}^{flap/lag}\}_j$ respectively for the flap and lag cases. The orthogonality condition between the i^{th} and j^{th} modes of flap and lag bending motion dictates that the following relation must apply

$$\int_{eR}^{R} \rho A(r) X_i^{flap,lag}(r) X_j^{flap,lag}(r) \mathrm{d}r = 0, \qquad i \neq j, \quad i,j = 1,...N \tag{B.3}$$

Substituting Eq. (3.36) into Eq. (B.3) results in an expression which is identical to the one given by Eq. (B.2) which is true due to Eq. (B.1). It has thus been shown that the orthogonality of the eigenvectors of $[A^{flap/lag}_{Lagrange}]$ due to their symmetric nature will also lead to the orthogonality of the final mode shapes given by Eq. (3.36). The analysis performed above can also be extrapolated in the context of modal amplitude normalization.

Appendix C

This appendix contains references to selected journal articles and conference publications produced, related to the work described within this thesis.

Journal Articles

- Goulos, I., Pachidis, V., DIppolito, R., Stevens, J., and Smith, C., "An Integrated Approach for the Multidisciplinary Design of Optimum Rotorcraft Operations," *Journal of Engineering for Gas Turbines and Power*, Vol. 134(9), 2012.

- Goulos, I., Pachidis, V., and Pilidis, P., "Lagrangian Formulation for the Rapid Estimation of Helicopter Rotor Blade Vibration Characteristics," *Article submitted to the Journal of the American Helicopter Society*, 2012.

- Goulos, I., Pachidis, V., and Pilidis, P., "Helicopter Rotor Blade Flexibility Simulation for Aeroelasticity and Flight Dynamics Applications," *Article submitted to the Journal of the American Helicopter Society*, 2012.

- Goulos, I., Pachidis, V., and Pilidis, P., "Effects of Fuselage Induced Velocity Perturbations on the Aeroelastic Response of a Hingeless Helicopter Rotor," *Article submitted to the Journal of Aircraft*, 2012.

Conference Proceedings

- Goulos, I., C.Celis, Pachidis, V., dIppolito, R., and Stevens, J., "Simulation framework development for aircraft mission analysis," *Proceedings of ASME Turbo Expo 2010, Glasgow, Scotland, UK*, Vol. 1, June 2010, pp. 341351.

- Goulos, I., Mohseni, M., Pachidis, V., dIppolito, R., and Stevens, J., "Simulation framework development for helicopter mission analysis," *Proceedings of ASME Turbo Expo, Glasgow, Scotland, UK*, Vol. 3, June 2010, pp. 843852.

- Goulos, I., Pachidis, V., DIppolito, R., Stevens, J., and Smith, C., "An Integrated Approach for the Multidisciplinary Design of Optimum Rotorcraft Operations," *Proceedings of ASME Turbo Expo, Copenhagen, Denmark*, No. GT2012-69583, 2012.

- Goulos, I., Pachidis, V., and Pilidis, P., "Helicopter Mission Performance Simulation using an Unsteady Aeroelastic Rotor Model," *Abstract submitted to the Proceedings of ASME Turbo Expo, San Antonio, Texas, USA*, June 2013.

- Goulos, I., Pachidis, V., DIppolito, R., Stevens, J., and Smith, C., "An Integrated Approach for the Multidisciplinary Optimization of Modern Rotorcraft Operations," *Proceedings of Aircraft Noise and Emissions Reduction Symposium, Marseille, France*, October 2011.

- dIppolito, R., Stevens, J., Pachidis, V., Berta, A., Goulos, I., and Rizzi, C., "A Multidisciplinary Simulation Framework for Optimization of Rotorcraft Operations and Environmental Impact," *2nd International Conference on Engineering Optimization*, 2012.

- Hempert, F., Goulos, I., Sethi, V., DIppolito, R., and DAuria, M., "Rotorcraft Engine Cycle Optimisation at Mission Level," *Abstract submitted to the Proceedings of ASME Turbo Expo, San Antonio, Texas, USA*, June 2013.

- Fakhre, A., Pachidis, V., Goulos, I., and Tafsheen, M., "Helicopter Mission Analysis for a Recuperated Turboshaft Engine," *Abstract submitted to the Proceedings of ASME Turbo Expo, San Antonio, Texas, USA*, June 2013.